UC Berkeley
UC Berkeley Electronic Theses and Dissertations

Title
Nuclear Data Evaluation of High-Energy Proton-Induced Reactions for Isotope Production

Permalink
https://escholarship.org/uc/item/4k69r77p

Author
Fox, Morgan

Publication Date
2021

Peer reviewed|Thesis/dissertation

Nuclear Data Evaluation of High-Energy Proton-Induced Reactions
for Isotope Production

by

Morgan B Fox

A dissertation submitted in partial satisfaction of the

requirements for the degree of

Doctor of Philosophy

in

Engineering – Nuclear Engineering

in the

Graduate Division

of the

University of California, Berkeley

Committee in charge:

Professor Lee Bernstein, Chair
Professor Karl van Bibber
Professor Massimiliano Fratoni
Professor David Shuster

Spring 2021

Nuclear Data Evaluation of High-Energy Proton-Induced Reactions
for Isotope Production

Abstract

Nuclear Data Evaluation of High-Energy Proton-Induced Reactions
for Isotope Production

by

Morgan B Fox

Doctor of Philosophy in Engineering – Nuclear Engineering

University of California, Berkeley

Professor Lee Bernstein, Chair

This dissertation details the first experiments of a newly formed Tri-laboratory Effort in Nuclear Data (TREND) between Lawrence Berkeley, Los Alamos, and Brookhaven National Laboratories. TREND was established to address lacking high-energy charged-particle data needs for isotope production by measuring proton-induced nuclear reaction cross sections from 35 to 200 MeV. The experimental methods and results for multiple stacked-target irradiations performed in support of this effort using arsenic, niobium, copper, and titanium targets are discussed. An extensive focus dedicated to the characterization of the ^{75}As(p,x)^{72}Se, ^{68}Ge excitation functions is included on account of their sought-after promise as generator nuclei for PET imaging.

In addition to providing direct information for the production of medical radionuclides, the TREND results were used to develop a new data analysis methodology for high-energy (p,x) reactions. Moreover, this thesis uniquely merges experimental work and evaluation techniques with the introduction of a standardized original evaluation procedure that can be used to optimize the planning and execution of isotope production with high-energy, high-intensity proton accelerators. The presented methodology provides insight into pre-equilibrium reaction dynamics and a host of nuclear data properties relevant to the accurate modeling of high-energy proton-induced reactions. Notably, this evaluation approach also includes a new method for charged-particle data validation.

Finally, this dissertation discusses the fabrication and characterization of the thin arsenic targets used in the stacked-target irradiations at the heart of the TREND experiments. The work herein aims to bolster modern targetry knowledge and depicts the difficulties and successes in meeting uniformity and thickness requirements for arsenic targets. A new thin-target characterization technique, developed using traditional neutron activation tools, that is reliable, accessible, and non-destructive is presented.

There exists untenable uncertainty and unreliability for the use of nuclear reaction codes in the medical isotope production community, particularly at high-energies, where charged-particle modeling suffers or is naïvely determined because little guiding data and evaluation exist. Altogether, this dissertation is an essential improvement of the infrastructure critical to the future of charged-particle isotope production and foundational nuclear data.

How can you not be romantic about baseball?

Contents

List of Figures

List of Tables

Acknowledgments

I have no doubt that this thesis was only possible because of the kindness, support, and guidance given to me by a great many people. Although I will never be able to repay their help, I would be remiss to not thank them.

Lee, my future is changed, and categorically better, because you took a chance to invite me into your world and be a truly wonderful adviser. You prioritized my learning, my research, and my well-being all these years, and even invited me into your family and your life, all while being an invaluable teacher and mentor. You have always encouraged me, motivated me, and put trust in me. I've had the chance to collaborate with incredible people that I would have otherwise never met, the chance to pretend to be an adult and a professional, and the chance to travel and enjoy an experience far beyond that of a standard grad student because of you. I wouldn't have considered any of this for any other adviser. Thank you.

Andrew and Jon, the two of you showed me more kindness and patience than could ever be expected. You both know, and I know, that this work met any sort of success, and exists in the first place, because of your efforts. You were fundamental in every aspect. You have both put in countless hours and worry and I cannot express how thankful I am for your generosity and intelligence. I could not have met more friendly people who were willing to spend time with me these past years.

Amanda, I am so appreciative of the chance I had to work with you, you are a great friend and mentor. It wasn't just the time you took to help with research and running reaction codes but it was the help with managing conferences, with the ins and outs of a whole new world of nuclear data evaluation, and with remembering to eat lunch. Eric, you were my introduction to so much of this graduate life and showed me how to navigate a great deal of research, thank you for being a great teacher and friend. Catherine, Joey, Austin, Jason, Chris – I am so lucky to have had the chance to be in the same group as you and get to work with you.

I owe sincere gratitude to Etienne Vermeulen, Ellen O'Brien, and Dmitri Medvedev, who brought me into their circle and worked tirelessly to create the research program from which I so generously benefited. You have all been truly good, thoughtful people that have gone out of your way to teach and be welcoming. This thanks extends further to the LANL-IPF and BNL-BLIP groups, including Eva Birnbaum, Cathy Cutler, Meiring Nortier, David Reass, Mike Connors, and a multitude of Accelerator Operations staff.

Thank you to the staff and scientists at the 88-Inch Cyclotron – Darren Bleuel, Bethany Goldblum, Josh Brown, Shamsu Basunia, Aaron Hurst, Thibault Laplace, Brien Ninemire, Scott Small, Nick Brickner, Devin Thatcher, and all the rest of the operations, research, radiation protection, and facilities members – who made much of this science possible and

were always willing to lend help or advice. A special thank you to Jon Batchelder, you have been an amazing mentor and a constant source of encouragement, guidance, and organization.

To Arjan Koning, thank you for setting aside time from a mountain of responsibilities to talk with some kid who had come up to you at a conference and to even stick with him from across the world. You are a good-hearted, willing teacher and a role model. I cannot overstate how fortunate I am to be able to stand on your foundational and expansive work.

I owe a debt to Wes Frey, the McClellan team, Mike Zach, and Evan Still, who were roped into this project but always had time to spare and could not have been more accommodating.

Thank you to the United States Department of Energy Isotope Program for the funding that provided me the opportunity for research at Berkeley and that put in place a supportive and fruitful collaborative network.

To my committee – Dr. van Bibber, Dr. Fratoni, and Dr. Shuster – thank you for the time you took from your own lives to be a part of this process, to genuinely care about my efforts, and for your feedback. It means the world to have professors like you.

Pedro, you're the best. It's been a time, eh? Maybe you talked me into it, maybe you didn't. We did it together and I'm happy to have a friend like you. Andrea, you are a wonderful and caring friend. I am grateful to have met the two of you.

To everyone from CHAT, who stuck with me all these years, you were friends with me when I was a munchkin with braces and you are friends with me now. Thanks for keeping Toronto close by. To my friends from Eng Phys at Queen's, we spent years helping each other and I wouldn't be where I am today without you. To my friends at Berkeley, I couldn't wipe the smile off my face around you – you made each day enjoyable. To the Nuclear Engineering department at UC Berkeley, thank you for the memorable years.

To the Green Bay Packers, Aaron Rodgers, the Blue Jays, Raptors, and Maple Leafs; To Kawhi for four pretty good bounces; To Bautista for a deep drive to left – some highs, some heartbreaks.

Jon, Mitch, and Matt – you three are an endless source of buffoonery and a scary amount of support at any hour on any day. You somehow kept me sane and I wouldn't trade you for anything in the world.

Mom, Dad, Andrew, Mitch, Shannon, Uncle Mark, Aunt Heather, Sam, Adam, Bubi and Zaidi, and Bubi and Zaidi – words obviously can't capture your support. For you, my success was a foregone conclusion – not because it was inevitable that I would be smart enough, or good enough, or deserving enough, but because you believed in me, and that was enough.

Chapter 1

Introduction

1.1 Fundamentals of Nuclear Data

Descriptions and quantification of governing nuclear phenomena, such as reactions, fission, and structure and decay, formally termed nuclear data, underpin the development of essential sectors of society, including nuclear medicine, nuclear energy, non-proliferation, national security, and basic science.

However, the determination of the best values and attendant uncertainties for these nuclear observables is non-trivial and an expert dedicated community consequently bears the charge to measure, compile, evaluate, and validate nuclear data.

Evaluated nuclear data are a culmination and reconciliation of extensive, unique, and carefully crafted experimental measurements and theoretical models to derive a recommended set of adopted values, which reside in specialized libraries and databases. These recommendations are our prevailing best understanding of nuclear data observables and properly standardize the data use.

In an iterative fashion, new accurate and well-documented measurements of nuclear observables are used to improve the predictive powers of the nuclear models used to generate the evaluated data. These models can in turn be used to reduce the intensive, personalized experimental burden that accompanies novel data applications in cases such as next generation reactor creation, enhanced non-proliferation material accounting for advanced fuel cycles, and the development of more efficient mechanisms for the production of radiopharmaceuticals.

Considerable resources across the international community have been dedicated to the evolution of nuclear data over the past 60 years. The overall inception, processing, and use of nuclear observables throughout this time comprise a "Nuclear Data Pipeline" that is described below.

1.1.1   The Nuclear Data Pipeline

The work-flow and connections of the pipeline, describing how nuclear data are created, evaluated, and permeated, are illustrated in Figure 1.1 [1].

The pipeline process begins with detailed experiments motivated by curiosity or application that directly contribute to the nuclear data knowledge base. The multitude of resulting experimental observables with their attendant uncertainties lead into the compilation component of the pipeline, where research sourced from published journals, conference proceedings, and/or disseminated internal lab reports are collected in the Nuclear Science References (NSR) database [1–3].

Extracted useable numerical values for nuclear data observables from the NSR additions are compiled into the unevaluated libraries EXFOR (EXchange FORmat) [4] and XUNDL (Experimental Unevaluated Nuclear Data List) [5].

The EXFOR data stream compiles information from nuclear reaction experiments. The dominant stored quantities in EXFOR are cross sections, available for all measured historical incident and outgoing particle types, and for varying energy and angle dependencies. Cross sections are the most routinely used nuclear data observable, as they measure the fundamental and ubiquitously required probability of an incident particle interacting with a target nucleus to produce a specific outcome. The remainder of EXFOR is composed of fission product yields, fission multiplicities, resonance parameters, polarization data, and a myriad of other experiment-specific quantities. XUNDL is an EXFOR parallel for nuclear structure and decay data, which includes information of binding energies, excited levels, gamma transitions, lifetimes, and deformation. These databases provide convenient and quick access to an encyclopedic record of nuclear science for current researchers to guide novel work [1].

At the unevaluated library level, data is compiled as a matter of comprehensiveness but there is limited inherent accuracy checks between results for equivalent measurements or reflection of "superior" data. There are compilation procedures and review codes in place to perform corrections of evident errors or self-inconsistencies within any individual work but the assembled data generally very closely follow the published references [3].

Instead, following compilation is an explicit evaluation step. Here, expert researchers with an understanding of theoretical and experimental nuclear physics reconcile the compilation databases and produce recommended values. Reconciliation is a broad term here that encompasses a significant, regulated effort to perform meticulous assessments of input experiments – their configurations, outputs, and uncertainties – often with joining detailed theoretical calculations that iteratively model and constrain observables. Only the careful implementation of numerous evaluation methods results in globally consistent adopted values with uncertainties, as best as possible.

For structure and decay data in XUNDL, this reconciliation yields the Evaluated Nuclear

Structure Data File (ENSDF) [6]. The assessments of EXFOR data lead to the Evaluated Nuclear Data File (ENDF) [7]. ENDF is managed by the National Nuclear Data Center (NNDC) in the United States but equivalent international organizations have also produced like evaluated libraries. These include the Japanese Evaluated Nuclear Data Library (JENDL) [8] managed by the Japan Atomic Energy Agency (JAEA) and the Joint Evaluated Fission and Fusion File (JEFF) [9] from the Nuclear Energy Agency (NEA). Nuclear data evaluation is an international collaboration, addressing matters of global impact.

These listed libraries are the most commonly accessed because of their broad relevance but even their expansive nature is not exhaustive. Application-specific evaluated libraries that are limited in scope but yield specialized, highly relevant observables for given interests, similarly exist within the pipeline [1, 3]. Examples of these focused libraries include the International Reactor Dosimetry and Fusion File (IRDFF-II) [10], the Evaluated Gamma-ray Activation File (EGAF) [11] of neutron capture gamma-ray cross sections, the IAEA-medical charged-particle cross section database [12], and the Atlas of Gamma-rays from the Inelastic Scattering of Reactor Fast Neutrons [13]. Additional evaluated libraries that also do not suitably align with structure or reaction classifications are present in the pipeline. Representative cases are the Atlas of Neutron Resonances [14] containing capture resonance parameters, the TALYS Evaluated Nuclear Data Library (TENDL) [15] that deviates from strict evaluation guides to provide completeness for nuclear data observables where other libraries cannot extrapolate, and the Reference Input Parameter Library (RIPL) [16], which is a collection of evaluated numerical data input parameters necessary for advanced nuclear reaction modeling codes. While RIPL pulls some data from ENSDF (discrete level information, gamma transitions, deformation parameters), this Input Parameter Library extends to also store optical potentials, continuous nuclear level densities and γ-strength functions, and fission barriers.

The generation and interaction of these numerous evaluated libraries represent the best attempt at the production of comprehensive recommended data needed to perform simulations and calculations, to a minimum degree of accuracy and consistency, for any given field of application.

In brief, the remainder of the pipeline concerns processing of the evaluated data into formats usable by typical nuclear physics codes, then validation of the processed results, and finally release to application users. Validation is a key step where the evaluated data is tested through a class of exactly known problems termed integral benchmarks [1, 3]. These benchmarks take numerous nuclear data quantities as simulation inputs for a cross-cutting data problem such as critical assembly analysis. Precisely measured observables from these integral benchmarks are validated against the state-of-the-art simulations. At this stage, evaluations can be corrected and analyzed for errors if the global inputs create an output inconsistent with known reality.
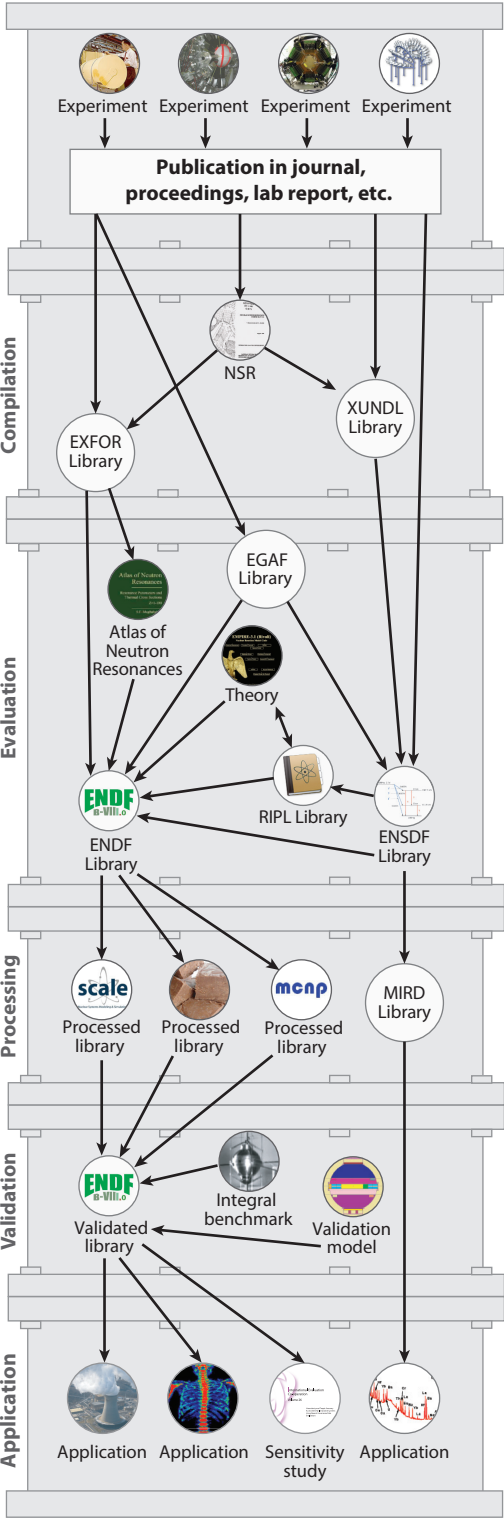
Figure 1.1: Graphical overview of the nuclear data pipeline [1]. The work-flow from experiments to evaluation to application is illustrated within this representation of concerted efforts to develop a best, recommended set of nuclear data observables.

1.1.2 A Skewed Evaluation Distribution

The history of human advancement in the nuclear age has justifiably brought certain highly-valued nuclear data observables to the forefront of systematic experimental measurement campaigns. The most prominent of these are neutron-induced reactions, including fission properties, and associated neutron parameters that are relevant to nuclear reactors and weapons. Even as applications of nuclear data have grown exponentially in recent decades, the dominance of neutron information is clear and easily described by the EXFOR data summary in Figure 1.2.

EXFOR has compiled information from nearly 24000 experiments since its inception but 46% of all the datasets are for neutron projectiles [4]. As evidenced in Figure 1.2, this is partly due to the earlier focus on neutron data versus all else, but the continued dominance, where neutron measurements still outweigh all charged-particle data combined to-date, reflects a lasting bias.

This bias, while benefiting the needs of next generation reactor development and safeguards, results in an overwhelming emphasis on neutron reaction information at $25\,\mathrm{meV}$, fast fission energies, and $14.1\,\mathrm{MeV}$ [1]. This has a profound impact for the field of accelerator-based isotope production, since charged-particle reactions instead play the central role.

The skew towards (n,x) reactions in compiled data further permeates to the downstream portions of the pipeline. Notably, only 21 elements have (p,x) ENDF evaluations (with only 10 having targets masses $A \geq 40$) despite the fact that these reactions account for 20% of the 24000 EXFOR entries, and approximately half of all compiled charged-particle cases [4]. This proton evaluation effort is dwarfed by the 106 elements evaluated for neutron reactions [7]. The evaluation for heavier incident charged-particles are almost entirely non-existent.

This disparity is actually more stark with further scrutiny. The proton evaluations are generally very limited and provide only basic elastic cross sections and a "lumped" cross section for everything else. Conversely, the neutron evaluations yield these same basic cross sections in addition to breakdowns into numerous specific reaction channels, detailed information for outgoing particle production, data with angular dependencies, resonance parameters, and uncertainty/covariance data.

Not surprisingly, the subsequent validation portion of the pipeline does not, and implicitly cannot, have the capacity to test charged-particle data.

This discrepancy highlights that many new measurements need to be made for reactions that carry important societal impact and that the data community needs to develop new tools for incorporating charged-particle data into the evaluation and validation sections of the pipeline.
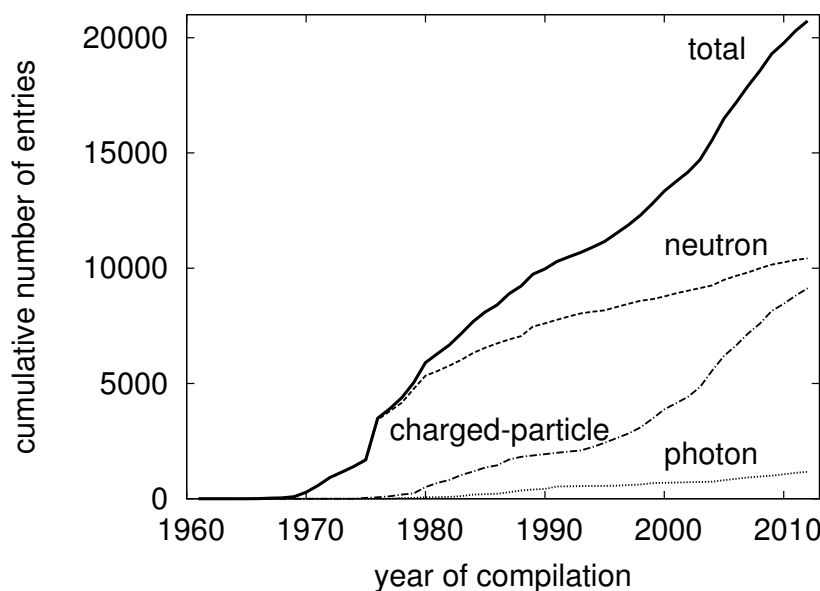
Figure 1.2: Evolution of cumulative number of EXFOR entries (experimental studies) throughout each year of compilation [17].

1.2 Isotope Production and Nuclear Data

Radionuclides near the valley of stability have unique properties that make them promising tools for an assortment of applications covering frequent issues such as the diagnosis and treatment of cancers, to more trailblazing cases of aerospace power and safety, and innovative environmental tracers.

The structure and decay nuclear data for these unstable nuclei are generally well-characterized through ENSDF. These data most notably include nuclide lifetimes, decay paths with complete descriptions of decay energetics and outgoing particles, and excited level information of daughter nuclei with key gamma transitions [1, 3].

In the nuclear medicine domain, different isotope-specific data lead to different specialized procedures. The most common worldwide medical radioisotope is ^{99m}Tc with a half-life of $t_{1/2} = 6.0067\,(5)$ hr. This technetium isomer decays predominantly via the emission of a single 140 keV γ-ray and is accessible by the "generator" parent nuclide ^{99}Mo ($t_{1/2} = 65.976\,(24)$ hr), typically produced from fission of ^{235}U in reactors [1, 18]. ^{99}Mo is termed a generator because it decays to the shorter-lived ^{99m}Tc on time scales suitable for widespread shipping such that the isomer is available for use in locations away from the production site as needed. The combination of an historically conventional ease of production for ^{99}Mo/^{99m}Tc by "piggy-backing" on the existing fleet of reactors, the nuclide half-lives, and their decay parameters – with the available established x-ray detection technology – formed an ideal synergy at the

advent of nuclear medicine. Today, ^{99m}Tc is used in 30 to 40 million single photon emission computed tomography (SPECT) imaging scans annually, representing 80% of all nuclear medicine procedures [19, 20].

This is the most obvious and popular example of intertwined nuclear data and medical isotope production, but the number of nuclei near the valley of stability, which can be used for medical applications is far more extensive. Nuclear medicine research includes β^+-, β^--, α-, and Auger electron emitting radionuclides that can yield increasingly efficacious diagnostic and therapeutic mechanisms. Hundreds of unstable nuclei meet criteria worth exploring and their future measurement and evaluation will necessarily benefit end-users through SPECT, position emission tomography (PET) with multimodal extensions of PET/MRI (magnetic resonance imaging) and PET/CT (computed tomography), brachytherapy, radioimmunotherapy, and theranostics [1].

However, the identification and prioritization of promising isotopes is a comparatively easy task relative to their actual production. Specifically, significant uncertainty and gaps in knowledge are present for the production cross sections of these promising nuclei off-stability, which generally require charged-particle-induced formation pathways and therefore suffer from the rooted neutron information data bias.

A rising concerted effort to address these nuclear data medical isotope production needs over the previous decade has generated a number of papers and explicit recommendations. Representative work, which include exhaustive lists of these data needs and overviews of current approaches to all nuclear medicine procedures are provided in [21–25].

1.2.1 Reactor and Accelerator Production

At surface level, the prevalence of compiled and evaluated neutron data seems to invite an obvious reactor-centric approach to medical isotope production. However, reactor production is not as multifaceted as expected and in modern day, actually suffers from a slew of external problems from non-proliferation concerns, capacity downtime and disruptions causing supply shortages, and aging reactor facility retirements [19, 20]. Moreover, reactor isotope formation mechanisms are predominantly (n,f) or (n,γ), meaning that not only are the bulk of evaluated neutron data extraneous but that many promising nuclei surrounding the valley of stability are also simply inaccessible when limited to these two reaction routes. Lastly, it is worth noting that the requirement of high specific activity for a radiopharmaceutical is often incompatible with neutron capture since the radionuclide cannot be chemically separated from the production target.

Consequently, a paradigm shift towards accelerator-based isotope production is underway in the field of nuclear medicine. Even the "poster-child" ^{99m}Tc is transitioning from reactor-only production. Particularly, charged-particle accelerators, offering direct charged-particle

reactions (p/d/t/^{3}He/...,x), the creation of high-intensity and energy neutrons from spallation neutron sources or deuteron breakup, or bremsstrahlung-generated photons, are versatile alternatives [19, 20].

Accelerators can spread production supply over a greater number of regional and local facilities to prevent disruptions, have full-time dedicated facilities, are free from restrictions of enriched fissile and problematic weapons-grade materials, and have little waste streams as compared to reactors [20]. Chiefly, accelerator production is appealing because of the access to a wider range of reaction routes and targets, meeting the requirements to reach the new specialized radionuclides that are stimulating the field.

Of course, isotope production through charged-particle accelerators is not an inherently novel application – many current diagnostic radionuclides are produced from accelerator technologies and many hospitals have accordingly already built local on-site low-energy medical cyclotrons. Perhaps the most ubiquitous example is the production of ^{18}F for PET. The short half-life of this radionuclide (109.77 (5) min [26]), and the lack of a longer-lived radionuclide generator, makes local production using a small cyclotron the only available option. Unfortunately, the low-energy accelerators used for ^{18}F can only produce a relatively limited number of radionuclides overall. Higher energy charged-particle accelerators are needed for the burgeoning demand of innovative emerging candidates and production routes central to the paradigm shift. Ultimately, charged-particle data measurements and evaluation form a critical path forward.

1.2.2 High-Energy Proton-Induced Evaluations

The leading accelerator facilities tackling these new isotope production and data research include the Isotope Production Facility at Los Alamos National Laboratory (IPF-LANL) and the Brookhaven LINAC Isotope Producer at Brookhaven National Laboratory (BLIP-BNL) in the United States, the TRIUMF laboratory in Canada, and iThemba LABS in South Africa [1]. These facilities perform regional isotope production using high-intensity, high-energy ($E_p \geq$100 MeV) (p,x) reactions on stable targets.

The historical (n,x) data skew in EXFOR and ENDF rears its head at these accelerators where the lack of proton data creates inescapable significant uncertainties that shroud target design, optimal beam parameters, and contamination co-production knowledge. Furthermore, production capabilities cannot be supplemented with theory since accurate modeling, particularly of these high-energy reactions, is notoriously difficult. At this juncture, only 8 datasets guide high-energy proton-induced reaction modeling for $E_p \geq 100$ MeV, leading to observed differences between theoretical predictions and eventual measurements on the order of 50–100% [27]. These 8 datasets from the available ≈24000 in EXFOR form the basis of high-energy proton-induced evaluations and theory. The dearth of high-energy proton-induced

data throughout the pipeline is unmistakable, and even within the neutron versus proton evaluation skew, there is this further energy range imbalance within the proton data itself.

The tasks of these accelerator facilities and the nuclear data community as a whole are then clear:

- Measure novel and effective (p,x) production cross sections for medical radioisotopes;

- Measure proton-induced secondary particle production at high-energies that bolster the data pipeline and are important for both recreating established reactor-based production and developing accelerators as versatile tools capable of concurrent multi-target production;

- Use the significant contribution of new measurements to develop high-energy proton data evaluations.

High-energy proton-induced reactions for medical isotope production are in-demand but the relevant nuclear data and associated development of the pipeline must be brought out from nascency.

1.3 Aim of Dissertation Work

The overall scope of this dissertation is to develop both nuclear data measurements and analysis/evaluation techniques for the production of medical isotopes using high-energy proton-induced reactions. This thesis details thorough experimental work performed as part of the TREND (Tri-laboratory Effort in Nuclear Data) measurement campaign at multiple high-energy proton accelerators and reports extensive proton reaction cross section data, from production thresholds up to 200 MeV. Specifically, this includes the investigation and exploration of proton reactions on niobium, arsenic, copper, and titanium targets.

In addition, this work uniquely spans both compilation and evaluation portions of the nuclear data pipeline, extending beyond basic cross section data creation to do detailed assessments of reaction theory, modeling parameters, and simulation predictions. Moreover, these theory studies transition into an original evaluation technique, merging experiment and evaluation for high-energy proton data in a first-of-its-kind procedure. This effort is an important, initial stepping stone in the path forward to more successfully building charged-particle data into the pipeline and more effectively using the data for applications.

This dissertation is organized into three chapters where the work therein follows from three manuscripts, which have been published or are in the publication process for peer-reviewed journals, and which have been presented at numerous conferences and workshops.

Chapter 2 presents the first iteration for combined high-energy proton data compilation and evaluation work following experiments conducted for p+^{93}Nb. A novel standardized evaluation procedure, initially crafted as a sensitivity study, is introduced in this chapter and comprehensively tested using the produced niobium data as well as prior existing lanthanum results from literature. Comments and reflections are subsequently developed surrounding high-energy reaction theory, and in particular, a previously unexplored transition from Hauser-Feshbach theory to the pre-equilibrium reaction mechanism is studied.

Chapter 3 is an extension to this original niobium analysis using experiments of p+^{75}As, ^{nat}Cu, and ^{nat}Ti. Specific nuclear medicine considerations are investigated here with the production of the ^{72}Se/^{72}As and ^{68}Ge/^{68}Ga PET generator systems via ^{75}As(p,x). The first measurements of ^{75}As(p,x)^{68}Ge as well as the most well-characterized excitation function for ^{75}As(p,4n)^{72}Se from threshold to 200 MeV are reported, and isotope production recommendations based on integral yield calculations are made. The measured data are further studied as part of the introduced standardized evaluation procedure and used to test the reaction theory considerations developed in Chapter 2. This additional Chapter 3 data work is pivotal to the continued evolution of the high-energy proton data evaluation process as it provides a more varied investigation of modeling theory inputs, most notably continuum properties such as nuclear level densities, and addresses multiple limitations that were unknown in the niobium and lanthanum cases.

Finally, Chapter 4 delivers an engineering aside into the target fabrication that makes data investigations and eventual theory work possible. The details of arsenic target preparation performed for the TREND experiments are given, which include an innovative environment-independent neutron activation approach to thin-target characterization that is a new methodology for charged-particle measurement setups.

The totality of this dissertation is an important step to developing the infrastructure critical to the future of charged-particle isotope production and foundational nuclear data.

Chapter 2

Investigating High-Energy Proton-Induced Reactions on Spherical Nuclei: Implications for the Pre-Equilibrium Exciton Model

In the latter months of 2018, the Isotope Program within the U.S. Department of Energy's Office of Science recognized the scarcity of high-energy charged-particle nuclear data hindering medical radionuclide production at regional accelerator facilities. In response, the Isotope Program established a collaborative effort comprised of researchers from Lawrence Berkeley, Los Alamos, and Brookhaven National Laboratories to address this lacking data for reactions relevant to the production of both current and novel radioisotopes.

The organizational support dedicated to developing charged-particle information reflects the growing importance of nuclear data to areas of great societal impact, not only limited to the creation of new drugs and treatments to combat illness. The national lab teaming ties together three prominent nuclear data facilities and provides an innovative capability to perform experiments and extract high-fidelity data across broad energy ranges with a larger set of parameter considerations than the norm. This chapter introduces this Tri-laboratory collaboration, termed throughout this dissertation as TREND (Tri-laboratory Effort in Nuclear Data), and details the associated experimental works that are the focal point of this thesis.

The three accelerators central to TREND are the 88-Inch Cyclotron at Berkeley, the Isotope Production Facility (IPF) in Los Alamos, and the Brookhaven LINAC Isotope Producer (BLIP) at Brookhaven.

The 88-Inch Cyclotron, commissioned in 1961, is a K=140 sector-focused isochronous

cyclotron with both light- and heavy-ion capabilities. It utilizes custom-designed Electron Cyclotron Resonance ion sources, providing the ability to extract any stable beam (with a variety of possible charge states) between protons and fully-stripped uranium beams [28]. The isochronous trait together with the ion sources even affords the capability for beam mixtures, or "cocktail beams", using ions of near-identical charge-to-mass ratio, which are used to measure single-event upsets relevant to the aerospace industry [29]. Charged-particle beams are extracted from the accelerator using electrostatic deflectors and are carried to a given experimental cave from steering by dipole switching magnets and focusing from quadrupole magnets. The 88-Inch Cyclotron was used in this dissertation work to produce proton beams with energies up to 55 MeV.

The Isotope Production Facility is a 2004 addition to the earlier constructed Los Alamos Neutron Science Center accelerating structures complex in 1972 [30], and provided intermediate energy (100 MeV) proton beams for the TREND experiments. IPF extracts a 100 MeV positive-ion hydrogen beam following initial proton injector ion sources and dual positive- and negative-ion beam acceleration in a drift-tube LINAC. While the positive-ions are diverted to IPF, the negative-ion beam is alternatively further injected into an 800 m side-coupled cavity linear accelerator to output ions at a maximum 800 MeV for a variety of other industrial, fundamental science, and national security research facilities. Irradiation at IPF occurs 40 feet below ground within a water-cooled target chamber. Both thin- and production targets alike are lowered into the proton beamline through a dedicated hot cell at the facility [31].

Built in 1972, and upgraded over the subsequent decades to increase high-current capabilities and reliability, BLIP was the pioneer facility to utilize high-energy proton accelerators for efficient and economical large-scale production of medical radionuclides [32]. The highest energy data produced by the TREND collaboration comes from BLIP where the delivered proton beam is a diverted excess of the 200 MeV, 500 foot proton LINAC supply that injects into larger synchrotrons (Booster, Alternating Gradient Synchrotron, and the Relativistic Heavy Ion Collider) at Brookhaven [33]. The BLIP beam enters a heavily shielded and cooled target irradiation site located 30 feet below ground, following a 30 m long transport line from its deflection point in the LINAC by bending magnets. A dedicated hot cell manages the delivery and recovery of irradiated material from the target station [33].

The initial goal of TREND is to measure (p,x) reactions relevant to isotope production from threshold to 200 MeV for as many exit channels as possible. This chapter expands on this cause and thoroughly details the stacked-target experimental methodology and analysis employed to extract proton-induced production cross sections. Niobium targets, which are relevant to isotope production as new beam monitor standards for intermediate-energy proton experiments, are the measurement focus of this initial portion of the dissertation. However, the reported cross section results form just one component of this chapter as this work additionally includes rigorous considerations of nuclear reaction code performance,

assessments of the gaps in modeling theory between Hauser-Feshbach and pre-equilibrium regimes, and the creation of an evaluation procedure with validation where none existed. The experimental and theoretical investigations of this section define the overall scope of this thesis and serve as a contextual and physics basis for succeeding chapters.

Relevant Publications:

M.B. Fox, A.S. Voyles, J.T. Morrell, L.A. Bernstein, A.M. Lewis, A.J. Koning, J.C. Batchelder, E.R. Birnbaum, C.S. Cutler, D.G. Medvedev, F.M. Nortier, E.M. O'Brien, and C. Vermeulen, Investigating high-energy proton-induced reactions on spherical nuclei: Implications for the preequilibrium exciton model, *Physical Review C*, 103(3):034601, 2021. `doi:10.1103/PhysRevC.103.034601`.

The text and figures of this paper (copyright American Physical Society 2021) [34], of which I was the primary author, are included in this chapter following necessary co-author permissions. The only changes made to the published article are alterations to some figures to better fit the page formatting, and renumbering of the references, equations, tables, and figures.

2.1 Abstract

A number of accelerator-based isotope production facilities utilize 100- to 200-MeV proton beams due to the high production rates enabled by high-intensity beam capabilities and the greater diversity of isotope production brought on by the long range of high-energy protons. However, nuclear reaction modeling at these energies can be challenging because of the interplay between different reaction modes and a lack of existing guiding cross section data. A Tri-lab collaboration has been formed among the Lawrence Berkeley, Los Alamos, and Brookhaven National Laboratories to address these complexities by characterizing charged-particle nuclear reactions relevant to the production of established and novel radioisotopes. In the inaugural collaboration experiments, stacked-targets of niobium foils were irradiated at the Brookhaven LINAC Isotope Producer ($E_p = 200\,\mathrm{MeV}$) and the Los Alamos Isotope Production Facility ($E_p = 100\,\mathrm{MeV}$) to measure ^{93}Nb(p,x) cross sections between 50 and 200 MeV. First measurements of the ^{93}Nb(p,4n)^{90}Mo beam monitor reaction beyond 100 MeV are reported in this work, as part of the broadest energy-spanning dataset for the reaction to date. ^{93}Nb(p,x) production cross sections are additionally reported for 22 other measured residual products. The measured cross section results were compared with literature data as well as the default calculations of the nuclear model codes TALYS, CoH, EMPIRE, and ALICE. The default code predictions largely failed to reproduce the measurements, with consistent

underestimation of the pre-equilibrium emission. Therefore, we developed a standardized procedure that determines the reaction model parameters that best reproduce the most prominent reaction channels in a physically justifiable manner. The primary focus of the procedure was to determine the best parameterization for the pre-equilibrium two-component exciton model via a comparison to the energy-dependent ^{93}Nb(p,x) data, as well as previously published ^{139}La(p,x) cross sections. This modeling study revealed a trend toward a relative decrease for internal transition rates at intermediate proton energies ($E_p = 20 - 60$ MeV) in the current exciton model as compared to the default values. The results of this work are instrumental for the planning, execution, and analysis essential to isotope production.

2.2 Introduction

The continued rise of nuclear medicine to study physiological processes, diagnose, and treat diseases requires improved production routes for existing radionuclides, as well as new production pathways for entirely novel radioisotopes [35]. The implementation of these new methodologies or products in nuclear medicine relies on accurate and precise nuclear reaction cross section data in order to properly inform and optimize large scale creation for clinical use [1, 12, 36–39]. A primary component in obtaining these data is a suitable reaction monitor, defined as a long-lived radionuclide with a well-known cross section as a function of incident beam energy, that can accurately describe beam properties during a production irradiation [28, 36, 38, 40, 41].

In the case of high-energy proton-induced reactions, which are important production routes at national accelerator facilities on account of the high beam intensities and large projectile range in targets [1, 12, 38], the ^{93}Nb(p,4n)^{90}Mo reaction is emerging as a valuable new monitor candidate as evidenced by [36].

In this work, proton-induced reaction cross sections for ^{93}Nb were measured for energies 50–200 MeV using the stacked-target activation technique. The results include the first cross section measurements for ^{93}Nb(p,4n)^{90}Mo beyond 100 MeV within the most comprehensive dataset for the reaction to date, spanning over the broadest energy range.

In addition to the (p,4n) channel, production cross sections were extracted for 22 additional reaction products. This extensive body of data forms a valuable tool to study nuclear reaction modeling codes and assess the predictive capabilities for proton reactions on spherical nuclei up to 200 MeV [27, 39, 42–45], which have been studied less than neutron-induced reactions [46]. It was demonstrated that default modeling predictions from TALYS, CoH, EMPIRE, and ALICE codes failed to reproduce the measured niobium data and required modifications to improve [47–50]. In this manuscript, we set forth a systematic algorithm to determine the set of reaction model input parameters, in a scientifically justifiable manner, that best

reproduce the most prominent reaction channels. The algorithm is built in the TALYS modeling framework and sets a premier focus on determining the best parameterization of the two-component exciton model in order to gain insight into high-energy pre-equilibrium reaction dynamics [27, 47, 51]. The algorithm was then further applied to existing high-energy ^{139}La(p,x) data. Taken together, this work suggests that the default internal transition rates of the exciton model must be modified as a function of exciton number and total system energy when considering residual product data from high-energy proton-induced reactions.

The fitting methodology proposed in this work aims to improve an accepted approach in cross section measurement literature where too few observables are used to guide modeling parameter adjustments, thereby potentially subjecting the modeling to compensating errors.

The results of this work should benefit the experimental and theoretical calculations central to isotope production planning and execution, as well as help inform the physical basis of the exciton model.

2.3 Experimental Methods and Materials

The charged-particle irradiations in this work were performed as part of a Tri-lab collaboration between Lawrence Berkeley National Laboratory (LBNL), Los Alamos National Laboratory (LANL), and Brookhaven National Laboratory (BNL). The associated experimental facilities were the 88-Inch Cyclotron at LBNL for proton energies of $E_p < 55$ MeV, the Isotope Production Facility (IPF) at LANL for $50 < E_p < 100$ MeV, and the Brookhaven LINAC Isotope Producer (BLIP) at BNL for $100 < E_p < 200$ MeV.

2.3.1 Stacked-Target Design

The stacked-target activation technique was employed in this work, where three separate target stacks were constructed and irradiated, each at a different accelerator facility. The stacked-target approach requires a layered ensemble of thin foils such that induced activation on these foils by a well-characterized incident charged-particle beam allows for the measurement of multiple energy-separated cross section values per reaction channel. Monitor foils are included among the thin foil targets in order to properly assess the beam intensity and energy reduction throughout the depth of the stack. Degraders are additionally interleaved throughout the stack to reduce and selectively control the primary beam energy incident upon each target foil [36, 39, 40].

2.3.1.1 LBNL Stack and Irradiation

The initial primary motivation for these Tri-lab stacked-target experiments was to determine residual nuclide production cross sections for ^{75}As(p,x) from threshold to 200 MeV, with a specific focus on the production of ^{68}Ge and ^{72}Se for PET imaging. However, the ^{76}Se compound system is non-spherical, which could necessitate the use of coupled-channel calculations in the reaction modeling. Deformed systems may also require the use of a modified Hauser-Feshbach code that extends angular momentum and level density considerations to include nuclei spin projections on the symmetry axis. This modification is presented in Grimes [52] and suggests an increased accuracy for deformed nuclei calculations versus the assumption of spherical symmetry inherent to the standard Hauser-Feshbach formalism. Yet these deformation aspects lie beyond the scope of this current paper and in turn, the results from the ^{75}As(p,x) measurements will be presented in a separate publication.

Consequently, the LBNL stack in this campaign focused only on arsenic targets and did not contain niobium foils. The experimental setup and procedure at this site will therefore not be discussed in this work.

2.3.1.2 LANL Stack and Irradiation

The IPF stack utilized 25 µm ^{nat}Cu foils (99.999%, LOT: U02F019, Part: 10950, Alfa Aesar, Tewksbury, MA 01876, USA), 25 µm ^{nat}Al foils (99.999%, LOT: Q26F026, Part: 44233, Alfa Aesar), 25 µm ^{nat}Nb foils (99.8%, LOT: T23A035, Alfa Aesar), and thin metallic ^{75}As layers electroplated onto 25 µm ^{nat}Ti foil backings (99.6%, TI000205/TI000290, Goodfellow Metals). ^{nat}Nb is 100% ^{93}Nb isotopic abundance.

Ten copper, niobium, and aluminum foils each were cut into 2.5 cm × 2.5 cm squares and their physical dimensions were characterized by taking four length and width measurements using a digital caliper (Mitutoyo America Corp.) and four thickness measurements taken at different locations using a digital micrometer (Mitutoyo America Corp.). Multiple mass measurements at 0.1 mg precision were taken after cleaning the foils with isopropyl alcohol. Ten titanium foils were cut to the same approximate sizes but the same dimensioning and weighting techniques could not be used due to the chemical and mechanical constraints of the collaboration-developed electroplating process. Instead, the nominal manufacturer thickness and density were accepted for the titanium, with confidence and uncertainties gathered from separate physical measurements of extra titanium foils not used in the stack. The creation and characterization of the accompanying 2.25 cm diameter arsenic depositions used in this stack will be described in detail in a future publication dedicated to the arsenic irradiation products. This characterization involved dimensional measurements, electron transmission, and reactor-based neutron activation analysis.

The electroplated arsenic targets, as well as the niobium foils, were sealed using LINQTAPE PIT0.5S-UT Series Kapton polyimide film tape composed of 12 µm of silicone adhesive on 13 µm of polyimide backing (total nominal 3.18 mg/cm^2). The copper and aluminum foils were not encapsulated in any tape.

The electroplated arsenic foils were attached to ten acrylic frames (1.5 mm in thickness), which protected the foils during handling and centered them in the bombardment position after the stack was fully arranged. The ten copper foils were treated in an identical manner. The aluminum and niobium foils were paired up and mounted on the front and back of the same frames due to physical space limitations of the machined 6061-T6 aluminum IPF target box. Nine aluminum 1100 series degraders were characterized in the same manner as the Cu, Nb, and Al foils and included in the stack to yield ten different beam energy "compartments" for cross section measurements. In each compartment, one ^{93}Nb+^{nat}Al target, one ^{75}As+^{nat}Ti target, and one ^{nat}Cu target were placed and bundled together using baling wire. The baling wire, attached at the top of the frames and not obstructing any target material, was necessary to aid the removal of the foils from the target box following irradiation using the hot cell's tele-manipulators. The assembled stack in the IPF target box can be seen in Figure 2.1, where it is also noted that the box has a 0.411 mm aluminum beam entrance window and is specially designed to be watertight since the IPF target station is located underwater. Additionally, stainless steel plates (approximately 100 mg/cm^2) were placed in the front and back of the stack. Post-irradiation dose mapping of the activated stainless plates using radiochromic film (Gafchromic EBT3) was used to determine the spatial profile of the beam entering and exiting the stack [36, 39].

The upstream beamline components at IPF have a significant effect on beam energy that must be taken into account [53]. Two materials exist upstream of the target box entrance window: the beam window separating beamline vacuum from the target chamber and a single cooling water channel defined by the distance between the beam window and the aluminum target box window during operation. The installed beam window is 0.381 mm thick Inconel alloy 718 and it is pre-curved toward the vacuum side of the beamline by 1.3 mm. However, under the hydrostatic and vacuum loading pressures experienced during operation, the beam window further elastically deforms toward the vacuum side. During operation at low beam currents, typical of this work, the beam window elastically deforms toward the vacuum side by approximately 0.12 mm. Given the geometry of the target box, this information implies that the proton beam travels through a cooling water channel 7.414 mm thick [53]. The combined upstream effects total an approximate effective degrader areal density of 1165 mg/cm^2.

The full detailed target stack ordering and properties for the LANL irradiation are given in Table 2.5 in Section 2.7. The stack was irradiated for 7203 seconds with an H$^+$ beam of 100 nA nominal current. The beam current, measured using an inductive pickup, remained stable under these conditions for the duration of the irradiation. The mean beam energy
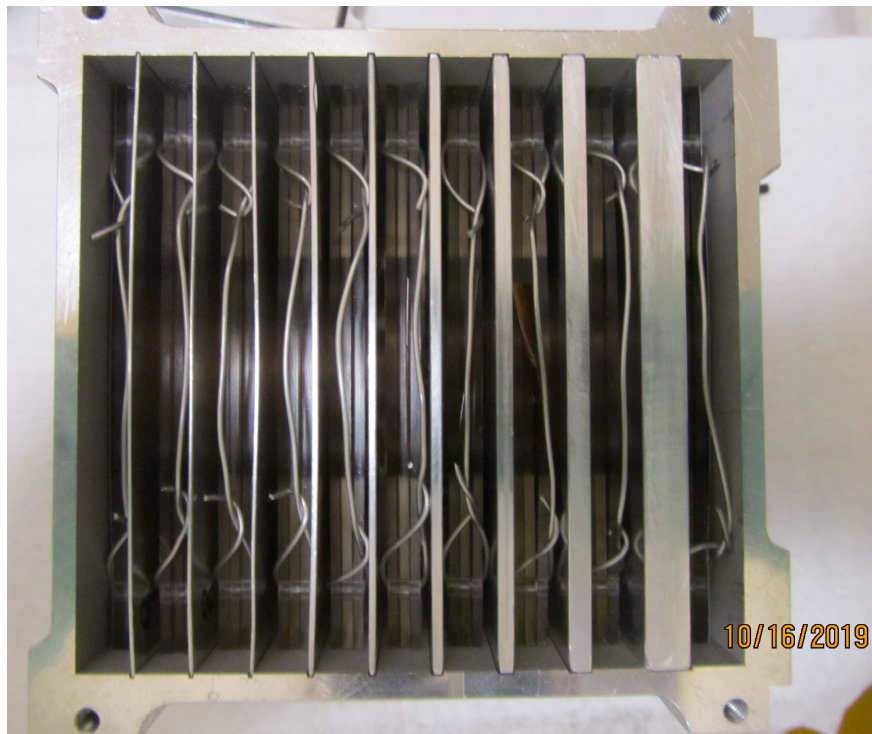
Figure 2.1: A top view of the assembled LANL target stack showing the ten target "compartments" separated by aluminum degraders. The beam enters through a 0.411 mm aluminum entrance window on the right hand side of the target box.

extracted was 100.16 MeV at a 0.1% uncertainty.

2.3.1.3 BNL Stack and Irradiation

The target stack for the BNL irradiation was composed of 25 µm ^{nat}Cu foils (99.95%, CU000420, Goodfellow Metals, Coraopolis, PA 15108-9302, USA), 25 µm ^{nat}Nb foils (99.8%, LOT: T23A035, Alfa Aesar), and thin metallic ^{75}As layers electroplated onto 25 µm ^{nat}Ti foil backings (99.6%, TI000205/TI000290, Goodfellow Metals). The arsenic targets were again produced by members of this collaboration and characterized similarly to the arsenic targets created for the LANL experiment. The copper, niobium, and titanium foils for BNL were prepared according to the process outlined for the same foils in Section 2.3.1.2.

Seven targets of each material were prepared for this irradiation and six copper degraders were in turn characterized to create seven energy compartments within the stack.

The electroplated arsenic targets were sealed using the same LINQTAPE PIT0.5S-UT Series Kapton polyimide film tape described in Section 2.3.1.2. The copper and niobium foils were encapsulated with DuPont Kapton polyimide film tape of 43.2 µm of silicone adhesive on 50.8 µm of polyimide backing (total nominal 11.89 mg/cm²). The foils were mounted to

plastic frames, with copper and niobium foils paired due to space limitations of the BLIP target box. Similar to the LANL irradiation, baling wire was used to secure one ^{nat}Cu+^{93}Nb target and one ^{75}As+^{nat}Ti target together in each energy compartment of the stack between degraders. The BNL target box, also specially designed to be watertight since the BLIP target station is located underwater, has a 0.381 mm aluminum beam entrance window. A single stainless steel plate could only be included at the beginning of the stack in this experiment to assess the physical beam profile post-irradiation due to space constraints.

BLIP facility upstream beamline components that influence beam properties were also included into the stack considerations. Beryllium and AlBeMet windows exist to facilitate the beamline vacuum connections; two stainless steel windows and two water cooling channels are also in place [54]. Together, these components give an approximately 1820 mg/cm^2 system that the proton beam must traverse before reaching the target box's aluminum window. Unlike IPF, possible deformation of the BLIP upstream windows under hydrostatic and vacuum loading conditions are not measured and may introduce unknown uncertainties to the stack characterization. Though the effect of these uncertainties is expected to be small due to the lower stopping power at a higher beam energy, corrections for potential changes to these upstream conditions are considered in the stack transport calculations in Section 2.3.3.

The BNL target stack (Table 2.6 in Section 2.7) was irradiated for 3609 seconds with an H$^+$ beam of 200 nA nominal current. The beam current during operation was recorded using toroidal beam transformers and remained stable under these conditions for the duration of the irradiation. The mean beam energy extracted was 200 MeV at a 0.2% uncertainty [55].

2.3.2 Gamma Spectroscopy and Measurement of Foil Activities

The collaborative nature of this work prompted the use of different types of germanium detectors and data acquisition systems to measure the induced activities of target foils.

2.3.2.1 LANL

The LANL counting took place at two locations. One ORTEC IDM-200-VTM High-Purity Germanium (HPGe) detector and one ORTEC GEM p-type coaxial HPGe detector (model GEM20P-PLUS) were used to capture short- and intermediate-lived activation species directly at the IPF site of target irradiation. The IDM is a mechanically-cooled coaxial p-type HPGe with a single, large-area 85 mm diameter × 30 mm length crystal and built-in spectroscopy electronics. The energy and absolute photopeak efficiency of the detectors were calibrated using standard ^{152}Eu, ^{207}Bi, and ^{241}Am sources as well as a mixed gamma source containing ^{57}Co, ^{60}Co, ^{109}Cd, and ^{137}Cs. The efficiency model used in this work is taken from the physical model presented by Gallagher and Cipolla [56]. The LANL countroom was further

commissioned to perform longer counts over a multi-week period, which was not possible at IPF. The countroom uses p-type ORTEC GEM series HPGes with aluminum windows.

Following the irradiation, the IPF target box was removed from the beamline and raised into the IPF hot cell. Tele-manipulators were used to disassemble the stack and extract the foils. The radiochromic film showed that an ≈1 cm diameter proton beam was fully inscribed within the samples throughout the stack. All target frames were wrapped in one layer of Magic Cover Clear Vinyl Self-Adhesive to fix any surface contamination. Due to elevated dose rates, only the arsenic, titanium, and copper targets were made available for counting on the day of irradiation. Initial data were acquired from 10–20 minute counts of the targets starting approximately 2 hours after the end-of-bombardment (EoB) at distances of 15 cm and 17 cm from the GEM detector face and 55 cm and 60 cm from the IDM face. One day post-irradiation, within 19 hours of EoB, the aluminum and niobium targets were accessible and counted multiple times along with the other targets throughout the day at positions of 15, 17, 25, 55, and 60 cm from the detector faces. Once appropriate statistics had been acquired to either establish necessary decay curves for induced products or characterize monitor reaction channels, all targets were packaged and shipped to the LANL countroom.

In the dedicated counting lab, the 40 available targets were first repeatedly cycled in front of detectors at 10–15 cm capturing 1 hour counts over the course of a week. The countroom curators varied the foil distance from the detector face on a regular basis to optimize count rate and dead time. The calibration data for each detector used, at each counting position, were collected each day and made available with the foil data. Over the following 6 weeks, cycling of the target foils in front of the detectors continued and count times were increased to 6–8 hours to capture the longest-lived activation products.

2.3.2.2   BNL

The BNL gamma spectroscopy setup incorporated two EURISYS MESURES 2 Fold Segmented "Clover" detectors in addition to two GEM25P4-70 ORTEC GEM coaxial p-type HPGe detectors and an ORTEC GAMMA-X n-type Coaxial HPGe detector (model GMX-13180). All detector efficiencies were calculated using a combination of ^{54}Mn, ^{60}Co, ^{109}Cd, ^{137}Cs, ^{133}Ba, ^{152}Eu, and ^{241}Am calibrated point sources, with the Gallagher and Cipolla [56] physical model. One GEM detector was situated in the BLIP facility at the irradiation site while the remaining detectors were in a counting lab in a neighbouring building.

Within 2 hours of EoB at BLIP, the copper foils and electroplated arsenic targets were removed from the hot cell and counted for over 10 minutes each using the GEM detector in the facility. The observed beam spot size on targets was ≈1 cm in diameter. Once the niobium foils had been pulled from the BLIP hot cell, all targets were transported to the nearby counting lab. There, the copper and arsenic foils were cycled first through 10–30 minute

counts, followed by hour long counts, on the Clovers and GEM at 10–15 cm from the detector faces. The niobium foils were assigned a similar counting scheme starting approximately 20 hours after EoB. Cycling and counting of the foils continued for an additional 24 hours.

Within two weeks of EoB, all targets were shipped back to LBNL. The subsequent gamma-spectroscopy at the 88-Inch Cyclotron utilized an ORTEC GMX series (model GMX-50220-S) HPGe, which is a nitrogen-cooled coaxial n-type HPGe with a 0.5 mm beryllium window and a 64.9 mm diameter × 57.8 mm long crystal. Multi-day to week-long counts of the copper, arsenic, and niobium foils were performed with the LBNL GMX over the course of 2+ months to ensure that all observable long-lived products could be quantified.

2.3.2.3 Activation Analysis

While the specifications of counting equipment and procedure varied between irradiations, the data analysis for the measurement of induced target activities and cross sections followed a standardized approach. The procedure is well-described in Voyles et al. [36] and Morrell et al. [39] but is included here for clarity and completeness.

The gamma emission peaks from decaying activation products were identified from the previously described gamma-ray spectra. These photopeaks were fit using the NPAT code package developed at UC Berkeley [57]. Example fits are shown in Figure 2.2 for a spectrum collected from the LANL Nb-SN1 target of the stack in Table 2.5 (see Section 2.7).

The activity A for each activation product of interest at a delay time t_d since the end-of-bombardment to the start of counting was then determined from the net counts found N_c after corrections for gamma intensity I_γ, detector efficiency ϵ, dead time, counting time, and self-attenuation within the foils according to:

$$A(t_d) = \frac{N_c \lambda}{(1 - e^{-\lambda t_{real}}) I_\gamma \epsilon} \frac{t_{real}}{t_{live}} F_{att}, \tag{2.1}$$

where λ is the decay constant for the radionuclide of interest, t_{real} and t_{live} describe the real and live time for detector acquisition, respectively, and F_{att} is the photon self-attenuation correction factor. F_{att} is calculated using photon attenuation cross sections retrieved from the XCOM database [58] and takes the convention that all activity is assumed to be made at the midplane of the foils.

The EoB activity A_0 for a given radionuclide was subsequently found from a fit to the relevant Bateman equation. Moreover, the benefit of repeated foil counts in this work and the use of multiple gamma-rays is evidenced here by providing multiple radionuclide activities at numerous t_d, which establish a consistent decay curve. Through a regression analysis of decay curves, it is possible to extract the A_0 for each activation product in a more accurate manner than simply basing its calculation on a single time point and a single gamma-ray observation.
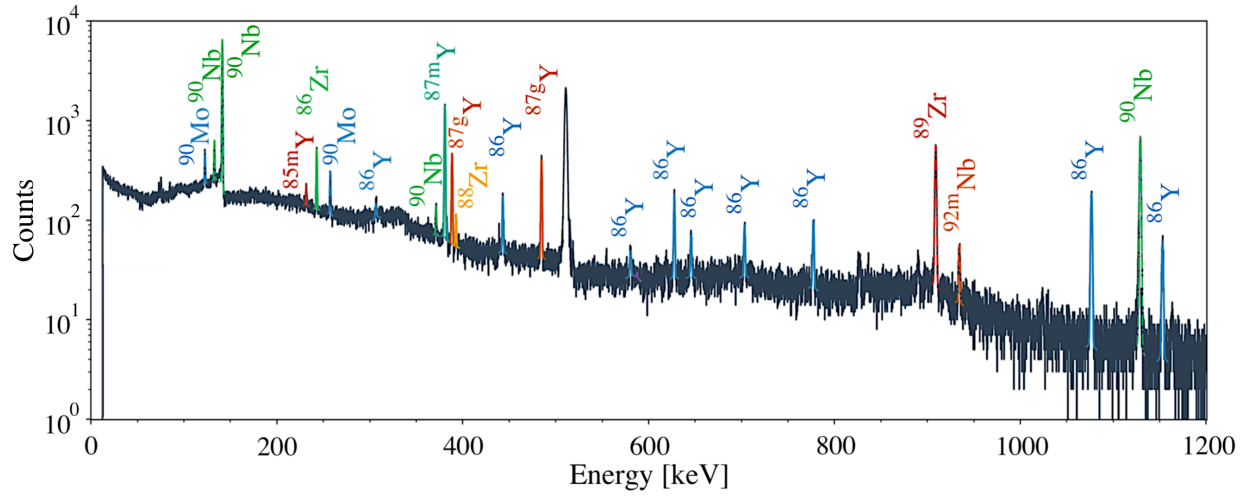
Figure 2.2: Example gamma-ray spectrum from the induced activation of a niobium target in the LANL stack at approximately $E_p = 91$ MeV. The spectrum was taken approximately 20 hours after EoB, and the smooth fits to the peaks of interest shown are produced by the NPAT package [57].

If an activation product of interest is populated without contribution from the decay of a parent radionuclide, the EoB activity is found from a fit to the first order Bateman equation:

$$A(t_d) = A_0 e^{-\lambda t_d}. \tag{2.2}$$

Typically, if it is needed to calculate EoB activities within a feeding chain in this work, the required calculation is only second order. This is the case for isomeric to ground state conversions as well as two-step beta-decay chains. In these circumstances, the decay curve is given by:

$$A_2(t_d) = A_{0,1} B_r \frac{\lambda_2}{\lambda_2 - \lambda_1} (e^{-\lambda_1 t_d} - e^{-\lambda_2 t_d}) + A_{0,2} e^{-\lambda_2 t_d}, \tag{2.3}$$

where $A_2(t_d)$ is still found from Equation (2.1), B_r is the decay branching ratio, and the 1 and 2 subscripts denote the parent and daughter nuclides, respectively, in the two-step decay chain. This two-step fit to calculate $A_{0,2}$ uses the independently determined $A_{0,1}$ from Equation (2.2) when possible, but otherwise both variables are fit together. The decay curve regressions in this work were additionally performed with the NPAT code package [57]. A regression example for the ^{86}Zr$\rightarrow^{86}$Y decay chain is shown in Figure 2.3.

The total uncertainties in the determined EoB activities had contributions from uncertainties in fitted peak areas, evaluated half-lives and gamma intensities, and detector efficiency calibrations. Each contribution to the total uncertainty was assumed to be independent and was added in quadrature. The impact of calculated A_0 uncertainties on final cross section results is detailed in Section 2.3.4.
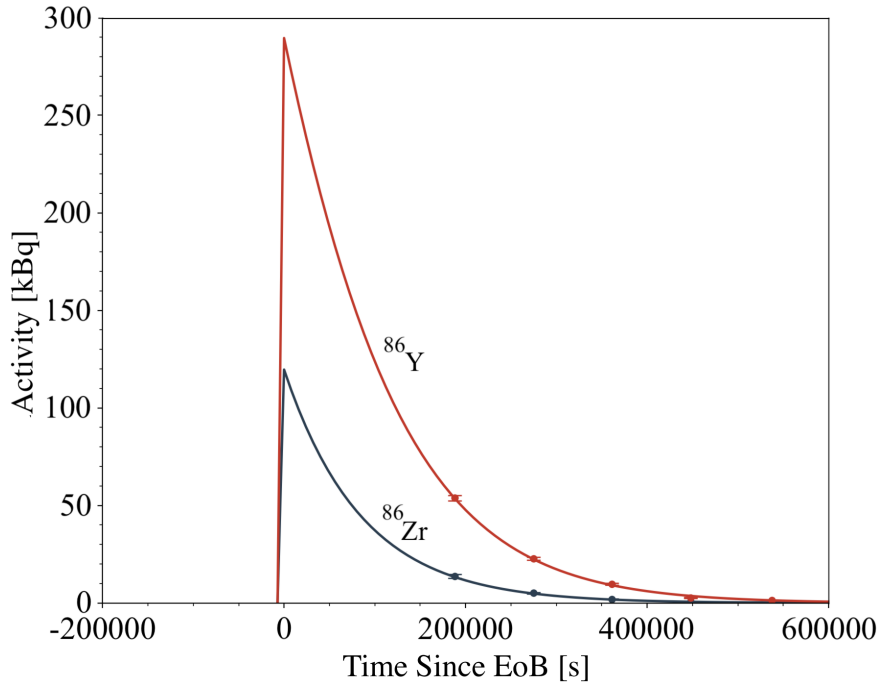
Figure 2.3: Example of initial activity fitting for two-step beta-decay chain of ^{86}Zr feeding ^{86}Y as residual products in the niobium irradiations.

2.3.3 Stack Current and Energy Properties

The methods of current monitoring during beam operation discussed in Sections 2.3.1.2 and 2.3.1.3 provide valuable information for the experimental conditions, their output is not sufficient to precisely describe the beam energy and intensity evolution throughout a target stack [36, 39–41]. Instead, more detailed calculations must be retrieved from monitor foil activation analysis, where known reaction cross sections can be used to measure beam current in the multiple energy positions of a stack.

The relevant proton fluence monitor reactions used in the irradiations were:

LANL

- ^{nat}Cu(p,x)^{56}Co, ^{58}Co, ^{62}Zn

- ^{nat}Ti(p,x)^{48}V

- ^{nat}Al(p,x)^{22}Na

BNL

- ^{nat}Cu(p,x)^{58}Co

where only reactions with IAEA-recommended data in the relevant proton energy ranges have been considered [59].

In the BNL irradiation, the lack of reliable data for high proton energy reactions precluded the use of most monitor channels and as a result only the ^{58}Co activation product was taken to extract the beam current. However, ^{nat}Cu(p,x)^{56}Co has significant data in this high-energy region and was preliminarily used as a validation of the beam current derived from the ^{58}Co calculations.

The A_0 for the monitor reaction products were calculated according to the formalism presented in Section 2.3.2.3. Since the beam was constant throughout the irradiation period, the proton beam current I_p was calculated at each monitor foil position by the relation:

$$I_p = \frac{A_0}{(\rho_N \Delta r)(1 - e^{-\lambda t_{irr}})\bar{\sigma}},$$ (2.4)

where I_p is output in units of protons per second, $(1 - e^{-\lambda t_{irr}})$ corrects for decay that occurred during the beam-on irradiation time t_{irr}, $\rho_N \Delta r$ is the relevant measured areal number density calculated from Tables 2.5 and 2.6 (see Section 2.7), and $\bar{\sigma}$ is the flux-weighted production cross section.

The $\bar{\sigma}$ formalism is needed to account for the energy width broadening resulting from energy straggle of the beam as it is propagated toward the back of the stack [36, 39–41]. Using the IAEA-recommended cross section data $\sigma(E)$ for the relevant monitor reactions [59], the flux-weighted cross section is calculated from:

$$\bar{\sigma} = \frac{\int \sigma(E)\phi(E)dE}{\int \phi(E)dE},$$ (2.5)

where $\phi(E)$ is the proton flux energy spectrum. $\phi(E)$ was determined here using an Anderson & Ziegler-based Monte Carlo code, as implemented in NPAT [57, 60]. The calculated energy spectrum resulting from the Anderson & Ziegler calculation in the LANL irradiation is shown in Figure 3.18 as an example.

The implementation of this monitor foil deduced current, following Equations (2.4) and (2.5), is shown for each irradiation site in Figure 2.5. Included in Figure 2.5 are weighted averages of all the available monitor foils for the fluence at each stack position. The weighted averages account for data and measurement correlations between the reaction channels in each compartment. An uncertainty-weighted linear fit is also included for each site as a global model to impose a smooth and gradual fluence depletion.
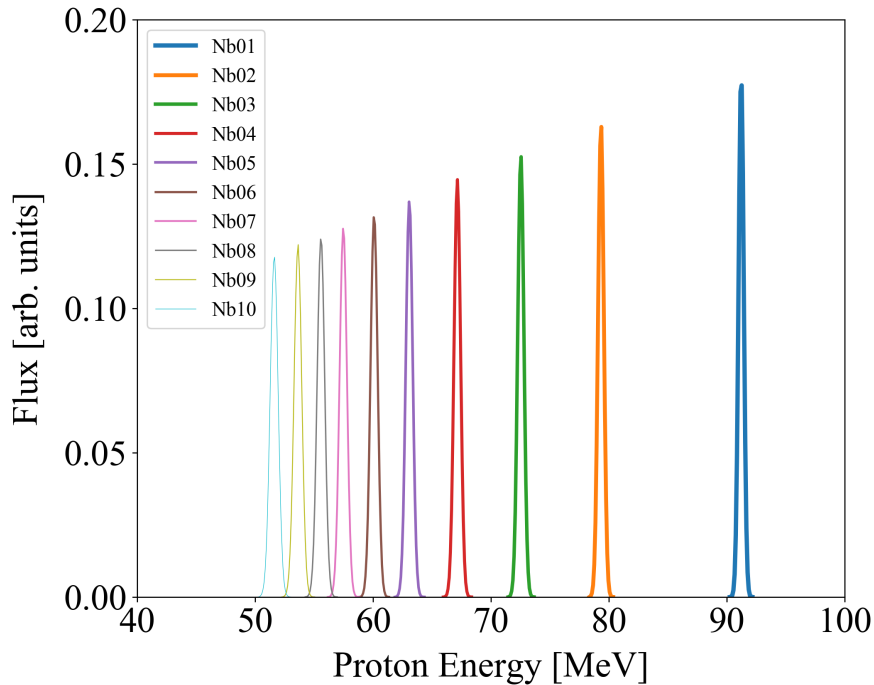
Figure 2.4: Visualization of the calculated proton energy spectrum for each niobium foil in the LANL stack.

Included in the results of Figure 2.5 is a reduction in systematic uncertainty using the "variance minimization" technique presented in Graves et al. [40], Voyles et al. [36], and Morrell et al. [39]. This technique was applied, as partial disagreement between the initial proton fluence predictions from each monitor channel in each energy compartment of the stack at each experiment site was observed. The disagreement was most noticeable near the rear of each stack where contributions of poor stopping power characterization, straggling, and systematic uncertainties from upstream components became most compounded. The independent measurements of proton fluence from the monitor reactions should all theoretically be consistent at each energy position given accurate monitor reaction cross sections and foil energy assignments. The variance minimization technique is a corrective tool applied to the stopping power in simulations to address this discrepancy through the treatment of the effective density of the Al/Cu degraders in each stack as a free parameter. This is reasonable because the majority of the stopping power for the beam occurs in the thick degraders. The free parameter can then be optimized by a reduced χ^2 minimization technique for the global linear fit of the monitor fluence data.

For both stacks, the degraders' effective densities were varied uniformly in the stopping power simulations by a factor of up to $\pm 25\%$ of nominal values. The resulting reduced χ^2 in each case is given in Figure 3.17. Figure 3.17 indicates that a change in degrader density, which is equivalent to a linear change in stopping power, of $+4.35\%$, and -1.84% compared to nominal measurements for the LANL and BNL stacks, respectively, minimizes the monitor

foil disagreement in each case. Previous stacked-target work has always shown a modest positive enhancement to the stopping power of $+2$–5%, which makes the BNL optimization interesting [36, 39]. It is likely that the negative adjustment in the BNL case is mostly due to compensation for the less well-known characterizations of the upstream cooling water channel and window deformation. It is also possible that some of this effect may be attributed to the use of copper degraders at BNL versus the aluminum degraders used at LANL and LBNL.

Monitor reactions that threshold in the energy region of the stack, such as ^{56}Co near the LANL stack rear, are extremely valuable in this minimization approach as they are most sensitive to changes in stopping power and energy assignment thereby providing physical limits for the problem. The relative shallowness of the BNL χ^2 curve is most likely due to the limitation of minimizing using just one monitor reaction. Note that this degrader density variation procedure is a computation tool to correct for poorly-characterized stopping power at these energies and does not mean that the actual degrader density was physically different than what was measured [39].

The minimized reduced χ^2 also provides optimized beam energy assignments for each foil in a stack from the corrected transport simulation. The energy assignments are the flux-averaged energies using $\phi(E)$ with uncertainties per foil taken as the full-width at half maximum. These energy assignments for the niobium targets are provided in Table 2.1.

In the BNL fluence results, the optimized global linear model provides an interpolation to each individual niobium foil with a better accuracy and uncertainty than just utilizing the sole ^{58}Co fluence prediction in each compartment. In the LANL fluence results, the linear fit was used for the variance minimization but the correlation-weighted-average values in each compartment were directly used for calculating production cross sections. This is possible without any need for interpolation or worry of model selection influence because of the contributions from multiple available monitor reactions.

2.3.4   Cross Section Determination

Given the activity, weighted-average beam current and energy, timing, and areal density factors previously discussed, the flux-averaged cross sections for products of interest in this work were calculated using Equation (2.6):

$$\sigma = \frac{A_0}{I_p(\rho_N \Delta r)(1 - e^{-\lambda t_{irr}})}. \tag{2.6}$$

The ^{93}Nb(p,x) cross section results are given in Table 2.1, which reports measurements for ^{93m}Mo, ^{92m}Nb, ^{91m}Nb, ^{90}Mo, ^{90}Nb, ^{89}Zr, ^{88}Zr, ^{88}Y, ^{87m}Y, ^{87}Y, ^{86}Zr, ^{86}Y, ^{86}Rb, ^{85m}Y, ^{84}Rb, ^{83}Sr, ^{83}Rb, ^{82m}Rb, ^{81}Rb, ^{75}Se, ^{74}As, ^{73}As, and ^{72}Se. The ^{75}As(p,x) data in addition to the ^{nat}Cu(p,x) and ^{nat}Ti(p,x) results will be detailed in a future publication.
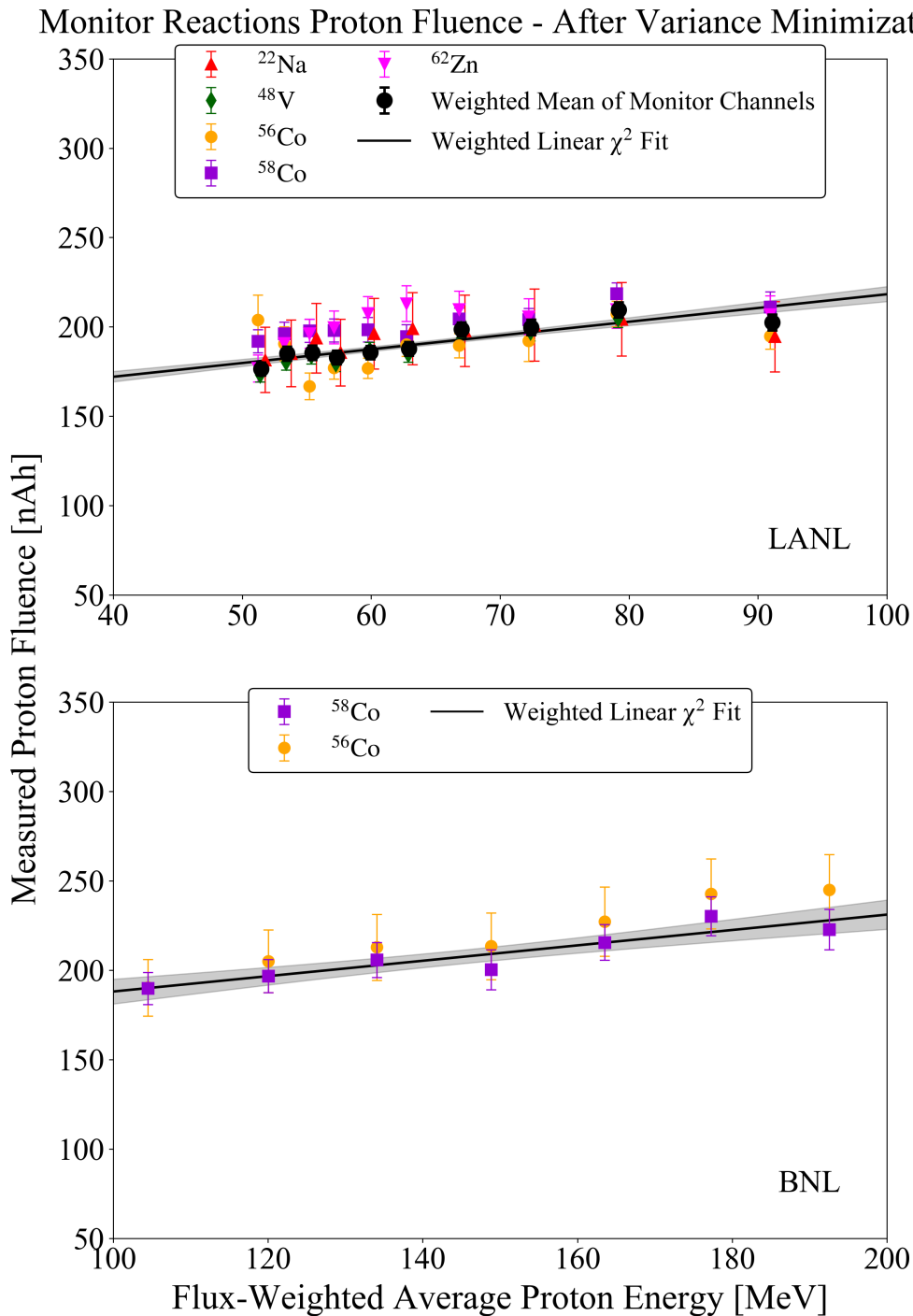
Figure 2.5: Plots of the proton beam current measured by monitor reactions in the LANL and BNL stacks following adjustments made by the variance minimization technique. The $^{nat}Cu(p,x)^{56}Co$ monitor reaction is plotted for BNL but its data were not used for any of the BNL fluence calculations or the variance minimization.
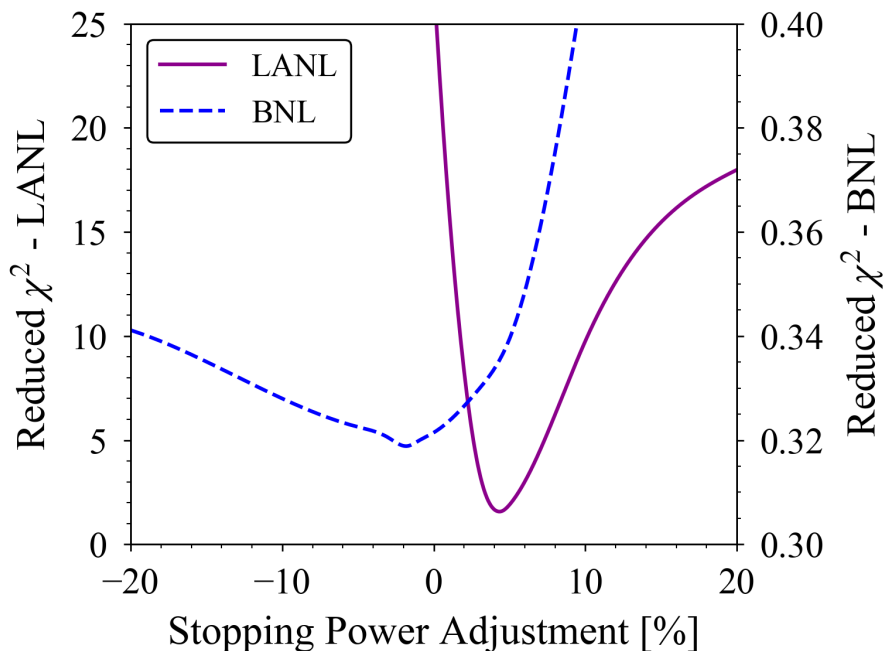
Figure 2.6: Result of χ^2 analysis used in the variance minimization technique to determine the required adjustment to stopping power within the proton energy spectrum calculations per stack.

A distinction is made in this work between cumulative, (c), and independent, (i), cross section values. Numerous reaction products in these irradiations were produced both directly and from decay feeding. Where the decay of any precursors could be measured and the in-growth contribution separated, or where no decay precursors exist, independent cross sections for direct production of a nucleus are reported. Where the in-growth due to parent decay could not be deconvolved, due to timing or decay property limitations, cumulative cross sections are reported.

The final uncertainty contributions to the cross section measurements include uncertainties in evaluated half-lives (0.1–0.8%), foil areal density measurements (0.05–0.4%), proton current determination calculated from monitor fluence measurements and variance minimization (2–4%), and A_0 quantification that accounts for efficiency uncertainty in addition to other factors listed in Section 2.3.2.3 (2–10%). These contributions were added in quadrature to give uncertainty in the final results at the 3–6% level on average (Table 2.1).

Table 2.1: Summary of cross sections measured in this work. Subscripts (i) and (c) indicate independent and cumulative cross sections, respectively. Uncertainties are listed in the least significant digit, that is, 119.8 (10) MeV means 119.8 ± 1.0 MeV.

^{93}Nb(p,x) Production Cross Sections [mb]								
E_p [MeV]	192.38 (73)	177.11 (77)	163.31 (81)	148.66 (86)	133.87 (92)	119.8 (10)	104.2 (11)	91.21 (52)	79.32 (58)
^{72}Se$_{(c)}$	0.066 (13)	0.0193 (26)	-	-	-	-	-	-	-
^{73}As$_{(c)}$	1.15 (30)	0.77 (18)	-	-	-	-	-	-	-
^{74}As$_{(i)}$	0.182 (12)	0.1071 (71)	-	-	-	-	-	-	-
^{75}Se$_{(c)}$	1.443 (76)	0.963 (25)	0.603 (21)	0.200 (24)	-	-	-	-	-
^{81}Rb$_{(c)}$	-	-	-	-	-	-	-	2.99 (55)	-
^{82m}Rb$_{(i)}$	10.55 (36)	9.28 (27)	8.39 (22)	6.86 (24)	4.93 (18)	3.65 (20)	3.49 (18)	3.07 (13)	1.06 (15)
^{83}Rb$_{(c)}$	40.0 (22)	36.8 (17)	35.0 (19)	30.9 (19)	27.0 (19)	15.97 (71)	5.59 (41)	6.27 (47)	7.12 (53)
^{83}Sr$_{(c)}$	32.3 (20)	29.1 (17)	27.1 (15)	25.0 (16)	20.5 (13)	13.2 (11)	3.64 (42)	3.88 (61)	5.13 (75)
^{84}Rb$_{(i)}$	3.11 (17)	2.89 (16)	2.64 (14)	2.32 (13)	2.06 (11)	1.701 (94)	0.699 (40)	0.563 (37)	0.436 (31)
^{85m}Y$_{(c)}$	-	-	-	-	-	-	-	26.1 (28)	18.8 (24)
^{86}Rb$_{(i)}$	-	0.256 (21)	-	-	-	-	-	-	-
^{86}Y$_{(i)}$	45.2 (11)	43.88 (93)	44.77 (84)	44.21 (84)	42.64 (80)	38.67 (88)	29.31 (78)	33.4 (13)	42.7 (15)
^{86}Zr$_{(c)}$	20.3 (18)	21.5 (19)	22.3 (19)	22.5 (19)	23.0 (19)	18.4 (16)	9.91 (90)	16.4 (15)	23.5 (20)
^{87}Y$_{(c)}$	106.5 (27)	110.3 (26)	112.9 (24)	115.7 (24)	120.2 (26)	123.7 (30)	103.2 (30)	106.1 (48)	56.2 (25)
^{87m}Y$_{(c)}$	86.5 (57)	89.4 (58)	92.5 (59)	94.6 (61)	98.4 (63)	99.2 (65)	82.4 (55)	87.9 (41)	47.1 (21)
^{88}Y$_{(i)}$	18.36 (52)	18.71 (46)	18.63 (40)	18.39 (38)	18.22 (39)	17.84 (41)	17.18 (47)	19.07 (62)	14.86 (48)
^{88}Zr$_{(c)}$	85.9 (48)	91.5 (50)	95.9 (51)	101.1 (54)	109.0 (58)	117.6 (64)	136.5 (77)	159 (12)	141.5 (95)
^{89}Zr$_{(c)}$	108.6 (36)	114.4 (35)	125.2 (43)	136.2 (52)	145.5 (50)	159.5 (59)	177.3 (63)	196 (15)	249 (16)
^{90}Nb$_{(i)}$	69.4 (22)	76.2 (21)	84.7 (21)	90.4 (24)	102.8 (25)	110.5 (31)	131.2 (39)	155.1 (46)	174.4 (49)
^{90}Mo$_{(i)}$	4.54 (33)	5.01 (34)	5.46 (32)	6.55 (59)	7.70 (70)	9.64 (88)	12.3 (11)	17.9 (11)	22.8 (14)
^{91m}Nb$_{(c)}$	14.1 (22)	14.7 (23)	14.7 (23)	17.3 (27)	17.3 (27)	20.5 (32)	22.0 (34)	25.8 (40)	27.3 (42)
^{92m}Nb$_{(i)}$	25.9 (12)	29.5 (13)	30.9 (13)	32.4 (14)	35.4 (15)	37.8 (16)	41.4 (19)	45.4 (24)	47.8 (26)
^{93m}Mo$_{(i)}$	-	-	-	-	-	-	-	1.069 (71)	0.75 (10)
E_p [MeV]	72.52 (62)	67.14 (65)	63.06 (68)	60.08 (71)	57.47 (73)	55.58 (75)	53.62 (77)	51.61 (80)	
^{83}Rb$_{(c)}$	5.32 (39)	2.31 (19)	0.71 (11)	0.19 (11)	-	-	-	-	
^{83}Sr$_{(c)}$	4.31 (68)	1.40 (59)	1.04 (55)	-	-	-	-	-	
^{84}Rb$_{(i)}$	0.625 (43)	0.637 (44)	0.533 (39)	0.368 (31)	0.250 (25)	0.143 (21)	0.078 (14)	-	
^{85m}Y$_{(c)}$	5.8 (13)	-	-	-	-	-	-	-	
^{86}Y$_{(i)}$	43.5 (15)	32.7 (12)	21.8 (10)	10.02 (61)	4.38 (46)	-	-	-	
^{86}Zr$_{(c)}$	28.0 (23)	22.1 (18)	12.3 (13)	5.9 (10)	2.50 (64)	1.58 (72)	-	-	
^{87}Y$_{(c)}$	61.5 (23)	78.3 (26)	101.1 (32)	115.3 (43)	116.2 (56)	109.3 (41)	97.3 (31)	86.9 (36)	
^{87m}Y$_{(c)}$	50.6 (23)	64.7 (30)	83.6 (39)	93.8 (43)	96.5 (45)	90.6 (43)	80.3 (38)	69.7 (36)	
^{88}Y$_{(i)}$	11.82 (41)	9.60 (35)	9.15 (34)	9.55 (36)	10.93 (60)	10.53 (40)	11.45 (42)	13.34 (47)	
^{88}Zr$_{(c)}$	92.0 (75)	45.2 (56)	27.3 (41)	24.0 (41)	25.4 (70)	27.6 (42)	31.9 (42)	41.0 (47)	
^{89}Zr$_{(c)}$	309 (21)	328 (17)	296 (21)	205 (15)	171 (23)	136 (14)	80.3 (86)	54.6 (77)	
^{90}Nb$_{(i)}$	201.0 (58)	225.0 (62)	271.2 (79)	307.2 (85)	350.7 (97)	369 (10)	394 (11)	429 (12)	
^{90}Mo$_{(i)}$	28.5 (17)	36.2 (22)	48.9 (36)	63.7 (37)	83.3 (46)	91.7 (51)	103.3 (57)	118.9 (63)	
^{91m}Nb$_{(c)}$	30.7 (47)	31.0 (48)	34.0 (53)	36.3 (56)	37.0 (62)	-	36.9 (57)	40.6 (63)	
^{92m}Nb$_{(i)}$	51.3 (28)	51.2 (32)	54.7 (30)	58.3 (30)	58.2 (31)	56.6 (30)	57.7 (29)	61.7 (32)	
^{93m}Mo$_{(i)}$	1.19 (12)	1.11 (14)	1.33 (15)	1.59 (20)	1.45 (24)	1.25 (19)	1.86 (25)	1.76 (18)	

2.4 Results and Discussion

The experimentally extracted cross sections are compared with the predictions of nuclear reaction modeling codes TALYS-1.9 [47], CoH-3.5.3 [48], EMPIRE-3.2.3 [49], and ALICE-20 [50], each using default settings and parameters, to initially explore variations between the codes and their sensitivity to pre-equilibrium reaction dynamics. Where measured cumulative cross sections are plotted, the corresponding code calculations shown also include the necessary parent production to estimate cumulative yields. Note, however, that ALICE-20 is not suited to calculate independent isomer or ground state production due to a lack of detailed angular momentum modeling.

Furthermore, in the code comparisons, the TALYS and ALICE codes account for potential deuteron, ^{3}He, and triton emissions at all incident proton energies. Default EMPIRE limits these emissions and CoH ignores these effects altogether. The TALYS output provides total production cross sections for these emission channels that can be used to estimate their influence. In TALYS, the cumulative deuteron, ^{3}He, and triton cross section is calculated as 3.1%, 3.5%, and 11.8% of the combined proton and neutron production at 50 MeV, 100 MeV, and 200 MeV, respectively. At each energy, the deuteron production dominates over ^{3}He and triton emissions. Therefore, while the inclusion of these more complex emission types accounts for mostly a small effect, it is a point of difference between the code calculations.

A summary of the key default models implemented in each code is given in Table 2.2.

Table 2.2: Default models implemented in reaction codes

Reaction Code	Proton/Neutron Optical Model	Alpha Optical Model	Level Density	Pre-Equilibrium
TALYS-1.9	Koning-Delaroche [61]	Avrigeanu (2014) [62]	Gilbert-Cameron constant temperature and Fermi gas model [47]	Two-component exciton model [27]
CoH-3.5.3	Koning-Delaroche	Avrigeanu (1994) [63]	Gilbert-Cameron constant temperature and Fermi gas model	Two-component exciton model
EMPIRE-3.2.3	Koning-Delaroche	Avrigeanu (2009) [64]	Enhanced Generalized Superfluid Model [49]	PCROSS one-component exciton model [49]
ALICE-20	Becchetti-Greenlees [50, 65]	Igo (1959) [66]	Shell-dependent Kataria-Ramamurthy model [50]	Hybrid Monte-Carlo Simulation pre-compound decay [50]

Comparisons with the TENDL-2019 library [51] are also made. Additionally, the cross section measurements in this work are compared to the existing body of literature data, retrieved from EXFOR [36, 42, 67–82].

The cross sections and code comparisons for four residual products of interest are described in detail below. The remaining cross section figures are given in Section 2.8 (Figures 2.44–2.62).

2.4.1 ^{93}Nb(p,4n)^{90}Mo Cross Section

As presented in Voyles et al. [36], the ^{93}Nb(p,4n)^{90}Mo reaction is compelling as a new, higher energy proton monitor reaction standard. The ^{93}Nb(p,4n) reaction channel is independent of any (n,x) contaminant production that could be due to secondary neutrons stemming from (p,xn) reactions and requires no corrections for precursor decays. ^{90}Mo decays with seven intense gamma lines ranging from near 100 keV to 1300 keV that allow for easy delineation on most detectors [83]. Further, the ^{90}Mo 5.56 ± 0.09 hr half-life is fairly flexible for a monitor reaction [83], as the isotope can still be readily quantified more than one day post-irradiation, as was done in the counting for these experiments.

The cross section results here, shown in Figure 2.7, align very well with the Voyles et al. [36] measurements in predicting a peak cross section of approximately 120 mb near 50 MeV.
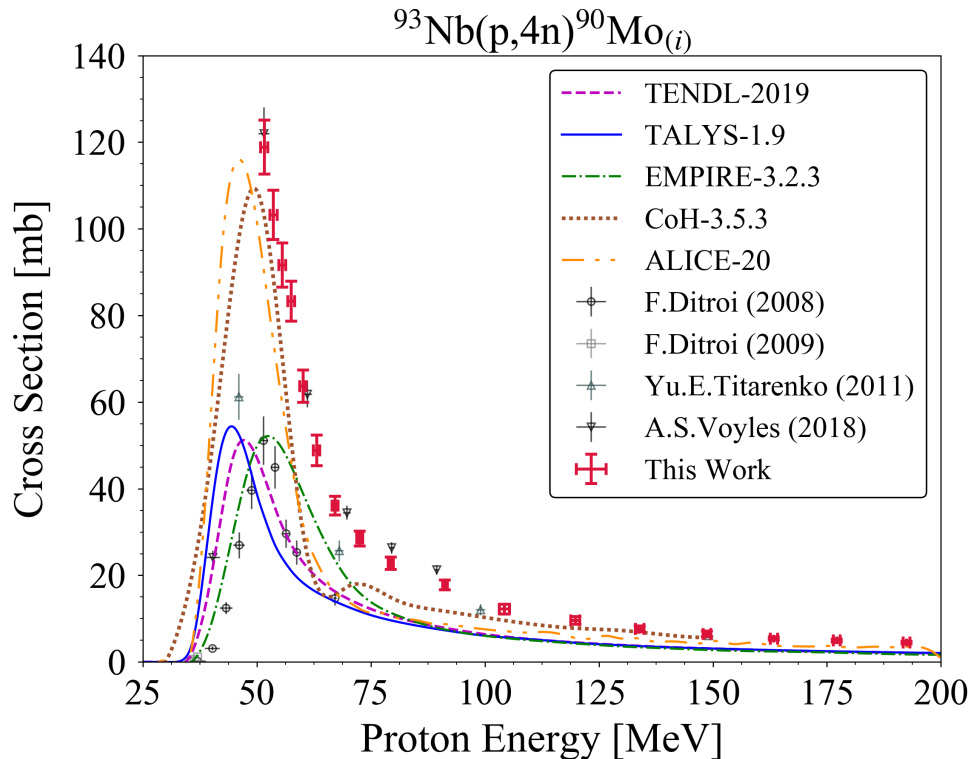
Figure 2.7: Experimental and theoretical cross sections for ^{90}Mo production, peaking near 120 mb around 50 MeV.

The Ditrói et al. [69] data in Figure 2.7 predicts a compound peak of less than half the magnitude observed in this work and Voyles et al. [36]. This underprediction appears as a

trend across numerous reaction products and can be seen in the remaining excitation function plots shown in Section 2.8. The Titarenko et al. [68] dataset is also slightly inconsistent with this work, as it too implies a smaller peak, though not as small as that put forth by Ditrói et al. [69].

Only CoH and ALICE reproduce the peak magnitude of the cross section, while TALYS, EMPIRE, and TENDL predict a smaller magnitude similar to Ditrói et al. [69]. Further, the TALYS and EMPIRE default calculations misplace the compound peak centroid relative to the other calculations. Although CoH and ALICE perform best, neither properly accounts for the increased production on the peak's high-energy falling edge due to a pre-equilibrium "tail" contribution.

This work gives the first measurements of ^{93}Nb(p,4n)^{90}Mo above $100\,\mathrm{MeV}$ and is the broadest energy-spanning dataset for the reaction to date. A recent proton irradiation with niobium targets was conducted in a separate experiment at LBNL for energies from $55\,\mathrm{MeV}$ to threshold in order to fully characterize the remaining low-energy side of the compound peak. These results will be discussed in a subsequent publication.

2.4.2 ^{93}Nb(p,p3n)^{90}Nb Cross Section

^{90}Nb is the most strongly-fed observed residual product stemming from proton reactions on niobium in this investigation, accounting for $\approx 30\%$ of the total non-elastic reaction value at its peak. The ^{90}Nb cross section data in this work were measured independently through a two-step beta-decay chain fit that accounted for contributions from its ^{90}Mo parent.

The ^{93}Nb(p,p3n)^{90}Nb results of this work (Figure 2.8) agree very well with the prior literature data and provide a well-characterized, significant extension beyond $75\,\mathrm{MeV}$.

No code matches the large compound peak magnitude of the experimental data. CoH and EMPIRE come the closest but suffer from their misplacement of the peak's energy by approximately $5\,\mathrm{MeV}$. The shapes of default TALYS, TENDL, and CoH show some affinity for the very pronounced high-energy pre-equilibrum tail in ^{90}Nb production whereas default ALICE and EMPIRE lack in this regard. The misprediction from ALICE here is in stark contrast to its close prediction of the neighbouring (p,4n) reaction.

It is particularly concerning for the global predictive power of ^{93}Nb(p,x) modeling that no code adequately reproduces this dominant reaction channel. Moreover, the proton emitted in the (p,p3n) channel is likely to result from pre-equilibrium emission at higher energies due to its suppression from the Coulomb barrier. The poor default predictions of this channel thereby suggest a systematic issue in the pre-equilibrium modeling of these codes.
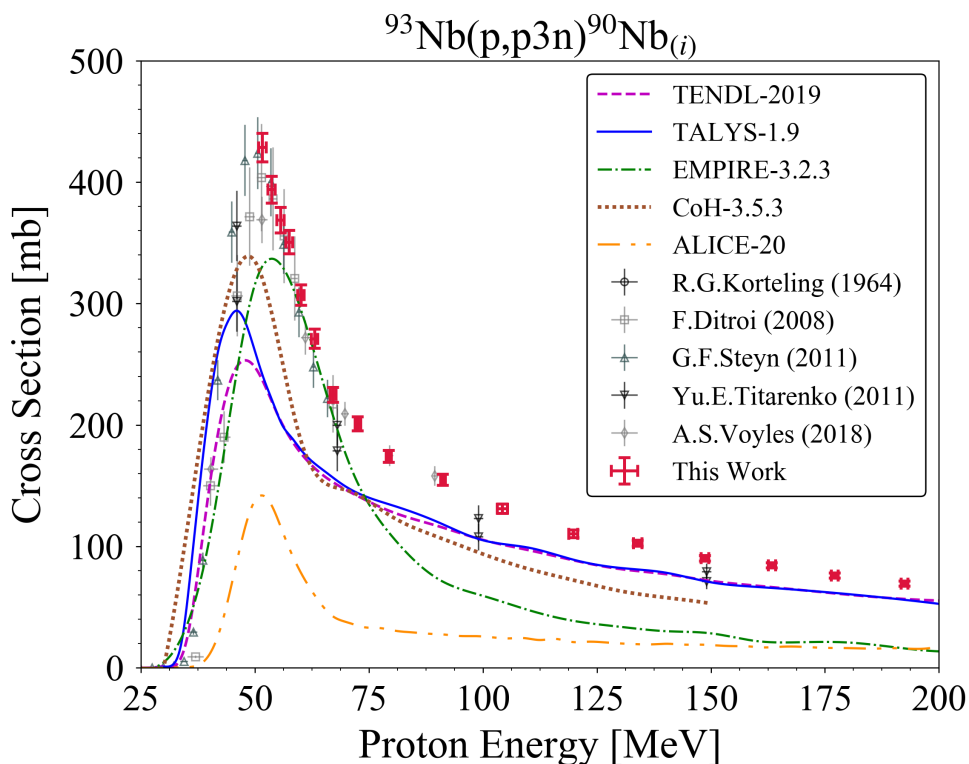
Figure 2.8: Experimental and theoretical cross sections for ^{90}Nb production, peaking near 425 mb around 50 MeV.

2.4.3 ^{93}Nb(p,x)^{89}Zr Cross Section

The lifetimes of ^{89}Zr precursor feeding nuclei (^{89}Mo, ^{89m}Nb, ^{89}Nb, ^{89m}Zr) were too short to be able to quantify their production in these irradiations given the counting procedures described in Sections 2.3.2.1 and 2.3.2.2 [84]. As a result, the measurement of ^{93}Nb(p,x)^{89}Zr, provided in Figure 2.9, is cumulative and includes contributions from all of these precursors as well as the ground state of ^{89}Zr.

^{89g}Zr is a useful positron emitting isotope for radiolabelling monoclonal antibodies to provide an accurate picture of dose distribution and targeting effectiveness in immunoPET [35, 85, 86]. Its 78.41 ± 0.12 hr half-life meshes nicely with the typical 2–4 day pharmacokinetic properties of monoclonal antibodies in tumours [84, 85]. Further, zirconium is especially attractive for this application because of existing commercially available chelating agents for labelling, which have been proven to remain bound in-vivo. Production of ^{89g}Zr via ^{93}Nb(p,x) using 200 MeV protons may offer an attractive alternative to the established ^{89}Y(p,n)^{89}Zr route used in low-energy cyclotrons, potentially facilitating ^{89}Zr production in locations such

as IPF and BLIP [85]. However, the co-production of ^{88}Zr ($t_{1/2} = 83.4 \pm 0.3$ d [87]) in the ^{93}Nb(p,x) path may make the low-energy (p,n) route more viable.
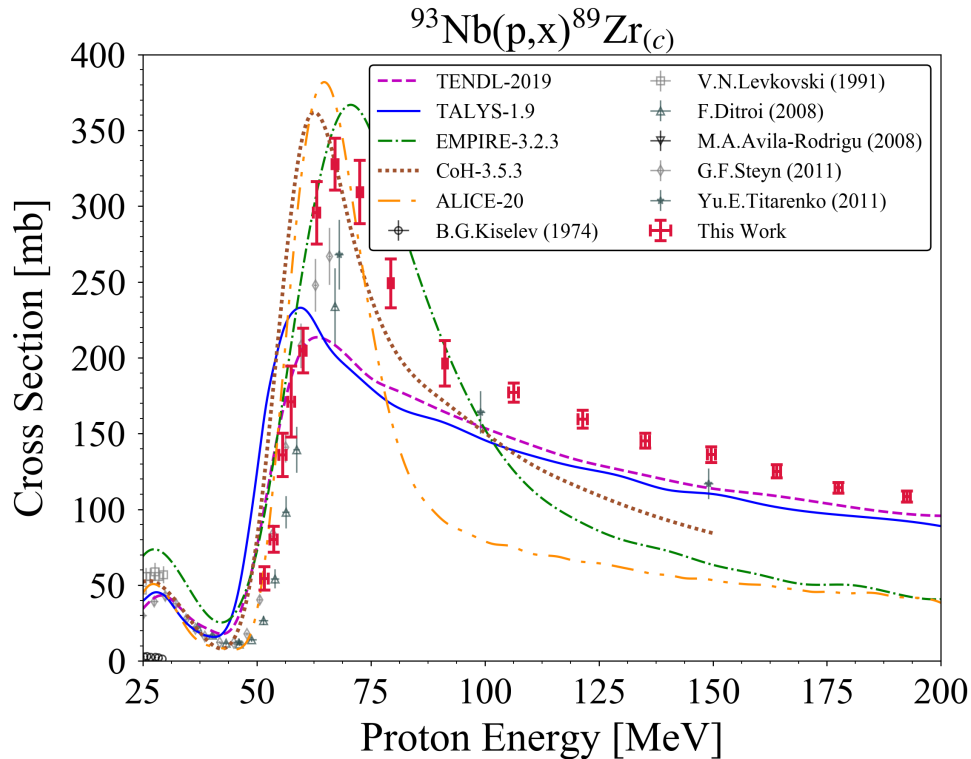
Figure 2.9: Experimental and theoretical cross sections for cumulative ^{89}Zr production, showing peaks for both ^{93}Nb(p,αn) and ^{93}Nb(p,2p3n) formation mechanisms.

This work gives the most complete description of the cumulative higher-energy production peak near 67 MeV and greatly extends the cross section information beyond 75 MeV, where only two prior data points existed. The larger higher-energy peak is indicative of independent ^{89}Zr formation through the ^{93}Nb(p,2p3n) mechanism in contrast to the lower-energy compound peak around 25 MeV, denoting formation by ^{93}Nb(p,αn). The measured values agree well with Steyn et al. [70] on the higher-energy peak rising edge, but predict a peak value of approximately 325 mb, which is larger than both Steyn et al. [70] and Titarenko et al. [68]. The Ditrói et al. [69] magnitude discrepancy is noticeable in this measurement where the dataset underpredicts both the rising edge and peak relative to all the other literature.

It is difficult to comment on the performance of the codes here due to the feeding from the three nuclei, and multiple isomeric states, involved in the calculations. It can be noted that there is still the persistent difficulty in properly modeling the pre-equilibrium effect throughout these nuclei though, which manifests in these codes as both a shift in the centroids for the higher-energy peak and a missing high-energy tail.

2.4.4 ^{93}Nb(p,x)^{86}Y Cross Section

The LANL and BNL irradiations in this investigation allowed for a measurement of ^{86}Y production from reaction threshold to near 200 MeV. As specifically referenced in Figure 2.3, the cumulative ^{86}Zr production could be directly determined, which then enabled an independent quantification of ^{86}Y. The 33% β^+ decay mode of ^{86}Y along with its 14.74 $\pm$ 0.02 hr half-life make it a promising surrogate for imaging the biodistribution and studying the absorbed dose of ^{90}Y (100% β^-) for bone palliative treatments [88, 89]. However, compared to the established ^{86}Y production routes using strontium targets, a niobium target based pathway introduces long-lived ^{88}Y (t$_{1/2}$ = 106.626 $\pm$ 0.021 d [87]) isotopic impurities and suffers a lower yield, making it less advantageous [90].

The extracted excitation function (Figure 2.10) is in excellent agreement with the measurements of Voyles et al. [36] and Titarenko et al. [68]. This wide-spanning dataset, similar to the Michel et al. [67] work, characterizes the full compound behaviour as well as the high-energy pre-equilibrium component. However, where there is good agreement to the Michel et al. [67] work below 100 MeV, our dataset predicts lower values for the remainder of the pre-equilibrium tail by 10–15 mb.
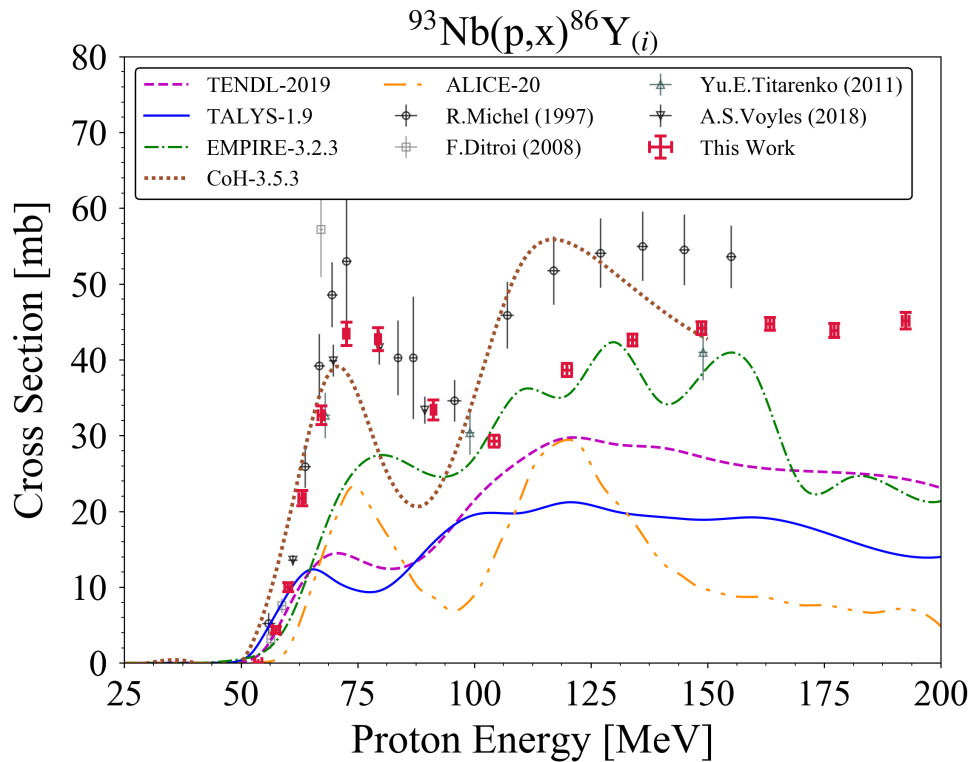
Figure 2.10: Experimental and theoretical cross sections for ^{86}Y production, spanning from reaction threshold to near 200 MeV.

^{86}Y is not a strongly-fed residual product channel, which gives some explanation to the variation between different code calculations. The theoretical predictions are sensitive to compensating effects from miscalculations in more dominant reaction channels. As a result, no code properly reproduces both the experimentally determined magnitude and shape of the excitation function using default parameters. CoH predicts the compound peak with the closest magnitude, though the peak centroid, falling edge, and pre-equilibrium shape are incorrect. TALYS and TENDL perhaps best represent the overall shape but are far lower in magnitude than the experimental data.

Other notable cross section results in this work include ^{82m}Rb, ^{83}Sr, and ^{84}Rb production, where data had been extremely sparse but now have their excitation functions well-characterized beginning from threshold. These cross section results, along with the measurements of all other observed nuclei, are detailed in Section 2.8.

2.5   High-Energy Proton Reaction Modeling

The large body of data measured here, in addition to the existing ^{93}Nb(p,x) literature data, presents a good opportunity to study high-energy proton reaction modeling on spherical nuclei. Our approach is to follow the procedure established for modeling high-energy (n,x) reactions by comprehensively fitting the most prominent residual product channels first, followed by the weaker channels. A critical focus in developing a consistent fitting procedure is to gain insight into pre-equilibrium reaction dynamics in an attempt to isolate shortcomings in the current theoretical understanding.

As a note, the fitting work presented here is based in the TALYS reaction code. TALYS has widespread use in the nuclear community and is an accessible code-of-choice for reaction cross section predictions. Further, TALYS incorporates the widely employed two-component exciton model for pre-equilibrium physics, which means that any outcomes derived in this work can be applied broadly by the nuclear reaction data evaluation community [47, 91–93].

2.5.1   Pre-Equilibrium in TALYS-1.9

The currently-used two-component exciton model in TALYS-1.9 was constructed through an extensive global pre-equilibrium study by Koning and Duijvestijn [27]. Their work relied on virtually all existing angle-integrated experimental continuum emission spectra for (p,xp), (p,xn), (n,xn), and (n,xp) reactions for A≥24 spanning incident energies between 7–200 MeV. No double-differential or residual product cross sections were included in the semi-classical two-component model development, but these results were expected to fall out naturally from

globally fitting the emission spectra. The decision to adopt the exciton model over other potential pre-equilibrium calculation methods is detailed by Koning and Duijvestijn [27].

The significant updates made by Koning and Duijvestijn [27] to previous two-component models include using a more recent optical model potential (OMP) for neutrons and protons, a new and improved determination of collision probabilities for intranuclear scattering to more or less complex particle-hole states, surface interactions specific to projectiles and targets, and greater detail applied to multiple pre-equilibrium emission. The most noteworthy of these changes is the collision probabilities, which use a new parameterization of the phenomenological squared matrix element for the effective exciton residual interaction applicable across the entire 7–200 MeV energy range [27, 92, 94].

Moreover, in the two-component exciton master equation used by Koning and Duijvestijn [27], which describes the temporal development of the composite system for projectile-target interaction in terms of exciton states characterized by proton and neutron particle and hole numbers, internal transition rates are defined to model particle-hole creation (λ^+), conversion (λ^0), and annihilation (λ^-). These transition rates govern the evolution of the total exciton state and are critical pieces for the overall pre-equilibrium energy-differential cross section calculation [92–94]. Formally, the model is approximated to disregard pair annihilation where it has been shown that decay rates to less complex exciton states are small compared to other processes in the pre-equilibrium part of the reaction and can be neglected [27, 92]. Transition rates are calculated from collision probabilities, determined using time-dependent perturbation theory and Fermi's golden rule to give expressions such as Equation (2.7) for a proton (π)-proton (π) collision $\lambda_{\pi\pi}$, leading to an additional proton particle-hole pair ($1p$) [47]:

$$\lambda_{\pi\pi}^{1p} = \frac{2\pi}{\hbar} M_{\pi\pi}^2 \omega. \tag{2.7}$$

In the collision probability definition given in Equation (2.7), ω is the particle-hole state density as a function of the exciton state configuration and excitation energy, as formulated by Dobeš and Běták [94]. An exciton state configuration is defined by $(p_\pi, h_\pi, p_\nu, h_\nu)$ with the proton (neutron) particle number as p_π (p_ν) and the proton (neutron) hole number as h_π (h_ν). $M_{\pi\pi}^2$, and the other corresponding proton and neutron (ν) permutations ($M_{\pi\nu}^2$ etc.), are average squared matrix elements of the residual interaction inside the nucleus that depend only on the total energy of the composite nucleus to describe two-body scattering to exciton states of different complexity [47]. In TALYS-1.9, the matrix element variations for like and unlike nucleons can be cast in terms of a total average M^2 by:

$$M_{xy}^2 = R_{xy} M^2, \tag{2.8}$$

with x and y denoting some combination of π and ν. R_{xy} is a free parameter with default values in TALYS-1.9 such as $R_{\pi\nu} = 1.0$ [47].

Given the complete body of experimental emission spectra data, the following semi-empirical expression for the total average squared matrix element is implemented in TALYS-1.9 for incident energies 7–200 MeV [47]:

$$M^2 = \frac{C_1 A_p}{A^3} \left[7.48 C_2 + \frac{4.62 \times 10^5}{\left(\frac{E^{tot}}{n A_p} + 10.7 C_3 \right)^3} \right], \tag{2.9}$$

where C_1, C_2, and C_3 are adjustable parameters, A is the target mass, A_p is the mass number of the projectile, n is the total exciton number, and E^{tot} is the total energy of the composite system. In particle-hole creation, the change in state exciton number is $\Delta n = +2$, while in a conversion transition $\Delta n = 0$.

For an incident proton projectile, a simplified visualization of the scattering with target nucleons defined by the exciton model is shown in Figure 2.11. Additionally, a schematic of the two-component transitions from an initial exciton state configuration of $(1, 0, 0, 0)$ to more complex states is given in Figure 2.12 [94].
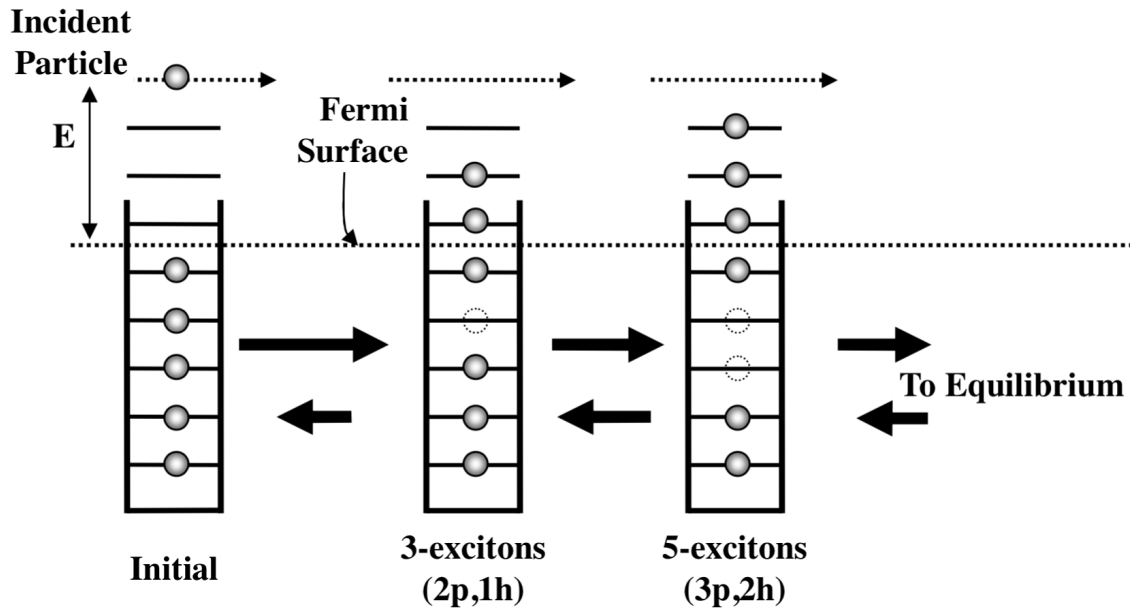
Figure 2.11: Illustration of the initial stages of reaction in the pre-equilibrium exciton model from Selman [95]. Solid horizontal lines are representative of single particle states in a potential well. Particles are shown as solid circles while holes are empty dashed circles [93].

Each state in Figure 2.12 has an associated mean lifetime $\tau(p_\pi, h_\pi, p_\nu, h_\nu)$ defined as the inverse sum of the various internal transition rates and the total emission rate [47]. As a result, the parameterization of M^2 is an essential component of the state lifetime calculation. Moreover, it can be noted from the representation in Figure 2.12 that in order to calculate the

overall energy differential pre-equilibrium cross section, the exciton model calculation must keep track of all emissions in addition to the part of the pre-equilibrium flux that has survived emission and now passes through new configurations. This survival population is generally denoted by $P(p_\pi, h_\pi, p_\nu, h_\nu)$ and is also calculated on the basis of the M^2 parameterization. The total emission rate W for an ejectile k of emission energy E_k is not a function of M^2 but is instead calculated from the optical model and ω [47].
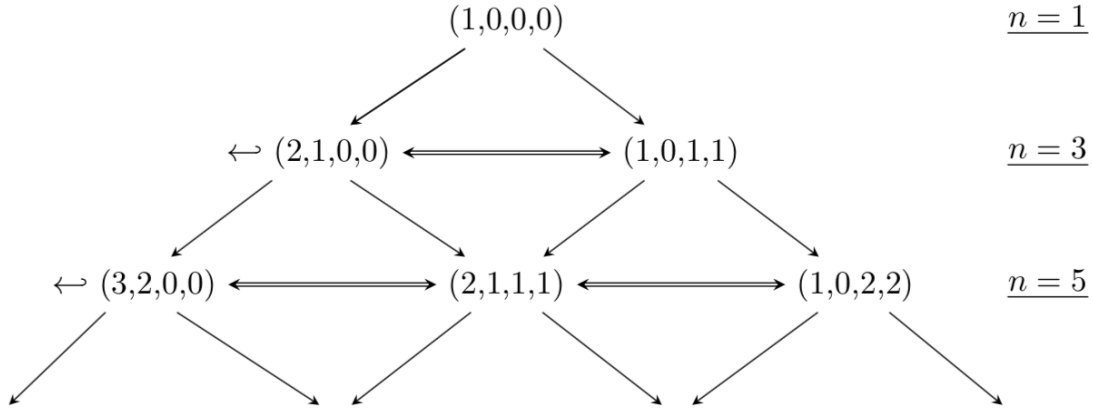
Figure 2.12: Scheme of the two-body interaction pathways in the two-component exciton model where individual exciton states are characterized by $(p_\pi, h_\pi, p_\nu, h_\nu)$. The particle-hole annihilation pathways to less complex states are neglected here. The single arrows represent particle-hole creation transitions and the double arrows represent conversion transitions. The hooked arrows represent the chance for particle emission to the continuum at the given exciton number n, where n is the sum of all present particles and holes in a configuration.

Given these considerations, the energy differential pre-equilibrium cross section can be calculated by [47]:

$$\frac{d\sigma_k^{PE}}{dE_k} = \sigma^{CF} \sum_{p_\pi=p_\pi^0}^{p_\pi^{max}} \sum_{p_\nu=p_\nu^0}^{p_\nu^{max}} W_k(p_\pi, h_\pi, p_\nu, h_\nu, E_k) \times \tau(p_\pi, h_\pi, p_\nu, h_\nu) P(p_\pi, h_\pi, p_\nu, h_\nu), \quad (2.10)$$

where σ^{CF} is the compound nucleus formation cross section, also calculated from the optical model. p_π^{max} and p_ν^{max} are particle numbers representing the equilibration limit for the scattering interactions at which point the Hauser-Feshbach mechanism handles the reaction calculations. In the case of multiple pre-equilibrium emissions, additional proton and neutron number dependencies are introduced into the exciton model, though M^2 and the internal transition rates play similar critical roles [27].

Ultimately, given that the level density and optical model parameters at high energies are well-characterized compared to the relative paucity of information surrounding pre-equilibrium dynamics, it can be argued that an exploration of pre-equilibrium emission resulting from the

exciton model in TALYS is centrally an exploration of the effective squared matrix element parameterization. TALYS's abundance of adjustable keywords related to M^2 make it an ideal tool to investigate this parameterization using measured residual product excitation function data. However, it will not be possible to entirely neglect the effects of level density and optical model adjustments on reaction observables and it is necessary to be cognizant of these additional degrees of freedom in any attempt to isolate M^2 effects [27].

2.5.2 Residual Product-Based Standardized Fitting Procedure

The approach pursued in this work to accurately reproduce production probabilities for high-energy proton-induced reactions on spherical nuclei using TALYS and its associated adjustable parameters is outlined in the flow chart of Figure 2.13. This fitting procedure prioritizes an examination of exciton model physics to help identify trends and biases within the current calculation technique.

A further motivation of this procedure is to avoid the compensating errors caused by current non-evaluation fitting methods that utilize too few experimental data and/or too simplistic parameter changes, which may ultimately hinder modeling as a whole. Particularly, simplistic or arbitrary parameter adjustments in TALYS, tuned to provide a better fit for a singular reaction channel of interest, are non-unique and may not hold a global physical basis because neighbouring reaction channels can suffer from the fit choice [42, 44, 46, 78, 79, 86, 96–100]. Nevertheless, these adjustment methods are representative of a norm in non-evaluation modeling work and can have real-world implications such as incorrect predicted yields during medical radioisotope production, high level co-production of an unwanted contaminant, or poor particle transport calculations. Even with a foundational understanding of the level density, OMP, and exciton model parameter adjustments, the interplay between the permutations and combinations of changes in each component is not well understood [27]. In turn, it is difficult to determine the most physically justifiable modeling parameters if the data from every open reaction channel is not known.

For example, consider the numerous modeling possibilities for the large residual product channel ^{93}Nb(p,p3n)^{90}Nb, as shown in Figure 2.14. The list of parameter adjustments in each modeling case is described in Section 2.9 (Table 2.7). It is qualitatively seen that ten different models, with arbitrary choices of which simplistic or complex parameters are adjusted, can reproduce similar improvement over the default prediction.

Still, it could be argued that one set of changes is quantitatively the best to model this channel. A χ^2-test using the experimental data demonstrates that models 1, 5, and 10 give the largest improvements over default. These models are indicated with dashed/dotted lines in Figure 2.14 and the χ^2 result of each parameter set is listed as well in Section 2.9. Given these best fits, it consequently seems logical to search for meaning in the altered parameters
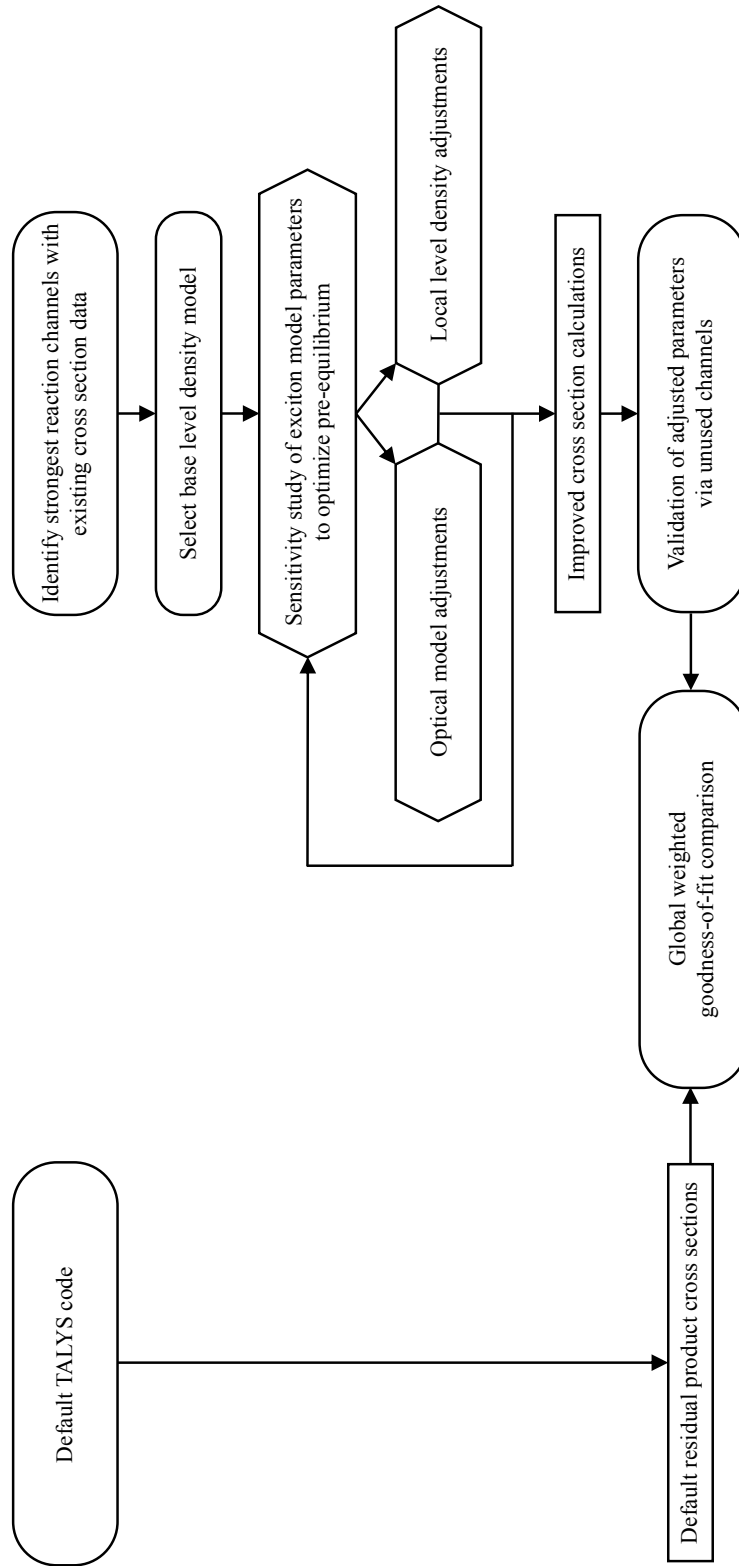
Figure 2.13: Proposed standardized reaction modeling code parameter adjustment procedure, reliant on residual product excitation function data, built to best fit multiple dominant reaction channels and gain justified insight into the pre-equilibrium mechanism.

and attribute their need to lacking physics in this charged-particle problem. However, simply applying these best fit models to surrounding reaction channels proves that these sets of parameter changes in fact do not improve the model's predictive capabilities. For example, in the ^{93}Nb(p,4n)^{90}Mo channel, which also makes up a large share of the reaction cross section, models 1, 5, and 10 from Figure 2.14 perform extremely poorly, as shown in Figure 2.15.

Instead, a more useful and realistic modeling approach should involve many prominent cross section channels and sensitivity studies. The inclusion of more experimental data and increased detail in the analysis process will yield a more unique and global solution along with the capability to justify the set of adjusted parameters while providing physics context for the predictions.

As outlined in Figure 2.13, this suggested improved fitting procedure for spherical nuclei begins by identifying and having accurate experimental data for numerous prominent residual product channels. This approach is anchored in examining the most probable outcomes where it is possible to best isolate the impact of model changes. Experimental data for weaker production channels are still involved and relevant but are weighted less heavily due to their high sensitivity to the behaviour of the dominant reactions.

Once the largest reaction channels have been identified, the following step is to select a level density model for all the nuclei involved in the interaction being studied such that there is a concrete foundation, based on the well-established compound nucleus model, to build model adjustments upon and put their effects in context. TALYS-1.9 provides six level density models, three that are microscopic calculations, which are preferred in this procedure for their better care of the physics involved and use in predictive scenarios versus the remaining three phenomenological models [47]. At this point, the proposed fitting approach reaches the key step of an exploration of the exciton model parameter space. Notably, the pre-equilibrium dynamics are adjusted the most in this suggested method. Both the OMP and exciton model parameterizations are based on very large global studies. However, deviations from the optical model default values represent a much greater change to the physics of the situation than tuning for the exciton model [27, 47, 61, 101]. The optical model fundamentally affects the nature of the particle-nucleus reaction while changing the exciton model parameters maintains the same pre-equilibrium physics basis but shifts evolution and emission rates within the model, which are not known precisely at the outset. In this manner, this fitting mechanism is specifically suited to isolate and gain insight into pre-equilibrium modeling for high-energy proton-induced reactions.
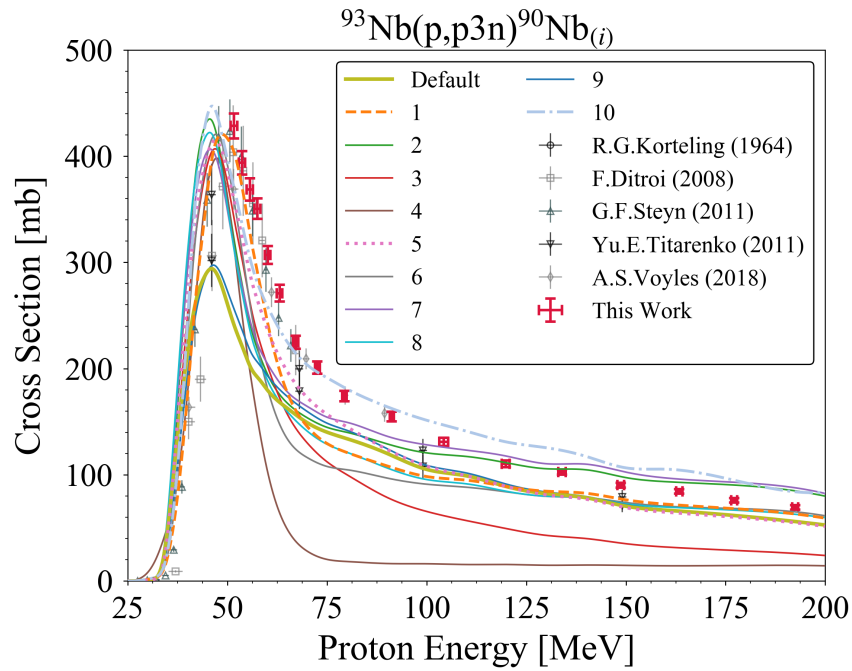
Figure 2.14: Evidence for non-unique modeling solution when only considering one reaction channel. Ten sets of different parameter changes are shown to reproduce similar improvement over the default prediction, with the three dashed cases performing best as assessed by a statistical test.
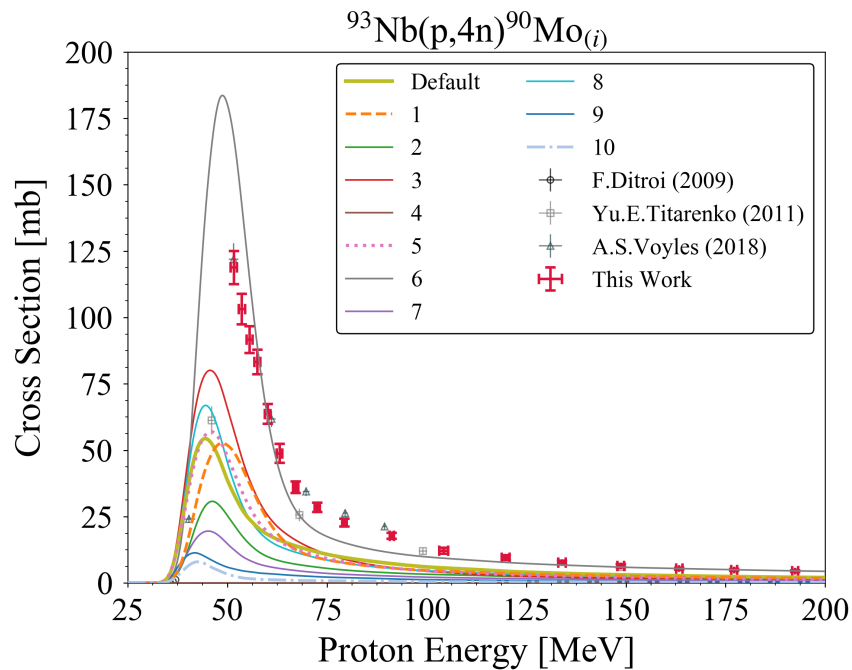
Figure 2.15: Extension of model adjustments, optimized to singularly reproduce the (p,p3n) channel, to a neighbouring channel demonstrating poor fit behaviour, especially for the three dashed cases that previously performed best.

The most significant of the available exciton model free parameters within TALYS are `M2constant`, `M2limit`, and `M2shift`, which adjust C_1, C_2, and C_3, respectively, in Equation (2.9). `M2constant`, `M2limit`, and `M2shift` are set to 1.0 as default in TALYS [47]. A decrease in `M2constant` reduces the transition rate to more complex exciton states, thereby increasing pre-equilibrium emission in the initial interaction stages and creating an overall harder emission spectrum with an increased high-energy tail. The opposite effect applies for an increase in `M2constant`. The `M2limit` controls the asymptotic behaviour of M^2 and its increase leads to scattering to more complex states at high energies, thereby preventing an overestimation of the high-energy tail, which pulls reaction cross section from the evaporation peak [27]. The `M2shift` affects the total system energy and can shift the exciton model strength along the projectile energy axis. Other parameters that alter the pre-equilibrium effects to a lesser degree also exist such as `Rgamma, Cstrip, Rnupi, preeqspin, gpadjust` etc., which are all described in the TALYS-1.9 manual and should be considered as well [47].

Once the components of the exciton model are set according to the behaviour of the largest reaction channels, there is an opportunity to perform some studies of OMP and level density parameters. These aspects can help optimize the fit founded on the exciton model changes for smaller residual production channels or localized outstanding discrepancies between theory and experiment. The OMP and level density adjustments here are minor corrective factors to the broader deduced pre-equilibrium modeling. These adjustments may require some iterations to reach convergence [46].

Lastly, a validation step is an important conclusion to this procedure. If the exciton, OMP, and level density adjustments set by the breadth of reaction channels considered are unique and correct, their application to channels not included in the initial sensitivity studies should yield appropriate fits. Cumulative excitation functions are good examples of unused data, where they may have large cross sections but the ambiguity from contributions of a chain of multiple nuclei and emission channels is not ideal for the initial sensitivity study. This is a test of the predictive capability of this procedure. Finally, a descriptive metric, such as a global χ^2-test, can be applied to compare the adjusted fit in all utilized channels from this procedure to the default calculation [46, 102, 103]. Ideally, the metric is properly weighted to reflect the emphasis on the most prominent reaction channels. Formulae for these weights are discussed in Section 2.5.3.

2.5.3 Fitting Procedure Applied to ^{93}Nb(p,x)

This work demonstrates the procedure outlined in Figure 2.13 for high-energy proton reactions on niobium. At present, this sensitivity study work is performed manually to better gauge the physical effects of different parameters and to mimic typical cross section

parameter adjustment work. Nine reaction channels are considered: ^{93}Nb(p,x)^{93m,90}Mo, ^{92m,90}Nb, ^{88,87,86}Zr, ^{88,86}Y, with ^{90}Nb, ^{90}Mo, and ^{88}Zr production as the most prominent.

In the base level density model choice step, the microscopic models were indeed found to have greater predictive power than the phenomenological models. The ^{93}Nb(p,4n)^{90}Mo reaction was found to be most sensitive to the level density model. Only the microscopic calculations from Goriely's tables using the Skyrme effective interaction (`ldmodel` 4) could produce a fit magnitude in the vicinity of the experimental data while maintaining adequate predictive power in the other considered channels [47]. The apparent sensitivity of ^{90}Mo production to angular momentum distributions in nuclei closer to the target ^{93}Nb therefore made it the constraint for a level density choice.

Once the level density model was chosen, the adjustment of pre-equilibrium could take place. The sensitivity study of the exciton model parameters showed that reducing `M2constant` from its default 1.0 value could best benefit high-energy tail behaviour across the prominent residual product cross sections. The tail-shape improvement came at the cost of unwanted reduced compound peak magnitudes, which could be compensated by an increase in `M2limit` and a decrease in `M2shift`. Marginal variations of the three `M2` parameters relative to each other given these constraints demonstrated a best fit for the largest available channels when `M2constant`=0.875, `M2limit`=4.5, and `M2shift`=0.6. Furthermore, this pre-equilibrium correction for the larger channels introduced a cascade effect that improved the compound peak behaviour of smaller cross section channels, giving confidence that these adjustments were globally beneficial. The numerous other additional scaling factors and modeling choices for pre-equilibrium available in TALYS were also explored but were shown to be insensitive relative to the `M2` parameters or physically inconsistent across the nine considered reactions here.

However, while compound peak improvement was seen in the weaker far-from-target channels, issues arose with their higher-energy cross section predictions deviating from the experimental data. This applies to nuclei such as ^{87,86}Zr and ^{86}Y, which exist on the other side of the $N = 50$ shell gap relative to the target ^{93}Nb. The base level density model choice, which served calculations for the niobium and molybdenum excitation functions well, proved to be a root cause for these unpredictable emission issues further from the target nucleus. The level densities of all nuclei involved in this charged-particle interaction are not perfectly modeled by the base choice and may require specific variations, as outlined in Figure 2.13. Adjusting the level density model for niobium and molybdenum nuclei relevant to emissions for these far-from-target residual products from `ldmodel` 4 to the Hilaire combinatorial calculation using the Skyrme force (`ldmodel` 5) was tested. This change produced a sufficient compensating effect to quell the incorrect high-energy behaviour in the majority of the far-from-target channels [47, 98]. Note that ^{93}Mo and ^{92}Mo needed to remain modeled by `ldmodel` 4 as these were key nuclei in the ^{90}Mo angular momentum constraint discovered

earlier in the base level density choice study.

Minor deviations to the optical model could then be considered to address outstanding discrepancies between prediction and experimental data. The key discrepancies remaining at this point in the analysis included a slight under-prediction of the ^{90}Nb production compound peak and falling edge versus a slight over-prediction of the same aspects in ^{90}Mo, as well as an incorrect competition between ^{86}Zr and ^{86}Y production, where the former was overestimated and pulled reaction flux from the latter. The zirconium and yttrium channels are inherently difficult to predict accurately as they are weaker reactions (with peak cross sections nearly an order of magnitude lower than the dominant channels comprising the initial tuning set) susceptible to large variations from compounding effects in the modeling. The larger ^{90}Nb and ^{90}Mo reactions were therefore the primary constraints for OMP parameter adjustments. Exploring the real and imaginary volume components of the OMP is the most physically sensible course for correcting the fit versus experimental data magnitude discrepancies, as these parameters directly affect particle flux loss and emission. The sensitivity study of the TALYS OMP volume terms revealed a significant reliance on only `rvadjust p/n/a` (multipliers to energy-independent radial factors of volume potentials) and `w1adjust p` (direct multiplier to proton imaginary volume potential well depth) in this charged-particle reaction setting [47, 61]. The other volume potential parameters may be relevant in a different context but are difficult to assess without double differential scattering information. Marginal changes to `rvadjust p/n/a` and `w1adjust p` demonstrated that only `w1adjust p` was needed to best improve the ^{90}Nb peak magnitude and falling edge. `w1adjust p` affects the overall proton reactivity and emission. An increase to `w1adjust p` from its 1.0 default to a value of 2.2 increased the cross section reasonably of all channels but most noticeably for ^{90}Nb production, especially relative to the ^{93}Nb(p,4n)^{90}Mo reaction.

A slight errant local competition between ^{90}Nb and ^{90}Mo still existed that could be improved by manually adjusting level densities using the `ctable` and `ptable` TALYS commands. This level density table adjustment can be applied to an individual nuclide and when adjusted by reasonable amounts only has sensitivity for the selected nuclide and its neighbours, thereby maintaining the good global behaviour set by all the previous parameter changes. ^{90}Mo required a `ctable` decrease to bring its production down while increasing the competing ^{90}Nb channel, allowing both predictions to align well with experimental data. The zirconium and yttrium competition issues also required `ctable` decreases to be resolved and even prompted a slight ^{87}Zr level density decrease as well. Adjusting the level densities in this manner for far-from-target nuclei holds a less clear physical meaning as the changes are potentially brought on by more complex reaction aspects, hidden from this sensitivity study work, that are lumped into this compensating correction. This is a part of the procedure described in Figure 2.13 but it should be emphasized that the most clear application of this approach is for dominant reaction channels.

All of the final derived parameter changes for ^{93}Nb(p,x) are listed in Section 2.10 (Table 2.8). The adjusted fits accompanying this more detailed parameter study are shown compared to the default TALYS calculation for the nine considered reaction channels in Figures 2.16–2.24. The fits shown apply from 0 to 200 MeV.
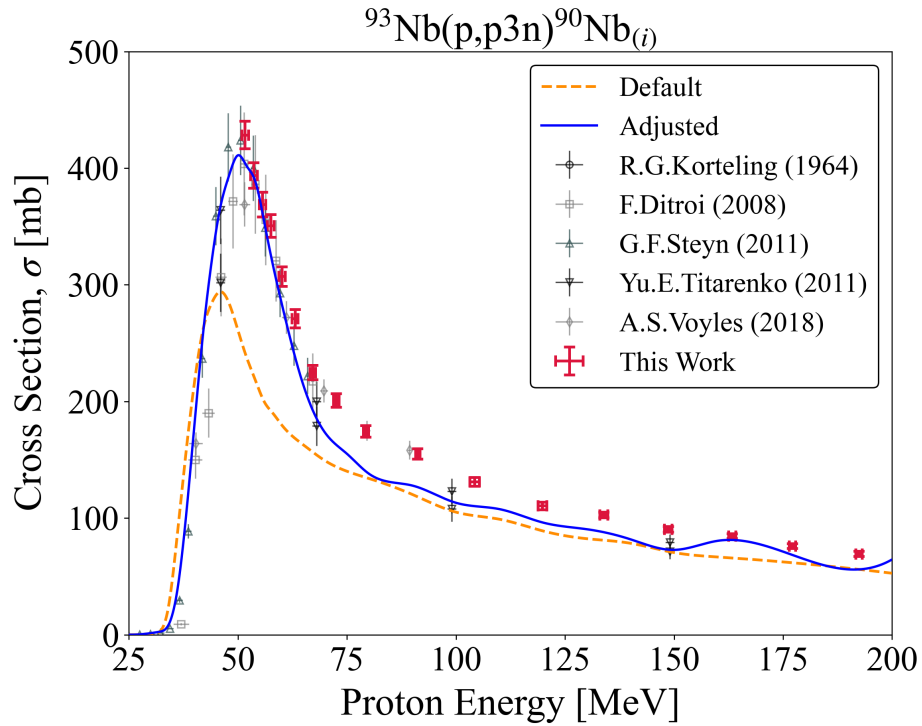
Figure 2.16: TALYS default and adjusted calculation for ^{90}Nb.
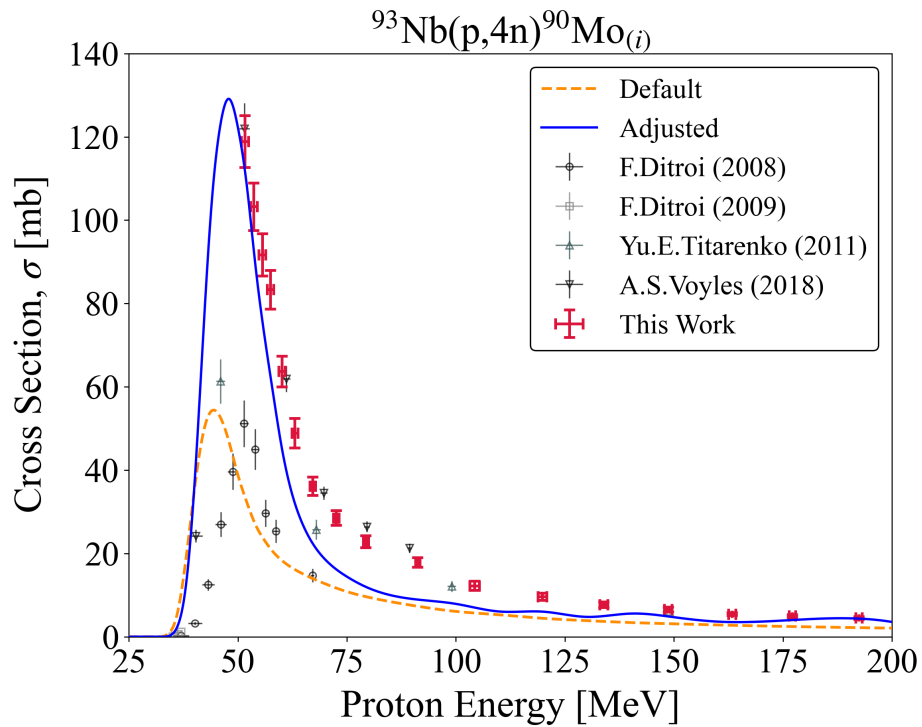
Figure 2.17: TALYS default and adjusted calculation for ^{90}Mo.
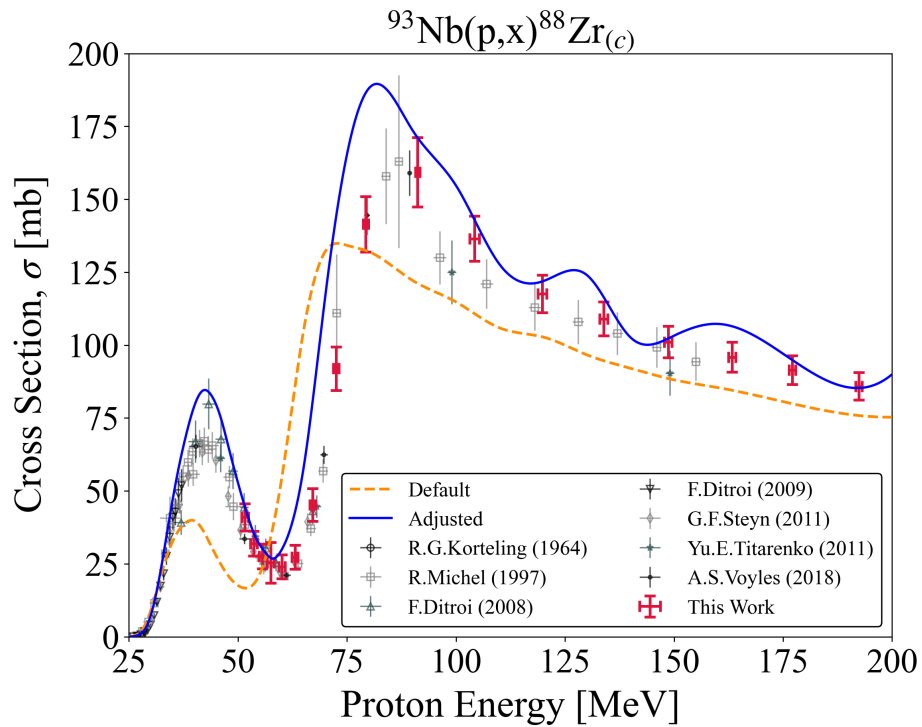
Figure 2.18: TALYS default and adjusted calculation for ^{88}Zr.
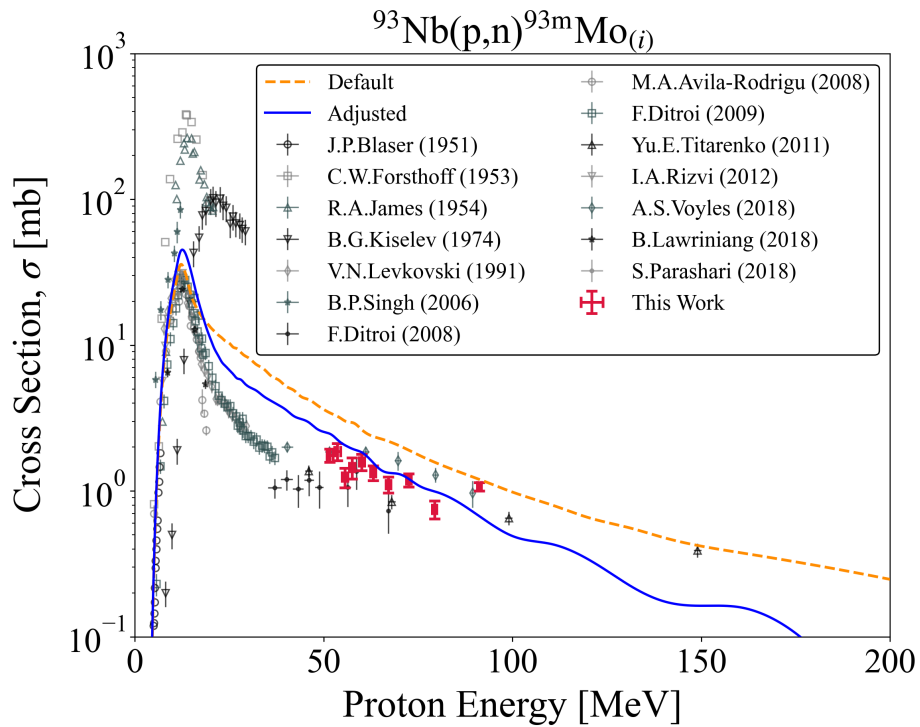
Figure 2.19: TALYS default and adjusted calculation for ^{93m}Mo.
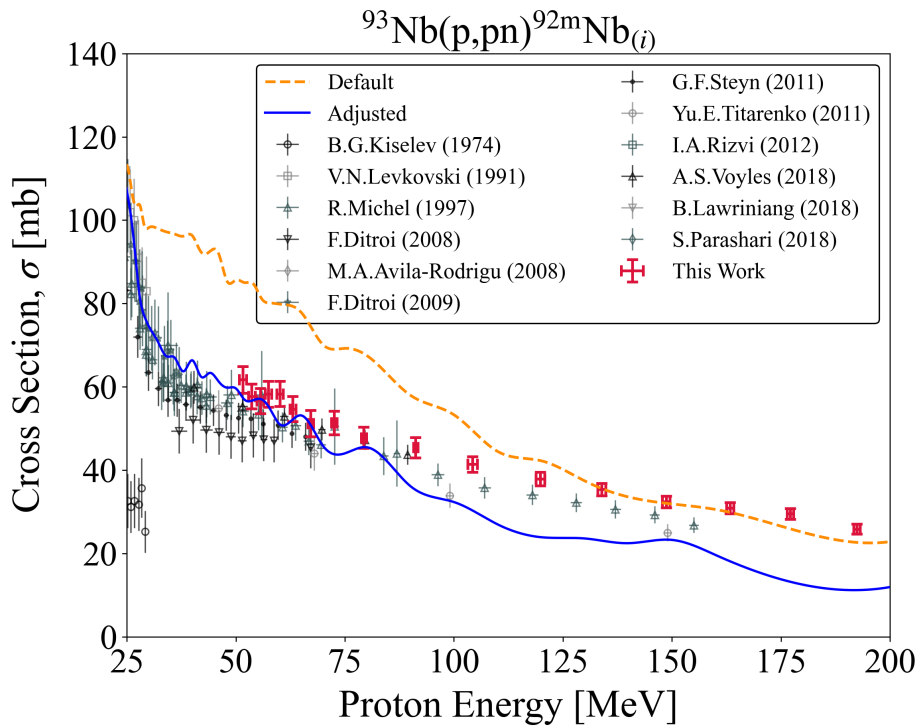
Figure 2.20: TALYS default and adjusted calculation for ^{92m}Nb.
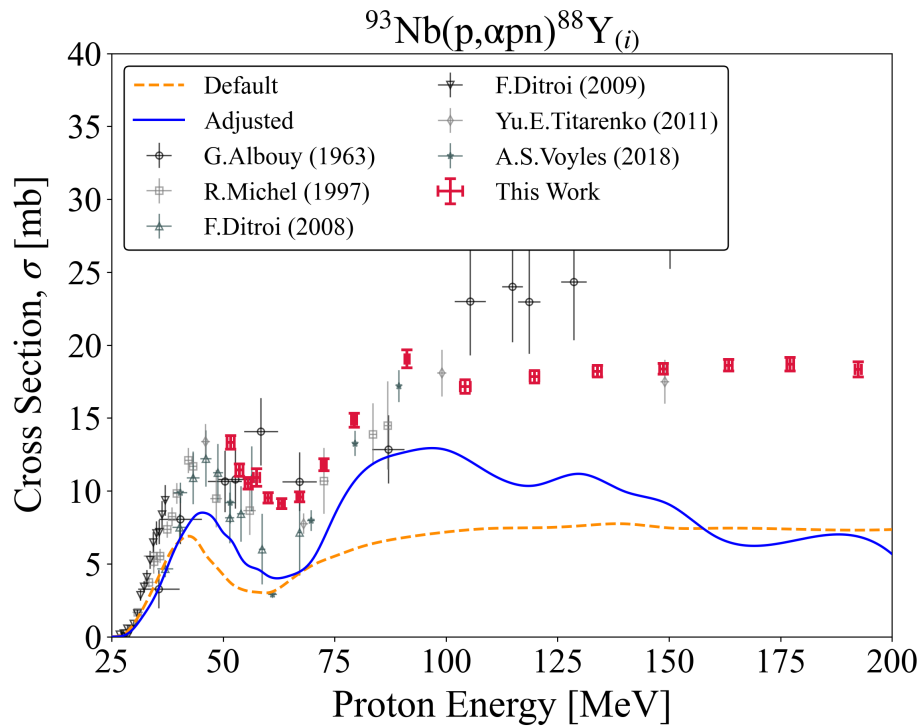
Figure 2.21: TALYS default and adjusted calculation for ^{88}Y.
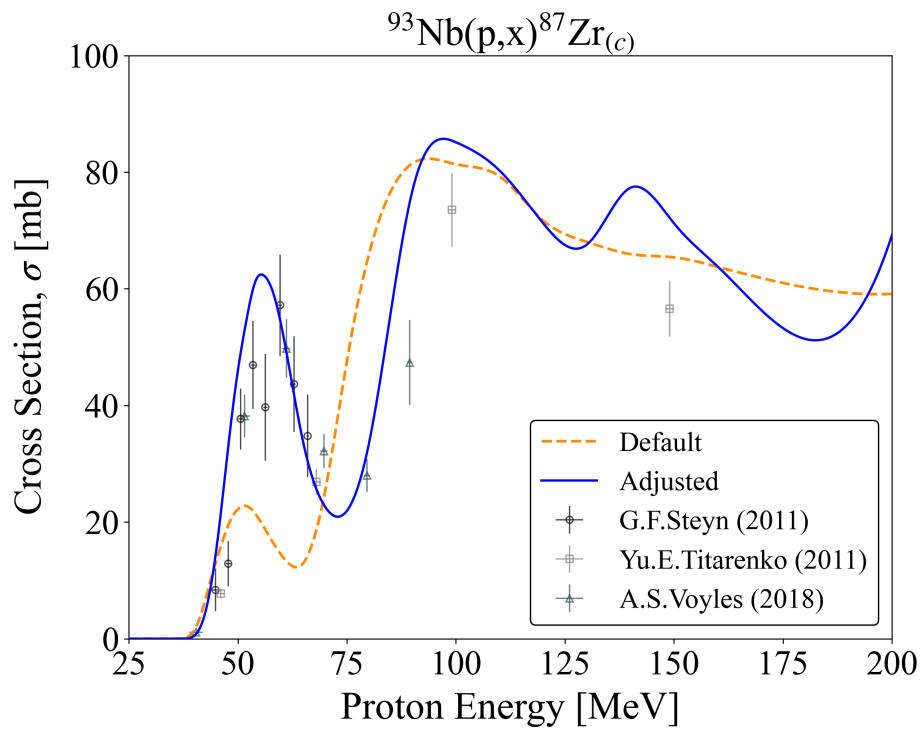
Figure 2.22: TALYS default and adjusted calculation for ^{87}Zr.
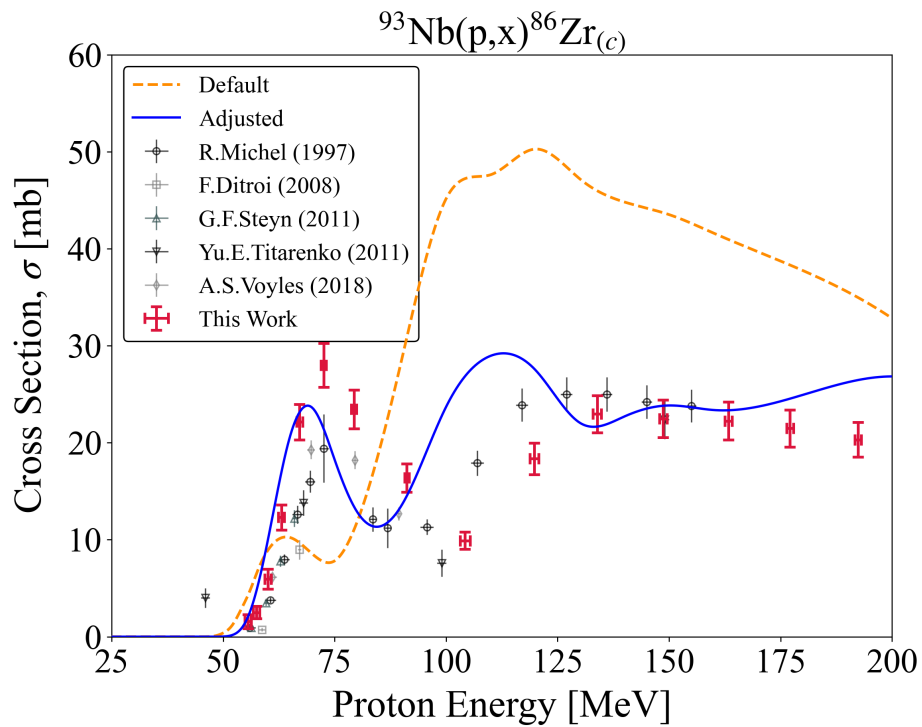
Figure 2.23: TALYS default and adjusted calculation for ^{86}Zr.
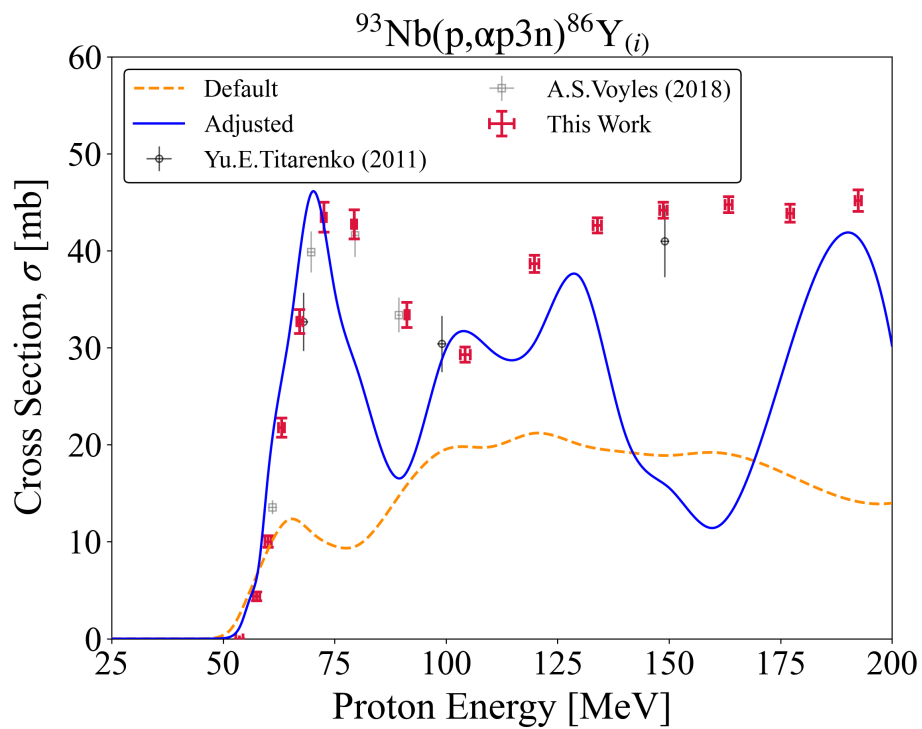
Figure 2.24: TALYS default and adjusted calculation for ^{86}Y.

2.5.3.1 Parameter Adjustment Validation

A crucial aspect in this suggested approach is validation of the derived parameters to ensure that it is justified to attribute physical meaning to their values. The ^{93}Nb(p,x)^{89}Zr, ^{89}Nb, ^{87}Y, ^{84}Rb reaction channels, with all but ^{84}Rb being cumulative data, were used for this purpose. The adjusted fit shown in Figures 2.25–2.28 continues to show improved behaviour over the default in these cases, especially in the compound peak regions.
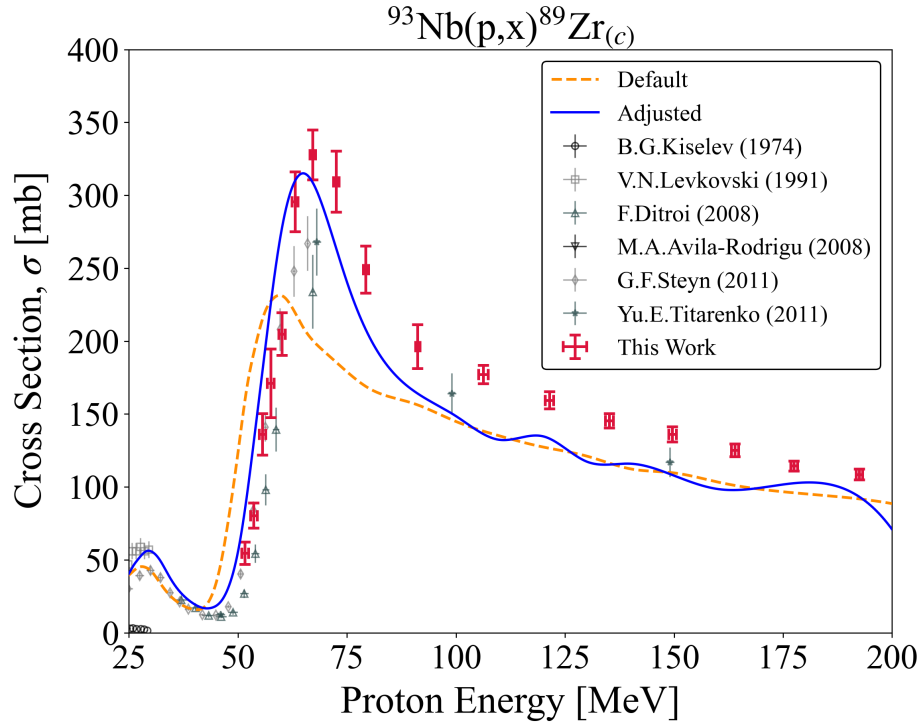
Figure 2.25: TALYS default and adjusted extended to ^{89}Zr.

The total chi-squared, χ^2_{tot}, used to compare the default and adjusted TALYS fit across all utilized and validation channels is given by:

$$\chi^2_{tot} = \frac{1}{N_c} \sum_{c=1}^{N_c} \chi^2_c w_c, \tag{2.11}$$

where N_c is the number of reaction channels considered, χ^2_c is the chi-squared value per channel, and w_c is the weighting per channel [46, 103]. Each χ^2_c is defined by:

$$\chi^2_c = \frac{1}{N_p} \sum_{i=1}^{N_p} \left(\frac{\sigma^i_T - \sigma^i_E}{\Delta \sigma^i_E} \right)^2, \tag{2.12}$$

where N_p is the number of data points from all experimental datasets in a given channel, σ_E^i are the experimental cross sections with $\Delta\sigma_E^i$ uncertainty, and σ_T^i is the TALYS cross section calculation [46, 103]. No exclusions or preference was given to the quality of data beyond weighting by uncertainty, which is in opposition to techniques typically used in an evaluation [46, 104]. Two weighting calculations were considered in this application, both of which tried to emphasize the importance of fits to the most prominent channels. One weighting methodology is to use the cumulative cross section of the TALYS calculation in a given channel relative to the sum of all channels' cumulative cross sections:

$$w_c = \frac{\sum_{i=1}^{N_p} \sigma_T^{ci}(E)}{\sum_{c=1}^{N_c} \sum_{i=1}^{N_p} \sigma_T^{ci}(E)}. \tag{2.13}$$
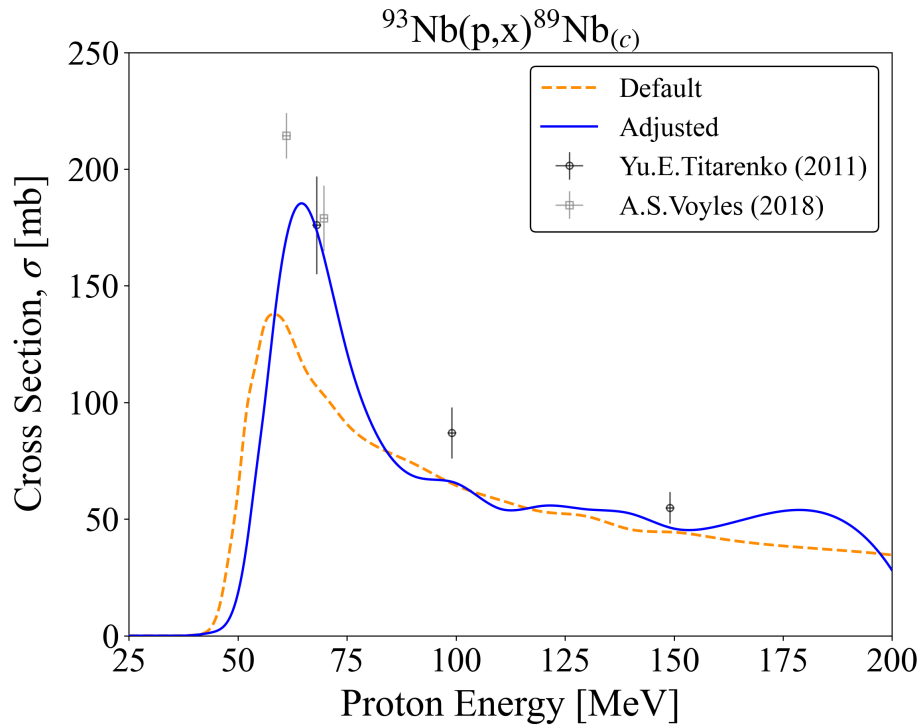
Figure 2.26: TALYS default and adjusted extended to ^{89}Nb.
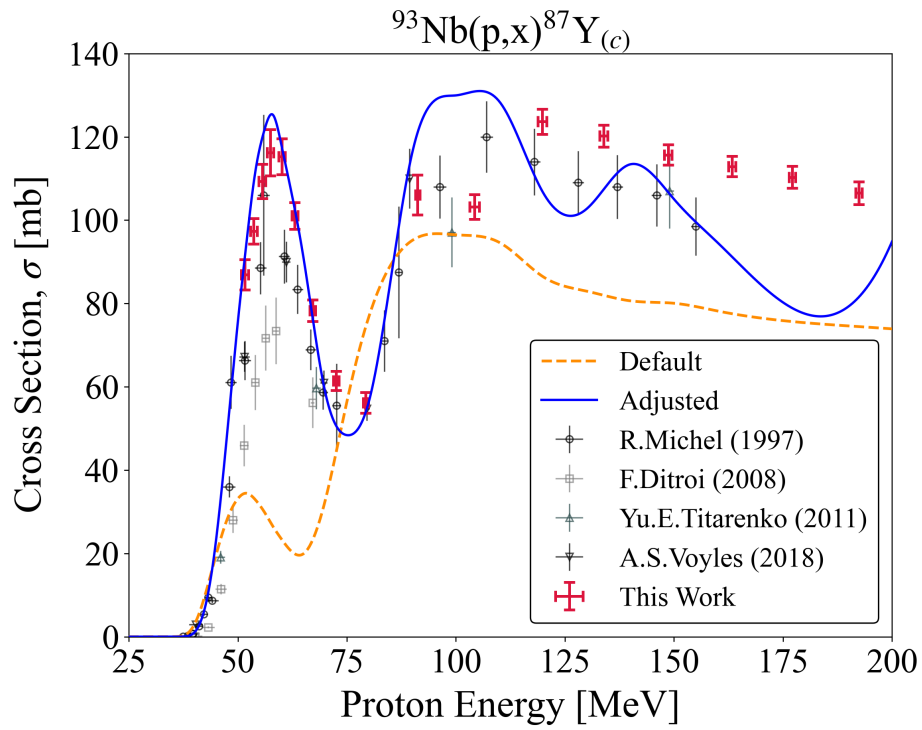
Figure 2.27: TALYS default and adjusted extended to ^{87}Y.
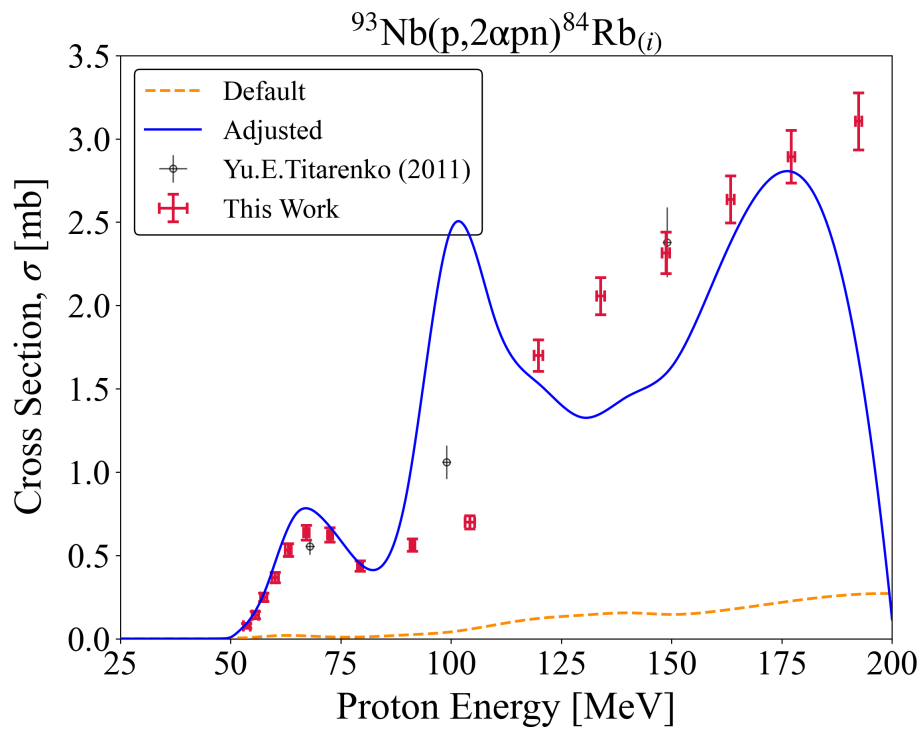
Figure 2.28: TALYS default and adjusted extended to ^{84}Rb.

The above "Cumulative σ" weighting potentially poses a risk of washing out the importance of large compound peaks that were significant to parameter adjustment studies but fall off at high energies such as the case with ^{90}Mo production. This issue could be resolved with an alternative "Maximum σ" weighting that considers the maximum production cross section reached in each channel relative to the sum of all channels' maximums:

$$w_c = \frac{\sigma_{T,max}^c}{\sum_{c=1}^{N_c} \sigma_{T,max}^c}. \tag{2.14}$$

The χ_{tot}^2 results based on both weighting methods are given in Table 2.3. In this case both weighting techniques yield similar results, which clearly show that the adjusted parameters fit performs much better for high-energy proton-induced reactions on niobium than the default prediction. Ultimately, this more realistic analysis method, even as a manual search, has produced a fit with a better performance than the default calculations with a justifiable limited set of parameter changes built from measured experimental data. This analysis is therefore an improved standard over the one-channel adjustment norm and can be a reasonable expectation for future parameter optimization data work.

Table 2.3: Global χ^2 metric describing goodness-of-fit for the default and adjusted TALYS calculations of ^{93}Nb(p,x).

Weighting Method	Default χ_{tot}^2	Adjusted χ_{tot}^2
Cumulative σ	15.6	3.37
Maximum σ	16.0	3.28

2.5.4 Fitting Procedure Applied to ^{139}La(p,x)

The same fitting approach detailed for niobium was also applied to high-energy proton-induced reactions on lanthanum. Eight reaction channels were used in the study: ^{139}La(p,x)^{137m,137g,135,134,133m,132}Ce, ^{135}La, ^{133m}Ba, with ^{135}Ce, ^{134}Ce, ^{137m}Ce, and ^{135}La production as the most prominent.

The cross section data for ^{139}La(p,x) are more limited than what was available in the niobium case. These eight channels only contain the three datasets of Tárkányi et al. [105], Becker et al. [37], and Morrell et al. [39], with the latter two characterizations utilizing stacked-target activation at LANL and LBNL, respectively, consistent with the work performed here.

In addition to a sparser body of data, there is a limited diversity of reaction products, where only the ^{135}La production gives insight into proton emission behaviour and only the ^{133m}Ba production gives insight into alpha emission behaviour. The measured cerium channels, comprising the bulk of the available data, are solely (p,xn) reactions. That being said, the

restricted dataset makes ^{139}La(p,x) a valuable application of the suggested fitting procedure as it can show the amount of predictive power that can be gained even from reactions that are being partially measured for the first time.

Note that the default TALYS calculations for lanthanum were significantly better than for niobium, whose dominant channels were predicted with extremely discrepant shapes, magnitudes, and positioning from the experimental data. As a result, the amount of parameter adjustments, fine tuning, and iteration needed to properly model the niobium can be considered higher than typical.

Firstly, the application of microscopic level densities over phenomenological ones in the lanthanum calculations provided immediate benefit, matching the observed rising edges and shapes of the dominant ^{135}Ce and ^{134}Ce compound peaks quite well. Similarly to the niobium, `ldmodel` 4 performed best and was chosen, though there was no apparent constraining residual product in this case and `ldmodel` 5 was a close next best choice.

The pre-equilibrium portion of the procedure revealed a need for adjustments of `M2constant`=0.85, `M2limit`=2.5, and `M2shift`=0.9 to the exciton model matrix parameterization. It should be noted that these parameters are all shifted in the same directions as in the niobium case, simply to a lesser extent, which emphasizes the better initial default guess here. A last additional pre-equilibrium change also included `Cstrip a`=2.0, where `Cstrip a` affects the transfer reaction contribution of (p, α) to the overall pre-equilibrium cross section. This helps to increase ^{133m}Ba production without much noticeable effect to the other considered channels.

For OMP fine tuning, the ^{135}La and ^{133m}Ba channels necessarily played important roles due to their particle emission diversity. The prevailing discrepancies in these two channels at this point included a slight overprediction of ^{135}La production and a minor underprediction of the ^{133m}Ba compound peak falling edge. A testing of the available TALYS OMP parameters demonstrated that `rvadjust p` and `rvadjust a` held the most sensitivity. The most accurate behaviour was extracted solely using `rvadjust p`=0.96. Finally, there was a small local competition error between ^{135}Ce and ^{134}Ce that could be corrected by a `ctable` increase to ^{135}Ce. There were far fewer confounding level density changes for the lanthanum relative to the niobium.

The total derived parameter changes for ^{139}La(p,x) are listed in Section 2.10 (Table 2.9). The adjusted TALYS fits from this procedure are given in Figures 2.29–2.36 compared to the default calculation and EXFOR data for the eight used reaction channels [37, 39, 105]. Given that the experimental data do not extend beyond 100 MeV, the fits are shown only up to this point.
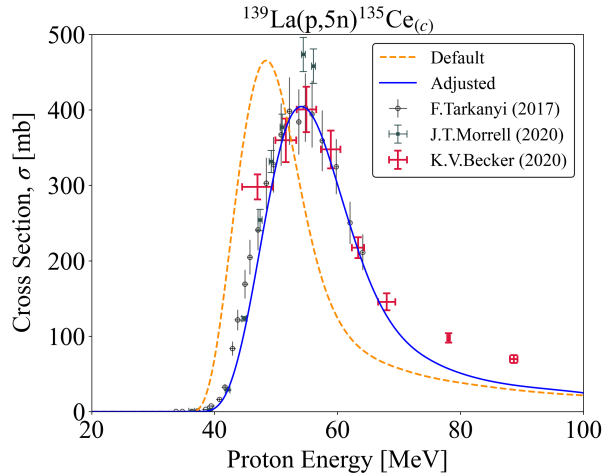
Figure 2.29: TALYS default and adjusted calculation for ^{135}Ce.
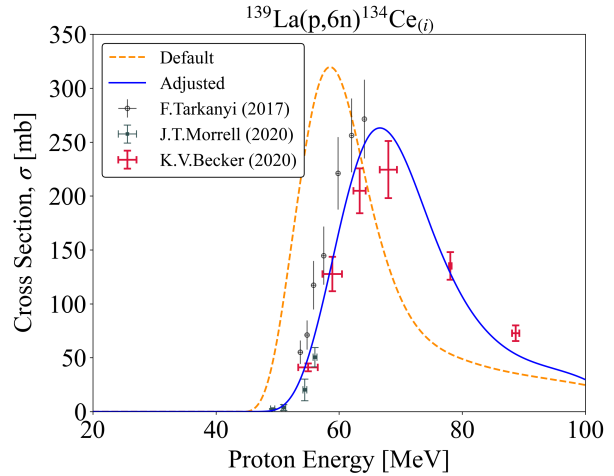
Figure 2.30: TALYS default and adjusted calculation for ^{134}Ce.
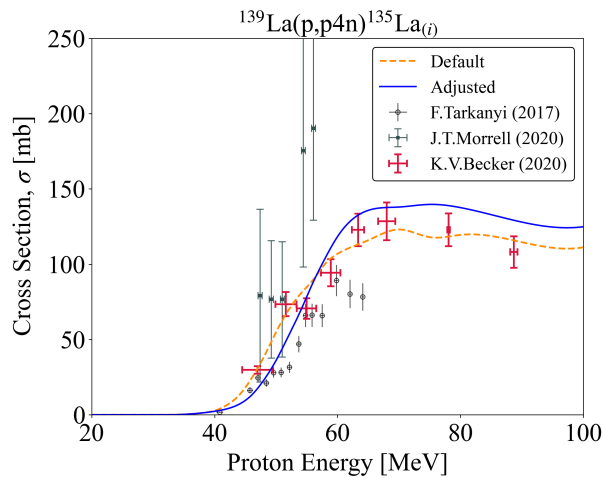
Figure 2.31: TALYS default and adjusted calculation for ^{135}La.
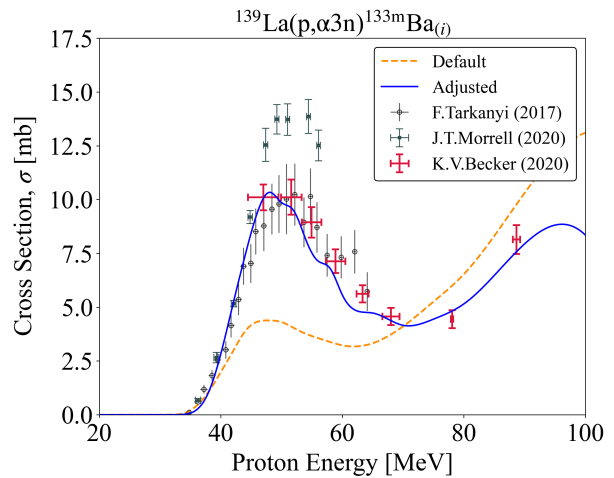
Figure 2.32: TALYS default and adjusted calculation for ^{133m}Ba.
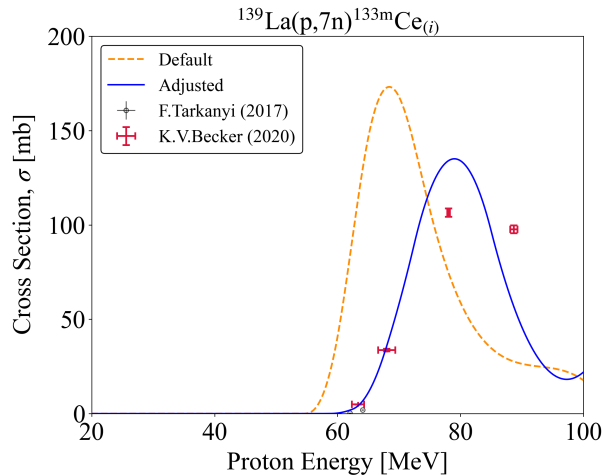
Figure 2.33: TALYS default and adjusted calculation for ^{133m}Ce.
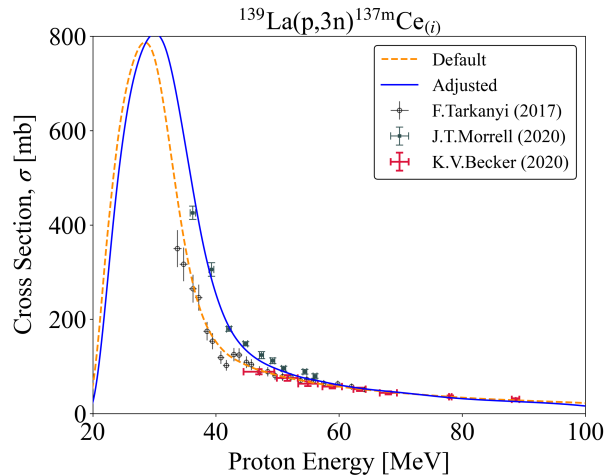
Figure 2.34: TALYS default and adjusted calculation for ^{137m}Ce.
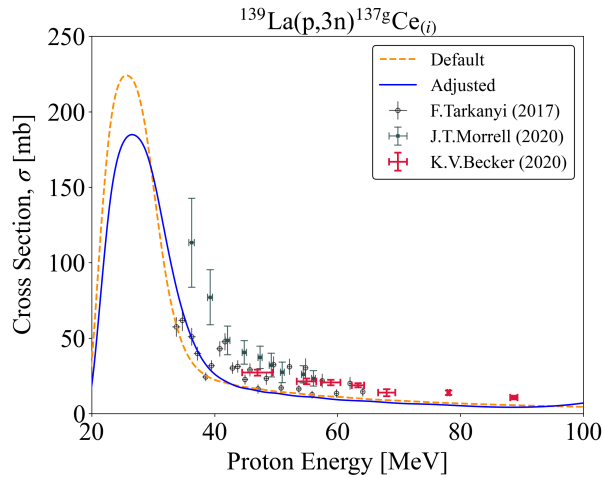
Figure 2.35: TALYS default and adjusted calculation for ^{137g}Ce.
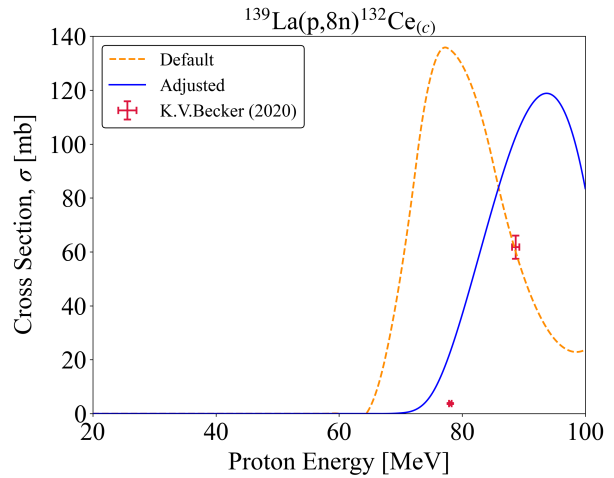
Figure 2.36: TALYS default and adjusted calculation for ^{132}Ce.

2.5.4.1 Parameter Adjustment Validation

Validation of this adjusted fit is performed via comparison to the ^{139}La(p,x)^{139}Ce, ^{133}La, ^{133g,131}Ba, ^{132}Cs channels, which were not used in the fitting approach due to their magnitudes or ambiguity/lack of data [106–108]. However, even in these channels, the adjusted fit is shown in Figures 2.37–2.41 to have impressive predictive power versus the default. Specifically, the predictive success for the single-particle out ^{139}La(p,n)^{139}Ce reaction, necessarily heavily influenced by pre-equilibrium, instills confidence in the adjusted parameters.
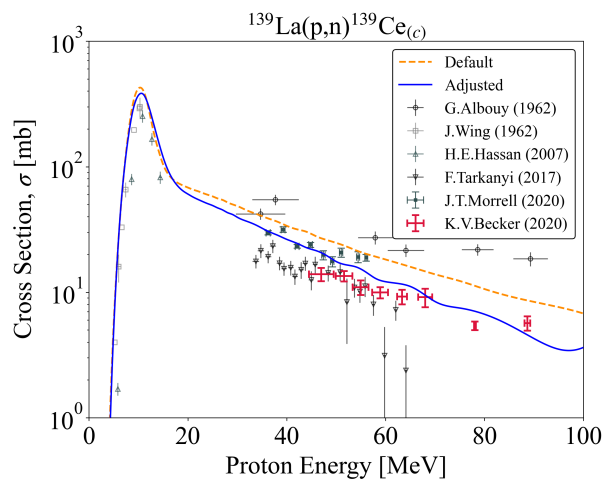
Figure 2.37: TALYS default and adjusted extended to ^{139}Ce.
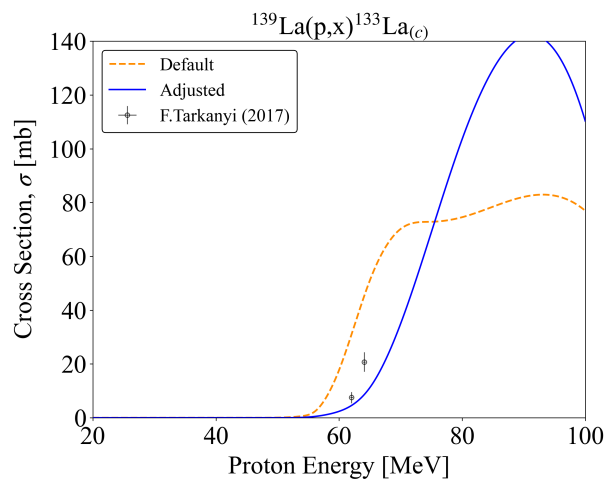
Figure 2.38: TALYS default and adjusted extended to ^{133}La.

The χ^2_{tot} results comparing the adjusted and default fit globally based on both weighting methods described in Section 2.5.3.1 are given in Table 2.4. Again, both weighting methodologies yield similar results, and it is evident that the adjusted fit outperforms the default prediction. In both the niobium and lanthanum presented cases of this work, the suggested standardized fitting procedure has produced improved results over the TALYS default in a comprehensive and justifiable manner.
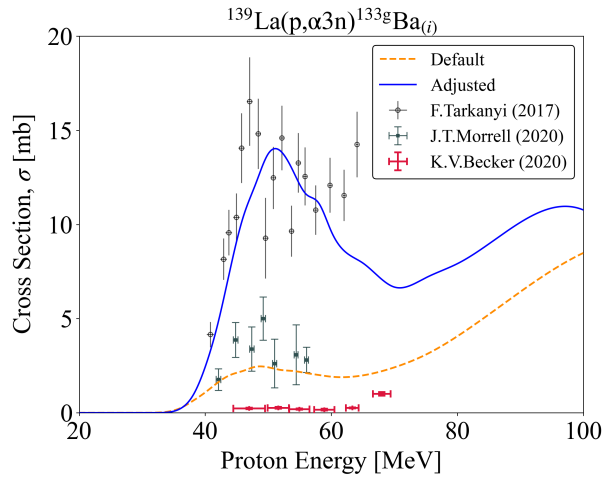
Figure 2.39: TALYS default and adjusted extended to ^{133g}Ba.
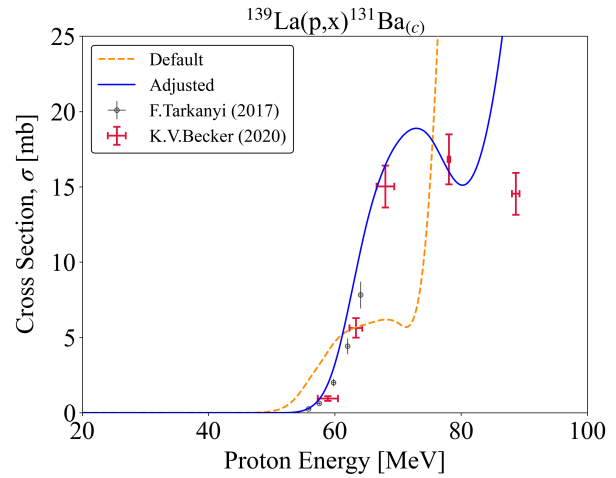
Figure 2.40: TALYS default and adjusted extended to ^{131}Ba.
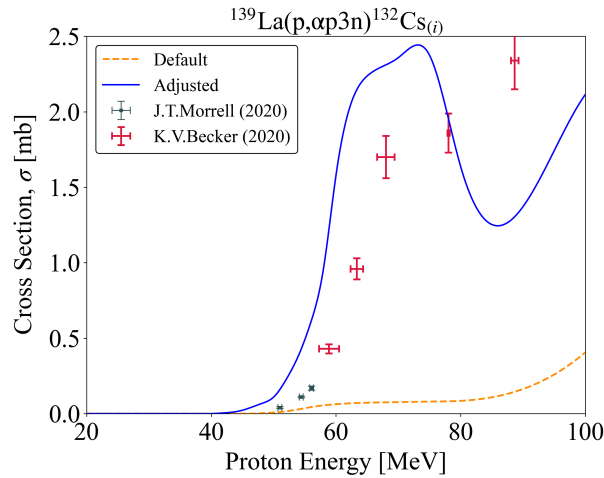
Figure 2.41: TALYS default and adjusted extended to ^{132}Cs.

Table 2.4: Global χ^2 metric describing goodness-of-fit for the default and adjusted TALYS calculations of ^{139}La(p,x). The very large improvement in χ^2 for the adjusted case may imply that the applied weights were too large, contributing to an inflated change versus the default.

Weighting Method	Default χ^2_{tot}	Adjusted χ^2_{tot}
Cumulative σ	87.8	1.89
Maximum σ	96.4	3.34

2.5.5 Interpretation of Parameter Adjustments

The success of this fitting approach suggests that physical meaning could be inferred from the adjustments made to the exciton model parameters. Moreover, the consistent adjustments made to the `M2` exciton parameters in both the niobium and lanthanum cases appears to reveal a systematic trend in how residual product excitation functions for high-energy proton-induced reactions on spherical nuclei are miscalculated in the current exciton model scheme. Across the prominent reaction channels explored in this work, there was a consistent underprediction of both the high-energy pre-equilibrium tails and compound peak magnitudes. It was seen that enforcing `M2constant`<1.0 could improve lacking tail behaviour while `M2limit`>1.0 with `M2shift`<1.0 helped compensate for the increased tail by creating more production in the compound peak. It is possible to further visualize and quantify this trend by plotting the magnitude of the squared effective interaction matrix element within the (E^{tot}, n) reaction phase space. Specifically, defining $\Delta_{adj-def}$ as the difference of normalized M^2 between the adjusted fit and the default calculation by:

$$\Delta_{adj-def} = \frac{M^2(E^{tot}, n)_{adj}}{M^2(E^{tot}, n)_{adj,max}} - \frac{M^2(E^{tot}, n)_{def}}{M^2(E^{tot}, n)_{def,max}}, \tag{2.15}$$

the relative strength of M^2 for the adjusted case can be compared to the relative strength of M^2 in the default case across all of the reaction phase space. The $\Delta_{adj-def}$ results for both the ^{93}Nb(p,x) and ^{139}La(p,x) modeling are plotted in Figure 2.42. It is seen that the adjustments for both targets exhibit the same trend that better modeling fits were achieved when there was a relative decrease for internal transition rates at intermediate proton energies $(E_p = 20 - 60$ MeV) in the exciton model as compared to default values. The relative decrease reduces the probability of formation of complex exciton states, and in turn the compound nucleus equilibration limit, in favour of pre-equilibrium emission. Furthermore, the location of the relative decrease in reaction phase space indicates that there is difficulty transitioning between the Hauser-Feshbach and exciton models for nuclear reactions. These exciton adjustments appear to act as a surrogate for better damping into the compound nucleus system.

The results of Figure 2.42 are additionally interesting because of the variation between the $\Delta_{adj-def}$ magnitudes for ^{93}Nb(p,x) and ^{139}La(p,x). The $\Delta_{adj-def}$ for ^{139}La(p,x) are smaller as a function of the better initial default residual product calculations in TALYS compared to ^{93}Nb(p,x). However, the root cause of this more pronounced default model failure in the niobium case is unknown, especially given that both niobium and lanthanum are structurally similar.

In total, the modeling adjustments in this work suggest the need to incorporate residual product excitation function data in some capacity into future exciton model parameterizations. Further, this trend applies for proton-induced reactions and perhaps implies a need to release the strict generality of having the same exciton model formulas for both incident protons and neutrons [27].

2.5.6 Future Considerations

Residual product excitation functions were not used in the initial exciton model parameterization by Koning and Duijvestijn [27] because of the complexity and uncertainties brought in by the additional level density and transmission coefficient models. This study has included this complexity and tried to isolate for these competing issues and uncertainties through the order of the fitting procedure and the focus on fitting many of the prominent channels, though difficulties still remain with their incorporation.

Furthermore, the adjusted parameters lead not only to changes in specific product reaction channels, but to the total non-elastic channel as well. Consider the difference in total non-elastic cross section for protons incident on niobium between the TALYS default, other evaluation databases, and the TALYS adjusted case, as given in Figure 2.43a [7, 8, 109–111]. The adjusted case argues for an increased high-energy cross section. While below 50 MeV, the adjusted calculation seems quite reasonable, above 50 MeV it is evident that there is a large discrepancy between it and the other predictions. However, it should be noted that the evaluations are all heavily constrained by a single high-energy data point, which may not fully represent reality. Nonetheless, they suggest that there should be less confidence in extension of the adjusted TALYS fit to far-from-target residual products such as Kr, Se, and As. It is possible that the poorer fit at high energies is also a reflection of the deterioration in the quality of level density predictions in general at such high excitations. It is likely that the employed microscopic models used in the fitting are less appropriate at such high energies than a more simple stochastic model such as a Fermi gas calculation, though this model too may break down near 200 MeV excitation energy [112]. This is a difficult consideration to experimentally check but might be a more realistic cause for error than the shell gap effects discussed in Section 2.5.3.
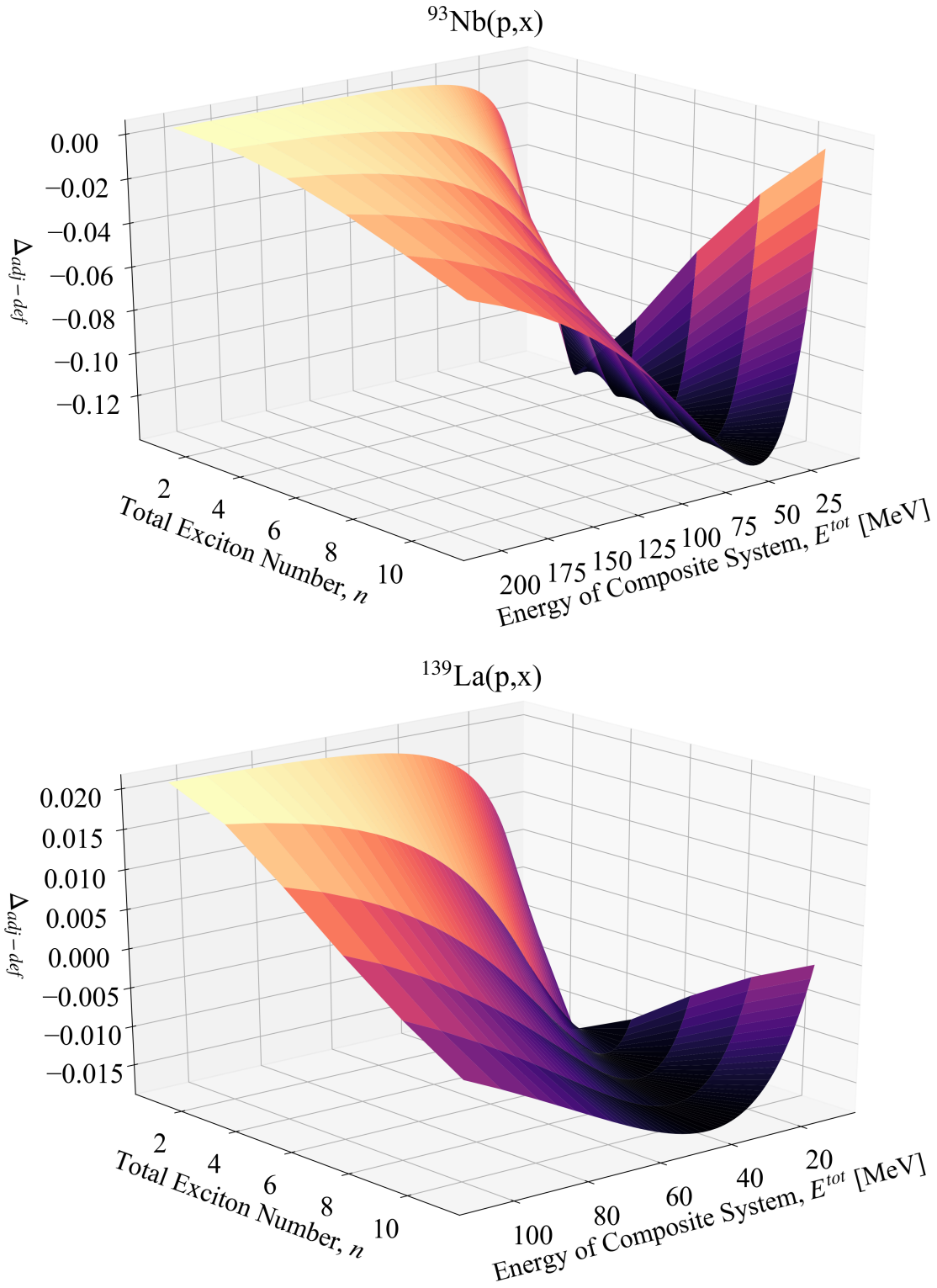
Figure 2.42: Visualization of impact from pre-equilibrium parameter adjustments across reaction phase space on the exciton model squared matrix element for the effective residual interaction. A consistent pattern is seen in the adjustments for the niobium and lanthanum cases, with more pronounced behaviour for the niobium. The colour scale is a mapping of the z-axis in each case.

A further neglected effect, which may be relevant to the code mispredictions seen at high energies for far-from-target products, is the incorporation of isospin conservation in the modeled reactions. The theoretical calculations of Grimes et al. [113] and Robson et al. [114] using a modified Hauser-Feshbach formalism including isospin effects and the experimental findings from works such as Lu et al. [115] and Kalbach-Cline et al. [116] explored this factor. They demonstrate that isospin conservation yields cross sections and particle emission spectra different from the Bohr independence hypothesis of compound nuclear decay including only angular momentum and from the typical exciton model for pre-equilibrium decay. Particularly, Grimes et al. [113] and Lu et al. [115] show that isospin selection rules for proton-induced reactions result in enhanced proton emission. These publications explored proton bombardment energies in the $10 - 20 \, \mathrm{MeV}$ range. Although the adjusted modeling fits in this work were appropriate at those incident energies, it is possible that the choice of level density parameters were an unknowing compensating factor for neglected isospin effects, which did not remain effectively compensating at higher energies. It is also possible that isospin effects are simply small for the target mass and energies under consideration here. We believe it would be a worthwhile experiment for the community to explore these isospin considerations through a study of particle emission spectra resulting from both p+^{93}Nb and α+^{90}Zr irradiations. Specifically, these reactions populate the same ^{94}Mo compound system with different isospins and the proximity of ^{94}Mo to the $N = 50$ shell gap may mean that pure isospin states exist that can be well-defined, making the compound system a suitable candidate for this type of structure investigation.

Unfortunately, it is not possible to derive any ^{93}Nb(p,non) data points from summed residual product cross sections measured in this work for a more in-depth fit comparison. The presented cross section results are not exhaustive enough for this calculation since stable and very short-lived isotope production was not measured. This potential non-elastic cross section issue, or the possible high-energy theoretical shortcomings, do not discredit the procedure shown here but instead emphasize that the approach suggested in this work is not meant to be on par with complete reaction evaluations. In general, this approach is a holistic and realistic methodology, grounded on observables and experimental data, that experimenters can perform to benefit theory and support further predictive work. Although, it is clear that the niobium fitting is an extreme case and looking at the total non-elastic cross section for protons incident on lanthanum in Figure 2.43b instills more confidence in this overall fitting process [109].

A worthwhile different way of continuing study on the departure of equal matrix elements for neutron-induced or proton-induced reactions may be to systematically study one reaction channel, instead of all reaction channels simultaneously as in this work. Hence, one could investigate whether (p,n) reactions for different nuclides would show the same exciton adjustment trends discovered here.
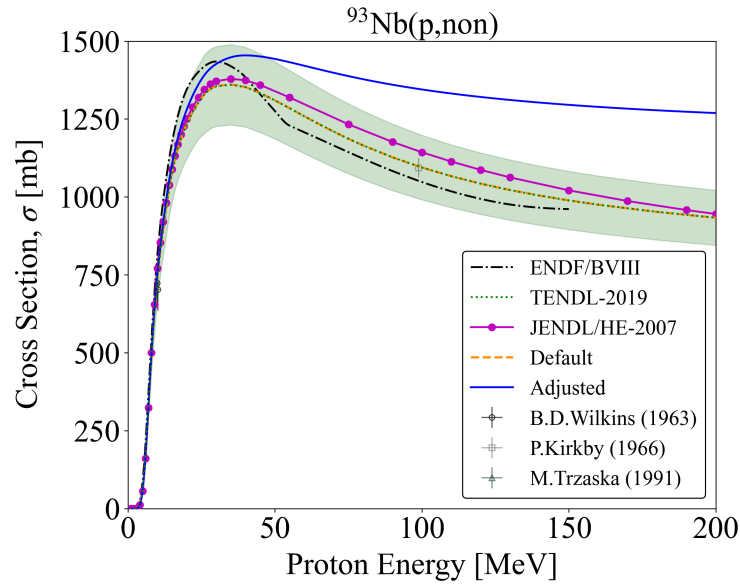
(a)
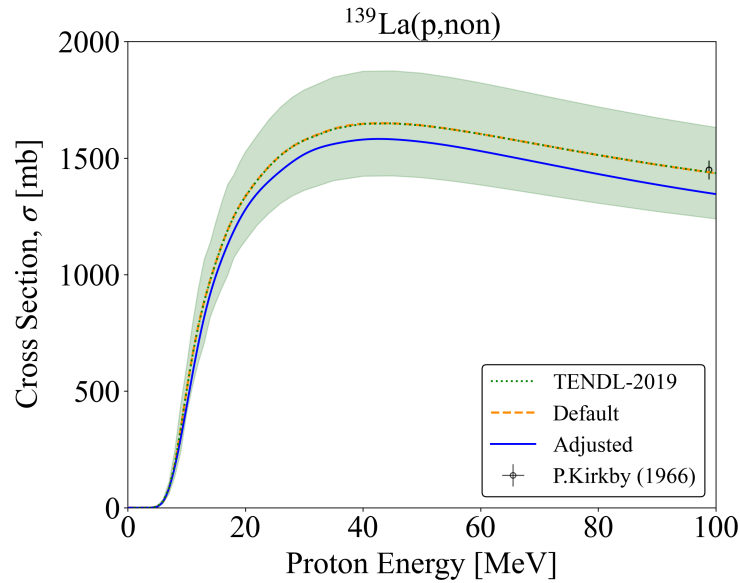
(b)

Figure 2.43: Comparison of experimental, evaluated, and theoretical non-elastic cross sections. The filled error bands are associated with the TENDL data.

In the future, this fitting procedure could expand to include emission spectra and double-differential data to try and improve the elastic versus non-elastic competition and potentially determine other corrective parameter adjustments that are simply not sensitive in the purely residual product data analysis [61]. Including the extra datasets can help clarify effects between level density models, the optical model, and pre-equilibrium parameterizations. Such

a procedure could be an inspiration and act as a stepping stone to the development of a charged-particle evaluated data database [117].

Although the sensitivity work performed in this paper was a manual search, it would be useful to incorporate automation, such as search techniques within a Bayesian framework, with the acquired exciton adjustment knowledge. This would help to more accurately determine a global minimum for parameter optimization and to better express the resolving power of different parameters and channels in a more quantitative fashion.

2.6 Conclusions

This work reports 23 sets of measured ^{93}Nb(p,x) residual product cross sections between 50–200 MeV as part of a Tri-lab collaboration between LBNL, LANL, and BNL. The reported cross sections greatly extend the datasets for numerous products and are of higher precision than a majority of previous measurements. The ^{93}Nb(p,4n)^{90}Mo monitor reaction of particular interest for intermediate proton energy stacked-target activation experiments was characterized beyond 100 MeV for the first time.

Given the measured data, an in-depth investigation of reaction modeling and pre-equilibrium mechanisms was conducted. A standardized parameter adjustment fitting procedure to improve default code predictions in a physically justifiable manner was proposed and applied to ^{93}Nb(p,x) and ^{139}La(p,x) cross section data as tests. The fitting approach focused on the current parameterization of the squared matrix element in the pre-equilibrium two-component exciton model. A systematic trend for the exciton parameter adjustments to correct high-energy tails and compound peak magnitudes was seen that implied the current parameterization is not wholly correct. This result suggests the need to incorporate residual product excitation function data in some capacity into future exciton model parameterizations and potentially create different parameterizations altogether for incident protons and neutrons.

The focus of this work was on presenting and interpreting the results from (p,x) reactions on spherical target nuclei (Nb and La). Subsequent papers will discuss additional data results from the Tri-lab collaboration for ^{75}As(p,x) reactions as well as the production and characterization of thin arsenic targets.

Data Availability Statement

The gamma-ray spectra and all other raw data created during this research are openly available at `http://doi.org/10.5281/zenodo.4648950` [118]. Upon publication, the experimentally determined cross sections will be uploaded to the EXFOR database.

2.7 Target Stack Designs

Details of the stacked-targets irradiated in this work are given in Tables 2.5 and 2.6.

Table 2.5: Target stack design for irradiation at IPF. The proton beam initially hits the stainless steel plate (SS-SN1) after passing through the upstream Inconel beam entrance window, a water cooling channel, and the target box aluminum window. The thickness and areal density measurements are prior to any application of the variance minimization techniques described in this work.

Target Layer	Thickness [µm]	Areal Density [mg/cm^2]	Areal Density Uncertainty [%]
SS-SN1 Profile Monitor	130.0	100.12	0.07
Al-SN1	27.33	7.51	0.21
Nb-SN1	25.75	23.08	0.12
As-SN1	4.27	2.45	8.2
Ti-SN1	25.00	11.265	1.0
Cu-SN1	24.33	19.04	0.13
Al Degrader 01	6307.0	1702.89	0.001
Al-SN2	26.67	7.58	0.32
Nb-SN2	24.75	22.67	0.08
As-SN2	4.30	2.46	8.3
Ti-SN2	25.00	11.265	1.0
Cu-SN2	24.00	18.90	0.36
Al Degrader 02	3185.5	860.09	0.02
Al-SN3	26.67	7.38	0.22
Nb-SN3	24.50	22.83	0.03
As-SN3	3.62	2.07	9.0
Ti-SN3	25.00	11.265	1.0
Cu-SN3	23.33	19.38	0.11
Al Degrader 03	2304.5	622.22	0.06
Al-SN4	28.00	7.34	0.18
Nb-SN4	25.50	22.57	0.16
As-SN4	3.54	2.03	9.2
Ti-SN4	25.00	11.265	1.0
Cu-SN4	24.67	19.24	0.11
Al Degrader 04	1581.3	426.94	0.04
Al-SN5	27.00	7.48	0.44
Nb-SN5	24.75	22.78	0.12
As-SN5	3.90	2.23	8.7

Continued on next page

Table 2.5 (*Continued*)

Target Layer	Thickness [µm]	Areal Density [mg/cm^2]	Areal Density Uncertainty [%]
Ti-SN5	25.00	11.265	1.0
Cu-SN5	25.00	19.09	0.17
Al Degrader 05	1033.8	279.11	0.06
Al-SN6	28.67	7.44	0.25
Nb-SN6	25.25	22.80	0.08
As-SN6	3.11	1.78	10
Ti-SN6	25.00	11.265	1.0
Cu-SN6	24.33	19.50	0.16
Al Degrader 06	834.8	225.38	0.22
Al-SN7	28.33	7.56	0.15
Nb-SN7	25.50	22.62	0.06
As-SN7	2.79	1.59	9.2
Ti-SN7	25.00	11.265	1.0
Cu-SN7	23.67	18.79	0.04
Al Degrader 07	513.5	138.65	0.10
Al-SN8	27.67	7.56	0.10
Nb-SN8	25.50	22.95	0.45
As-SN8	2.20	1.26	9.0
Ti-SN8	25.00	11.265	1.0
Cu-SN8	24.00	19.06	0.23
Al Degrader 08	517.3	139.66	0.43
Al-SN9	27.00	7.47	0.36
Nb-SN9	25.00	22.53	0.24
As-SN9	2.57	1.47	9.9
Ti-SN9	25.00	11.265	1.0
Cu-SN9	26.33	19.19	0.12
Al Degrader 09	517.8	139.79	0.09
Al-SN10	28.00	7.41	0.17
Nb-SN10	24.75	22.82	0.02
As-SN10	1.94	1.11	10
Ti-SN10	25.00	11.265	1.0
Cu-SN10	25.67	18.87	0.18
SS-SN10 Profile Monitor	130.0	100.12	0.07

Table 2.6: Target stack design for irradiation at BLIP. The proton beam initially hits the stainless steel plate after passing through the upstream beam windows, water cooling channels, and target box aluminum window. The thickness and areal density measurements are prior to any application of the variance minimization techniques described in this work.

Target Layer	Thickness [μm]	Areal Density [mg/cm^2]	Areal Density Uncertainty [%]
SS Profile Monitor	120.2	95.16	0.58
Cu-SN1	26.00	22.34	0.10
Nb-SN1	25.75	22.75	0.25
As-SN1	1.89	1.08	9.9
Ti-SN1	25.00	11.265	1.0
Cu Degrader 01	5261.1	4708.07	0.02
Cu-SN2	26.75	22.41	0.11
Nb-SN2	24.75	22.91	0.19
As-SN2	2.94	1.68	9.0
Ti-SN2	25.00	11.265	1.0
Cu Degrader 02	4490.7	4018.99	0.04
Cu-SN3	26.50	22.26	0.05
Nb-SN3	24.00	22.67	0.31
As-SN3	3.06	1.75	10
Ti-SN3	25.00	11.265	1.0
Cu Degrader 03	4501.8	4028.84	0.03
Cu-SN4	26.00	22.29	0.15
Nb-SN4	24.75	22.70	0.23
As-SN4	4.85	2.78	9.9
Ti-SN4	25.00	11.265	1.0
Cu Degrader 04	4243.9	3797.96	0.03
Cu-SN5	25.50	22.35	0.04
Nb-SN5	25.00	22.54	0.12
As-SN5	7.26	4.15	12
Ti-SN5	25.00	11.265	1.0
Cu Degrader 05	3733.8	3341.56	0.03
Cu-SN6	26.25	22.34	0.08
Nb-SN6	25.00	22.36	0.24
As-SN6	4.93	2.82	9.0
Ti-SN6	25.00	11.265	1.0
Cu Degrader 06	3783.0	3385.41	0.04
Cu-SN7	25.75	22.26	0.09
Nb-SN7	25.75	22.62	0.10
As-SN7	12.62	7.22	9.3
Ti-SN7	25.00	11.265	1.0

2.8   Measured Excitation Functions

Plots of extracted cross sections in this work are given with reference to existing literature data, TENDL-2019, and reaction modeling codes TALYS-1.9, EMPIRE-3.2.3, CoH-3.5.3, and ALICE-20 using default parameters [36, 42, 67–82]. Subscripts (i) and (c) in figure titles indicate independent and cumulative cross sections, respectively.
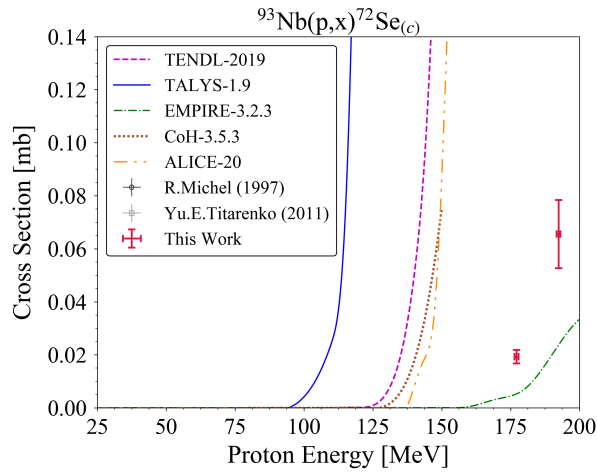
Figure 2.44: Experimental and theoretical cross sections for ^{72}Se production.
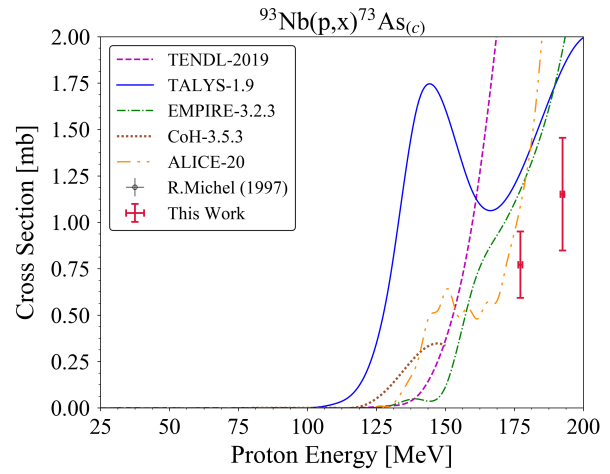
Figure 2.45: Experimental and theoretical cross sections for ^{73}As production.
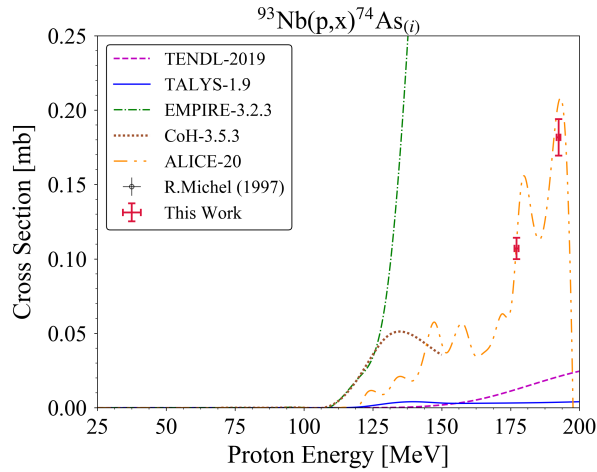
Figure 2.46: Experimental and theoretical cross sections for ^{74}As production.
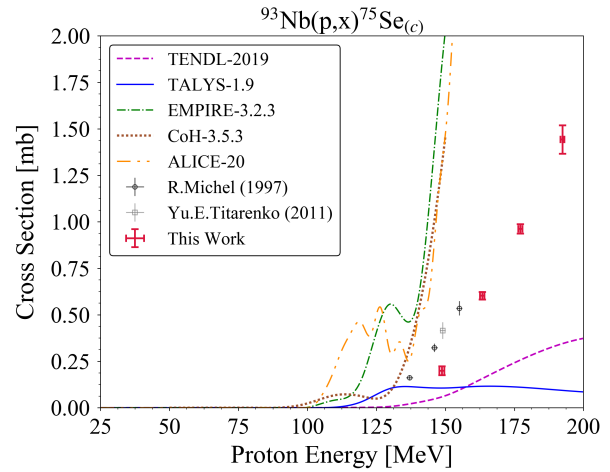
Figure 2.47: Experimental and theoretical cross sections for ^{75}Se production.
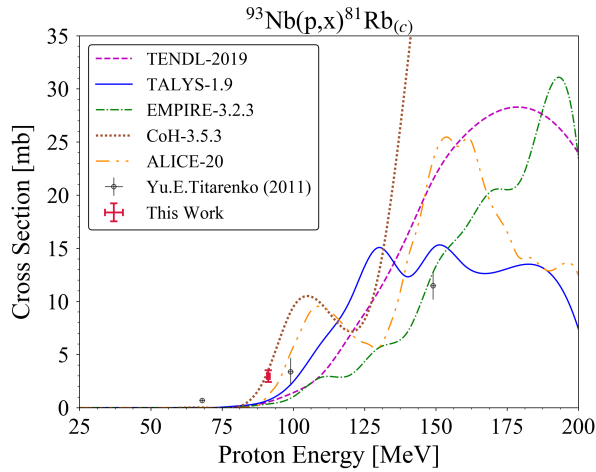
Figure 2.48: Experimental and theoretical cross sections for ^{81}Rb production.
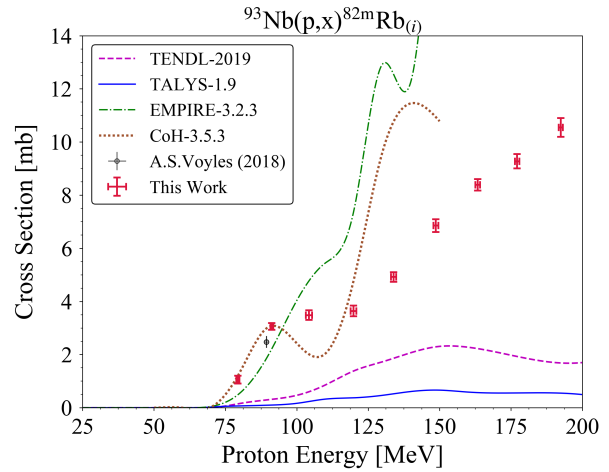
Figure 2.49: Experimental and theoretical cross sections for ^{82m}Rb production.
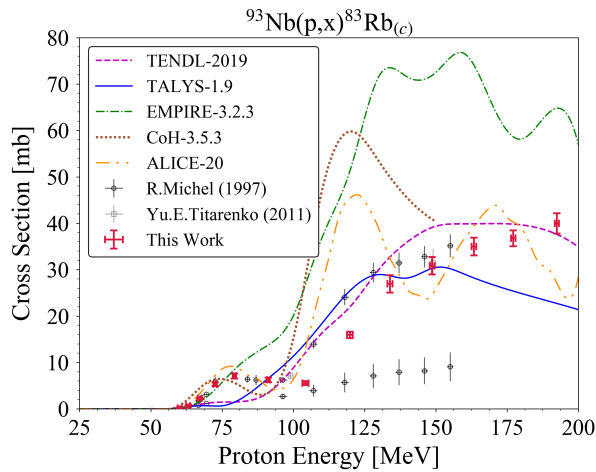
Figure 2.50: Experimental and theoretical cross sections for ^{83}Rb production.
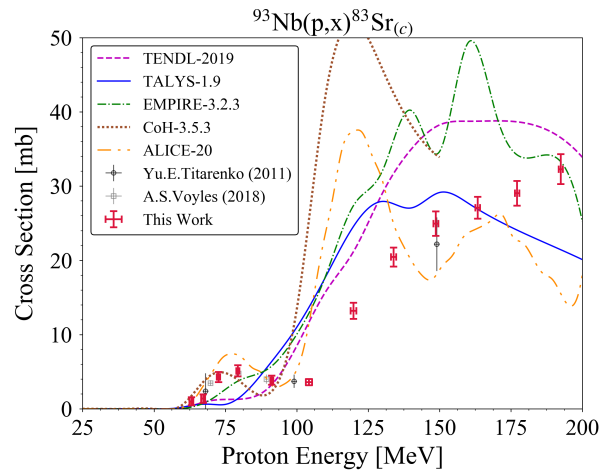
Figure 2.51: Experimental and theoretical cross sections for ^{83}Sr production.
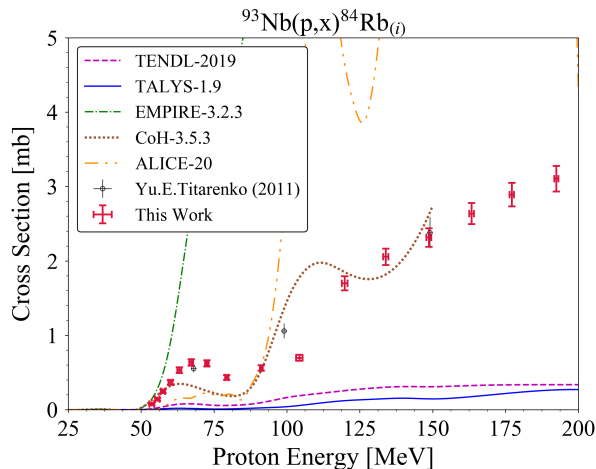
Figure 2.52: Experimental and theoretical cross sections for ^{84}Rb production.
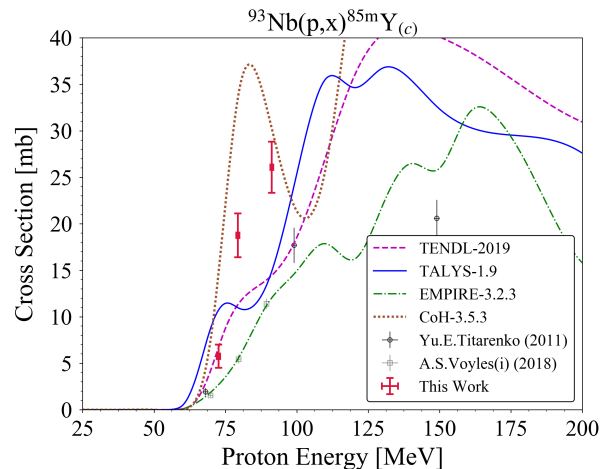
Figure 2.53: Experimental and theoretical cross sections for ^{85m}Y production.
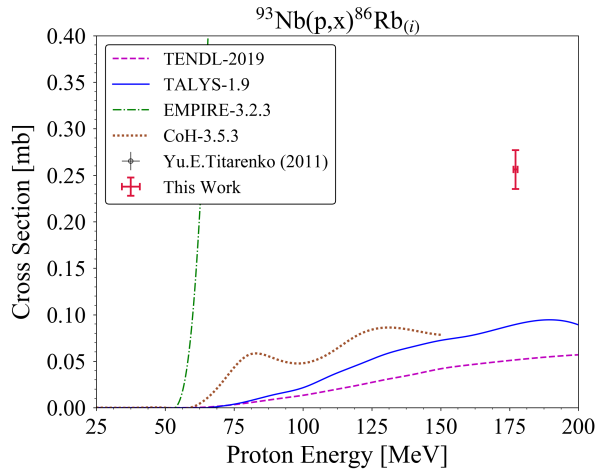
Figure 2.54: Experimental and theoretical cross sections for ^{86}Rb production.
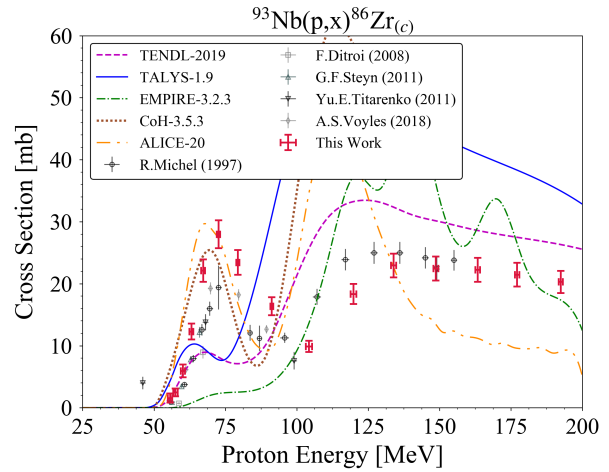
Figure 2.55: Experimental and theoretical cross sections for ^{86}Zr production.
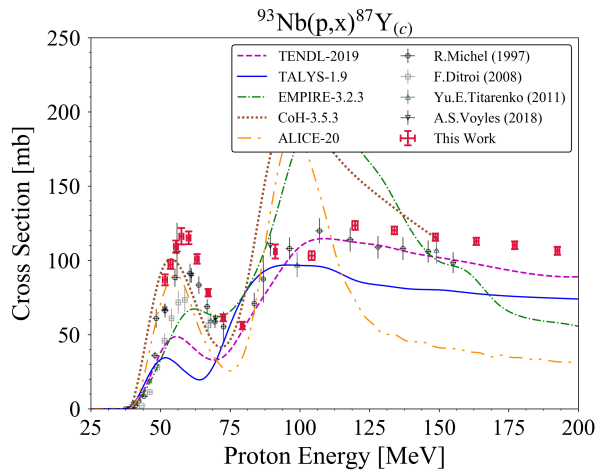
Figure 2.56: Experimental and theoretical cross sections for ^{87}Y production.
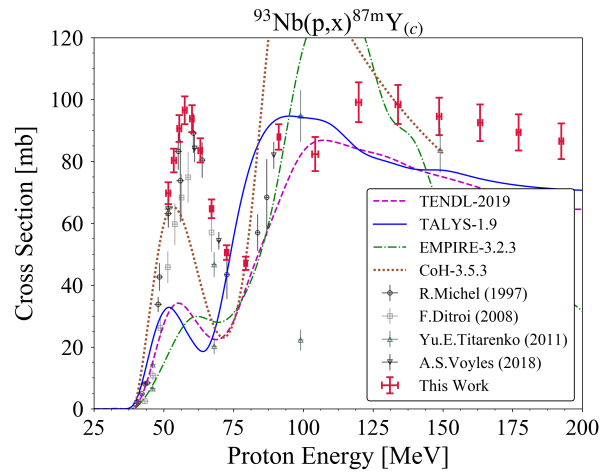
Figure 2.57: Experimental and theoretical cross sections for ^{87m}Y production.
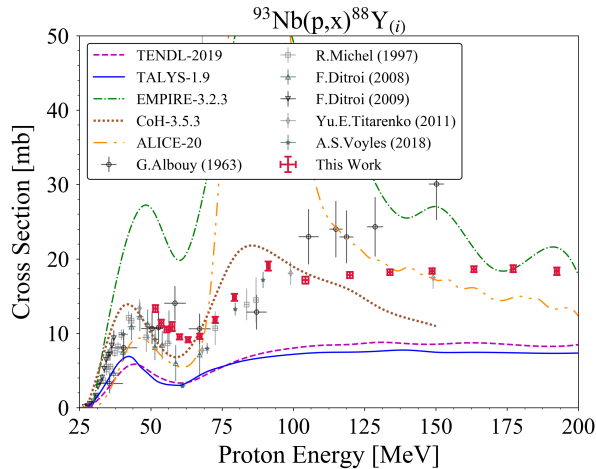
Figure 2.58: Experimental and theoretical cross sections for ^{88}Y production.
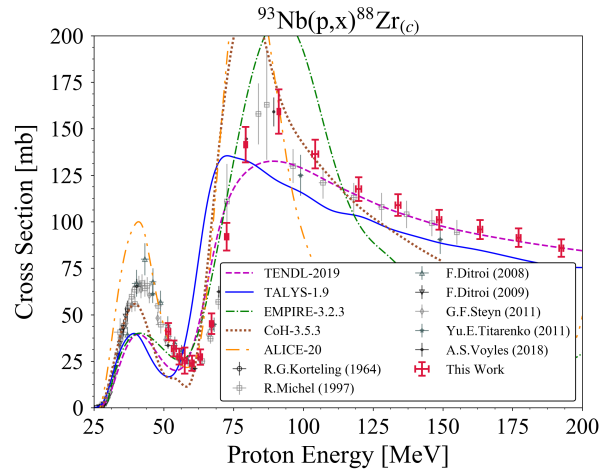
Figure 2.59: Experimental and theoretical cross sections for ^{88}Zr production.
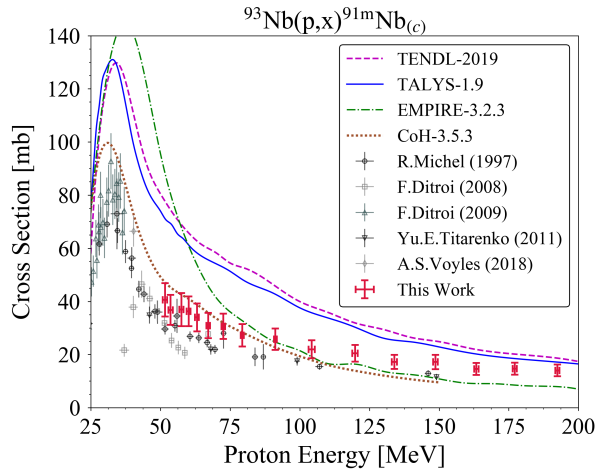
Figure 2.60: Experimental and theoretical cross sections for ^{91m}Nb production.
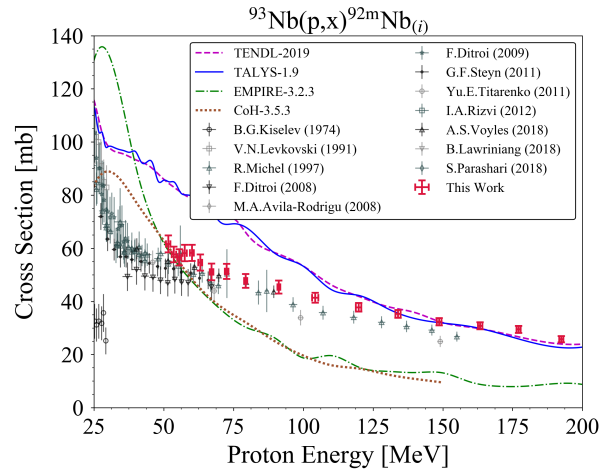
Figure 2.61: Experimental and theoretical cross sections for ^{92m}Nb production.
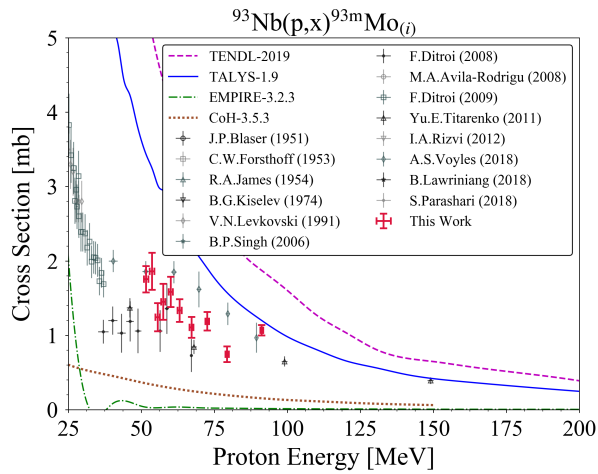
Figure 2.62: Experimental and theoretical cross sections for ^{93m}Mo production.

2.9   Non-Unique TALYS Parameter Adjustments

Table 2.7 outlines the ambiguity surrounding TALYS parameter adjustments when modeling is based on a single excitation function.

Table 2.7: Details of modeling cases used to reproduce similar behaviour for ^{93}Nb(p,p3n)^{90}Nb reaction, shown in Figures 2.14 and 2.15.

Model Number	Parameter Adjustments	χ^2_ν
Default	—	57.9
1	ldmodel 5 strength 4 preeqmode 3	24.0
2	ldmodel 2 strength 1 M2constant 1.8 avadjust p 0.85 rvadjust p 1.35	50.3
3	ldmodel 1 strength 2 M2constant 3.0 M2shift 2.2 M2limit 2.0	118.9
4	ldmodel 3 strength 2 M2constant 7.0 M2shift 0.1 M2limit 5.0 preeqmode 1 w1adjust p 1.5 v1adjust p 1.1 rvadjust p 1.33	298.4
5	ldmodel 6 strength 8 M2constant 0.95 M2shift 0.95 M2limit 3.0 w1adjust p 1.4 ctable 41 90 0.15	34.5

Table 2.7 (*Continued*)

Model Number	Parameter Adjustments	χ^2_ν
6	ldmodel 4 strength 5 M2constant 2.3 M2shift 0.6 M2limit 0.8 w1adjust p 1.3 rvadjust n 1.3 rvadjust a 0.85	57.8
7	ldmodel 1 strength 2 M2constant 1.7 w1adjust p 1.2 v1adjust p 1.05 rvadjust p 1.25	46.9
8	jlmomp y preeqmode 3 lwadjust 1.08	67.3
9	ldmodel 1 strength 2 M2constant 0.85 localomp n rvadjust n 0.85 v1adjust n 1.25 ctable 42 90 -1.0	45.1
10	ldmodel 5 strength 4 M2constant 3.3 ctable 42 88 -1.2 ctable 42 87 -1.2 ctable 41 90 1.6 ctable 41 86 -1.0 ctable 40 86 -1.8	23.5

2.10 TALYS Parameter Adjustments From Fitting Procedure

The derived parameter adjustments from the fitting procedure applied to the ^{93}Nb(p,x) and ^{139}La(p,x) data are listed in Tables 2.8 and 2.9.

Table 2.8: ^{93}Nb(p,x) best fit parameter adjustments derived from proposed procedure. The `equidistant` keyword adjusts the width of excitation energy binning and will be a default in updated TALYS versions. The `strength` keyword selects the gamma-ray strength model and has little impact in this charged-particle investigation, so it is chosen as one of the available microscopic options.

Parameter	Value
ldmodel	4 5 $^{94-86}$Nb 5 ^{94}Mo, $^{91-86}$Mo
strength	5
equidistant	y
M2constant	0.875
M2limit	4.5
M2shift	0.6
w1adjust p	2.2
ctable	39 86 -0.6 40 86 -0.35 40 87 -0.85 42 90 -0.5
ptable	39 86 2.0

Table 2.9: ^{139}La(p,x) best fit parameter adjustments derived from proposed procedure.

Parameter	Value
ldmodel	4
strength	5
equidistant	y
M2constant	0.85
M2limit	2.5
M2shift	0.9
cstrip a	2.0
rvadjust p	0.96
ctable	58 135 0.6

Chapter 3

Measurement and Modeling of Proton-Induced Reactions on Arsenic from 35 to 200 MeV

This chapter reports the majority of high-energy proton-induced cross section data measured in this dissertation and represents overall completion of the first year of TREND experiments.

Chapter 2 provides the principal purpose and methodology of this thesis but was limited to constrained data studies of niobium targets due to issues in determining the areal densities of the arsenic targets and complications of the reaction modeling effort arising from deformation in the p+^{75}As system. In the following sections, these considerations are properly addressed and remaining cross section measurements for 55 residual product excitation functions from ^{75}As, ^{nat}Cu, and ^{nat}Ti targets are reported. Included in this data contribution are the best quantifications of the ^{75}As(p,x)^{72}Se, ^{68}Ge reactions as valuable, novel routes to PET generator systems. An extensive discussion is dedicated to the ramifications of these new reported data in the context of already established medical isotope production.

The large influx of data is also necessarily used for further development of the proposed high-energy proton data evaluation procedure. The adaptability and flexibility of the procedure is explored with specific care given to newly discovered contributing factors of coupled-channels calculations, input parameter effects in unseen reaction channels from the activation/decay gamma-ray stacked-target technique, and missing level density data for nuclides off-stability. A reflection of the Chapter 2 pre-equilibrium exciton model adjustments is also provided alongside updated comments of local and global theory changes and their accompanying physical meanings. The outcome of these studies is a more nuanced evaluation approach, better suited to act as a stepping stone for the greater nuclear data community.

Moreover, the reported findings illuminate many previously "unknown unknowns" in the evaluation process and are significant to user communities considering applications such as radiation shielding or transport, who have prior used these high-energy models, but have essentially used them at a naïve level with no guiding data or parameter adjustments.

3.1 Abstract

^{72}As is a promising positron emitter for diagnostic imaging that can be employed locally using a ^{72}Se generator. However, current reaction pathways to ^{72}Se have insufficient nuclear data for efficient production using regional 100–200 MeV high-intensity proton accelerators. In order to address this deficiency, stacked-target irradiations were performed at LBNL, LANL, and BNL to measure the production of the ^{72}Se/^{72}As PET generator system via ^{75}As(p,x) between 35 and 200 MeV. This work provides the most well-characterized excitation function for ^{75}As(p,4n)^{72}Se starting from threshold. Additional focus was given to report the first measurements of ^{75}As(p,x)^{68}Ge and bolster an already robust production capability for the highly valuable ^{68}Ge/^{68}Ga PET generator. Thick target yield comparisons with prior established formation routes to both generators are made. In total, high-energy proton-induced cross sections are reported for 55 measured residual products from ^{75}As, ^{nat}Cu, and ^{nat}Ti targets, where the latter two materials were present as monitor foils. These results were compared with literature data as well as the default theoretical calculations of the nuclear model codes TALYS, CoH, EMPIRE, and ALICE. Reaction modeling at these high-energies is typically unsatisfactory due to little prior published data and many competing physics models. Therefore, a detailed assessment of the TALYS code was performed with simultaneous parameter adjustments applied according to a standardized procedure. Particular attention was paid to the formulation of the two-component exciton model in the transition between the compound and pre-equilibrium regions, with a linked investigation of level density models for nuclei off of stability and their impact on modeling predictive power. This paper merges experimental work and evaluation techniques for high-energy charged-particle isotope production in an extension to an earlier study of this kind.

3.2 Introduction

Multi-hundred MeV regional proton accelerators are promising sites for the large scale production of medical radionuclides due to the high production rates enabled by their high-intensity beam capabilities and the long range of high-energy protons. However, the ability to reliably conduct isotope production at these accelerators and model relevant (p,x) reactions in the 100–200 MeV range is hampered by a lack of measured data.

In the effort to improve this state of proton-induced nuclear reaction data, irradiations of arsenic have been performed. The formation of ^{72}Se and ^{68}Ge from ^{75}As(p,x) are of particular interest for their application in diagnostic imaging as generators or "cows" for their decay daughters, ^{72}As and ^{68}Ga, respectively. The present general production data for ^{72}Se at incident proton energies in the 35–200 MeV range are scarce to non-existent. Low-energy ^{68}Ge production data have been thoroughly assessed and already contribute to a robust production capability set over the past decade, but extending knowledge for ^{68}Ge formation at higher-energies too should benefit its overall application. The 35–200 MeV range is especially relevant because it is characteristic of the Los Alamos Isotope Production Facility (IPF) and the Brookhaven LINAC Isotope Producer (BLIP), where medical isotopes are created for widespread use.

^{72}As ($t_{1/2} = 26.0$ h, 87.8% β^+ [119]) is a favourable positron emitting radioisotope for the imaging of slower biological processes. Its longer half-life makes ^{72}As-labelled radiopharmaceuticals useful for the observation of long-term metabolic processes, such as the enrichment and distribution of antibodies in tumour tissue, by positron emission tomography (PET) [12, 120]. ^{72}As offers the similar slow kinetic behaviour as the PET isotope ^{124}I ($t_{1/2} = 4.176$ d, 22.7% β^+ [121]) albeit with a lesser fraction of non-positron decays [122]. Furthermore, ^{72}As can form a promising pair with ^{77}As ($t_{1/2} = 38.83$ h, 100% β^-, 683 keV $E_{\beta^-,max}$ [123]) for combined imaging and radiotherapy [55, 124, 125]. The high sulfur affinity of arsenic, promoting its covalent binding to thiol groups, along with the high toxicity ^{77}As, make ^{72}As/^{77}As an unique theranostic candidate [124, 126].

Current production methods for ^{72}As require a charged-particle beam in an accelerator setting. Existing accelerator pathways rely on ^{nat}Ge targets via the ^{nat}Ge(p/d,xn)^{72}As mechanisms in the 10–50 MeV incident particle energy range [12, 127]. However, these direct routes to ^{72}As constrain its use to medical centres nearby the production facility due to a half-life not appropriate for long-term shipping or storage. Additionally, direct production from ^{nat}Ge suffers from low thick target yields at these low incident energies and from co-production of the longer-lived radioisotopic impurities ^{74,73,71}As [12, 127]. Instead, recognition of the longer-lived ^{72}Se ($t_{1/2} = 8.40$ d [119]) as the parent precursor to ^{72}As creates the possibility for a ^{72}Se/^{72}As generator system [120, 125, 127]. Production through means of a generator results in ^{72}As creation free from other radioarsenic contaminants and shipping restrictions to medical facilities across the globe. Measurements of a ^{nat}Br(p,x)^{72}Se production route have been undertaken but the thick target yields, even approaching 200 MeV incident protons, are relatively low [12, 55, 128, 129]. Bromine targets subjected to high power may also pose heating and/or reactivity problems [128, 129]. The alternatively explored formation mechanism of $^{nat/70}$Ge(α,xn)^{72}Se also suffers from low yields due to the short range of required lower energy α-particles combined with a relatively small (< 100 mb) production peak [130].

In contrast, proton-induced reactions on arsenic offer a potentially improved production pathway to the ^{72}Se/^{72}As generator system. The combination of an expected sufficient cross section over a wide energy range with a naturally monoisotopic (^{75}As), stable material that can be appropriately formed into thick targets makes high-intensity, high-energy proton irradiations an enticing approach.

^{68}Ga ($t_{1/2} = 67.71$ min, 88.91% β^+ [131]) has emerged as a significant short-lived positron emitter alongside the ubiquitous ^{18}F for PET imaging in cases of general cancer, glioma, hypoxia, neuroendocrine tumours, and more [132, 133]. ^{68}Ga readily forms stable complexes with DOTA (a synthetically flexible metal chelating agent) and HBED, allowing peptides and other small molecules to be radiolabeled at high specific activities [31, 134]. NETSpot, using ^{68}Ga-DOTA, is an FDA approved PET imaging agent for neuroendocrine cancers [134]. Further, the compatibility of ^{68}Ga with a prostate-specific membrane antigen targeting ligand (PSMA-11 with HBED chelator) has led to a sought-after, highly successful PET tracer for the diagnosis of prostate cancer [132, 134, 135]. However, in a similar fashion to ^{72}As, direct production by typical ^{65}Cu(α,n)^{68}Ga and ^{68}Zn(p,n)^{68}Ga routes suffer from the same local accelerator production and shipping time constraints that inhibit widespread use [12]. Conversely, an indirect pathway to ^{68}Ga, through its long-lived ^{68}Ge ($t_{1/2} = 270.93$ d [131]) parent, constitutes an effective generator system more applicable for societal application.

While the elution and separation chemistry of the ^{68}Ge/^{68}Ga system has been extensively developed, nuclear data for ^{68}Ge production remains partially incomplete [133]. The ^{nat}Ga(p,xn)^{68}Ge route is the heavily studied, successful favourite of accelerator sites globally – particularly the prominent facilities of IPF, BLIP, and iThemba labs – but data only reaches up to 100 MeV. Other ^{69}Ga(p,xn)^{68}Ge, ^{nat}Ge(p,pxn)^{68}Ge, and ^{66}Zn(α,2n)^{68}Ge low-energy pathways have been explored but are less ideal due to excitation functions that peak in the 15–35 MeV range, which may be suboptimal for thick target yields, and present target manufacturing and purity concerns [31, 133]. Studying proton-induced reactions on arsenic gives a chance to strengthen the community's total understanding of ^{68}Ge/^{68}Ga formation.

In this work, proton-induced nuclear reaction data for ^{75}As were measured for energies 35–200 MeV using the stacked-target method as part of the DOE Isotope Program's Tri-laboratory Effort in Nuclear Data (TREND) between Lawrence Berkeley National Laboratory (LBNL), Los Alamos National Laboratory (LANL), and Brookhaven National Laboratory (BNL) [34]. We report the first cross section measurements for ^{75}As(p,x)^{68}Ge and the most well-characterized excitation function of ^{75}As(p,4n)^{72}Se to-date. Thick target yields are additionally calculated from the measured excitation functions and compared to established formation routes for the generator radionuclides to better inform accelerator facilities of optimal production parameters.

This stacked-target work has further provided 53 other high-energy (p,x) production cross section datasets for residual nuclei stemming from ^{75}As, ^{nat}Cu, and ^{nat}Ti targets.

These extensive measurements were also used to assess the predictions of multiple nuclear reaction codes. The standardized fitting procedure for reaction model parameters and pre-equilibrium adjustments developed in Fox et al. [34] was applied to the arsenic data, with an investigative focus to check if the proposed exciton model trends are seen.

In addition to studying pre-equilibrium, the fitting procedure provided insight into the appropriate level density models for a swath of nuclei. A discussion of the impact of level density knowledge on modeling predictive power is presented with a reflection of the limitations imposed on creating recommended high-energy charged-particle data.

The combination of experimental measurement and evaluation study presented in this work creates data with immediate application while contributing to an increasingly prioritized future need for high-energy modeling in the nuclear data community [136].

3.3 Experimental Methods and Materials

This work was performed within the same experimental conditions of Fox et al. [34]. Charged-particle stacked-target irradiations were carried out at the 88-Inch Cyclotron at LBNL for proton energies of $E_p < 55$ MeV, at IPF at LANL for $50 < E_p < 100$ MeV, and at BLIP at BNL for $100 < E_p < 200$ MeV.

The stacked-target technique is a typical methodology for charged-particle irradiations to simultaneously measure multiple high-fidelity energy-separated cross section values per reaction channel. A stacked-target includes thin foils of a target of interest in combination with thick degraders and monitor foils. The degraders selectively reduce the primary beam energy throughout the stack while the monitor foils can be used to characterize the evolving beam properties as it propagates through the targets. Detailed explanations of the technique can be read in [34, 36, 39, 40, 137, 138].

3.3.1 Stacked-Target Design

Individual stacks were created for each irradiation at each experimental site. The three stacks differed slightly in composition according to the physical constraints of each site's irradiation geometry and as a function of expected residual radionuclide production based on beam current and energy parameters.

3.3.1.1 LBNL Stack and Irradiation

The 88-Inch Cyclotron stack consisted of 25 μm ^{nat}Cu foils (99.95%, CU000420, Goodfellow Metals, Coraopolis, PA 15108-9302, USA) and thin metallic ^{75}As layers electroplated onto 10 μm or 25 μm ^{nat}Ti foil backings (99.6%, TI000213/TI000290, Goodfellow Metals).

Nine copper foils each were cut into 2.5 cm × 2.5 cm squares and characterized by taking four length and width measurements using a digital caliper (Mitutoyo America Corp.) and four thickness measurements taken at different locations using a digital micrometer (Mitutoyo America Corp.). Each foil was also massed multiple times using an analytical balance at 0.1 mg precision after being cleaned with isopropyl alcohol. The characterization of the approximately 2.25 cm diameter arsenic depositions onto titanium, picture in Figure 3.1, was a more intensive process involving particle transmission and neutron activation analysis. These details and the description of the associated electroplating creation process are given in Chapter 4, while the resulting thickness and areal density values can be seen in Table 3.1.

All targets were then sealed using DuPont Kapton polyimide film tape of either 43.2 μm of silicone adhesive on 25.4 μm of polyimide backing (total nominal 7.77 mg/cm^2) or 43.2 μm of silicone adhesive on 50.8 μm of polyimide backing (total nominal 11.89 mg/cm^2). The encapsulated foils were mounted to the center of hollow 5.7 cm × 5.7 cm aluminum frames. The frames protected the foils during handling and centered them in the beam pipe after the stack was fully arranged in the target box seen in Figure 3.2.

Multiple aluminum degraders were characterized in the same manner as the copper foils and included in the stack to yield nine different beam energy "compartments" for cross section measurements. One copper foil and one electroplated arsenic foil were placed into each of the nine compartments in the target box. Stainless steel plates (approximately 100 mg/cm^2) were placed near the front and back of the stack for post-irradiation dose mapping using radiochromic film (Gafchromic EBT3) in order to examine the spatial profile of the beam entering and exiting the stack. The full detailed target stack ordering and properties for the LBNL irradiation are given in Table 3.1.

Figure 3.1: View of individual electroplated arsenic depositions on titanium backings within Kapton seals. The top target is sampled from the LBNL stack and is pictured after proton irradiation, where slight bubbling in the Kapton seal exists as a result of beam heating. The bottom target is part of the BNL stack prior to proton irradiation.
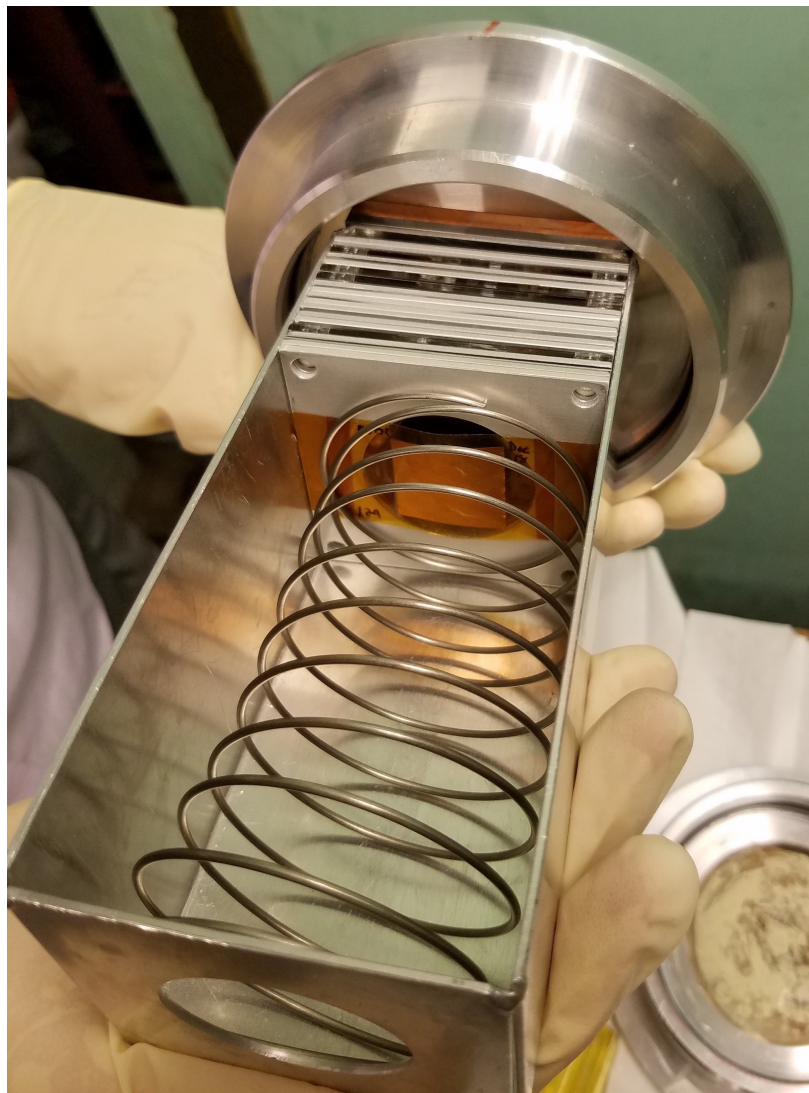
Figure 3.2: A top view of the assembled LBNL target stack prior to loading into the cyclotron beam pipe. The beam is first incident on the front facing copper target shown in the photo, as described in Table 3.1.

The stack was irradiated at the 88-Inch Cyclotron for 3884 seconds with a nominal 192 nA proton beam. The total collected charge of the beam was measured using a current integrator connected to the electrically-isolated target holder, which was used to determine that the beam current was stable over the duration of the experiment. The mean beam energy extracted was 55.4 MeV at a 1% uncertainty.

Table 3.1: Target stack design for irradiation at the 88-Inch Cyclotron. The proton beam initially hits the Cu-SN1 target and is subsequently transported through the rest of the shown stack order. The thickness and areal density measurements are prior to any application of the variance minimization techniques described in this work.

Target Layer	Thickness [μm]	Areal Density [mg/cm²]	Areal Density Uncertainty [%]
Cu-SN1	24.81	22.23	0.33
As-SN1	3.24	1.85	9.8
Ti-SN1	25.00	11.265	1.0
SS Profile Monitor	130.0	100.12	0.07
Al Degrader E1	253.0	68.31	0.10
Al Degrader E2	252.7	68.24	0.10
Cu-SN2	24.88	22.29	0.08
As-SN2	1.69	0.97	9.9
Ti-SN2	25.00	11.265	1.0
Al Degrader D1	674.2	174.44	0.05
Cu-SN3	24.88	22.29	0.06
As-SN3	1.81	1.04	9.9
Ti-SN3	25.00	11.265	1.0
Al Degrader D2	664.5	174.87	0.06
Cu-SN4	24.87	22.28	0.04
As-SN4	2.22	1.27	10
Ti-SN4	25.00	11.265	1.0
Al Degrader E3	253.1	68.35	0.10
Cu-SN5	24.97	22.37	0.06
As-SN5	1.95	1.12	9.9
Ti-SN5	25.00	11.265	1.0
Al Degrader F1	181.5	46.91	0.12
Al Degrader F2	192.2	48.97	0.14
Cu-SN6	24.85	22.27	0.09
As-SN6	1.30	0.74	11
Ti-SN6	25.00	11.265	1.0
Al Degrader E4	252.9	68.29	0.10
Cu-SN7	24.67	22.11	0.39
As-SN7	2.36	1.35	8.9
Ti-SN7	10.00	4.506	1.0
Al Degrader C1	970.0	261.48	0.03
Cu-SN8	24.80	22.22	0.06
As-SN8	0.94	0.54	9.7
Ti-SN8	25.00	11.265	1.0
Al Degrader E5	252.7	68.24	0.10
Cu-SN9	24.90	22.31	0.10
As-SN9	0.57	0.32	10
Ti-SN9	25.00	11.265	1.0
SS Profile Monitor	130.0	100.48	0.07

3.3.1.2   LANL Stack and Irradiation

The LANL stack included copper, niobium, aluminum, and electroplated arsenic targets. The stack composition is described in detail in Fox et al. [34], where characterization procedures were very similar to the LBNL setup. A summary of the stack is provided in this paper in Table 2.5 (see Section 2.7). The stack was irradiated for 7203 seconds with an H^+ beam of 100 nA nominal current. The beam current, measured using an inductive pickup, remained stable under these conditions for the duration of the irradiation. The mean beam energy extracted was 100.16 MeV at a 0.1% uncertainty.

3.3.1.3   BNL Stack and Irradiation

The BNL stack was composed of copper, niobium, and electroplated arsenic targets. The exact specifications of the stack are given in Fox et al. [34] and a summary can be seen in Table 2.6 (see Section 2.7). The stack was irradiated for 3609 seconds with an H^+ beam of 200 nA nominal current. The beam current during operation was recorded using toroidal beam transformers and shown to remain stable under these conditions for the duration of the irradiation. The mean beam energy extracted was 200 MeV at a 0.2% uncertainty [55].

3.3.2   Gamma Spectroscopy and Measurement of Foil Activities

3.3.2.1   LBNL

The gamma spectroscopy at the 88-Inch Cyclotron utilized an ORTEC GMX series (model GMX-50220-S) High-Purity Germanium (HPGe) detector and seven ORTEC IDM-200-VTM HPGe detectors. The GMX is a nitrogen-cooled coaxial n-type HPGe with a 0.5 mm beryllium window, and a 64.9 mm diameter, 57.8 mm long crystal. The IDMs are mechanically-cooled coaxial p-type HPGes with single, large-area 85 mm diameter × 30 mm length crystals and built-in spectroscopy electronics. The energy and absolute photopeak efficiency of the GMX and IDMs were calibrated using standard ^{133}Ba, ^{137}Cs, and ^{152}Eu sources. The efficiency model used in this work is the physical model presented by Gallagher and Cipolla [56].

Foil activity data was first collected from counts beginning approximately 45 minutes after the end-of-bombardment (EoB) and removal of the target stack from the beamline. The copper and electroplated arsenic foils were initially cycled through multiple 5–30 minute counts on the GMX during the 24 hours immediately following the irradiation. The counting distances from the GMX detector face were varied from 80 cm to 15 cm during this period subject to dead time constraints. Each electroplated arsenic foil was then transferred to an individual IDM detector where counts were collected in 1 hour intervals at a 10 cm distance from the IDM face over the next three weeks. The repeated counts of each foil

helped to establish consistent decay curves for residual nuclides and reduce uncertainty in the spectroscopy analysis, particularly aiding in the determination of longer-lived products. Final 12–24 hour counts for the copper foils were captured on the GMX near the end of the three week period to record appropriate statistics for long-lived monitor channels.

The radiochromic film, activated by the stainless steel plates, showed that an ≈1 cm diameter proton beam was centered on the stack foils and properly inscribed within the size-limiting borders of the arsenic deposits throughout the stack.

3.3.2.2 LANL

The LANL experiment used a series of GEM and IDM HPGe detectors. The foil counting at LANL followed a similar cycling routine to LBNL, with counting times ranging from 10 minutes during the first hours after EoB to upwards of 8 hours over the course of 6 weeks after the irradiation for the stack's 40 total targets. The LANL counting scheme is given explicitly in Fox et al. [34]. Notably, the electroplated arsenic targets of the LANL stack were shipped to LBNL in order to perform multi-week long counts with the LBNL GMX to better capture the ^{68}Ge signal, which remained weak in the longest of the LANL counts.

3.3.2.3 BNL

The BNL gamma spectroscopy setup incorporated two EURISYS MESURES 2 Fold Segmented "Clover" detectors in addition to one GMX and two GEM detectors. Foils were cycled in front of the many detectors for repeated short counts of 30 minutes or less during the first 24 hours after EoB. Data collection at BNL continued with multi-hour target counts for an additional day before the targets were shipped back to LBNL, arriving within two weeks after EoB. The LBNL GMX was used for multi-day to week-long counts of the copper, electroplated arsenic, and niobium foils over the course of the next 2+ months.

Further details of the BLIP activation and spectroscopy is provided in Fox et al. [34].

3.3.2.4 Activation Analysis

The UC Berkeley code package NPAT [57] (recently superseded by Curie [139]), with built-in nuclear structure and reaction databases, was used to analyze the collected gamma spectra from each irradiation. Decay curves for observed residual products were constructed from the count data with appropriate timing, efficiency, and attenuation corrections. EoB activities A_0 were then determined by fitting decay curves with applicable Bateman equations [34, 36, 39]. A sample gamma-ray spectrum from an electroplated arsenic target is given in Figure 3.3.
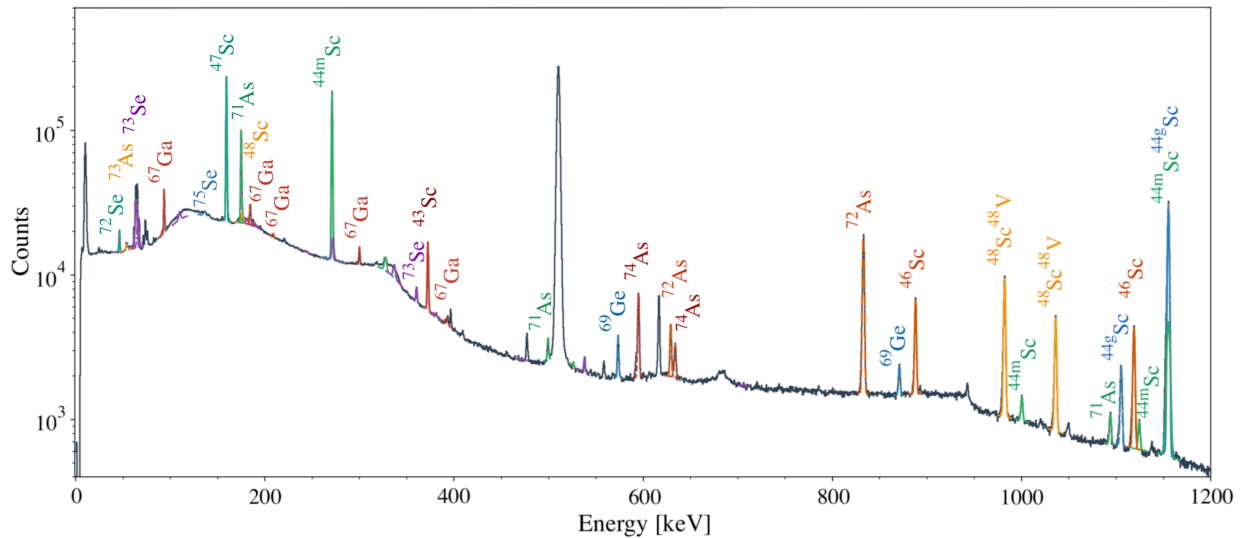
Figure 3.3: Example gamma-ray spectrum from the induced activation of an electroplated arsenic target in the LANL stack at approximately $E_p = 91$ MeV. The spectrum was taken slightly beyond 2 days after EoB and the smooth fits to the peaks of interest shown are produced by the NPAT package [57].

Independent, (i), A_0 results were determined from decay curve fits where decay contributions from any precursors of a residual product could be distinguished or where no parent decay in-feeding existed. In cases where precursor contributions could not be distinguished, either due to timing or decay property limitations, cumulative, (c), A_0 values for a residual product within a decay chain were instead calculated.

The total uncertainties in the determined EoB activities had contributions from fitted peak areas, evaluated half-lives and gamma intensities, regression parameters, and detector efficiency calibrations. Each contribution to the total uncertainty was assumed to be independent and was added in quadrature. The impact of calculated A_0 uncertainties on final cross section results is detailed in Section 3.3.4.

3.3.3 Stack Current and Energy Properties

The proton beam energy and current at each target in a given stack was determined by monitor foil activation data, NPAT's Anderson & Ziegler-based Monte Carlo particle transport code, and a "variance minimization" approach, following the established methodology presented in Voyles et al. [36], Morrell et al. [39], Graves et al. [40].

The ^{nat}Ti(p,x)^{48}V, ^{46}Sc and ^{nat}Cu(p,x)^{63,62}Zn, ^{58}Co monitor reactions, taken from the IAEA-recommended data reference for charged-particle reactions [59], were used for the LBNL beam characterization. The results after variance minimization are shown in Figure

3.4 with plotted weighted averages of all the monitor reaction fluence predictions in each stack compartment. The weighted averages account for data and measurement correlations between the monitor reaction channels at each position in the stack and were used to create the uncertainty-weighted linear fit, also included in Figure 3.4 [140]. The fit acts as a global model to impose a smooth and gradual fluence depletion and provides an interpolation for the fluence and energy of each individual target of interest in the stack. This optimized linear model after variance minimization shows an approximately constant 207 nAh fluence throughout the LBNL stack.

Further details of the monitor foil calculations, variance minimization approach, and energy determinations for the LBNL experiment can be reviewed in Section 3.7. An in-depth discussion of this same beam characterization procedure for the LANL and BNL stacks is provided in Fox et al. [34].

The final deduced energy assignments with uncertainty for targets in all three stacks are provided in Tables 3.2, 3.3, and 3.4.
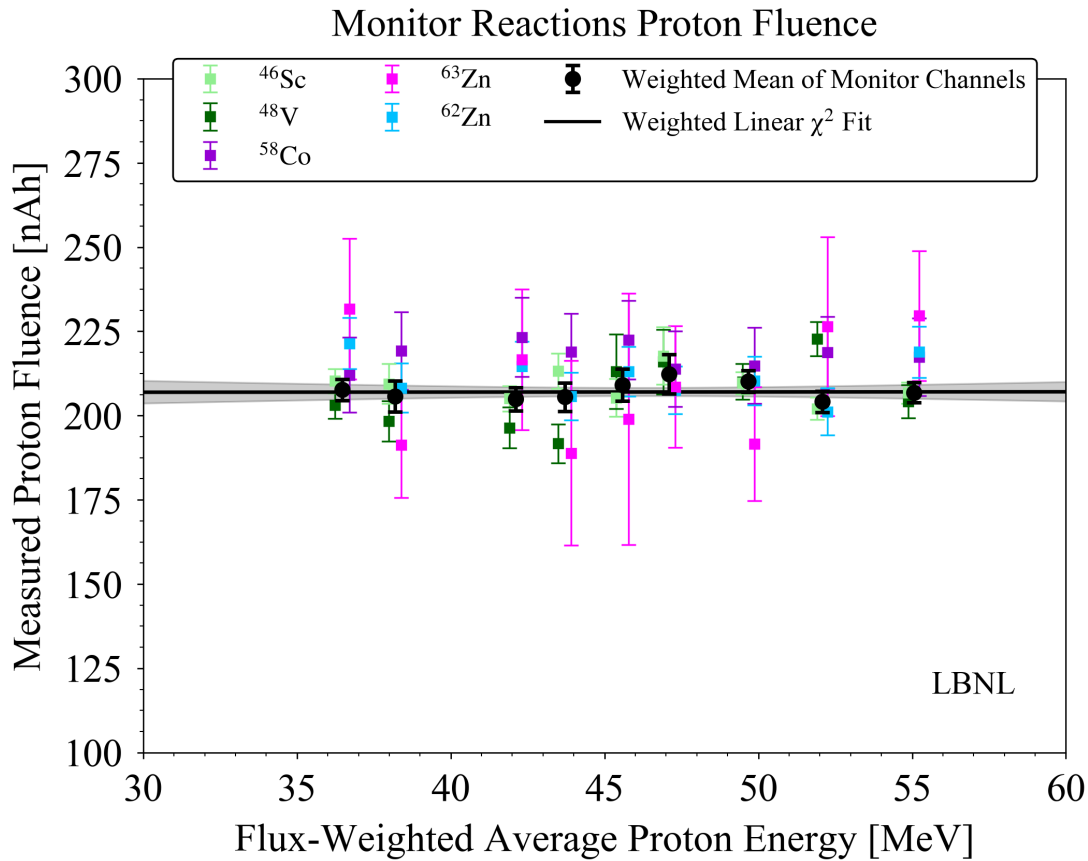
Figure 3.4: Plot of the proton beam fluence measured by monitor reactions in the LBNL stack following adjustments made by the variance minimization technique.

3.3.4   Cross Section Determination

Cross sections for observed products in this work were calculated from the typical activation formula,

$$\sigma = \frac{A_0}{I_p(\rho_N \Delta r)(1 - e^{-\lambda t_{irr}})}, \tag{3.1}$$

where I_p is the beam current in protons per second at a given foil in a stack, $\rho_N \Delta r$ is the relevant foil's areal number density, λ is the decay constant for the observed residual product of interest, and t_{irr} is the beam-on irradiation time.

Measured ^{75}As(p,x) cross sections are reported in Table 3.2 for ^{75,73,72}Se, $^{74-70}$As, $^{72,68-66}$Ga, ^{69,68,66}Ge, ^{69m,65}Zn, and $^{60,58-56}$Co.

^{nat}Cu(p,x) production cross sections for ^{65,63,62}Zn, ^{64,61,60}Cu, $^{60,57-55}$Co, ^{59}Fe, ^{57,56}Ni, ^{56,54,52}Mn, ^{51,49,48}Cr, ^{48}V, and ^{47,46,44m}Sc are given in Table 3.3.

^{nat}Ti(p,x) experimental cross section results for ^{48}V, $^{48-46,44m,44g,43}$Sc, ^{47}Ca, ^{44}Ti, and ^{43,42}K are listed in Table 3.4.

In Tables 3.2 3.3, and 3.4, the cross sections for residual products are marked as either independent, (i), or cumulative, (c), referencing the distinction discussed in Section 3.3.2.4 surrounding decay chains.

The final uncertainty contributions to the cross section measurements include uncertainties in evaluated decay constants (0.02–1.0%), foil areal density measurements (0.05–11%), proton current determination calculated from monitor fluence measurements and variance minimization (0.6–3.4%), and A_0 quantification that accounts for efficiency uncertainty in addition to other factors listed in Section 3.3.2.4 (1.5–14%). These contributions were added in quadrature to give uncertainty in the final results at the 3.5–15% level on average.

3.4   Results and Discussion

The measured data from select reactions of particular interest to the medical applications community or for nuclear reaction modeling purposes are discussed in detail below. Plots of all other reported cross sections are given in Section 3.8 (Figures 3.19–3.69).

The experimentally extracted cross sections are compared with the predictions of nuclear reaction modeling codes TALYS-1.95 [47], CoH-3.5.3 [48], EMPIRE-3.2.3 [49], and ALICE-20 [50], each using default settings and parameters. A discussion of these default conditions and assumptions is provided in Fox et al. [34]. Comparisons with the TENDL-2019 library [51] are also made.

Additionally, the cross section measurements in this work are compared to the existing body of literature data, retrieved from EXFOR [36, 38–40, 45, 55, 67, 100, 141–177].

Table 3.2: Summary of arsenic cross sections measured in this work. Subscripts (i) and (c) indicate independent and cumulative cross sections, respectively. Uncertainties are listed in the least significant digit, that is, 49.5 (14) MeV means 49.5 ± 1.4 MeV.

^{75}As(p,x) Production Cross Sections [mb]								
E_p [MeV]	192.28 (49)	177.01 (51)	163.21 (54)	148.55 (58)	133.75 (62)	119.66 (67)	104.09 (73)	91.09 (51)	79.19 (56)
^{56}Co$_{(c)}$	0.823 (98)	0.337 (34)	0.581 (64)	0.436 (48)	0.169 (28)	-	-	-	-
^{57}Co$_{(c)}$	3.04 (46)	1.36 (18)	2.03 (28)	1.68 (25)	0.51 (17)	-	-	-	-
^{58}Co$_{(i)}$	3.62 (80)	-	2.81 (33)	2.25 (26)	0.84 (11)	0.32 (24)	0.07 (8)	-	-
^{60}Co$_{(i)}$	8.8 (11)	1.89 (20)	1.70 (20)	1.06 (14)	-	-	-	-	-
^{65}Zn$_{(c)}$	45.8 (77)	47.6 (58)	47.4 (63)	35.1 (43)	29.2 (38)	31.4 (38)	10.8 (15)	-	-
^{66}Ga$_{(c)}$	11.1 (66)	24.9 (66)	31 (17)	24.1 (98)	16.0 (42)	-	14.6 (39)	5.43 (89)	5.33 (95)
^{66}Ge$_{(c)}$	-	-	-	1.15 (49)	1.18 (22)	-	-	-	-
^{67}Ga$_{(c)}$	39.1 (46)	44.8 (45)	43.2 (47)	42.1 (43)	38.6 (49)	36.7 (36)	35.0 (39)	20.6 (19)	25.5 (24)
^{68}Ga$_{(i)}$	41.7 (83)	39.2 (62)	41.3 (58)	40.7 (69)	35.5 (53)	42.8 (55)	39.5 (52)	-	-
^{68}Ge$_{(c)}$	30.7 (46)	26.9 (30)	26.4 (32)	22.8 (27)	21.9 (30)	20.3 (23)	13.0 (16)	11.1 (22)	24.1 (41)
^{69m}Zn$_{(i)}$	1.24 (19)	1.38 (22)	1.38 (17)	1.26 (14)	1.02 (24)	1.29 (13)	0.75 (13)	-	-
^{69}Ge$_{(c)}$	36.9 (43)	40.5 (43)	41.6 (50)	37.0 (42)	36.9 (49)	42.5 (44)	35.0 (39)	19.8 (20)	16.2 (16)
^{70}As$_{(c)}$	15.9 (18)	16.4 (17)	17.7 (19)	16.4 (17)	17.2 (21)	23.2 (23)	27.1 (28)	36.9 (39)	43.7 (45)
^{71}As$_{(c)}$	40.0 (45)	49.2 (51)	55.2 (64)	55.8 (60)	64.3 (79)	76.2 (76)	73.4 (75)	-	91.8 (85)
^{72}Ga$_{(c)}$	-	-	-	1.39 (57)	3.07 (95)	1.89 (68)	3.38 (82)	2.20 (29)	2.31 (49)
^{72}As$_{(i)}$	70.3 (77)	82.6 (82)	80.3 (90)	89.2 (94)	97 (12)	122 (12)	116 (12)	-	108.8 (99)
^{72}Se$_{(i)}$	6.12 (72)	6.90 (75)	8.12 (94)	8.09 (89)	8.4 (11)	11.2 (12)	11.6 (13)	-	15.2 (16)
^{73}As$_{(i)}$	95 (17)	125 (19)	138 (24)	128 (24)	138 (26)	166 (28)	172 (31)	180 (42)	174 (24)
^{73}Se$_{(c)}$	11.9 (15)	14.0 (16)	14.8 (17)	15.6 (18)	18.0 (24)	23.0 (25)	23.5 (27)	22.8 (29)	25.7 (35)
^{74}As$_{(i)}$	98 (11)	112 (12)	113 (16)	118 (14)	124 (18)	138 (14)	148 (18)	-	123 (12)
^{75}Se$_{(i)}$	5.55 (59)	6.65 (63)	7.47 (79)	6.80 (69)	7.44 (89)	9.23 (88)	9.48 (95)	6.08 (52)	10.10 (87)
E_p [MeV]	72.39 (60)	67.00 (64)	62.92 (67)	59.93 (69)	57.31 (72)	55.42 (74)	54.9 (13)	53.46 (76)	52.0 (14)
^{66}Ga$_{(c)}$	2.88 (64)	-	-	-	-	-	-	-	-
^{67}Ga$_{(c)}$	16.4 (18)	6.2 (10)	2.32 (77)	1.00 (78)	0.91 (74)	-	-	-	-
^{68}Ge$_{(c)}$	41.4 (72)	39.2 (69)	31.1 (54)	14.1 (20)	-	-	-	-	-
^{69}Ge$_{(c)}$	17.6 (19)	20.6 (22)	25.6 (26)	34.5 (40)	39.4 (42)	37.4 (40)	41.5 (44)	39.6 (45)	35.8 (39)
^{70}As$_{(c)}$	33.1 (40)	-	2.3 (10)	-	-	-	-	2.3 (16)	-
^{71}As$_{(c)}$	131 (13)	143 (14)	130 (12)	128 (14)	103 (11)	74.9 (77)	63.9 (65)	53.6 (61)	32.3 (34)
^{72}Ga$_{(c)}$	1.72 (51)	2.25 (47)	-	1.26 (47)	-	1.31 (48)	-	1.03 (34)	-
^{72}As$_{(i)}$	146 (14)	169 (17)	188 (18)	238 (26)	262 (26)	249 (24)	277 (28)	266 (28)	246 (25)
^{72}Se$_{(i)}$	23.0 (25)	28.5 (31)	34.2 (36)	49.3 (58)	57.1 (62)	57.9 (62)	59.8 (63)	62.7 (71)	80 (12)
^{73}As$_{(i)}$	229 (32)	244 (35)	252 (35)	323 (47)	325 (47)	282 (40)	-	346 (60)	320 (53)
^{73}Se$_{(c)}$	37.4 (48)	39.0 (55)	45.2 (55)	54.2 (81)	62.1 (82)	57.0 (80)	60.1 (69)	65.4 (89)	65.4 (76)
^{74}As$_{(i)}$	153 (16)	158 (17)	157 (16)	186 (21)	185 (19)	169 (17)	188 (20)	170 (19)	182 (19)
^{75}Se$_{(i)}$	13.2 (12)	14.2 (13)	14.4 (13)	16.9 (18)	17.7 (17)	16.2 (15)	15.2 (16)	16.9 (18)	16.1 (18)
E_p [MeV]	51.44 (78)	49.5 (14)	47.0 (15)	45.4 (15)	43.6 (16)	41.9 (16)	38.0 (17)	36.3 (18)	
^{69}Ge$_{(c)}$	40.6 (48)	31.5 (34)	27.6 (31)	17.6 (20)	13.0 (16)	12.0 (12)	-	-	
^{71}As$_{(c)}$	39.6 (48)	17.4 (19)	9.7 (11)	6.44 (77)	8.2 (11)	3.46 (39)	-	-	
^{72}Ga$_{(c)}$	-	-	-	-	-	-	0.21 (13)	-	
^{72}As$_{(i)}$	280 (30)	226 (23)	219 (22)	207 (22)	-	131 (12)	73.8 (85)	41.9 (55)	
^{72}Se$_{(i)}$	79.3 (92)	85 (14)	87 (13)	93 (10)	72.0 (85)	58.3 (73)	25.4 (40)	9.3 (14)	
^{73}As$_{(i)}$	345 (52)	359 (65)	469 (79)	460 (69)	570 (100)	587 (85)	680 (110)	600 (94)	
^{73}Se$_{(c)}$	80 (12)	69.6 (79)	91 (10)	92 (11)	114 (14)	205 (21)	235 (26)	307 (37)	
^{74}As$_{(i)}$	186 (22)	181 (19)	194 (21)	193 (21)	-	234 (23)	218 (24)	239 (27)	
^{75}Se$_{(i)}$	18.0 (19)	17.8 (20)	17.0 (18)	17.2 (20)	21.8 (35)	23.8 (23)	25.0 (31)	26.5 (39)	

Table 3.3: Summary of copper cross sections measured in this work. Subscripts (i) and (c) indicate independent and cumulative cross sections, respectively.

^{nat}Cu(p,x) Production Cross Sections [mb]									
E_p [MeV]	192.54 (49)	177.28 (52)	163.49 (54)	148.86 (58)	134.08 (62)	120.02 (67)	104.49 (74)	90.94 (52)	79.03 (57)	72.22 (61)
^{44m}Sc$_{(i)}$	0.289 (12)	0.1338 (63)	0.0784 (85)	0.0444 (40)	-	-	-	-	-	-
^{46}Sc$_{(i)}$	0.572 (21)	0.335 (11)	0.2381 (65)	0.1065 (59)	0.0616 (30)	0.0375 (24)	-	-	-	-
^{47}Sc$_{(c)}$	0.261 (46)	0.182 (31)	0.218 (26)	-	-	-	-	-	-	-
^{48}V$_{(c)}$	2.346 (84)	1.560 (47)	1.162 (30)	0.689 (29)	0.499 (15)	0.298 (45)	-	-	-	-
^{48}Cr$_{(c)}$	0.0707 (35)	0.0437 (19)	0.0263 (27)	0.0207 (11)	-	-	-	-	-	-
^{49}Cr$_{(c)}$	0.943 (67)	0.624 (60)	0.411 (46)	-	-	-	-	-	-	-
^{51}Cr$_{(c)}$	11.59 (42)	9.79 (29)	8.44 (21)	6.46 (26)	5.33 (13)	4.35 (13)	1.676 (68)	1.220 (61)	0.427 (49)	0.469 (43)
^{52}Mn$_{(c)}$	5.34 (19)	4.72 (14)	4.22 (11)	3.34 (12)	2.733 (70)	1.934 (59)	1.727 (70)	1.759 (67)	0.509 (22)	0.1008 (63)
^{54}Mn$_{(i)}$	16.26 (59)	15.72 (48)	14.88 (38)	13.4 (12)	12.48 (31)	11.05 (32)	7.30 (27)	6.63 (23)	3.87 (15)	3.86 (17)
^{55}Co$_{(c)}$	2.04 (11)	2.12 (11)	1.995 (97)	2.06 (10)	1.813 (91)	1.679 (90)	1.77 (10)	2.50 (18)	1.43 (11)	0.647 (60)
^{56}Mn$_{(c)}$	2.52 (15)	2.54 (15)	2.46 (14)	2.18 (13)	2.07 (13)	1.85 (11)	1.40 (10)	1.186 (57)	1.106 (54)	0.927 (43)
^{56}Co$_{(i)}$	12.50 (43)	12.65 (35)	12.57 (29)	13.18 (34)	12.29 (27)	11.55 (31)	10.51 (37)	10.31 (44)	12.12 (49)	12.68 (56)
^{56}Ni$_{(c)}$	0.072 (59)	0.089 (12)	0.116 (12)	0.105 (13)	0.131 (15)	0.093 (15)	-	0.0884 (75)	0.1103 (82)	0.1070 (81)
^{57}Co$_{(c)}$	43.0 (35)	42.3 (14)	43.1 (12)	43.6 (11)	44.5 (12)	44.7 (14)	42.2 (16)	44.7 (14)	37.7 (11)	36.9 (11)
^{57}Ni$_{(c)}$	1.687 (85)	1.787 (66)	1.820 (61)	1.776 (57)	-	-	-	1.76 (11)	1.286 (83)	1.391 (89)
^{59}Fe$_{(c)}$	1.180 (51)	1.209 (45)	1.189 (40)	1.100 (50)	1.097 (36)	1.045 (38)	0.923 (40)	0.931 (33)	0.867 (29)	0.817 (29)
^{60}Co$_{(c)}$	11.72 (47)	13.66 (61)	13.73 (48)	11.28 (55)	12.41 (35)	12.24 (38)	12.01 (48)	14.21 (42)	12.50 (37)	11.48 (36)
^{60}Cu$_{(c)}$	8.01 (42)	9.37 (48)	10.75 (57)	13.77 (77)	11.4 (10)	15.1 (14)	16.5 (19)	16.87 (75)	16.0 (10)	17.38 (90)
^{61}Cu$_{(c)}$	29.9 (16)	33.2 (16)	36.4 (17)	39.0 (17)	42.9 (19)	46.6 (22)	55.7 (29)	60.6 (30)	54.3 (29)	72.5 (35)
^{62}Zn$_{(i)}$	1.71 (11)	2.16 (13)	1.86 (12)	2.44 (14)	2.39 (15)	3.42 (19)	3.26 (21)	-	-	-
^{63}Zn$_{(i)}$	3.52 (34)	4.32 (45)	5.25 (63)	6.05 (87)	5.52 (97)	5.73 (93)	-	8.40 (52)	10.90 (71)	12.98 (78)
^{64}Cu$_{(i)}$	26.3 (15)	31.7 (18)	30.8 (34)	35.1 (18)	36.6 (35)	40.7 (22)	44.7 (39)	52.0 (57)	40.4 (55)	50.3 (51)
^{65}Zn$_{(i)}$	1.13 (26)	1.52 (20)	1.61 (16)	1.53 (11)	1.938 (83)	2.200 (78)	2.69 (11)	2.868 (95)	3.257 (95)	3.68 (11)
E_p [MeV]	66.81 (65)	62.73 (68)	59.73 (71)	57.11 (73)	55.21 (75)	55.2 (13)	53.24 (77)	52.2 (14)	51.22 (80)	49.9 (14)
^{51}Cr$_{(c)}$	0.512 (37)	0.409 (38)	0.328 (33)	0.278 (29)	-	-	-	-	-	-
^{54}Mn$_{(i)}$	4.70 (17)	4.95 (33)	4.70 (27)	4.10 (20)	3.41 (15)	3.58 (14)	2.65 (11)	2.31 (13)	1.848 (74)	1.25 (10)
^{55}Co$_{(c)}$	0.169 (22)	0.077 (15)	0.060 (20)	0.043 (12)	0.0394 (92)	0.0127 (40)	-	-	0.0162 (69)	-
^{56}Mn$_{(c)}$	0.644 (33)	0.460 (25)	0.243 (18)	0.171 (15)	0.161 (14)	0.101 (13)	0.089 (11)	-	0.0541 (91)	-
^{56}Co$_{(i)}$	10.95 (46)	7.66 (32)	4.47 (18)	2.405 (99)	1.272 (62)	-	0.713 (39)	-	0.373 (57)	-
^{56}Ni$_{(c)}$	0.0837 (61)	0.0518 (37)	0.0330 (28)	0.0144 (28)	0.0082 (26)	-	0.0076 (22)	-	0.0043 (13)	-
^{57}Co$_{(c)}$	42.4 (13)	50.0 (21)	55.9 (23)	59.5 (26)	58.7 (26)	64.6 (50)	58.0 (25)	55.6 (12)	54.8 (24)	49.9 (10)
^{57}Ni$_{(c)}$	1.78 (11)	2.32 (10)	2.61 (12)	2.73 (12)	2.60 (12)	2.608 (99)	2.38 (11)	1.942 (62)	1.985 (90)	1.502 (47)
^{59}Fe$_{(c)}$	0.775 (27)	0.690 (29)	0.618 (26)	0.516 (22)	0.419 (19)	-	0.322 (14)	-	0.227 (10)	-
^{60}Co$_{(c)}$	11.68 (36)	12.22 (49)	12.15 (47)	11.60 (46)	10.88 (51)	10.34 (41)	10.77 (49)	10.04 (39)	10.28 (40)	9.53 (36)
^{60}Cu$_{(c)}$	18.6 (15)	27.2 (23)	-	26.1 (38)	26.4 (29)	30.1 (27)	-	33.6 (25)	-	29.5 (25)
^{61}Cu$_{(c)}$	82.8 (39)	89.7 (42)	-	91.9 (44)	94.2 (45)	91.1 (42)	93.6 (45)	94.0 (42)	97.5 (47)	103.7 (45)
^{63}Zn$_{(i)}$	12.29 (88)	14.0 (11)	16.3 (13)	17.5 (16)	17.9 (20)	-	-	-	-	-
^{64}Cu$_{(i)}$	61.7 (60)	51.4 (56)	63.0 (62)	66.6 (66)	59.7 (56)	60.7 (30)	55.4 (59)	56.1 (28)	62.7 (62)	57.3 (32)
^{65}Zn$_{(i)}$	4.05 (11)	4.21 (20)	4.39 (19)	4.66 (21)	4.79 (24)	4.53 (23)	5.32 (28)	4.65 (25)	5.30 (26)	5.51 (28)
E_p [MeV]	47.3 (15)	45.8 (15)	43.9 (16)	42.3 (16)	38.4 (17)	36.7 (18)				
^{54}Mn$_{(i)}$	0.533 (15)	0.160 (43)	0.091 (29)	0.020 (18)	0.076 (30)	0.092 (28)				
^{57}Co$_{(c)}$	36.36 (68)	29.27 (61)	17.91 (41)	11.09 (29)	1.446 (96)	0.398 (34)				
^{57}Ni$_{(c)}$	0.909 (32)	0.634 (26)	0.309 (19)	0.1257 (93)	-	-				
^{60}Co$_{(c)}$	8.78 (16)	7.72 (31)	7.12 (31)	5.95 (32)	4.95 (27)	4.35 (24)				
^{60}Cu$_{(c)}$	19.3 (22)	9.3 (21)	5.5 (17)	4.7 (18)	-	-				
^{61}Cu$_{(c)}$	112.6 (48)	125.9 (54)	137.7 (59)	156.9 (67)	179.8 (77)	187.4 (82)				
^{64}Cu$_{(i)}$	58.1 (31)	66.5 (33)	59.7 (30)	64.9 (31)	63.1 (33)	74.4 (36)				
^{65}Zn$_{(i)}$	5.57 (12)	5.50 (26)	6.19 (27)	6.32 (29)	6.97 (30)	7.33 (34)				

Table 3.4: Summary of titanium cross sections measured in this work. Subscripts (i) and (c) indicate independent and cumulative cross sections, respectively.

	^{nat}Ti(p,x) Production Cross Sections [mb]								
E_p [MeV]	192.26 (49)	176.99 (51)	163.18 (54)	148.52 (58)	133.72 (62)	119.63 (67)	104.05 (74)	91.05 (51)	79.15 (57)
^{42}K$_{(i)}$	7.54 (78)	6.45 (70)	6.83 (66)	6.34 (67)	6.92 (64)	5.56 (62)	6.10 (88)	6.73 (47)	6.48 (43)
^{43}K$_{(i)}$	2.62 (10)	2.493 (90)	2.84 (11)	2.34 (10)	2.23 (10)	2.116 (83)	1.95 (13)	1.830 (58)	1.349 (45)
^{43}Sc$_{(c)}$	16.5 (11)	15.9 (11)	12.8 (22)	15.17 (95)	17.1 (11)	20.0 (14)	-	22.8 (19)	15.0 (16)
^{44g}Sc$_{(i)}$	25.1 (13)	26.5 (16)	27.9 (13)	28.49 (97)	28.5 (10)	31.5 (17)	31.7 (15)	32.2 (19)	39.3 (22)
^{44m}Sc$_{(i)}$	11.46 (44)	11.88 (40)	12.71 (37)	13.43 (39)	14.47 (80)	14.82 (85)	19.1 (16)	21.34 (72)	22.29 (73)
^{44}Ti$_{(c)}$	2.7 (18)	2.8 (11)	3.3 (10)	4.37 (42)	3.3 (17)	4.55 (49)	-	-	-
^{46}Sc$_{(i)}$	34.0 (13)	36.1 (12)	38.2 (11)	39.3 (10)	39.3 (11)	40.9 (13)	41.5 (16)	42.1 (15)	42.3 (13)
^{47}Ca$_{(c)}$	0.167 (22)	0.187 (27)	0.168 (30)	0.158 (39)	-	-	-	-	-
^{47}Sc$_{(i)}$	25.7 (21)	25.84 (98)	26.53 (87)	26.82 (84)	26.2 (13)	26.70 (97)	26.0 (28)	23.5 (12)	22.4 (11)
^{48}Sc$_{(i)}$	2.31 (15)	2.35 (16)	1.85 (44)	1.88 (13)	2.53 (31)	-	2.65 (42)	2.45 (13)	2.35 (13)
^{48}V$_{(i)}$	3.62 (13)	4.11 (13)	4.16 (12)	4.86 (12)	5.60 (17)	6.24 (20)	7.06 (28)	-	-
E_p [MeV]	72.34 (61)	66.95 (64)	62.87 (67)	59.88 (70)	57.26 (72)	55.36 (74)	54.9 (13)	53.40 (76)	51.9 (14)
^{42}K$_{(i)}$	6.94 (49)	7.32 (51)	6.57 (43)	5.62 (37)	4.30 (31)	3.23 (23)	2.86 (20)	2.77 (22)	1.72 (11)
^{43}K$_{(i)}$	1.295 (46)	1.358 (44)	1.339 (45)	1.425 (48)	1.408 (48)	1.532 (51)	1.400 (34)	1.439 (54)	1.333 (28)
^{43}Sc$_{(c)}$	15.4 (14)	13.9 (15)	15.2 (14)	15.7 (17)	17.9 (17)	18.6 (20)	14.22 (84)	19.0 (17)	15.83 (88)
^{44g}Sc$_{(i)}$	35.4 (23)	-	30.4 (17)	27.7 (17)	21.3 (27)	24.65 (78)	21.3 (12)	22.22 (71)	22.2 (12)
^{44m}Sc$_{(i)}$	23.03 (78)	21.13 (69)	18.18 (61)	15.97 (53)	14.23 (47)	13.52 (45)	12.02 (24)	12.79 (42)	10.48 (22)
^{46}Sc$_{(i)}$	44.8 (16)	48.0 (16)	50.0 (17)	51.8 (21)	53.2 (19)	55.5 (21)	-	55.3 (18)	-
^{47}Sc$_{(i)}$	23.2 (11)	23.7 (11)	23.8 (11)	23.9 (11)	23.6 (11)	23.5 (11)	20.82 (65)	22.7 (11)	19.08 (64)
^{48}Sc$_{(i)}$	2.33 (12)	2.30 (12)	2.28 (13)	2.18 (15)	2.131 (87)	2.02 (13)	1.649 (85)	2.01 (12)	1.596 (44)
E_p [MeV]	51.39 (79)	49.5 (14)	46.9 (15)	45.4 (15)	43.5 (16)	41.9 (16)	38.0 (17)	36.2 (18)	
^{42}K$_{(i)}$	1.67 (16)	1.151 (90)	0.786 (67)	0.670 (80)	0.571 (55)	-	0.378 (45)	-	
^{43}K$_{(i)}$	1.394 (52)	1.169 (25)	0.863 (19)	0.645 (17)	0.473 (12)	-	0.1122 (65)	-	
^{43}Sc$_{(c)}$	20.6 (22)	16.12 (90)	16.32 (91)	15.80 (92)	-	13.18 (85)	9.38 (58)	6.54 (42)	
^{44g}Sc$_{(i)}$	23.24 (72)	19.4 (12)	22.7 (15)	22.3 (16)	23.8 (17)	25.1 (11)	29.8 (11)	33.73 (97)	
^{44m}Sc$_{(i)}$	12.86 (42)	11.54 (26)	12.00 (28)	11.61 (22)	12.16 (28)	12.24 (26)	15.03 (39)	13.45 (32)	
^{46}Sc$_{(i)}$	59.7 (21)	-	-	-	-	-	-	-	
^{47}Sc$_{(i)}$	23.0 (11)	20.41 (87)	20.89 (92)	19.87 (50)	20.37 (72)	19.16 (57)	23.62 (93)	22.35 (70)	
^{48}Sc$_{(i)}$	2.01 (12)	1.836 (70)	1.809 (51)	1.684 (91)	1.627 (49)	1.370 (52)	1.296 (62)	1.003 (70)	

3.4.1 ^{75}As(p,4n)^{72}Se Cross Section

^{72}Se decays 100% by electron capture to the 1^+ first excited state in ^{72}As. This leaves a 45.89 keV ($I_\gamma = 57.2\%$) γ-ray as the only direct detectable signature of ^{72}Se formation from the irradiations given the HPGe equipment used in this work. However, ^{72}Se production could additionally be quantified using the ^{72}As decay gamma-rays after ^{72}Se/^{72}As were in secular equilibrium at least 11 days after EoB. The results from each measurement method were seen to be very comparable but only the secular equilibrium values were recorded, and plotted in Figure 3.5, due to comparatively reduced uncertainties.
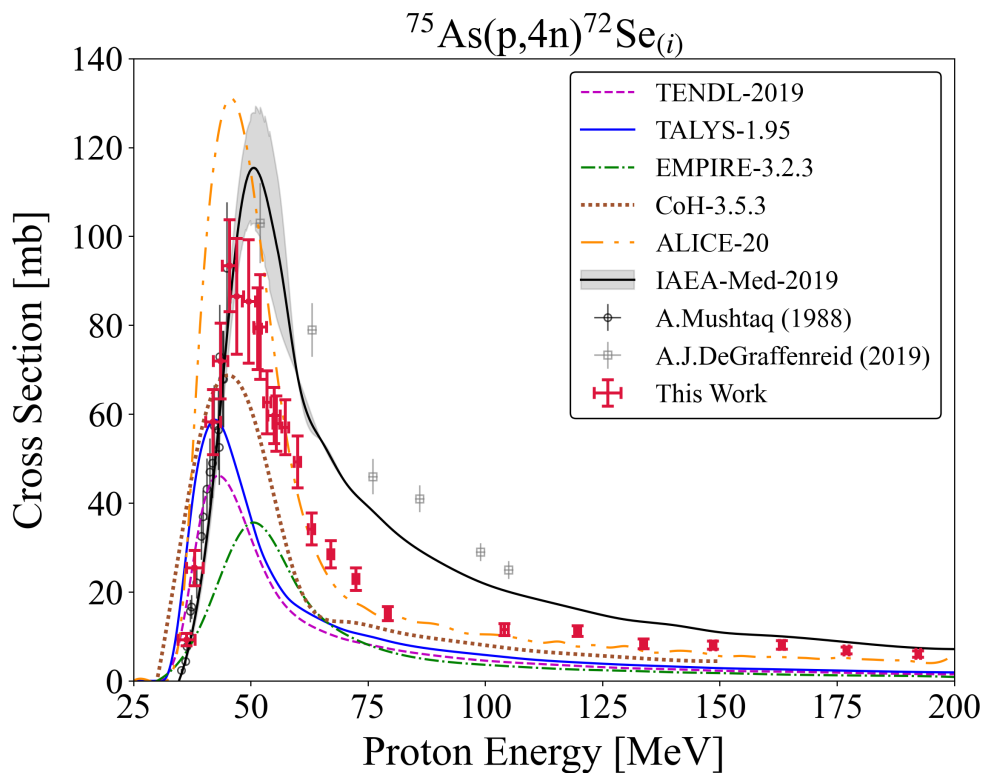
Figure 3.5: Experimental and theoretical cross sections for ^{72}Se production, peaking near 90 mb around 50 MeV.

Only two prior experimental datasets partially measured this excitation function. The Mushtaq et al. [141] results cover the low energy production from threshold towards the maximum of the compound peak near 50 MeV and agree well with the measurements of this work. The second prior experimental dataset from DeGraffenreid et al. [55] covers a broader higher-energy portion of the excitation function between 52–105 MeV. A large discrepancy exists between the DeGraffenreid et al. [55] data and the values reported here. This difference is most evident for the cross section above 60 MeV where our measurements demonstrate a much more constrained "bell-shape" for the compound peak with a pre-equilibrium "tail" that decreases in magnitude quicker than expressed by DeGraffenreid et al. [55]. These differences are possibly partly a function of the contrasting experimental methodologies between this work and DeGraffenreid et al. [55]. DeGraffenreid et al. [55] did not use a stacked-target technique, but instead used multiple irradiations with thicker GaAs wafer targets, a much larger beam current, and analysis by chemical dissolution of the targets with subsequent radioassays on an HPGe using solution aliquots.

The TALYS, CoH, and ALICE reaction codes, along with the TENDL evaluation, demonstrate a similar shape though all but ALICE underpredict the compound peak cross section magnitude. Incorrect compound peak energy centroids are a pervasive error among all the

calculations for this channel, generally as a function of the codes' poor threshold predictions. TENDL perhaps best matches the experimental threshold and rising edge behaviour of the excitation function but its incorrect magnitude muddles the overall comparison of the evaluation to the data.

In general, the variation in peak centroid location between the codes is typical and is a function of the differing pre-equilibrium calculations. Small differences between pre-equilibrium models in the codes can amplify the impact caused by particles emitted in pre-equilibrium that carry a significant amount of energy, which ultimately alter which compound nucleus is formed at a given incident energy [39]. Consequently, the improper pre-equilibrium tail modeling among TALYS, CoH, EMPIRE, and TENDL is noteworthy because it is an error that will propagate to the thresholding and rising edge behaviour in residual products that are energetically downstream of this (p,4n) channel.

Moreover, EMPIRE performs worst among the codes likely on account of these incorrect pre-equilibrium results for residual products more near the target nucleus. In this ^{72}Se channel, the errors in EMPIRE manifest as an estimated rising edge with a much too small slope and the largest magnitude underprediction.

The production cross section of ^{72}Se has also been evaluated as part of an IAEA coordinated research project (IAEA-Med-2019) focused on the recommendation of data for medical radionuclides, and in specific, diagnostic positron emitters [12]. The DeGraffenreid et al. [55] data were not avaialble at the time of the IAEA evaluation and though the IAEA prediction reaches a similar peak to DeGraffenreid et al. [55], which is above the peak predicted in this work, the IAEA recommendation does not support the very broad compound peak.

It is worth reflecting that these ^{72}Se production results, i.e. the proper characterization of an excitation function from threshold to 200 MeV where little prior data existed, are emblematic of the overall TREND endeavour.

3.4.2 ^{75}As(p,x)^{68}Ge Cross Section

The results reported here represent the first measurement of this channel. The ^{68}Ge production cross section proved difficult to quantify in this work due to its long half-life ($t_{1/2} = 270.93$ d [131]) and the lack of gamma-ray emissions. Moreover, ^{68}Ge decays 100% by electron capture directly to the ground state of ^{68}Ga. As a result, it was necessary to rely on the still weak, but strongest available, 1077.34 keV ($I_\gamma = 3.33\%$) γ-ray from the decay of ^{68}Ga to measure the ^{68}Ge formation cross section [178]. ^{68}Ga is short-lived with a 67.71 minute half-life and it quickly falls into secular equilibrium with ^{68}Ge [131]. Therefore, all 1077.34 keV emissions measured in the arsenic target spectra taken months after the irradiation dates were solely attributable to the decay of the initial cumulative ^{68}Ge population. Week- to

multi-week-long counts were required to achieve reasonable statistics for the 1077.34 keV signal.

The ensuing measured ^{75}As(p,x)^{68}Ge excitation function is given in Figure 3.6. No cross sections were extracted from the LBNL irradiation or the rear-end of the LANL stack as the incident proton energies were below or too near threshold for measurable ^{68}Ge production. The given excitation function in Figure 3.6 is the first measurement of ^{68}Ge formation from arsenic up to 200 MeV as no prior experimental datasets exist. The excitation function shows a peak of approximately 42 mb at 72 MeV due to the ^{75}As(p,α4n)^{68}Ge pathway and a high-energy increasing pre-equilibrium tail from formation mechanisms where α-particle emission is replaced by 2p2n.
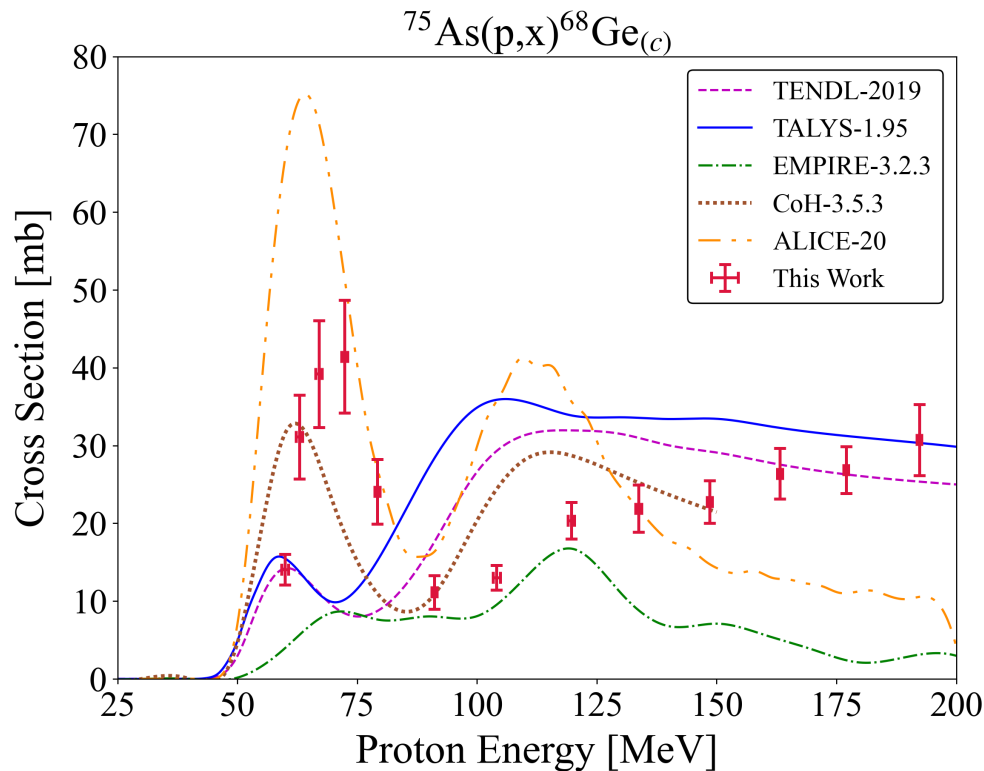
Figure 3.6: Experimental and theoretical cross sections for ^{68}Ge production, peaking near 42 mb around 72 MeV.

Interestingly, EMPIRE's overprediction of the compound peak energy centroid for ^{72}Se production versus all other codes (Figure 3.5) is also seen for the ^{68}Ge excitation function except it is a fairly accurate representation of reality in Figure 3.6. However, this energy comparison is the endpoint of EMPIRE's accuracy as its excitation function shape and magnitude are markedly incorrect.

ALICE continues to overestimate the compound peak magnitude and it even incorrectly predicts a higher-energy second compound peak rather than a pre-equilibrium tail. CoH

performs similarly to ALICE but at a more correct magnitude albeit at a shifted centroid energy of near 10 MeV below the experimental data. Both TALYS and TENDL correctly demonstrate a significant pre-equilibrium tail with an approximately correct shape but the relative magnitudes between their peaks and tails are erroneous.

It is important to temper expectations for the predictive power of these codes in calculating the ^{68}Ge production seen here since this is a cumulative result, which requires calculation contributions from many residual products and ultimately only makes up a minor $\approx 5\%$ of the total non-elastic cross section.

3.4.3 ^{75}As(p,3n)^{73}Se Cross Section

The ^{75}As(p,3n)^{73}Se excitation function is the most well-characterized residual product channel from existing literature data. The measured cross sections extracted from the LBNL and LANL irradiations are shown in Figure 3.7 to agree very well with these existing results. Note that the reported cross sections are cumulative and include the formation contribution from the short-lived parent isomer ^{73m}Se ($t_{1/2} = 39.8\,\text{min}$) in addition to the longer-lived ($t_{1/2} = 7.15\,\text{hr}$) ground state [179]. The results of the BNL irradiation help to extend the excitation function and characterize its tail behaviour up to 200 MeV. The consistency between our results and the literature data compiled in EXFOR builds confidence in the energy and current assignments determined in this work as well as the overall measurement and data analysis methodology.

The default TALYS and EMPIRE predictions both underestimate the compound peak magnitude, EMPIRE decidedly more so than TALYS, while TALYS also shifts the peak energy lower than experimentally observed. The ALICE calculation performs best here with an appropriate peak magnitude and nearly proper tail shape, which is just incorrectly shifted similar to TALYS. TENDL replicates TALYS very closely other than a slightly reduced peak. CoH significantly mispredicts the channel's rising edge resulting in a more severe energy shift than both TALYS and ALICE.

The measured falling edge of the production compound peak is additionally relevant to the medical community as ^{75}As(p,3n) has been shown as the most advantageous route to the nonstandard positron emitter ^{73}Se [180]. In this vein, the production of ^{73}Se has also been evaluated by the IAEA and this recommended fit is given in Figure 3.7 [12]. The IAEA fit is seen to agree very well with the measured data in this paper.

It is worth noting that although the cross section averages only $\approx 40\,\text{mb}$ from 50–200 MeV, the greater range of incident protons at 200 MeV as compared to 50 MeV would lead to a more than doubling in the overall ^{73}Se production rate. This brief consideration is representative of the value inherent to high-current, high-energy proton accelerator facilities and rationalizes the effort to measure high-energy reaction data for worthwhile targets such as arsenic.
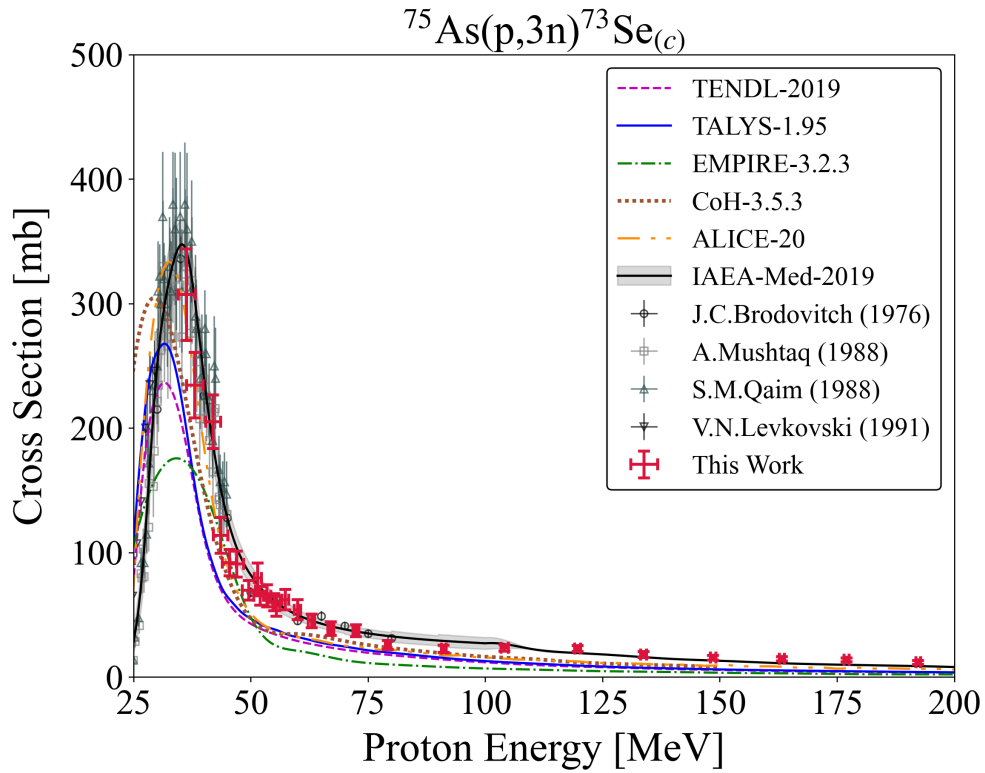
Figure 3.7: Experimental and theoretical cross sections for ^{73}Se production, peaking near 330 mb around 35 MeV.

3.4.4 ^{75}As(p,p3n)^{72}As Cross Section

The direct measurement of ^{72}Se decay allowed for the subsequent independent cross section quantification of ^{72}As. The cross section results are presented in Figure 3.8 and are the measured first data of this reaction channel.

The modeling predictions all perform fairly similarly in this channel in contrast to the large variations seen for nearby ^{72}Se and ^{73}Se production. EMPIRE, CoH, and ALICE underpredict the high-energy cross section for ^{72}As relative to TALYS and TENDL, though the former trio of codes have the better energy placement of the compound peak centroid.
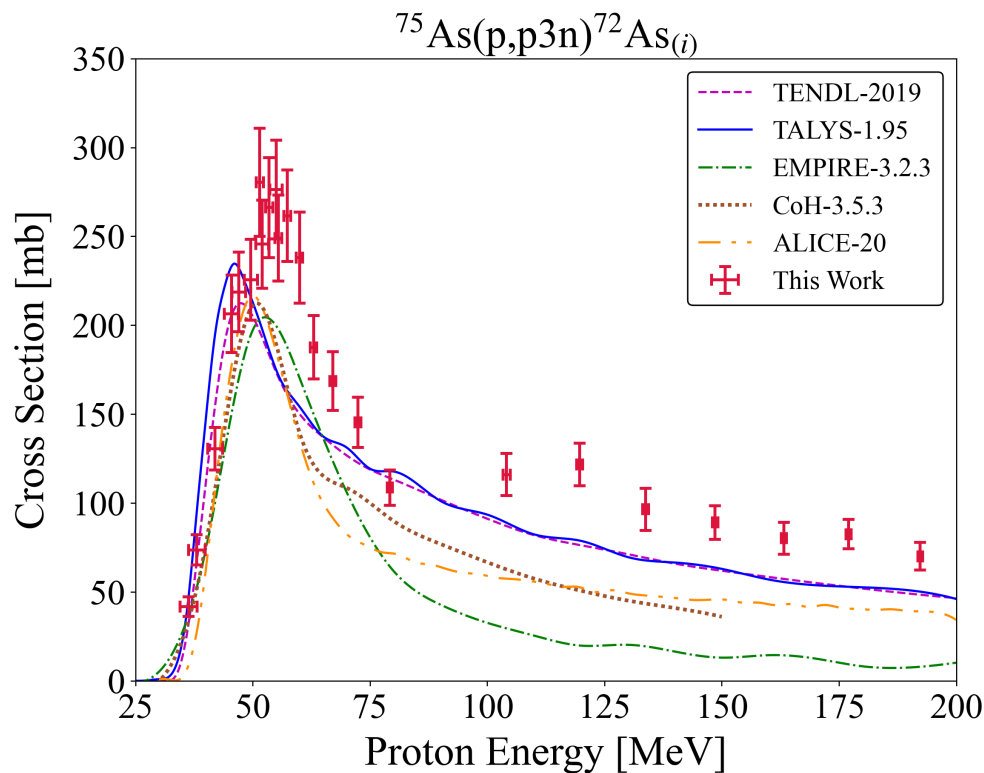
Figure 3.8: Experimental and theoretical cross sections for ^{72}As production, peaking near 275 mb around 55 MeV.

3.4.5 ^{nat}Ti(p,x)$^{44m/g}$Sc Cross Section

The production of ^{44g}Sc ($t_{1/2} = 3.97$ hr [181]) is of general interest as an emerging radiometal for nuclear imaging and theranostic purposes [12, 180, 182, 183]. While the measurements of the ^{nat}Ti(p,x)$^{44m/g}$Sc excitation functions extracted from the titanium monitor foils included in the target stacks may not give an ideal production route for this medical application, these cross section results do give the only observable isomer and ground state pair from the three irradiations. As a result, this work provides a large update to the ^{44m}Sc ($t_{1/2} = 58.61$ hr, $J^{\pi} = 6^+$) to ^{44g}Sc ($t_{1/2} = 3.97$ hr, $J^{\pi} = 2^+$) [181] isomer-to-ground state ratio via ^{nat}Ti(p,x), as seen in Figure 3.9 and recorded in Table 3.5.

This is data that could be used by the reaction modeling community to gain insight into angular momentum deposition over a broad range of incident particle energies.

Table 3.5: Isomer-to-ground state production ratio for ^{nat}Ti(p,x)$^{44m/g}$Sc covering incident proton energies from 36 to 192 MeV.

E_p [MeV]	$\sigma(^{44m}\mathrm{Sc})/\sigma(^{44g}\mathrm{Sc})$
192.26 (49)	0.456 (29)
176.99 (51)	0.449 (32)
163.18 (54)	0.455 (25)
148.52 (58)	0.471 (21)
133.72 (62)	0.508 (34)
119.63 (67)	0.470 (37)
104.05 (74)	0.603 (59)
91.05 (51)	0.664 (45)
79.15 (57)	0.566 (37)
72.34 (61)	0.650 (48)
62.87 (67)	0.598 (40)
59.88 (70)	0.577 (40)
57.26 (72)	0.668 (88)
55.36 (74)	0.548 (25)
54.9 (13)	0.563 (34)
53.40 (76)	0.576 (26)
51.9 (14)	0.472 (27)
51.39 (79)	0.554 (25)
49.5 (14)	0.595 (40)
46.9 (15)	0.529 (37)
45.4 (15)	0.521 (39)
43.5 (16)	0.512 (39)
41.9 (16)	0.488 (23)
38.0 (17)	0.505 (23)
36.2 (18)	0.399 (15)

Multiple experiments have measured this ratio previously for less than 50 MeV and there is agreement between the high-energy end of these measurements and the lowest energy results of this work [140, 150–153].

The EMPIRE, CoH, and TENDL predictions for the isomer-to-ground state ratio are also shown in Figure 3.9 for comparison. The EMPIRE and CoH predictions markedly underestimate the ratio, however this result is a function of varying errors. In EMPIRE's case, the ratio is incorrect due to an overestimation of ^{nat}Ti(p,x)^{44g}Sc production (see Figure 3.22 in Section 3.8) while the CoH misprediction is instead a function of underestimation for ^{nat}Ti(p,x)^{44m}Sc production (Figure 3.23 in Section 3.8).
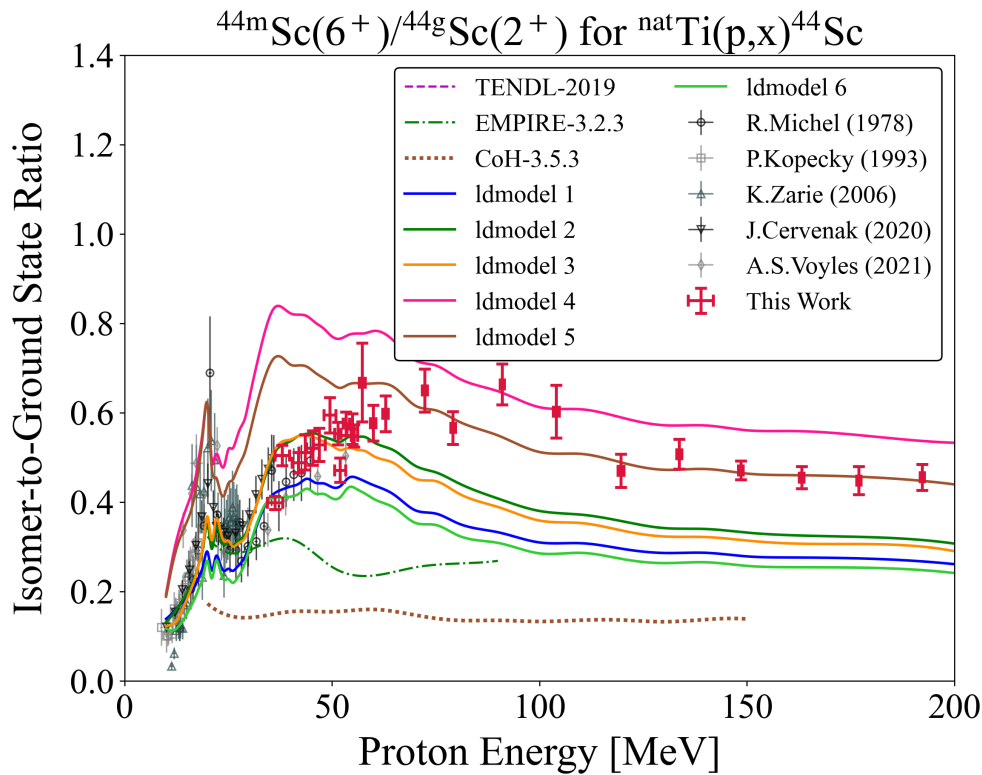
Figure 3.9: Experimental and theoretical results for the isomer-to-ground state production ratio for ^{nat}Ti(p,x)$^{44m/g}$Sc. The predictions from all 6 TALYS level density models are shown, where `ldmodel` 1 is equivalent to the TALYS default.

In the compound peak energy region of the $^{44m/g}$Sc excitation functions (25–45 MeV), competition with other exit residual product channels is minimized. Hence the optical model impact and transmission coefficient effects are minimized and the isomer-to-ground state data in Figure 3.9 is largely a function of the level density of ^{44}Sc. Consequently, comparing the isomer-to-ground state predictions from TALYS's numerous nuclear level density models is a conventional brief investigation of this data. These TALYS predictions are the remaining comparisons shown in Figure 3.9.

The `ldmodel` 1 in TALYS is the default Gilbert-Cameron constant temperature and Fermi gas model, but `ldmodel` 2, the Back-shifted Fermi gas model, appears to perform best in Figure 3.9 over the largest energy range. Though, it is perhaps noteworthy that the high-energy portion of the data is best reproduced by two of TALYS's microscopic level density models - `ldmodel` 4 and `ldmodel` 5. The exact nature of these microscopic models, and all six models in total, can be reviewed in the TALYS-1.95 manual [47].

A single iteration of the Fox et al. [34] fitting procedure was additionally applied for ^{nat}Ti(p,x) to try and glean more insight on the effect of level density choice for the relevant nuclei. It was found that an overall best fit to the multiple observed residual product

channels (see Table 3.4 for product list) was still achieved using `ldmodel` 2 but that an energy dependent increase in the spin cut-off parameter was also included among the model adjustments. The spin cut-off increase, set to begin globally at $E_p = 40\,\text{MeV}$ in this case, broadens the width of the angular momentum distribution of the level densities involved in the ^{nat}Ti(p,x) reaction [47]. This adjusted best fit can be seen versus the unadjusted `ldmodel` 2 case for the isomer-to-ground state ratio in Figure 3.10.

It is interesting to observe that beyond ≈125 MeV, the ratio remains relatively constant, thereby indicating a limit to the maximum amount of angular momentum that can be imparted to the system. This is a reflection of the mechanics of the pre-equilibrium process.

This is evidently only an elementary investigation of the angular momentum in ^{44}Sc and neighbouring nuclei, and a detailed investigation is outside the intent of this paper. Altogether, this discussion is still presented to inform the value and scarcity of these types of ratio datasets over wide energy regions, and to provide motivation for further analysis.
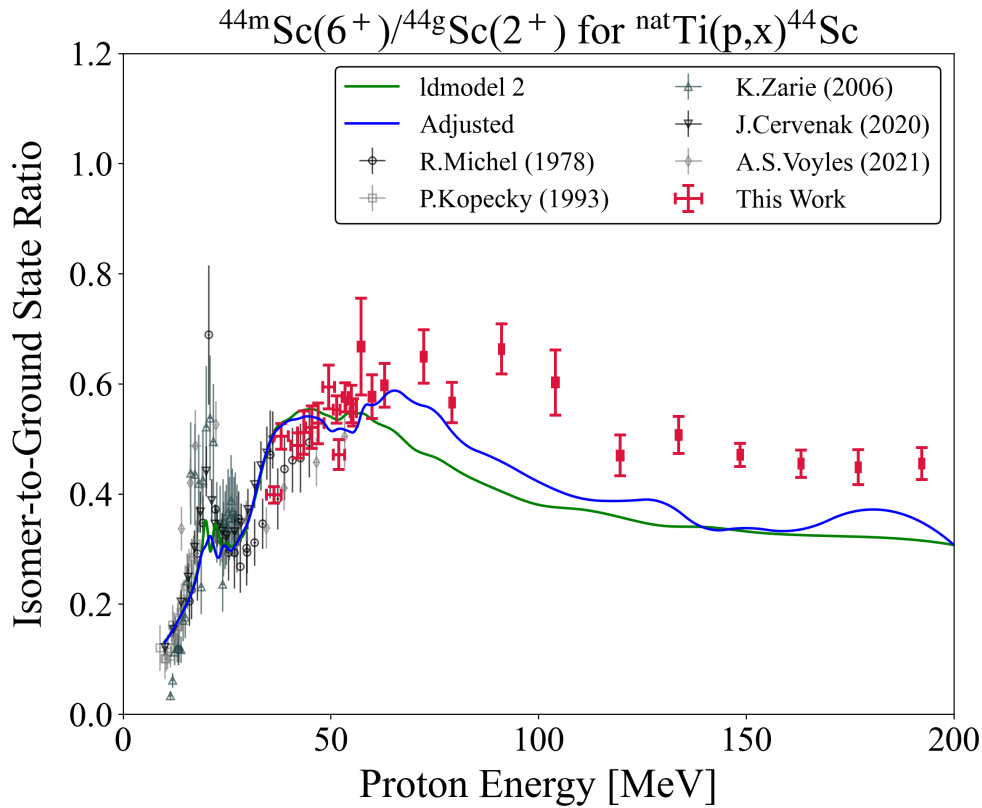
Figure 3.10: Comparison of the TALYS `ldmodel` 2 model prediction for the isomer-to-ground state production ratio for ^{nat}Ti(p,x)$^{44m/g}$Sc with a TALYS fit using adjusted parameters, including a spin cut-off increase.

3.4.6 ^{nat}Cu(p,x) Cross Sections

The numerous ^{nat}Cu(p,x) cross sections measured here are in good agreement with the existing body of literature data and help to populate the more sparse regions of measurements between 100–200 MeV. Plots of these copper excitation functions are provided in Section 3.8. Similar to the ^{73}Se results (Figure 3.7), the ^{nat}Cu(p,x) comparisons with existing data lend credence to our analysis methodology as well as our measurement extensions to regions with no prior cross sections.

3.4.7 Predicted Physical Thick Target Yields

Instantaneous thick target yields for ^{75}As(p,x)^{72}Se, ^{68}Ge were calculated from the measured cross section results and are plotted in Figure 3.11. A comparison to the yields from earlier discussed established production routes for these generator nuclei in Section 3.2 are also included.
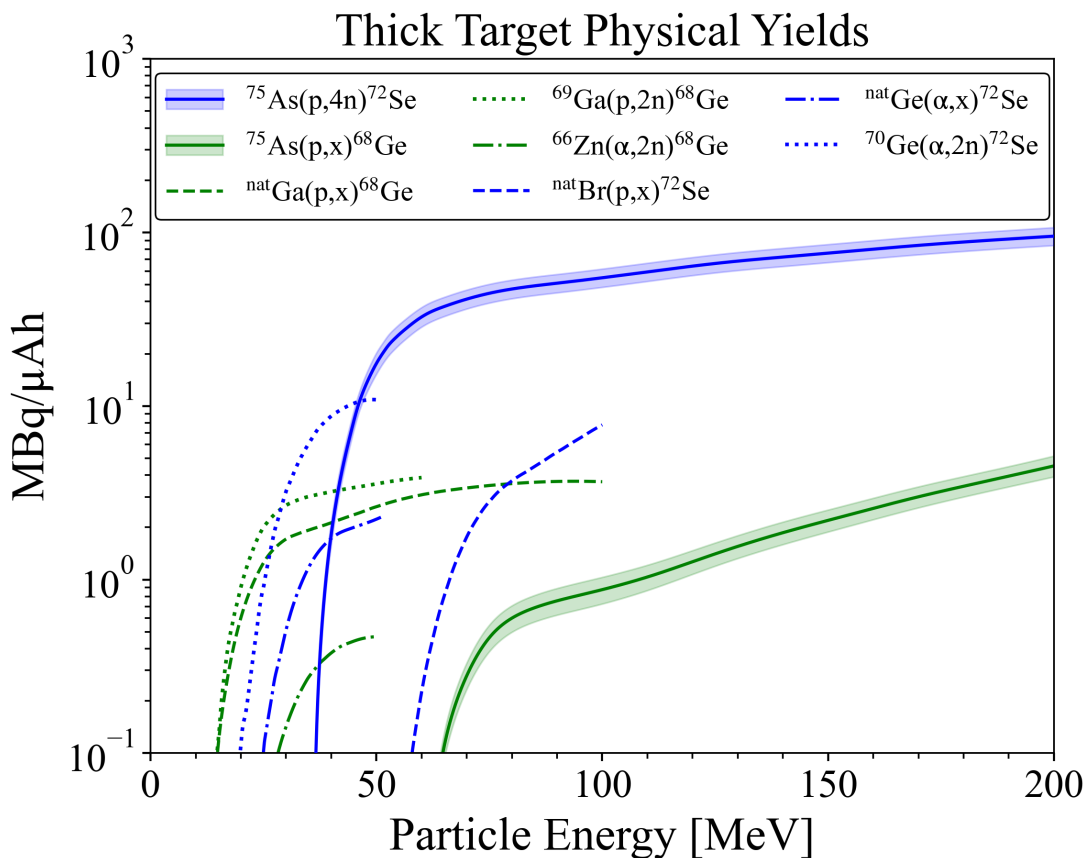
Figure 3.11: Yields for the PET generator radionuclides ^{72}Se and ^{68}Ge according to established production routes and the new arsenic-based routes measured in this work [129, 130, 143, 184–191].

The data from TREND suggests that across all relevant incident particle energies beyond reaction threshold, the ^{75}As(p,4n)^{72}Se is the optimal production pathway to the ^{72}Se/^{72}As generator system. The arsenic target route offers an increase in yield of greater than an order of magnitude versus the current methods, while still affording radioisotopically pure production as best as possible. Specifically, no charged-particle production route to the ^{72}Se/^{72}As generator system is uncontaminated from $^{75-73}$Se co-production. However, it is expected that ^{72}As will be efficiently separated from the parent ^{72}Se when needed, and that the co-produced $^{75-73}$Se will also follow the chemical separation [125, 127]. Additionally, the ^{75}As(p,4n) pathway avoids any potential long-lived ^{74,73,71}As contamination.

It is seen that at incident proton energies nearing 200 MeV, the yield from ^{75}As(p,x)^{68}Ge can rival and exceed the production route based on already employed natural gallium targets. Specifically, Figure 3.11 predicts an $\approx$18% increase for the arsenic-based yield at 200 MeV (4.5 > 3.8 MBq/µAh). Nevertheless, a p+^{75}As approach is expected to co-produce more stable germanium and ^{71}Ge→^{71}Ga contamination versus the p+^{nat}Ga route, leading to reduced ^{68}Ge specific activity. Arsenic targets would also introduce a need for additional, potential lossy, separation chemistries due to long-lived selenium and arsenic products not present from p+^{nat}Ga. Therefore, uprooting the successful established gallium route for arsenic is unwarranted. Still, this ^{75}As(p,x)^{68}Ge study gives valuable information in the context of total arsenic reactions, contributes to the knowledge base of the essential ^{68}Ge/^{68}Ga system, and demonstrates the importance of measuring these high-energy reactions, which can very easily produce large yields due to the long range of high-energy protons.

3.5   Charged-Particle Reaction Modeling

The effort to explore and improve the current nuclear reaction models for charged-particles, and perhaps more specifically charged-particles at high incident energies, is continued in this work. Explicitly, the TALYS residual product based fitting procedure presented by Fox et al. [34] is applied to ^{75}As(p,x) given the unique, large body of proton-induced data measured here.

The nine reaction channels ^{75}As(p,x)^{75,73,72}Se, ^{74,73,71}As, ^{69}Ge, ^{68,67}Ga were simultaneously used for the parameter adjustment investigation. ^{73}Se, ^{73}As, ^{69}Ge, and ^{68}Ga were considered as the most important fitting cases due to a combination of factors such as cross section magnitude, diversification of particle emission types, and impact on production competition with neighbouring nuclei.

3.5.1 Deformation Effect of ^{75}As

While the cases of ^{93}Nb(p,x) in Fox et al. [34] and of ^{75}As(p,x) here have similar attributes - both utilize data from the same experiments, which cover the same energy range of interest, and both are monoisotopic targets in nearby mass ranges - the documented deformation of ^{75}As is a notable change from the spherical ^{93}Nb [192–195]. This potentially introduces a complication to the direct application of the fitting procedure from Fox et al. [34]. Specifically, it would be necessary to address coupled-channels (CC) calculations or other angular momentum modifications to the typical spherically symmetric Hauser-Feshbach formalism prior to any further parameter changes [52].

The RIPL-3 imported TALYS value for the ^{75}As quadrupole deformation parameter is -0.25, which suggests a strongly oblate deformation [16, 47]. In fact, RIPL-3 lists strong oblate deformation for the arsenic isotopes $A = 68 - 76$. While some experimental evidence supports these values for the neutron deficient cases and transitions around $N = Z$, it is quite rare that the neutron rich isotopes would demonstrate oblate rather than prolate deformation [196, 197]. An investigation using a Nilsson diagram gives further support that ^{75}As is actually prolate in nature. Finally, ENSDF and the original datasets incorporated into the structure evaluation provide experimental evidence of the prolate condition for ^{75}As and actually list a quadrupole deformation parameter of +0.314 (6) [192].

TALYS, however, does not include any deformation coupling schemes for arsenic isotopes and as a result, a spherical OMP basis is used in the predictive calculations, thereby potentially neglecting a significant physics aspect of the problem. It was therefore necessary to manually create a coupling scheme to see whether this has an effect on final results. Yet, the level scheme of ^{75}As does not present any ideal vibrational or rotational bands for coupling and its deformation is very likely either soft vibrational or soft rotational [198, 199].

On further examination, the $3/2^-$ ground state with the $5/2^-$ level at 279.543 keV and the $7/2^-$ level at 821.620 keV appear to form a rotational band. The $5/2^-$ level shows the expected strong γ-ray transition ($I_\gamma = 100.0$ (5)%) of M1 character to the ground state, while the $7/2^-$ excited level shows both a strong E2 transition to the ground state ($I_\gamma = 100.0$ (15)%) and weaker M1 transition to the $5/2^-$ level ($I_\gamma = 9.6$ (11)%), generally in line with behaviour expected from a rotational band. Further, the $7/2^-$ E2 transition is $20 - 40$ Weisskopf units, providing evidence for its collective behaviour. This three-level rotational band coupling scheme was added to TALYS.

It was also noticed that the neighbouring nuclei ^{76,74}Se and ^{76,74}Ge demonstrate vibrational character [200, 201] and have vibrational coupling schemes implemented in TALYS for CC calculations (^{76}Ge has actually recently been shown as rigid triaxially deformed [202]). These neighbouring properties provide motivation to model the arsenic target as soft vibrational rather than rotational.

Unfortunately, TALYS's implementation of the ECIS-06 code for optical model and CC calculations is unsuited for a pure vibrational coupling scheme for odd-Z nuclei, and the weak-coupling model has to be used in such cases. Moreover, the only odd-Z nucleus with any sort of vibrational deformation file in TALYS is ^{241}Am, where vibrational collectivity is built on top of rotational character. Therefore, taking the ^{241}Am deformation formatting as a guide, a weak vibrational band consisting of the ^{75}As $9/2^+$ (303.9243 keV), $5/2^+$ (400.6583 keV), and $1/2^+$ (860.0 keV) levels were added to a second created coupling scheme including the prior discussed rotational band. In this suggested vibrational band, the $1/2^+$ level is dominated by transition to $5/2^+$, which then has an E2 transition to the $9/2^+$ of 77 Weisskopf units. The $9/2^+$ de-excitation is dominated by E3 decay to the ground state. This second mixed rotational+vibrational coupling scheme was also added to TALYS.

Elsewhere, this treatment for adjusting the global spherical optical model by a CC approach to implement a deformed optical model for ^{75}As calculations has been used in Shibata et al. [199] and Kawano [198]. The Shibata et al. [199] work is an evaluation of neutron nuclear data on ^{75}As up to 20 MeV for JENDL-4 and uses a similar rotational coupling scheme to the one presented here but substitutes the $5/2^-$ level at 279.543 keV with a $5/2^-$ level at 572.41 keV. Shibata et al. [199] uses the quadrupole deformation parameter $\beta_2 = -0.19$ within a rigid-rotator model. In their evaluation, they found it necessary to additionally tune the matrix element parameter as well as the pickup and knockout contributions for their pre-equilibrium model relevant to the residual product cross sections of (n,γ), (n,p), (n,2n), and (n,α). However, the JENDL-4 evaluation still found limited success in fitting the ^{75}As(n,p) channel after accounting for both deformation and pre-equilibrium changes. Shibata et al. [199] considered other solutions attempts that included level density and optical model parameter changes concerning both ^{75}As and ^{75}Ge but could not simultaneously improve the (n,p) channel while maintaining good global behaviour elsewhere.

Kawano [198] performed their CC calculations using the CoH reaction code and probed the collectivity effects of ^{75}As for incident neutrons. They explored the total and some close-to-target residual product cross sections up to 20 MeV, similar to Shibata et al. [199]. In comparison to ENDF/B-VII.0 results, the Kawano [198] calculations demonstrated improvement in reproducing the total cross section but did require model parameter adjustments for the individual reaction channels, not always leaving satisfactory results. Kawano [198] used the RIPL-3 suggested strong oblate deformation of arsenic.

In this p+^{75}As modeling work, the CC calculations in TALYS for arsenic, when invoking either the custom rotational+vibrational deformation or the pure rotational deformation scheme, together with the ENSDF-accepted prolate deformation parameter, proved to have minimal impact on the predictions for residual product excitation functions. Any alterations that were present were not seen to be consistent improvements versus the default spherical optical model calculations. This is not an entirely unusual result given the higher energies

under consideration and the overall expected lower level of collectivity for this target nucleus. It should be noted that this is not an exhaustive investigation of arsenic deformation, CC calculations, or collectivity models, and no structure or theory statements can be made. This result is only a statement of the sensitivity of the modeling under the conditions of this work.

Given the observed unremarkable changes, the inability to disentangle effects of CC calculations from more dominating level density, optical model, and pre-equilibrium parameter adjustments, and the imperfections of previously established deformed fitting approaches, the decision was made to treat ^{75}As spherically within TALYS and implement the fitting procedure from Fox et al. [34] identically.

3.5.2   Fitting Procedure Applied to ^{75}As(p,x)

Firstly, the application of microscopic level density models proved beneficial as compared to the default phenomenological Gilbert-Cameron constant temperature model or the placement of compound peak centroids. However, it was seen that no one microscopic level density model best reproduced the excitation functions across all the observables. Instead, level density calculations from Goriely's tables using the Skyrme effective interaction (`ldmodel` 4) [203] proved to be most accurate for the close-to-target residual products, and specifically for $^{72-76}$Se and their competition with close-to-target arsenic products. Yet, applying `ldmodel` 4 to all nuclei involved in ^{75}As(p,x) created pre-equilibrium tails biased too high above the experimental data for Ga, Ge, and other α-emission residual product excitation functions farther from the target. Conversely, it was observed that the temperature-dependent Hartree-Fock-Bogolyubov level density calculations using the Gogny force (`ldmodel` 6) [204] did not suffer from the magnitude bias problems in the far-from-target channels, but failed to model the close-to-target Se and their correlations unlike `ldmodel` 4.

Therefore, two microscopic level density models were used, where `ldmodel` 4 was applied to the aforementioned grouping of selenium nuclei and `ldmodel` 6 was applied for all else. Further details of these level density considerations can be reviewed in Section 3.5.2.1.

The pre-equilibrium parameter adjustments in the next portion of the procedure were indeed found to follow the systematic trend described in Fox et al. [34], with `M2constant`=0.80, `M2limit`=3.9, and `M2shift`=0.55. Furthermore, the value for the constant of the proton and neutron single-particle level density parameter used for calculations of the exciton model particle-hole state densities was altered from its default `Kph`=15 to `Kph`=15.16. Other pre-equilibrium modeling changes were manipulations of the stripping and knockout reaction contributions for outgoing alpha, deuteron, triton, and ^{3}He particles. These manipulations were performed using the TALYS `Cstrip` and `Cknock` keywords. The precise adjusted values can be viewed in Table 3.7 in Section 3.9.

Subsequent iterative simultaneous tuning of optical model and individual level density parameters were needed to aid the compound reaction regime and to fix erroneous production competitions between clustered products.

The need for nuclide-specific level density changes arises from discrepancies between measured and modeled data where global changes to exciton or optical model parameters can not resolve the singular problems. These nuclide-specific adjustments were most evident for ^{73}As production, where both the adjusted fit to this point and the default calculation were nearly 200 mb smaller than the observed results. As in Fox et al. [34], these level density manipulations per nuclide could be performed with the TALYS `ctable` and `ptable` commands when microscopic level density models are implemented.

The effects of `ctable` and `ptable` to create an adjusted level density $\rho(E_x, J, \pi)$ are explicitly given by,

$$\rho(E_x, J, \pi) = \exp(c\sqrt{E_x - \delta})\rho_{mic}(E_x - \delta, J, \pi), \tag{3.2}$$

where `ctable` is the c constant, `ptable` is the δ constant (denoted as the "pairing shift"), and $\rho_{mic}(E_x - \delta, J, \pi)$ are the tabulated microscopic level density calculations as a function of excitation energy E_x, angular momentum J, and parity π. The produced tables in TALYS have not been adjusted to experimental data and have $c = 0$ and $\delta = 0$ by default. The implementation of `ctable` and `ptable` under the definition of Equation (3.2) then provides necessary scaling flexibility at both low and high energies [47].

Since the production of ^{73}As is most heavily correlated with the neighbouring exit channels ^{72,73}Se and ^{74}As, the `ctable` and `ptable` effects on ^{73}As necessitated corresponding nuclide-specific level density changes in ^{72,73}Se and ^{74}As as well.

The most suitable optical model adjustments were found to be `d1adjust n`=1.75 and `d1adjust p`=1.55, which multiply the energy-dependent imaginary surface-central potential well depth for neutron and protons, respectively. These multiplicative changes lead to increased particle emission from the surface region of the nucleus, and thus to increased emission of high-energetic particles, particularly at lower incident proton energies. In turn, these alterations create a more pronounced pre-equilibrium spectrum that contributes additional production within the compound regions of residual product excitation functions and some additional production to their tails.

Although these are not unsubstantial multiplication factors, the energy dependence of the surface potential means that the adjustment impact is large in the vicinity of low threshold channels at lower incident proton energies but becomes only a minor change above ≈ 50 MeV as the volume potentials increase and dominate absorption/emission. For example, at $E_p = 20$ MeV, the default imaginary surface-central potential well depth for protons on ^{75}As is 8.4 MeV while the adjusted well depth is $1.55\times$ larger at 13.0 MeV. This 4.6 MeV difference

is a relevant change around low residual product threshold energies but by $E_p = 75\,\mathrm{MeV}$, this default versus adjusted well depth difference is reduced to just $1.5\,\mathrm{MeV}$. The difference then falls below an $1\,\mathrm{MeV}$ at $E_p = 90\,\mathrm{MeV}$, and is reduced down to $0.1\,\mathrm{MeV}$ at $E_p = 200\,\mathrm{MeV}$. Similar behaviour is true for the change to the imaginary surface-central potential well depth for neutrons. Furthermore, at $E_p = 20\,\mathrm{MeV}$, the imaginary volume potential is $5-7\times$ smaller than the imaginary surface potential for both neutrons and protons in the adjusted case, but by $E_p = 75\,\mathrm{MeV}$, the imaginary volume potential has grown to be $2-3\times$ larger. The imaginary volume potential only becomes increasingly more dominant, growing to be $50-70\times$ larger by $E_p = 200\,\mathrm{MeV}$.

It is possible that portions of the `d1adjust` changes should actually be substituted with changes to the imaginary surface diffusivity parameter, but this cannot be unambiguously determined using only residual product cross section data and instead requires angle-differential cross section information [61]. This limited diversity of high-E_p fit data is a common theme that permeates the limitations of this approach to parameter adjustments as well as prevents much physical meaning to be gleaned from the modeling. These limitations are further explored in Section 3.5.4.

An additional increase to proton absorptivity and emissivity across a wider range of energies, to increase peaks and tails for numerous channels consistently, was still warranted by the experimental data. This was implemented with an increase to the imaginary volume potential well depth for protons by `w1adjust p=1.21`.

The default TALYS alpha optical model of Avrigeanu et al. [62] was deliberately chosen as it performed best for the considered As and Ge channels. The deuteron optical model of Han et al. [205] was applied instead of the default model from standard Watanabe folding [206]. This deuteron adjustment is minor compared to the alpha model effect but does better match the experimental peak and tail behaviour in observed residual product channels for $A \leq 72$.

Lastly, an additional minor nuclide-specific case for level density adjustments that became relevant as a result of iterating over the above parameter changes was ^{71}As. This adjustment included corresponding small changes to ^{68}As, ^{69}Ge, and ^{69}Ga as a function of correlated production competition.

The lone prominent outstanding modeling discrepancy among the considered channels was an overprediction of ^{67}Ga production. It is likely that this difference represents a sensitivity limit for this fitting procedure through a manual approach. Moreover, given the massive parameter space for adjustments in TALYS, it is realistic that the fitting here ends in a local variance minimum, unable to perfectly match all prioritized ($\approx 15\%$ of total cross section) and minor ($\leq 5\%$ of total cross section) residual products. We can correct for this ^{67}Ga error by reducing the nuclide-specific level density, but this change is likely a compensating correction in this context and does not contribute to any increase in predictive power.

(a)

(b)

(c)

(d)

(e)

(f)

(g)

(h)

(i)
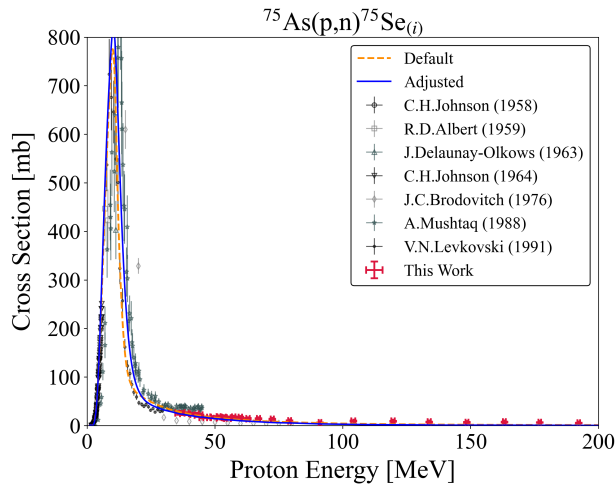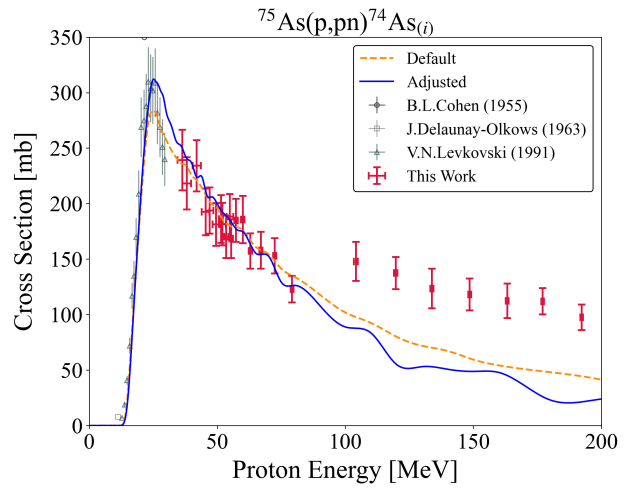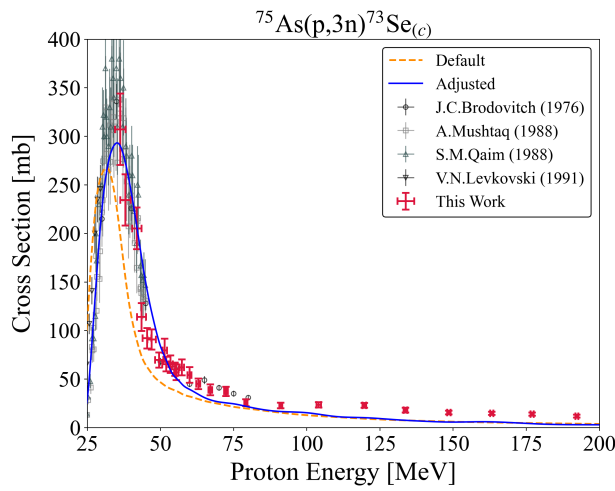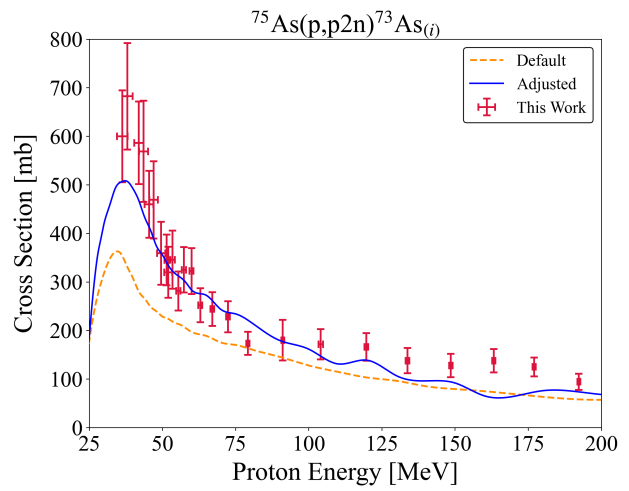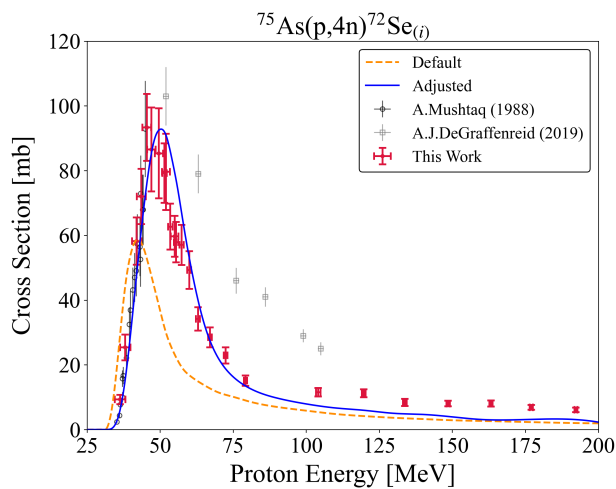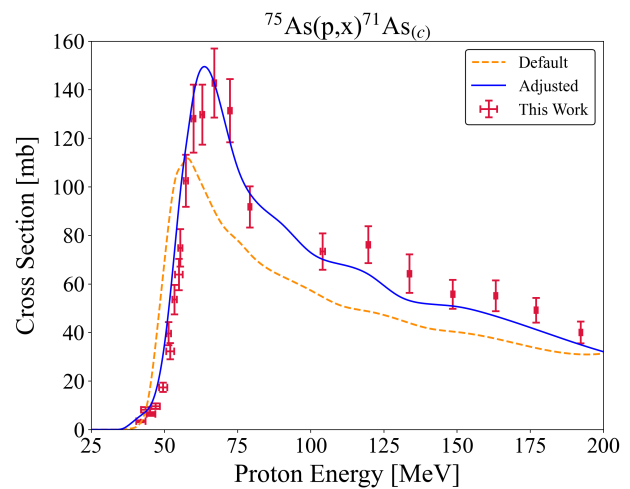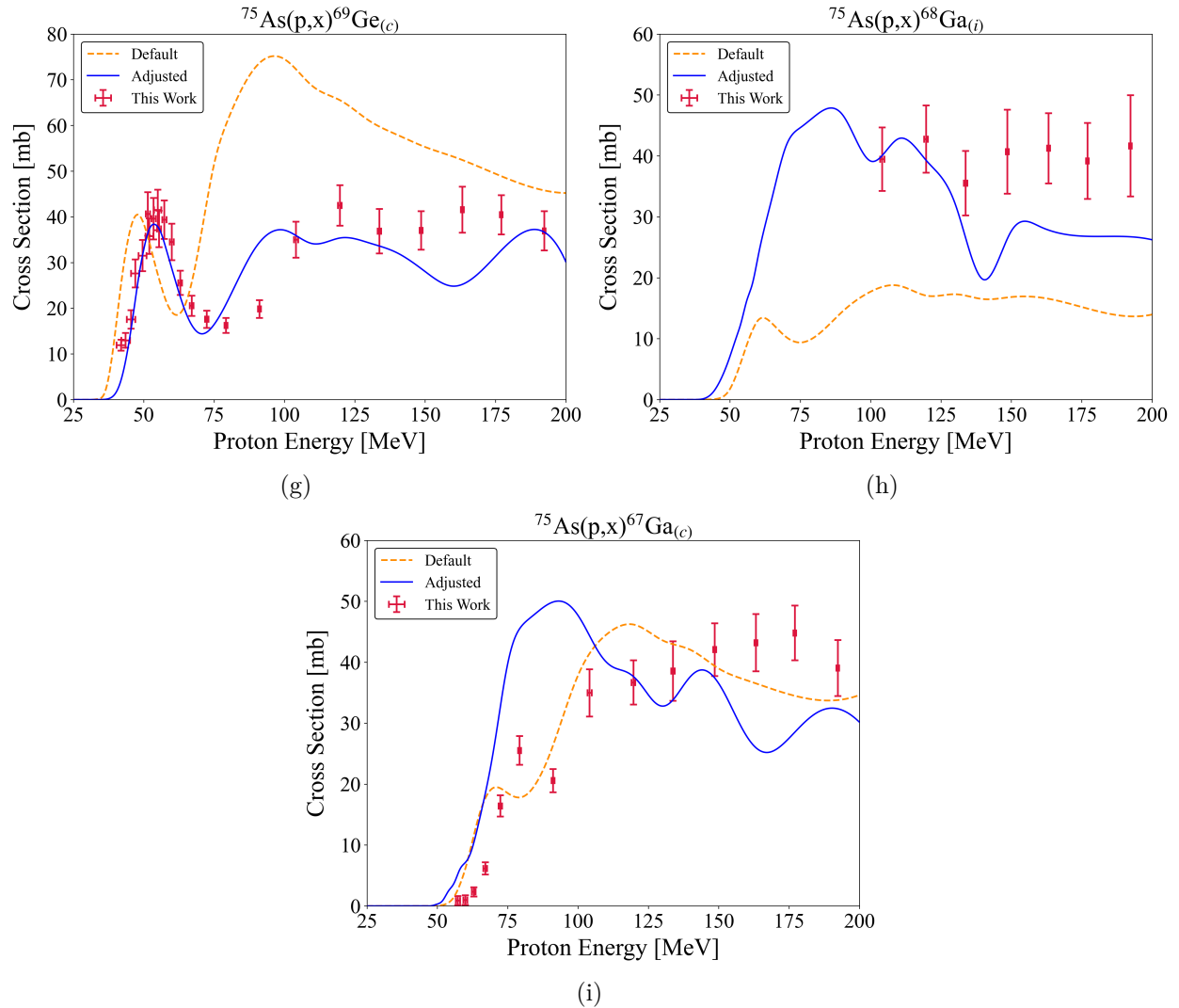
Figure 3.12: TALYS default and adjusted calculations for residual products of proton-induced reactions on arsenic up to 200 MeV.

All parameter changes creating this total adjusted fit are given in Table 3.7 in Section 3.9. Figure 3.12 presents the adjusted fit compared to the default TALYS calculation for the nine considered reaction channels up to an incident proton energy of 200 MeV.

Overall, we put forth a large number of level density scalings, either directly or as a correlation consequence, and though this is not unexpected given the prior lack of data and ambiguity for the reactions and energies of interest [204, 207], it is important to reflect on the intricacies of performing such a number of scalings. This discussion is presented in Section 3.5.2.1.

Additionally, context for our suggested parameter adjustments can be gleaned from the "best" parameters file for n+^{75}As included with TALYS-1.95 [47]. This best parameterization

contains multiple level density scalings (with the back-shifted Fermi gas model as a base) in addition to multiple optical model real potential radii and diffusivity adjustments, some of which reach upwards of 11% different from default and are made energy-dependent. Similar stripping and knock-out contributions to the suggestions in the work exist as well. Our adjustments generally work to avoid potential unphysical changes to geometry parameters and the real potential instead to focus on the imaginary potential. This focus is likely more appropriate for high-energy residual product cross section datasets versus lower energy scattering and resonance data important to n+^{75}As.

3.5.2.1   Level Density Adjustments

Figure 3.13 directly shows the magnitude of all manually adjusted level density cases with reference to the base `ldmodel` choice. The total level density of ^{73}As has been significantly increased (Figure 3.13c), as warranted by the experimental data, while a significant decrease is seen in ^{67}Ga although for less direct reasons (Figure 3.13i).

The proposition of these many level density changes is substantiated by the global fit success seen in Figure 3.12 and described in Section 3.5.3 but still requires more scrutiny. Furthermore, it is necessary to, at minimum, consider the impact of these level density changes on the residual product channels for which there were no experimental data and were unaccounted for either independently or cumulatively throughout the fitting procedure. Specifically, due to limitations of the activation technique to measure stable or some very-short lived nuclei production, the ^{75}As(p,x)^{74}Se, $^{74-70}$Ge, and $^{73,71-69}$Ga channels, for $A > 65$ and $Z > 30$, were hidden from the fitting observations. Accordingly, it is essential to have a "performance check" for these hidden channels, where the TALYS default and adjusted fits can be compared to monitor for any egregious shape or magnitude changes brought on by the level density adjustments.

The fit performance for ^{74}Se is of particular interest since had there been experimental data, the channel would have been one of the prominent excitation functions for the fitting procedure. This ^{74}Se performance check is given in Figure 3.14 and the difference between the default and adjusted is certainly acceptable.

(a)

(b)

(c)

(d)

(e)

(f)

(g)

(h)

(i)
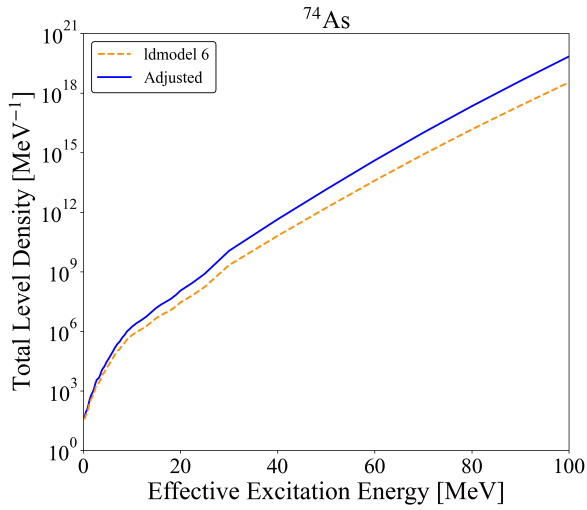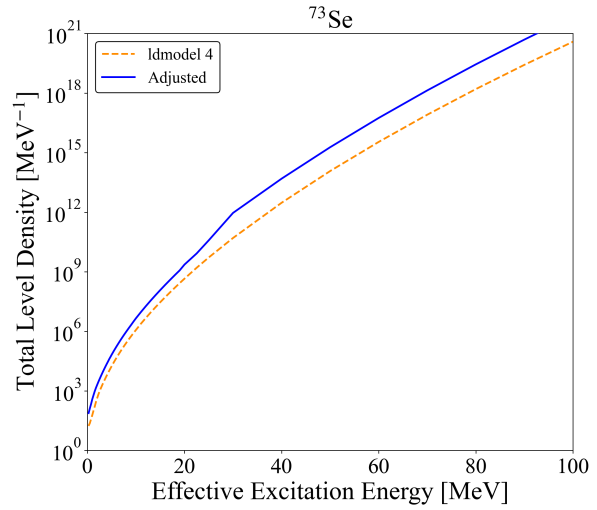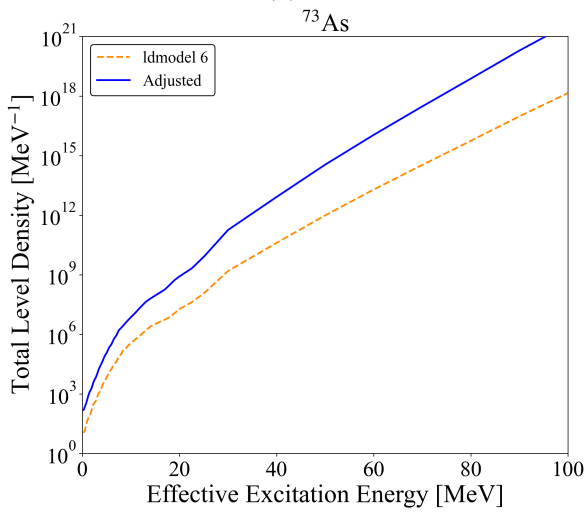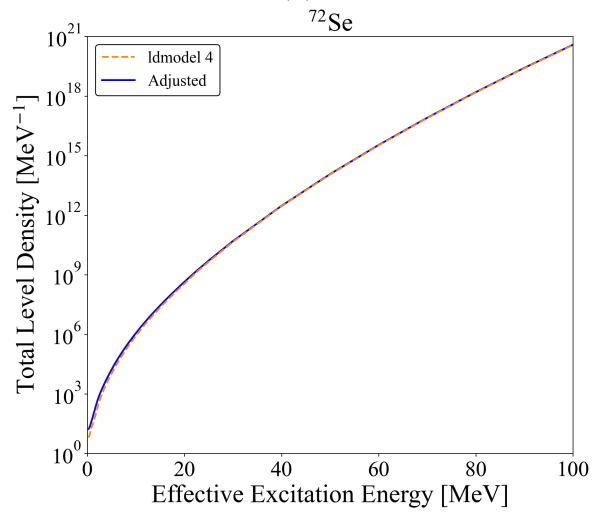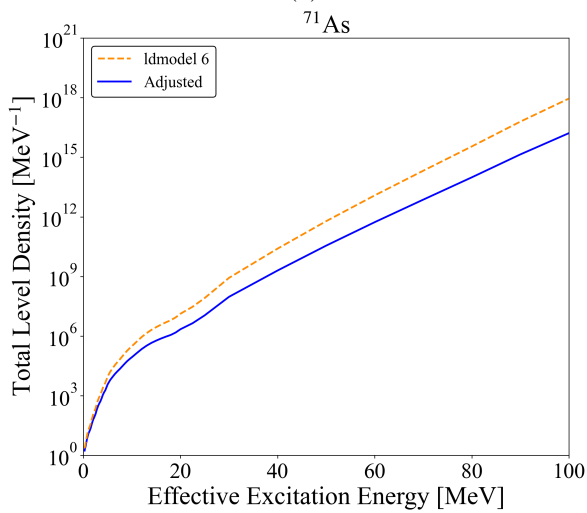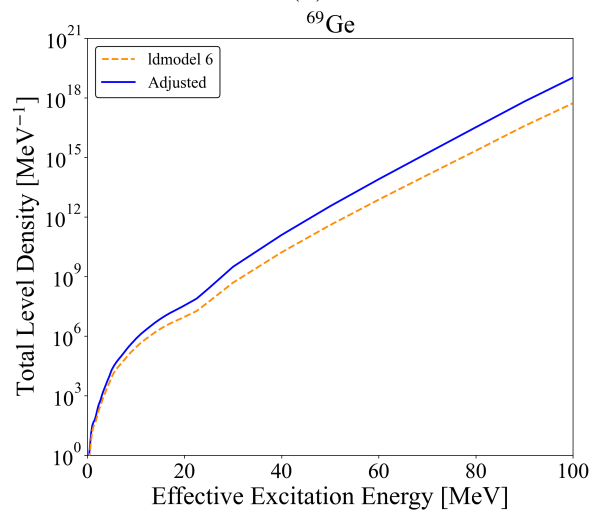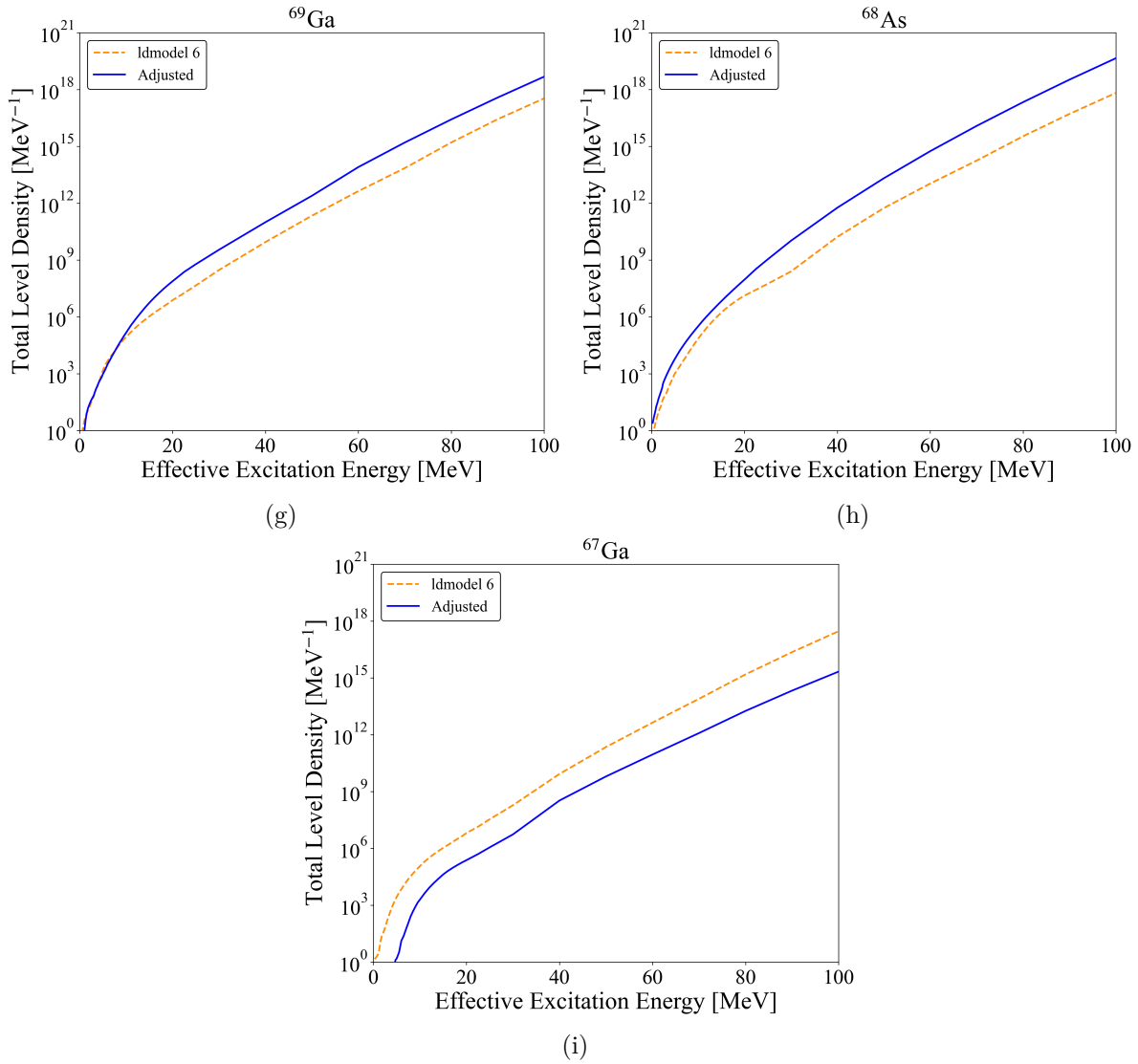
Figure 3.13: Magnitude of all level density scalings implemented as part of the global fitting procedure for residual products of proton-induced reactions on arsenic up to 200 MeV.

In the unobserved Ge and Ga channels, there continues to be no obviously incorrect changes from the default to adjusted cases. Magnitude differences for most of these products reach ≈5-7 mb and excitation function shape continuity is maintained within expectations. The adjusted ^{70}Ge production is the most significantly changed hidden channel from default, with a maximum difference of ≈40 mb in the compound peak region. Therefore, when confined to residual product datasets, there are no obvious indications that the bulk of the level density adjustments made here are not viable. Even if new experimental data were to be collected for these "hidden" channels, which disagreed with the adjusted fit, it is likely that since no

drastic changes have been made, the parameters can be properly updated to include the new information.

It is also worth remarking that using multiple level density models in this work is not a qualification or statement that one model more accurately reflects physical behaviour. Instead, we can only conclude that multiple level density models, and nuclide-specific changes, were simply scalings needed to best match the available experimental data, which has been seen in other work as well [207, 208]. There is likely no clear physical insight about the models that can be taken from these fits alone.

Perhaps some of the need for scaling is due to inconsistent or lacking discrete level data that feeds into the level density models. The residual products of interest generally exist off the line of stability and resonance parameters are unknown [208–210]. In ^{70}As and ^{72}As, only 68 and 65 experimental discrete levels, respectively, as stored in the RIPL-3 database, inform the level density calculations [47]. This is compared to isotopes such as ^{71,73,75}As where over 120 experimental levels each are used.
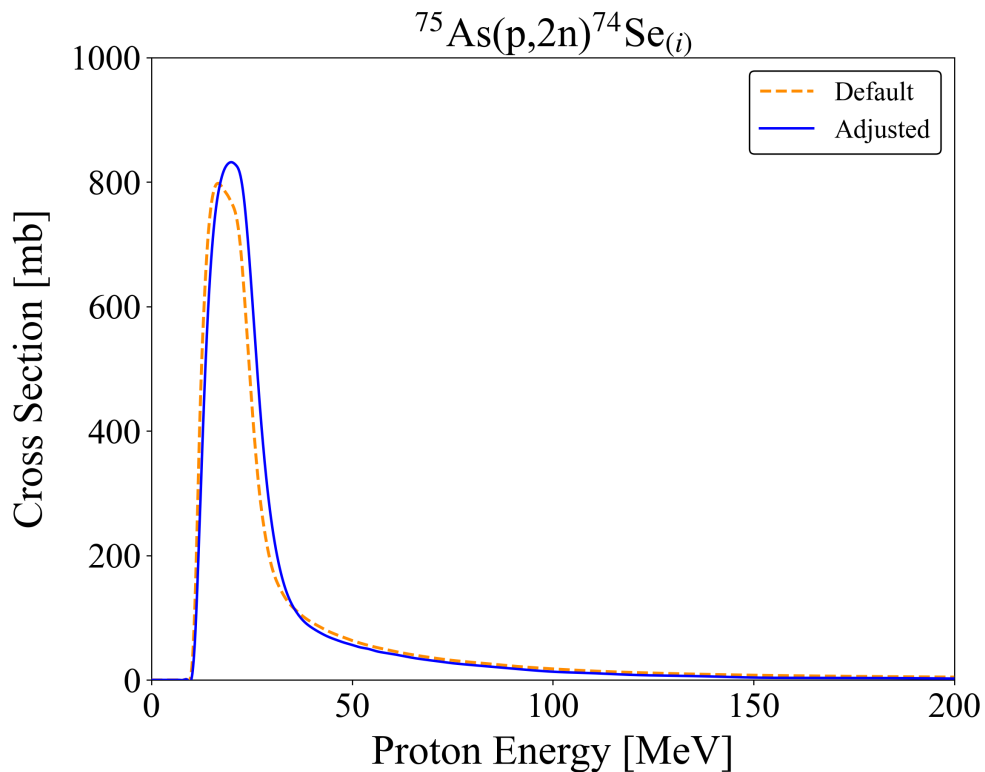
Figure 3.14: Performance check for behaviour of the adjusted fit in ^{74}Se, the largest unobserved channel from the fitting procedure.

A similar pattern exists for ^{72}Se where only 52 experimental discrete levels inform calculations as compared to much more well known $^{73-76}$Se isotopes. If there are missing

levels relatively low in the level scheme, then the level density model may be adjusted to the wrong number of assumed complete levels. This lack of data exists for ^{66,67}Ge and ^{66,68}Ga within their respective isotope chains as well. Ultimately, it is conceivable that incomplete structure data leads to numerous compensating level density effects in this mass region, which may themselves be a key contributor to the adjusted scalings as opposed to any inherent issues with the models [208–210].

It is also possible that a disregard of isospin effects in the current TALYS calculations, missing collective enhancement effects for nuclei far from stability, or deterioration of the microscopic level density models altogether at the high excitation energies relevant to this work, have prompted the need for the corrective scalings [113, 210]. A future experiment examining $\alpha+^{72}$Ge, which populates the same ^{76}Se compound system as p+^{75}As but with different isospin, could provide some additional information.

The overall viability of the level density adjustments in this modeling work in combination with the other modeling parameter changes are further justified in Section 3.5.3.

3.5.3 Parameter Adjustment Validation

As proposed in Fox et al. [34], validation for the suggested parameter changes can be performed by applying the adjusted fit to reaction channels not included in the initial adjustment sensitivity studies in Section 3.5.2. In this work, the validation channels ^{75}As(p,x)^{72,70}As, ^{68,66}Ge, ^{72,66}Ga, ^{69m,65}Zn, ^{60,58,57,56}Co and help test for cumulative cross section effects and far-from-target modeling stability. Figure 3.15 demonstrates the adjusted fit behaviour in these validation channels, where consistently improved predictive power is seen.

It is also possible to further analyze the total non-elastic cross section predictions of the default and adjusted TALYS models, together with the TENDL evaluation (Figure 3.16). No experimental data points guide the ^{75}As(p,non) predictions, commensurate with the little prior published data for the residual product excitation functions as a whole. Even with the new data results of this paper, due to the unseen reaction products described in Section 3.5.2.1, it is not viable to derive any ^{75}As(p,non) data points from summing the measured cross sections. The adjusted (p,non) remains within the TENDL uncertainty band and its increase versus the default is defensible. Specifically, the adjusted (p,non) shares the same shape as the TENDL evaluation and the default prediction, which are based on global fits to other targets, and the increase in magnitude is validated based on changes seen in residual product channels such as ^{73}As in Figure 3.12d.

(a)　　　　　　　　　　　　　　　　　(b)
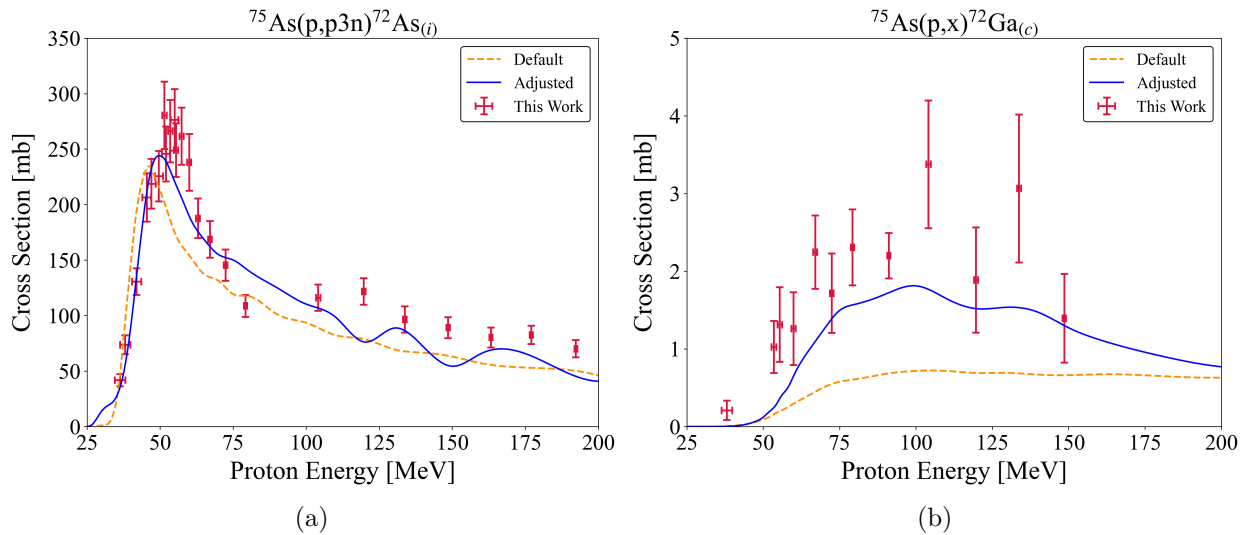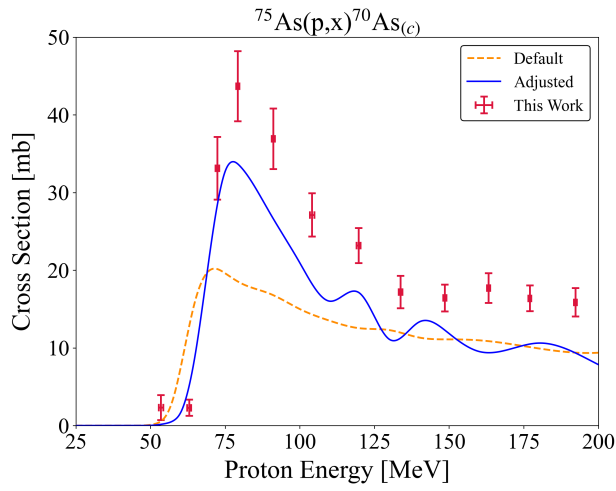
(c)
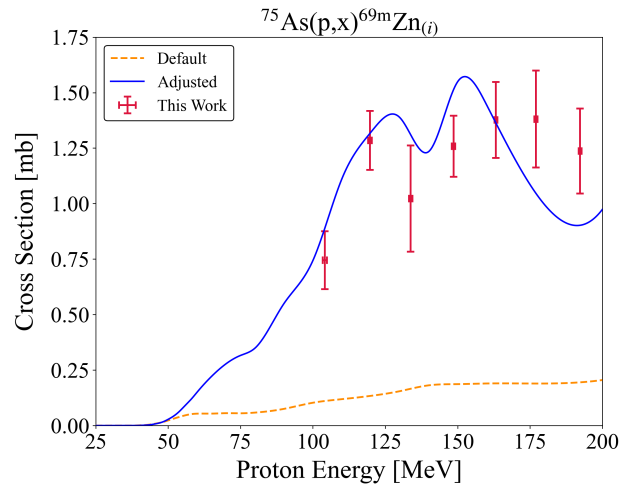
(d)
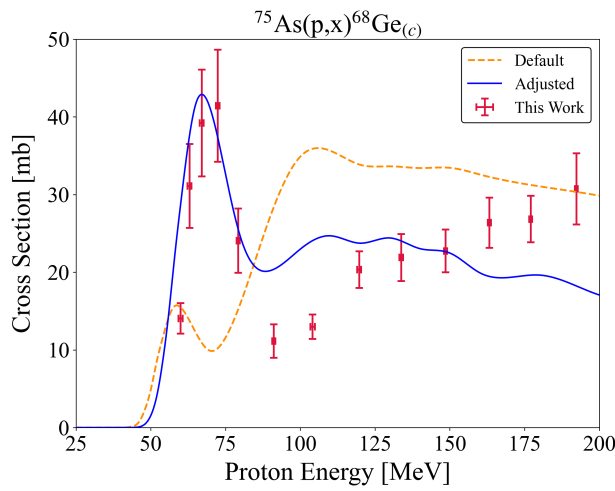
(e)
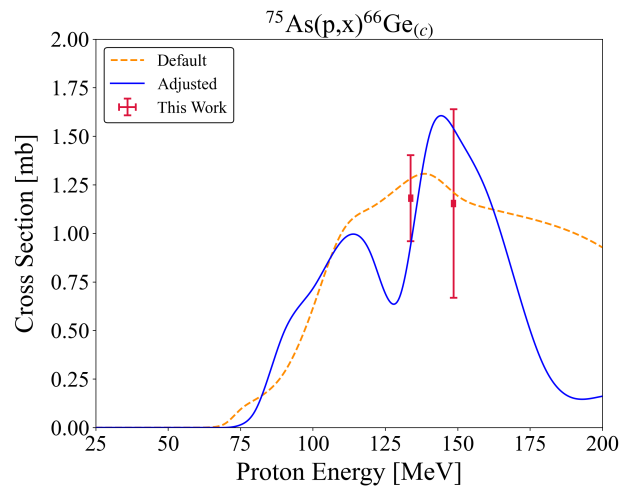
(f)
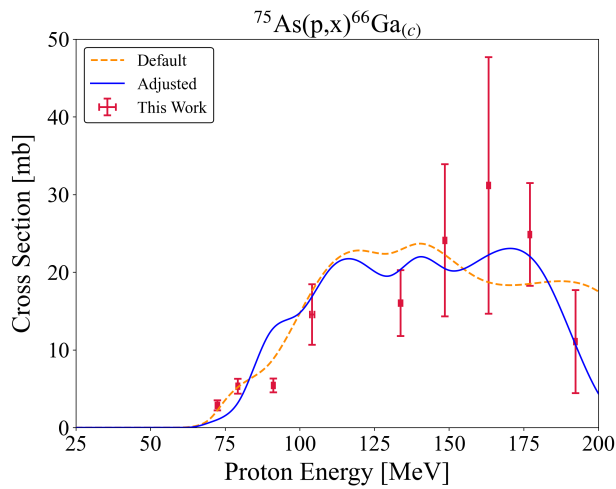
(g)
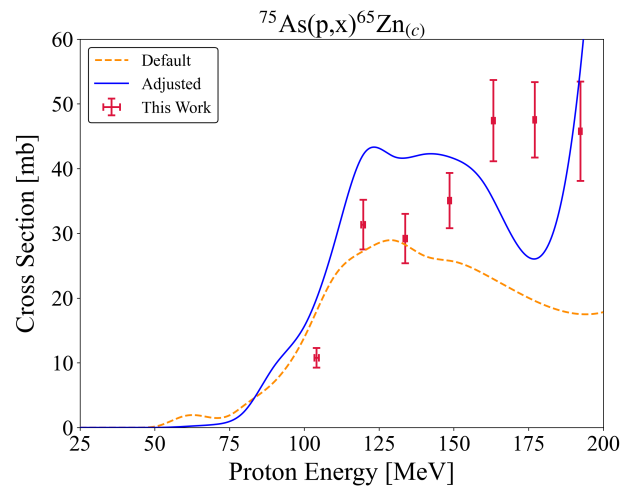
(h)
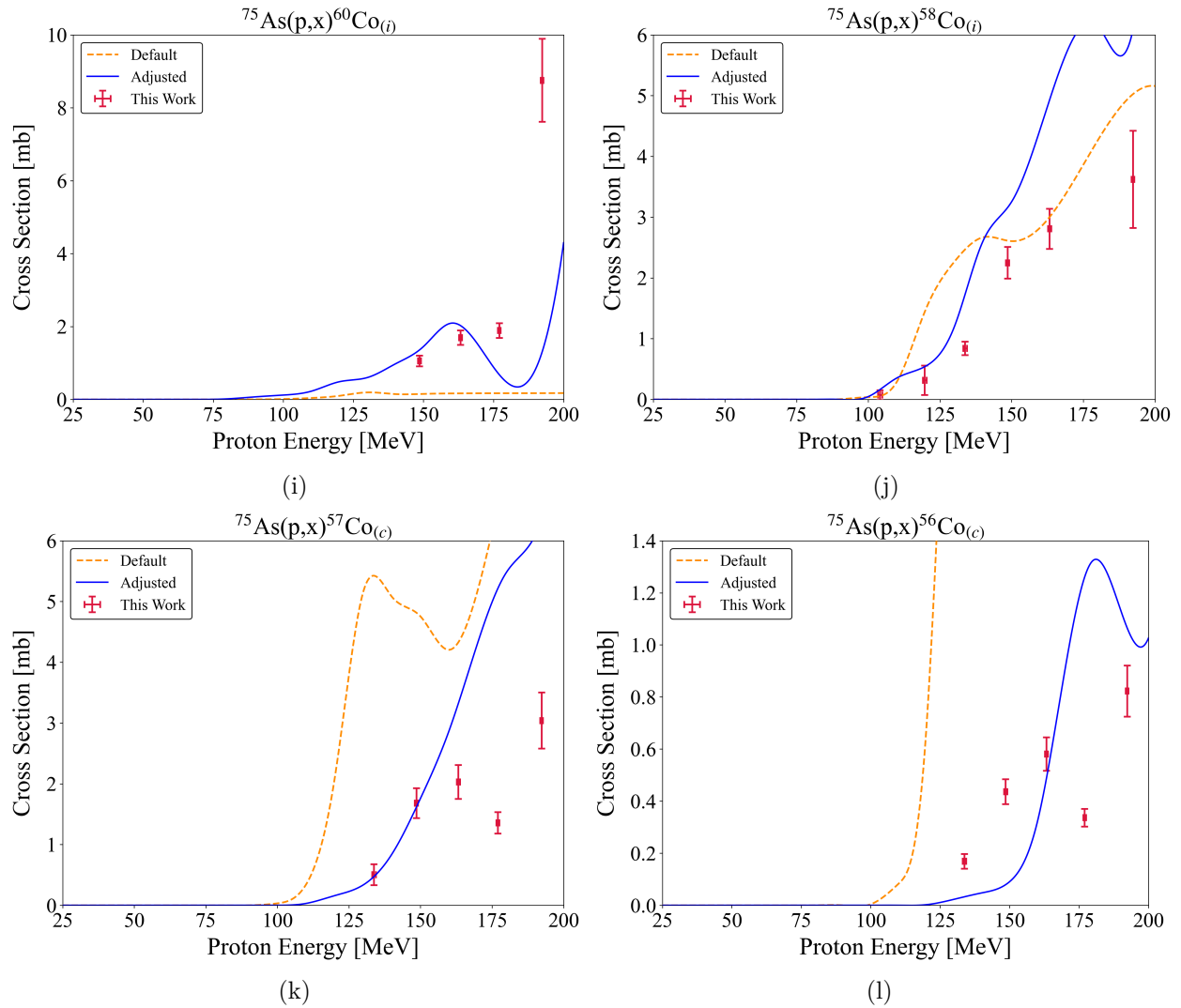
Figure 3.15: TALYS default and adjusted calculations extended to residual products not used in the parameter adjustment sensitivity studies.

A χ^2_{tot} descriptive metric for comparing the default and adjusted TALYS fits across all presented excitation functions, following the formalism described in Fox et al. [34], is given in Table 3.6. Both weighting methodologies yield similar results and the adjusted fit is seen to outperform the default prediction. The χ^2_{tot} values are partially deflated relative to the ^{93}Nb(p,x) and ^{139}La(p,x) results in Fox et al. [34] on account of the heavy dependence on the arsenic cross section measurements provided in this work and their associated larger uncertainties (9.0–15%) stemming from the electroplating process. Consequently, the χ^2_{tot} results are more usefully viewed as a relative measure between fits rather than as absolute

measure of goodness.

Table 3.6: Global χ^2 metric describing goodness-of-fit for the default and adjusted TALYS calculations of ^{75}As(p,x). Low χ^2_{tot} values, and a case of $\chi^2_{tot} < 1.0$, are seen as a function of large weights associated with the measured arsenic data.

Weighting Method	Default χ^2_{tot}	Adjusted χ^2_{tot}
Cumulative σ	2.55	0.58
Maximum σ	3.58	1.25

3.5.4   Alternative Solutions and Limitations of the Fitting Procedure

The `M2constant`=0.80, `M2limit`=3.9, and `M2shift`=0.55 exciton model adjustments suggested in this paper match the trend of `M2constant`<1.0, `M2limit`>1.0, and `M2shift`<1.0 changes from the ^{93}Nb(p,x) and ^{139}La(p,x) fitting cases in Fox et al. [34]. As a result, the same systematic behaviour of a decrease for internal transition rates at intermediate proton energies ($E_p = 20 - 60$ MeV) in the exciton model as derived from the Nb and La cases is seen in the As as well.

However, due to the mathematical formulation of the exciton model in TALYS, which can be reviewed in detail in Koning and Duijvestijn [27], it has been found that in fact `M2constant`<1.0, `M2limit`>1.0, and `M2shift`<1.0 is not a required condition to generate the systematic behaviour. Instead, numerous sets of (`M2constant`,`M2limit`,`M2shift`) will reproduce the same decrease for internal transition rates and replicate the residual product cross section predictions of Section 3.5.2. For example, both (2.45, 0.7, 1.2) and (1.1, 2.85, 0.7) satisfy these conditions for the ^{75}As(p,x) fitting. Thus, the transition rate trend result from Fox et al. [34] is corroborated in this work but the `M2` adjustment requirements to create this trend are revised. Moreover, since multiple triplets all predict the expected systematic behaviour for the reaction phase space transitioning between the Hauser-Feshbach and exciton models for nuclear reactions, it is not possible to conclude which triplet is more accurate without more diversified datasets such as particle emission spectra or prompt gamma yields by ^{75}As(p,xγ) [207].

Indeed, this lack of diversified datasets is the overall limiting factor of the fitting procedure in its current state. The TALYS parameter space is extremely large and the effects of many parameters are hidden from high-energy residual product modeling. Furthermore, the secondary effects from pre-equilibrium, optical model, level density, and coupled-channels changes that are made cannot be deduced without other data types, which detracts from physical insights that can be made about the modeling physics in this work [211]. Prompt

gamma data or emission spectra could act to concretely identify certain parameters as well as greatly reduce the remaining parameter space, all creating a more suitable and physical fit solution. Of course, these additional data types would themselves only be able to inform small portions of the incident energy range explored through stacked-target activation and would not be as useful without the abundance of residual product data. Clearly, continued high-energy reaction measurements of all types are needed and complementary.
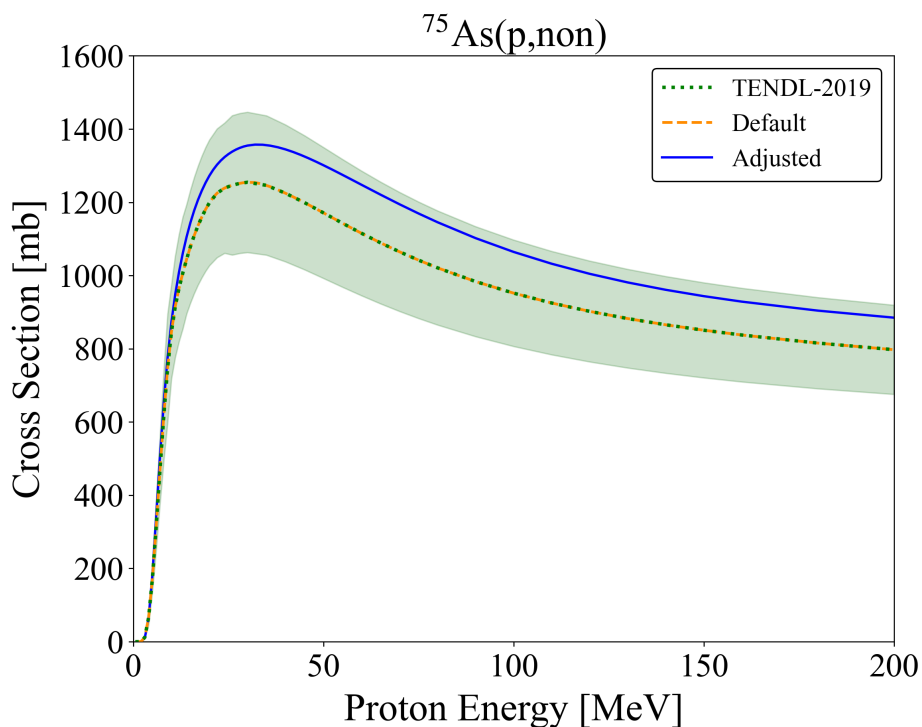
Figure 3.16: Comparison of evaluated and theoretical non-elastic cross sections. The filled error bands are associated with the TENDL data.

The size of the parameter space is a further limiting element since it leads to local minimum results for the fitting procedure, as was discussed for ^{67}Ga in this work. The implementation of automated searching and/or machine learning could likely mitigate this problem and would be in line with the sentiment of evaluators in the nuclear data community [136, 212].

Overall, these shortcomings emphasize that the thought process of the Fox et al. [34] fitting procedure is most relevant because it principally builds evaluation considerations into nuclear data work. This is an important introductory step for where no formalism or data existed and the evolution of this type of thought process better aligns data work and evaluations as a necessary path forward.

3.6 Conclusions

This work furthers the Tri-laboratory Effort in Nuclear Data by reporting 55 sets of measured ^{75}As(p,x), ^{nat}Cu(p,x), and ^{nat}Ti(p,x) residual product cross sections between 35 and 200 MeV. The measured data most notably include the first cross section results for ^{75}As(p,x)^{68}Ge and the best characterized excitation function of ^{75}As(p,x)^{72}Se to-date, which are important for the production of the ^{68}Ge/^{68}Ga and ^{72}Se/^{72}As PET generator systems.

We have additionally continued to develop the Fox et al. [34] formalism for high-energy reaction modeling using the newly available measured ^{75}As(p,x) data. The modeling study in this paper corroborated the pre-equilibrium exciton model findings presented in Fox et al. [34] surrounding the transition between the compound and pre-equilibrium regions in TALYS. Furthermore, as part of this study, we provided an in-depth discussion on the limitations to modeling predictive power caused by the lack of level density knowledge for nuclei off of stability.

This paper merges experimental work and evaluation techniques for high-energy charged-particle isotope production in an initial analysis of this kind. The consideration of these different aspects of the nuclear data pipeline together is a priority moving forwards that will benefit future data compilation, evaluation, and application.

Data Availability Statement

The γ-ray spectra and all other raw data created during this research are openly available at `http://doi.org/10.5281/zenodo.4648950` [118]. On publication, the experimentally determined cross sections will be uploaded to the EXFOR database.

3.7 Proton Current Variance Minimization

The applied variance minimization technique for the LBNL irradiation is summarized in Figure 3.17. A 4.23% increase to stopping power in simulations, implemented through an equivalent increase to degraders' effective density in the stack, best reduced proton fluence measurement disagreements between different monitor channels in each energy compartment. This is in general agreement with results of past stacked-target work that have shown a needed modest positive enhancement to the stopping power of +2–5% [36, 39, 40].

The associated proton flux spectrum propagating through the stack, after variance minimization, is provided in Figure 3.18. The energy assignments for each foil in a stack are then the flux-averaged energies from the spectrum with uncertainties per foil taken as the full width at half maximum.

This same calculation methodology can be reviewed in detail for the LANL and BNL stacks in Fox et al. [34]
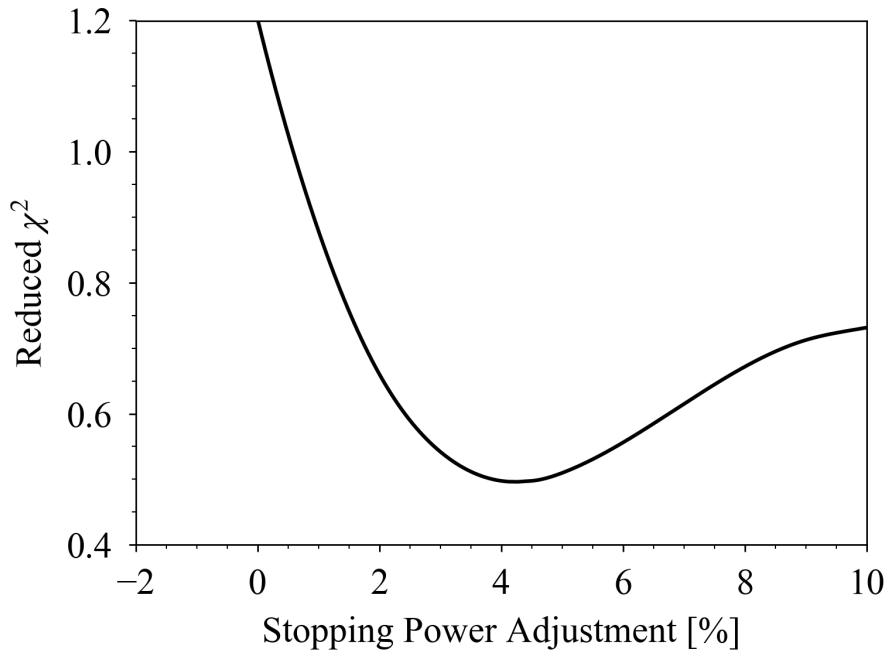
Figure 3.17: Result of χ^2 optimization used in the variance minimization of the global linear fit to the monitor fluence data, indicating a required increase to stopping power in transport simulations.
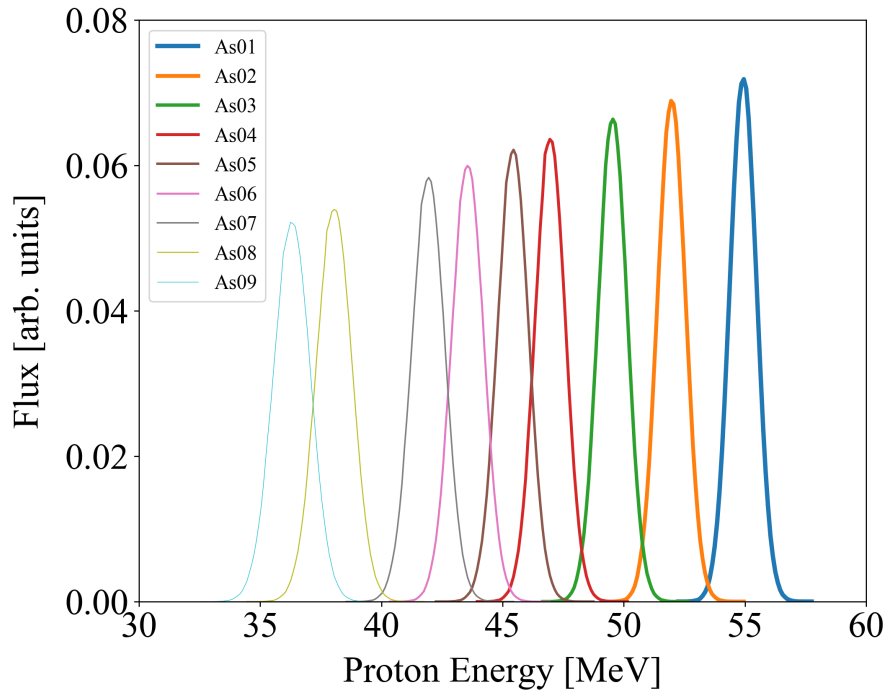
Figure 3.18: Visualization of the calculated proton energy spectrum for each arsenic target in the LBNL stack, following variance minimization.

3.8 Measured Excitation Functions

Plots of extracted cross sections in this work are given (Figures 3.19–3.69) with reference to existing literature data, TENDL-2019, and reaction modeling codes TALYS-1.9, EMPIRE-3.2.3, CoH-3.5.3, and ALICE-20 using default parameters [36, 38–40, 45, 55, 67, 100, 141–177]. Subscripts (i) and (c) in figure titles indicate independent and cumulative cross sections, respectively.
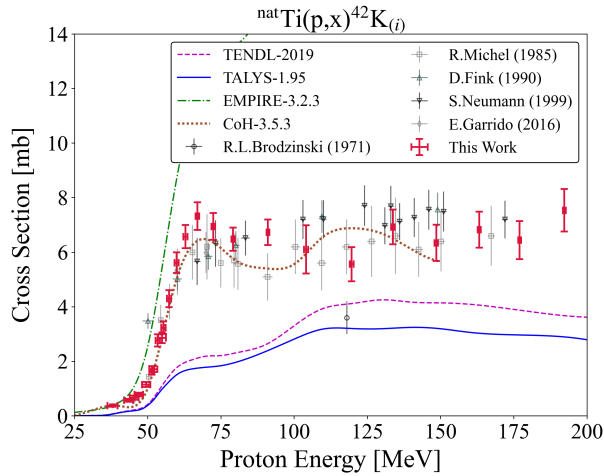
Figure 3.19: Experimental and theoretical cross sections for ^{42}K production.
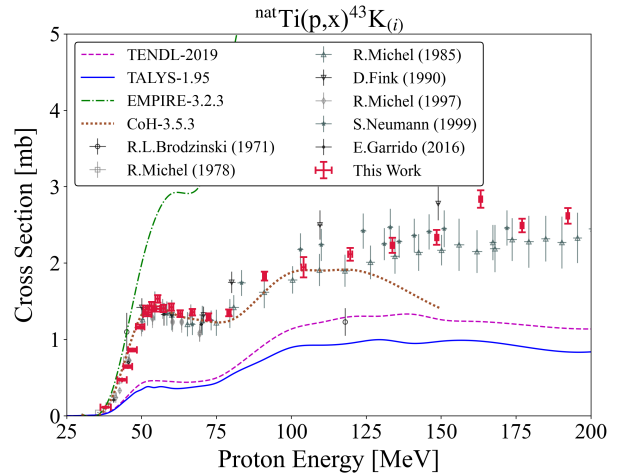
Figure 3.20: Experimental and theoretical cross sections for ^{43}K production.
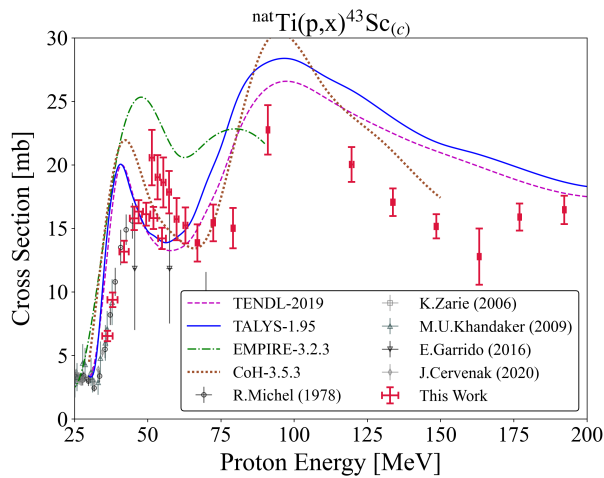
Figure 3.21: Experimental and theoretical cross sections for ^{43}Sc production.
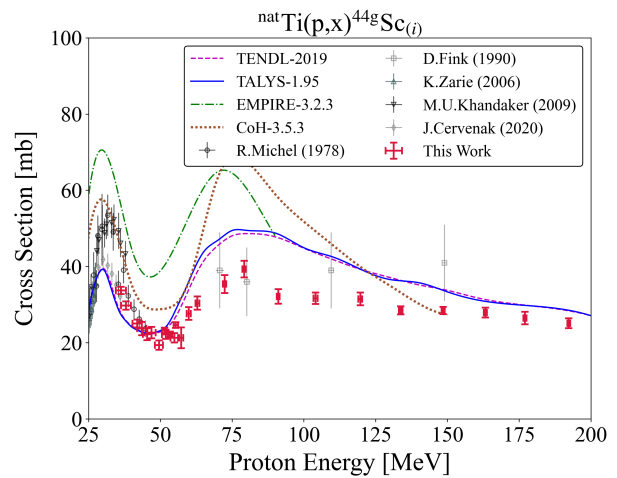
Figure 3.22: Experimental and theoretical cross sections for ^{44g}Sc production.
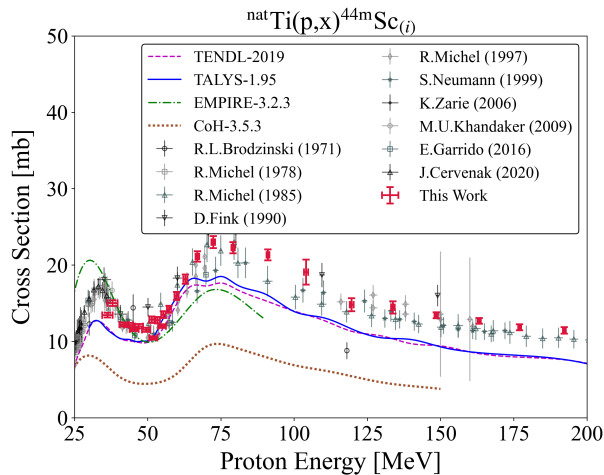
Figure 3.23: Experimental and theoretical cross sections for ^{44m}Sc production.
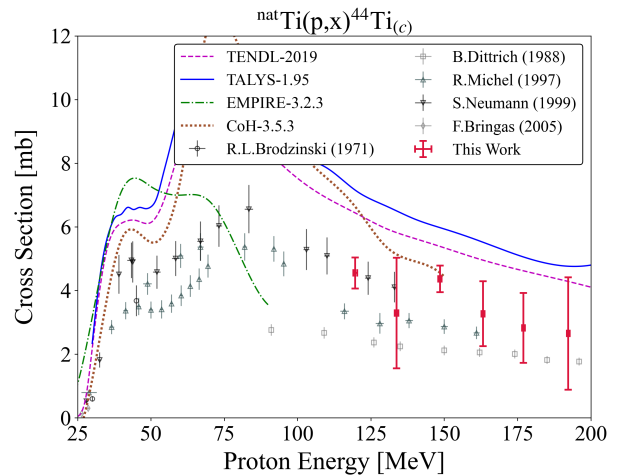
Figure 3.24: Experimental and theoretical cross sections for ^{44}Ti production.
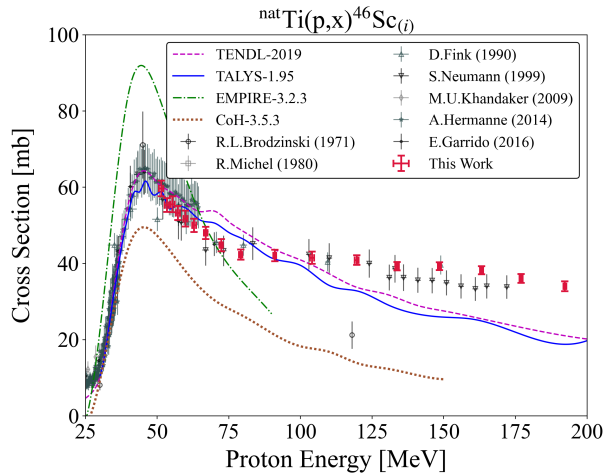
Figure 3.25: Experimental and theoretical cross sections for ^{46}Sc production.
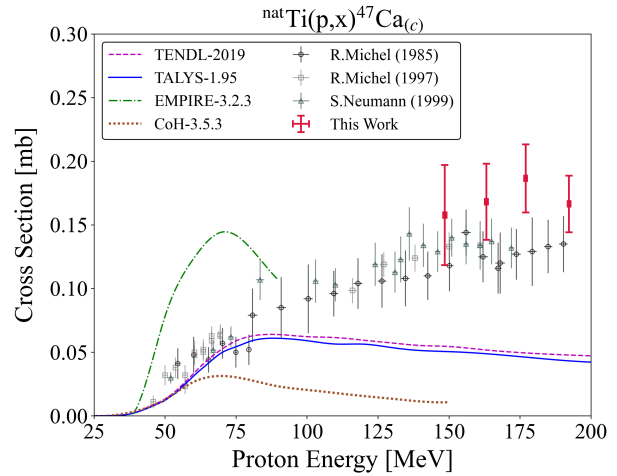
Figure 3.26: Experimental and theoretical cross sections for ^{47}Ca production.
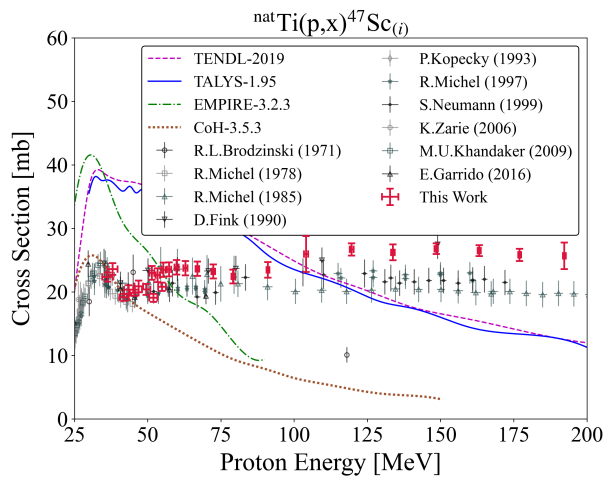
Figure 3.27: Experimental and theoretical cross sections for ^{47}Sc production.
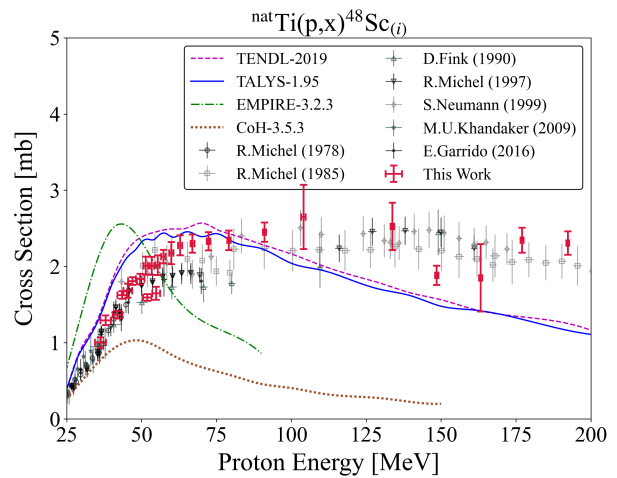
Figure 3.28: Experimental and theoretical cross sections for ^{48}Sc production.
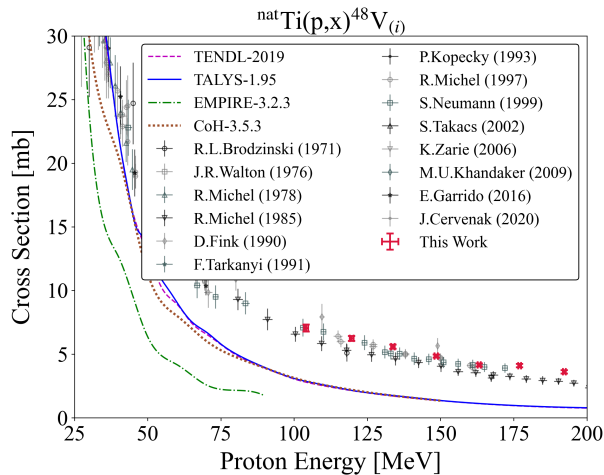
Figure 3.29: Experimental and theoretical cross sections for ^{48}V production.
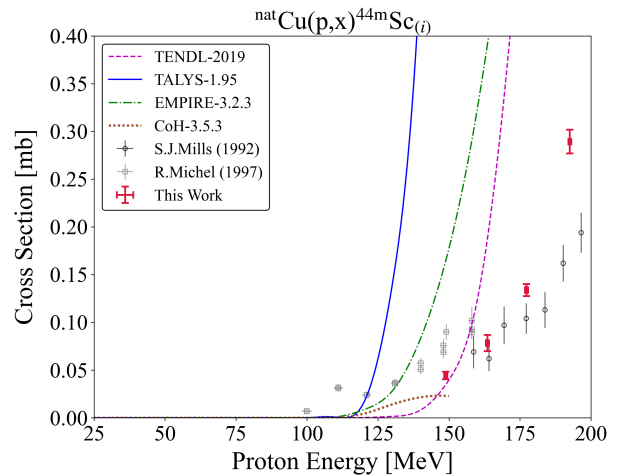
Figure 3.30: Experimental and theoretical cross sections for ^{44m}Sc production.
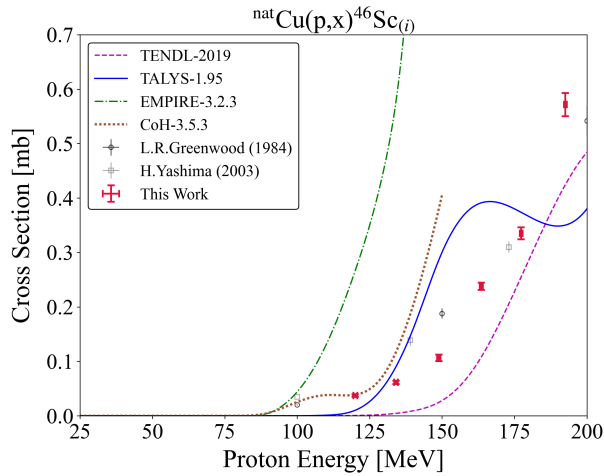
Figure 3.31: Experimental and theoretical cross sections for ^{46}Sc production.
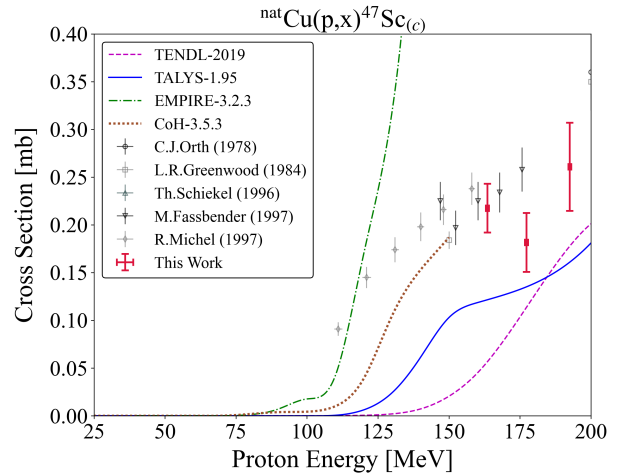
Figure 3.32: Experimental and theoretical cross sections for ^{47}Sc production.
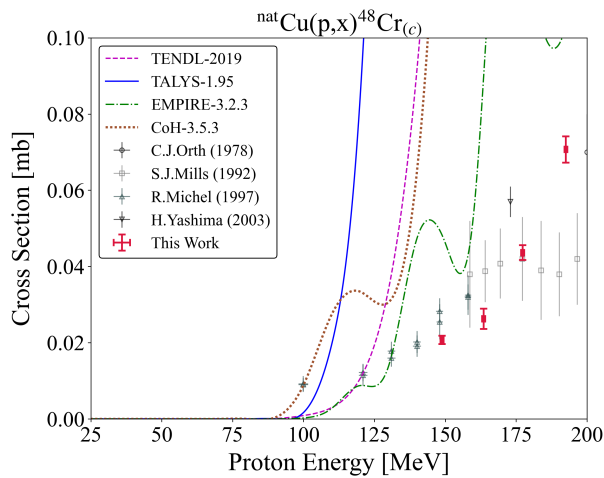
Figure 3.33: Experimental and theoretical cross sections for ^{48}Cr production.
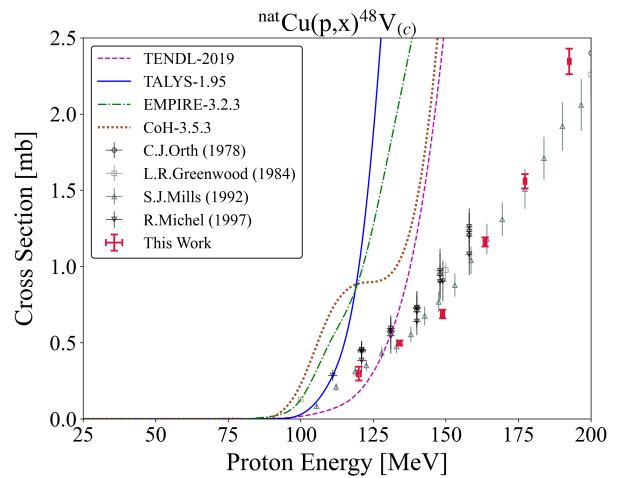
Figure 3.34: Experimental and theoretical cross sections for ^{48}V production.
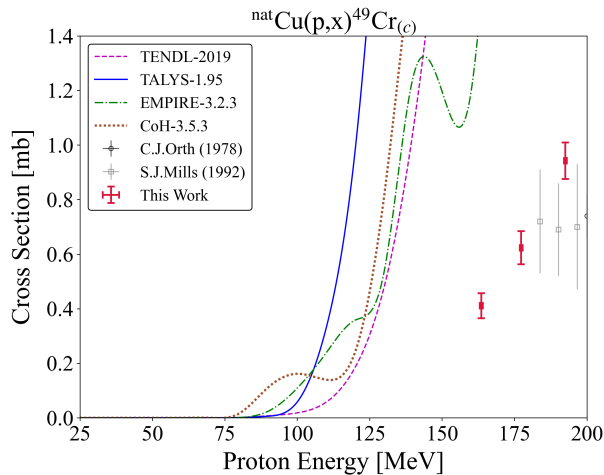
Figure 3.35: Experimental and theoretical cross sections for ^{49}Cr production.
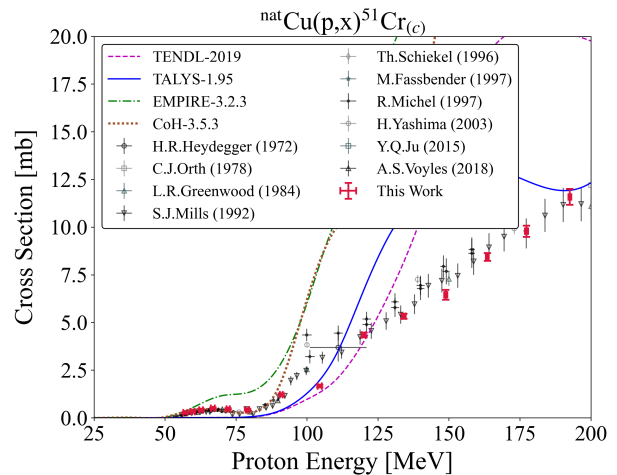
Figure 3.36: Experimental and theoretical cross sections for ^{51}Cr production.
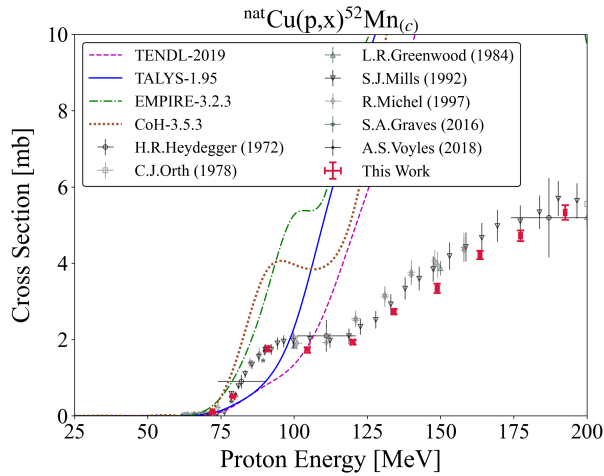
Figure 3.37: Experimental and theoretical cross sections for ^{52}Mn production.
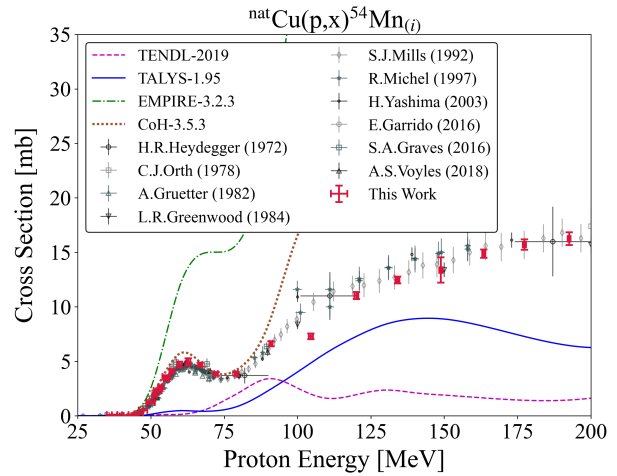
Figure 3.38: Experimental and theoretical cross sections for ^{54}Mn production.
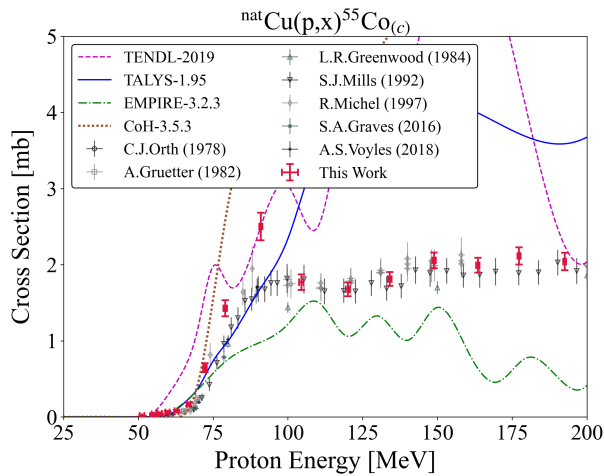
Figure 3.39: Experimental and theoretical cross sections for ^{55}Co production.
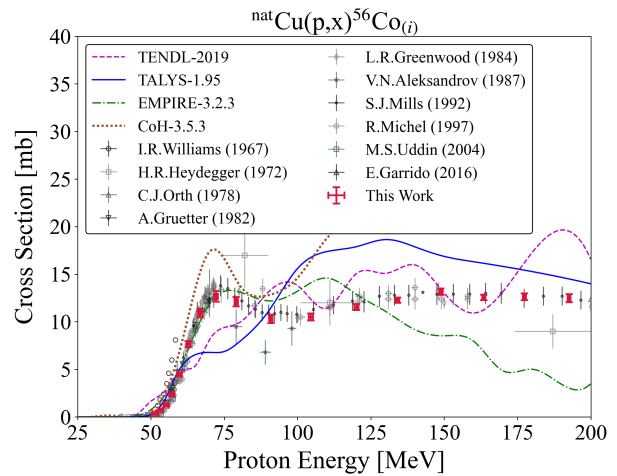
Figure 3.40: Experimental and theoretical cross sections for ^{56}Co production.
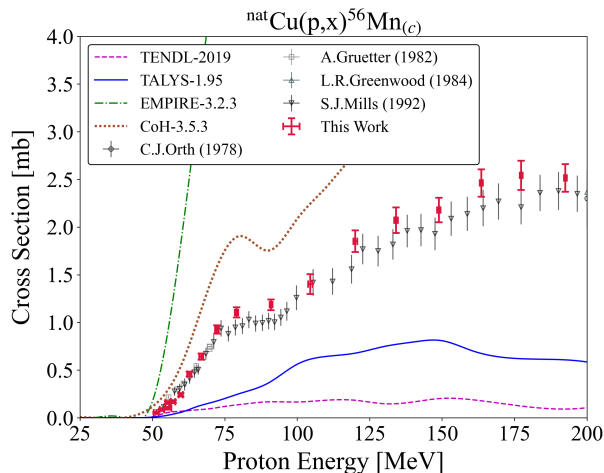
Figure 3.41: Experimental and theoretical cross sections for ^{56}Mn production.
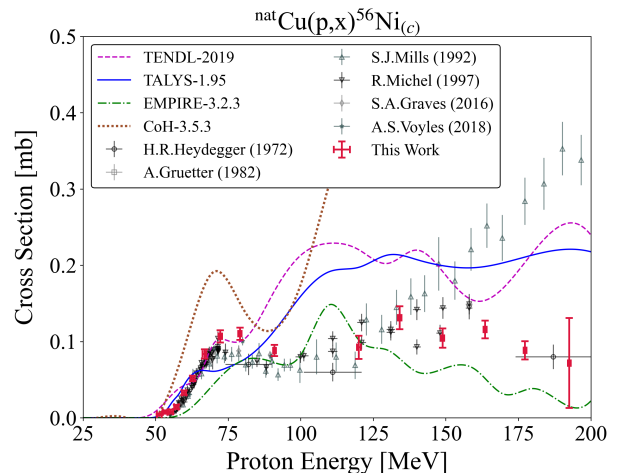
Figure 3.42: Experimental and theoretical cross sections for ^{56}Ni production.
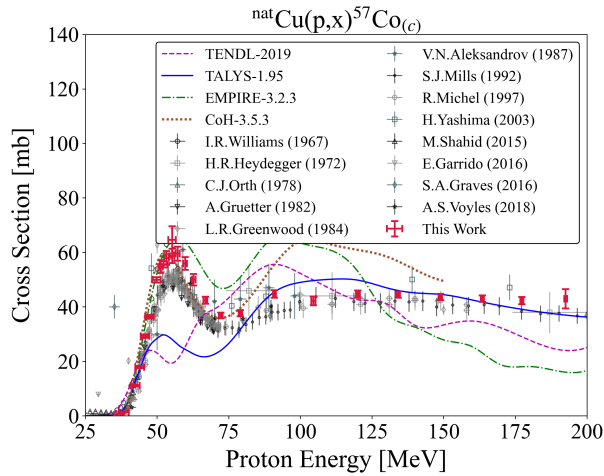
Figure 3.43: Experimental and theoretical cross sections for ^{57}Co production.
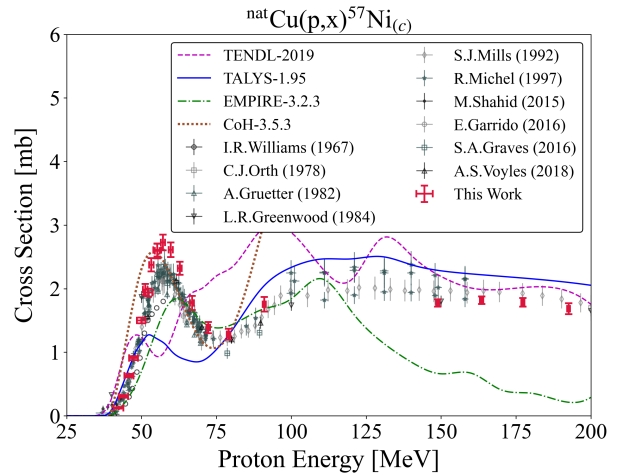
Figure 3.44: Experimental and theoretical cross sections for ^{57}Ni production.
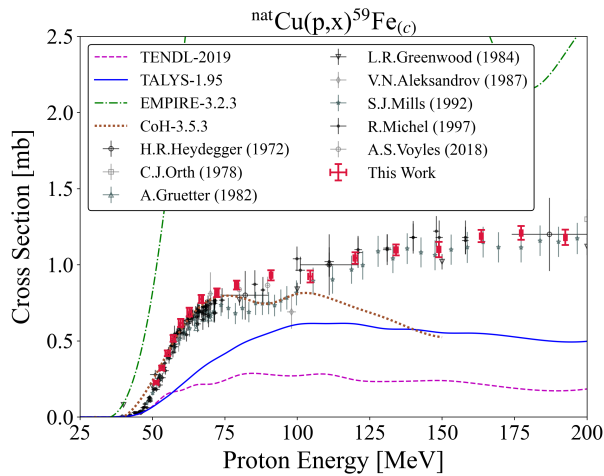
Figure 3.45: Experimental and theoretical cross sections for ^{59}Fe production.
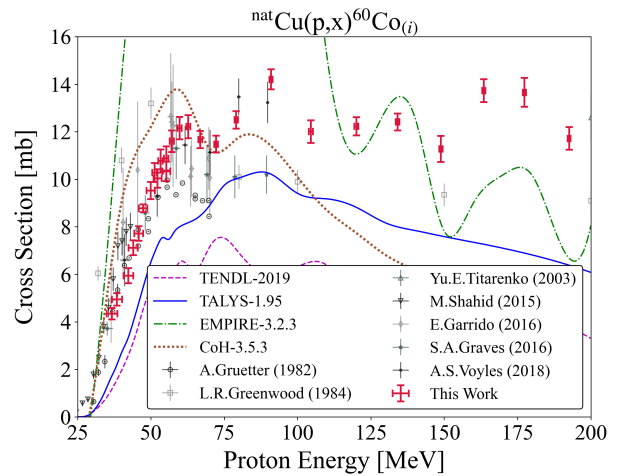
Figure 3.46: Experimental and theoretical cross sections for ^{60}Co production.
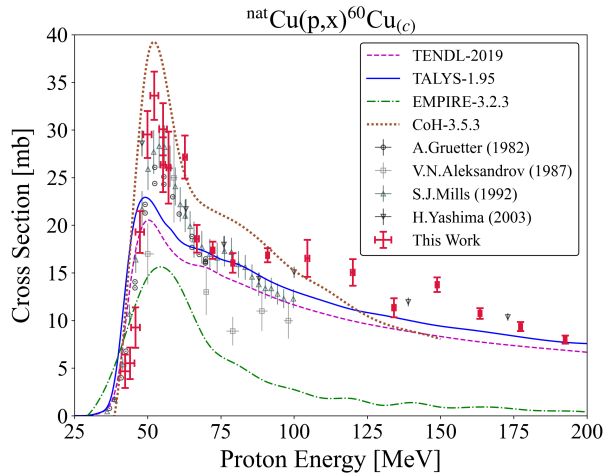
Figure 3.47: Experimental and theoretical cross sections for ^{60}Cu production.
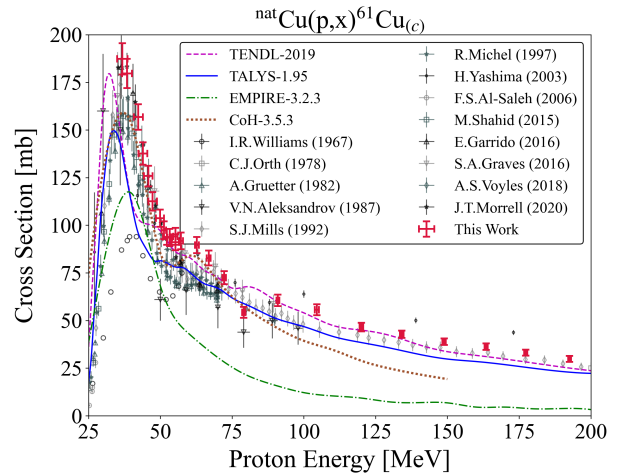
Figure 3.48: Experimental and theoretical cross sections for ^{61}Cu production.
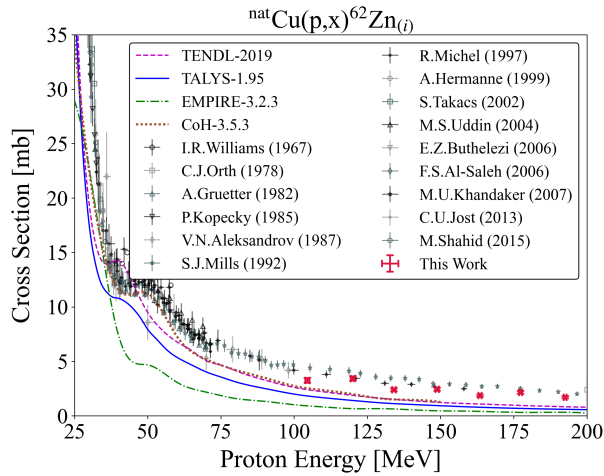
Figure 3.49: Experimental and theoretical cross sections for ^{62}Zn production.
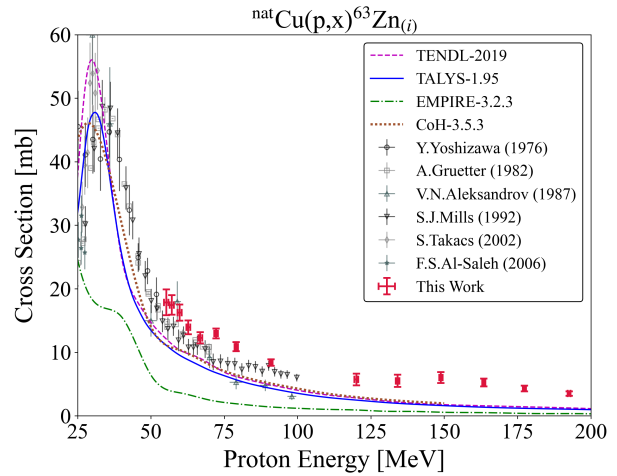
Figure 3.50: Experimental and theoretical cross sections for ^{63}Zn production.
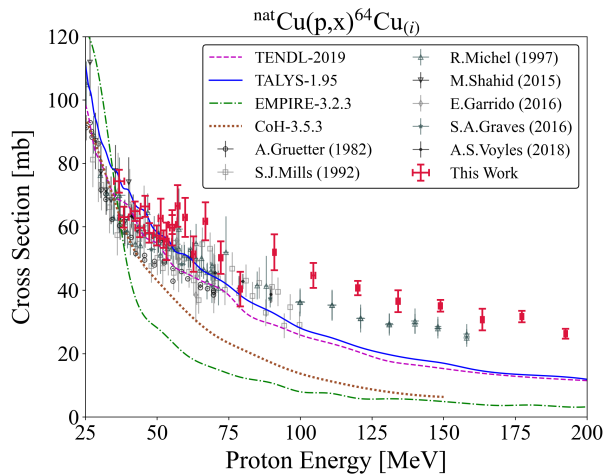
Figure 3.51: Experimental and theoretical cross sections for ^{64}Cu production.
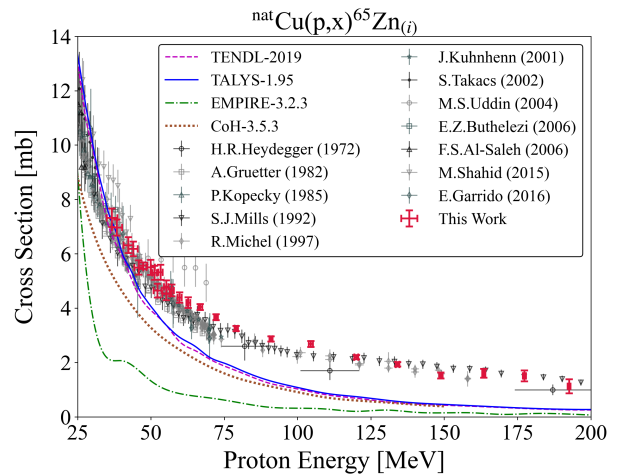
Figure 3.52: Experimental and theoretical cross sections for ^{65}Zn production.
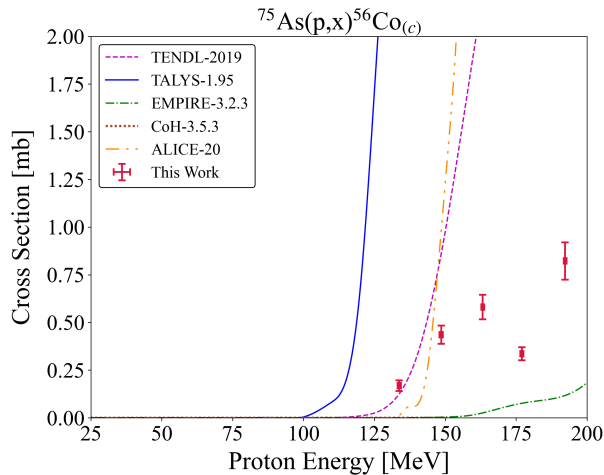
Figure 3.53: Experimental and theoretical cross sections for ^{56}Co production.
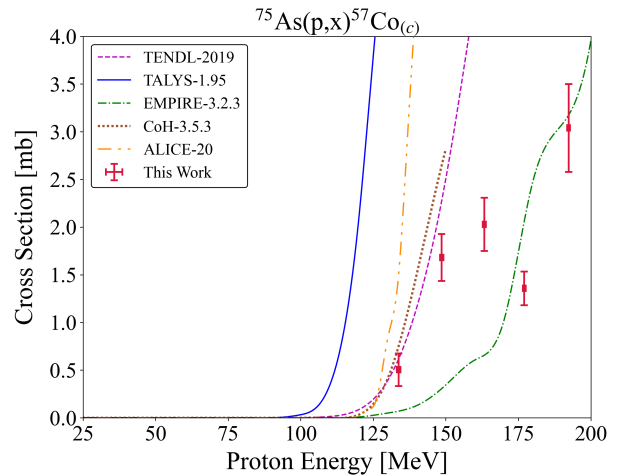
Figure 3.54: Experimental and theoretical cross sections for ^{57}Co production.
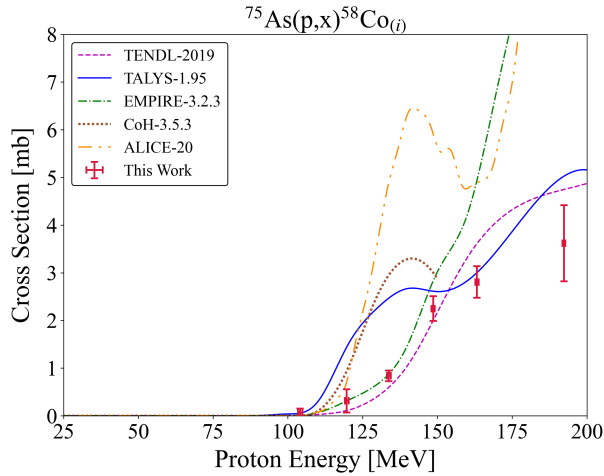
Figure 3.55: Experimental and theoretical cross sections for ^{58}Co production.
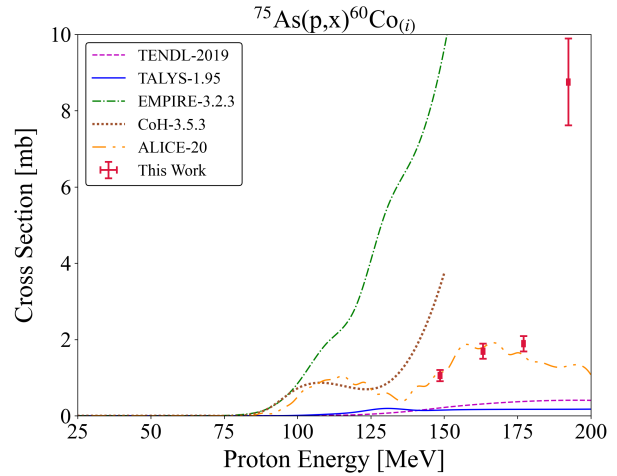
Figure 3.56: Experimental and theoretical cross sections for ^{60}Co production.
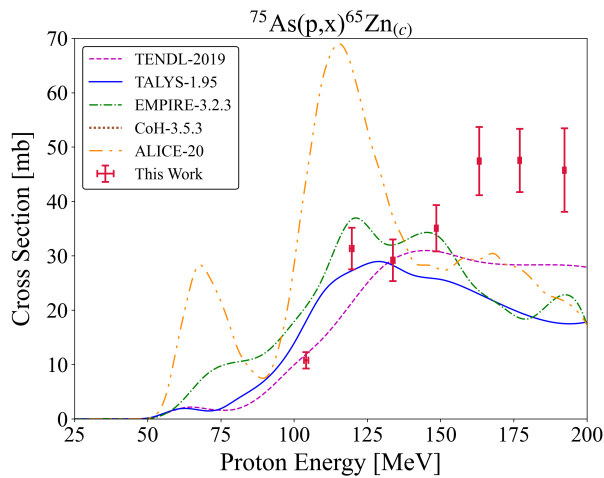
Figure 3.57: Experimental and theoretical cross sections for ^{65}Zn production.
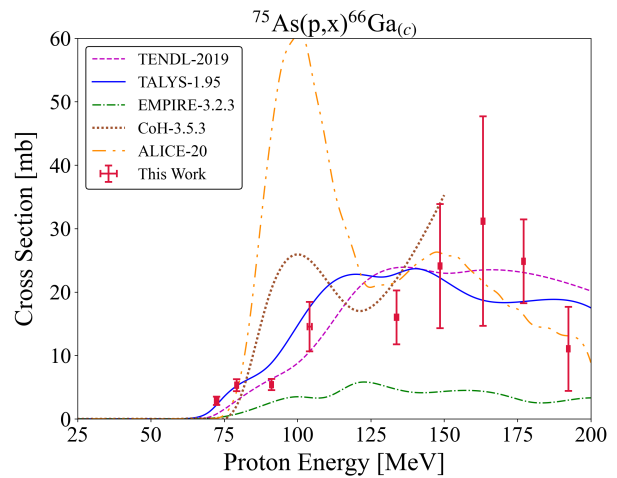
Figure 3.58: Experimental and theoretical cross sections for ^{66}Ga production.
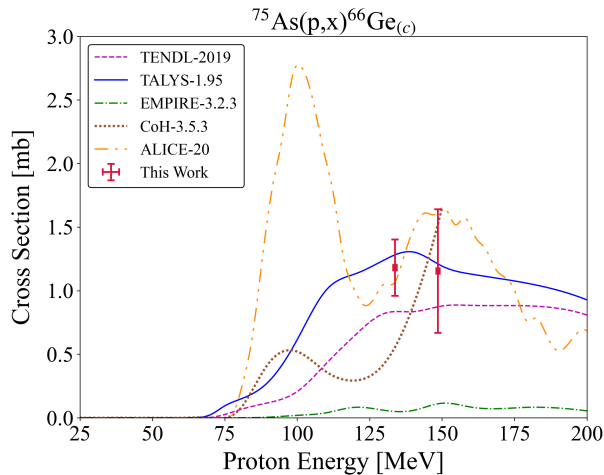
Figure 3.59: Experimental and theoretical cross sections for ^{66}Ge production.
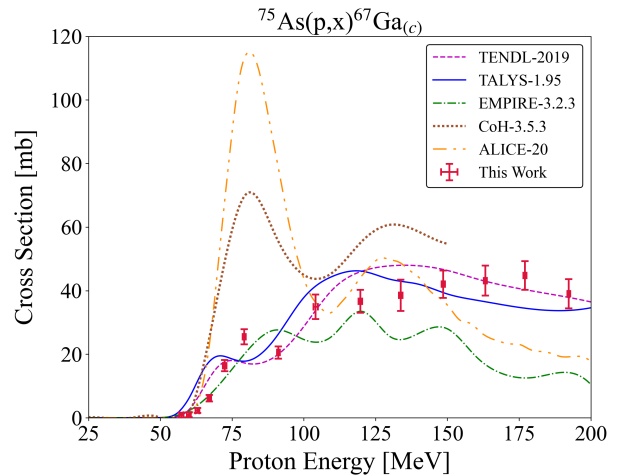
Figure 3.60: Experimental and theoretical cross sections for ^{67}Ga production.
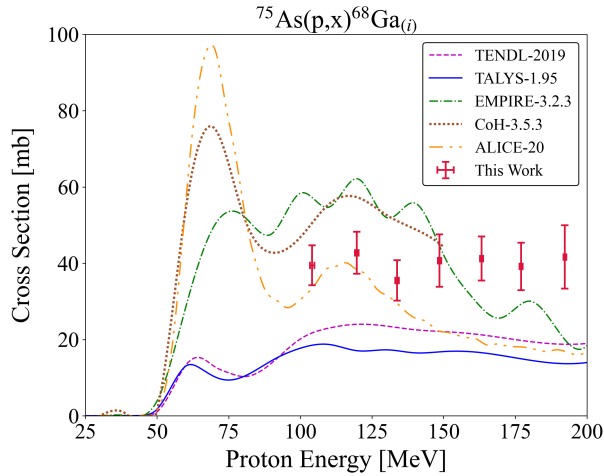
Figure 3.61: Experimental and theoretical cross sections for ^{68}Ga production.
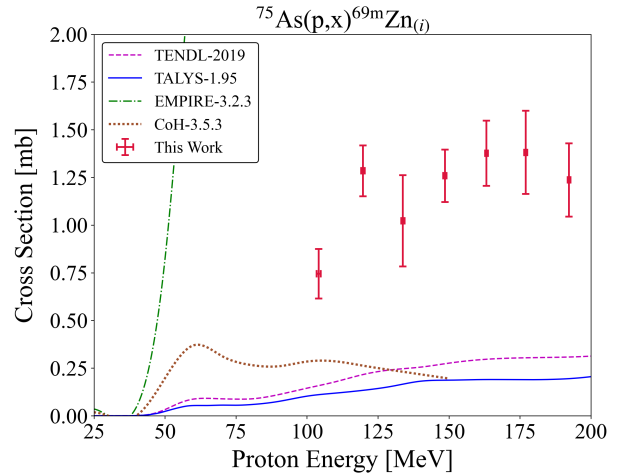
Figure 3.62: Experimental and theoretical cross sections for ^{69m}Zn production.
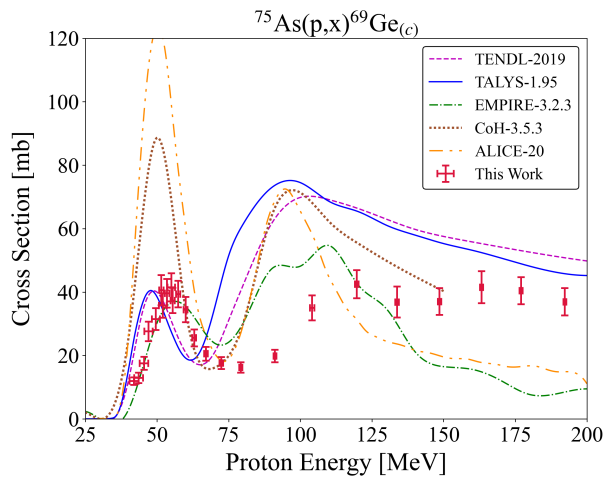
Figure 3.63: Experimental and theoretical cross sections for ^{69}Ge production.
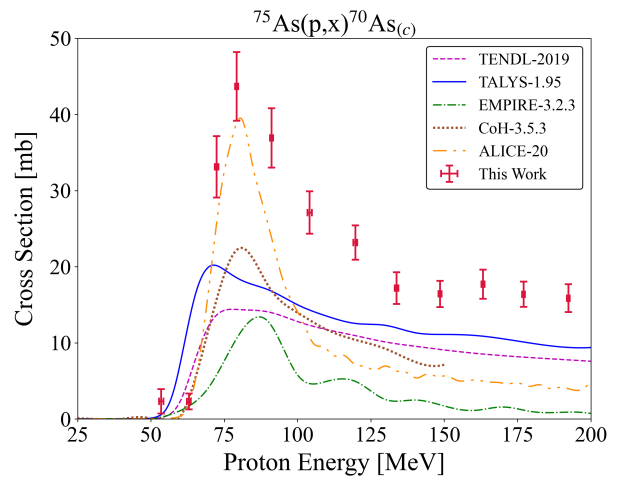
Figure 3.64: Experimental and theoretical cross sections for ^{70}As production.
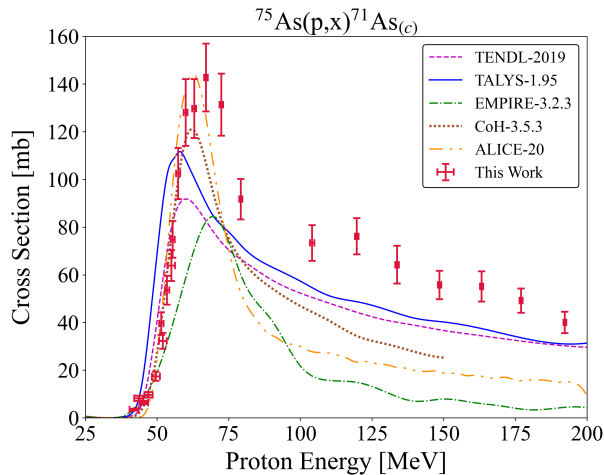
Figure 3.65: Experimental and theoretical cross sections for ^{71}As production.
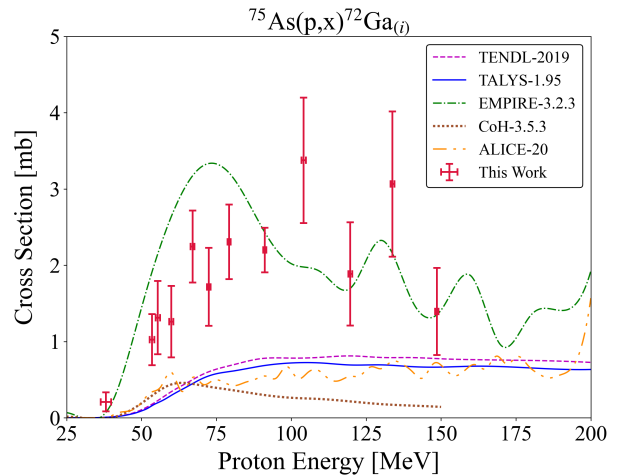
Figure 3.66: Experimental and theoretical cross sections for ^{72}Ga production.
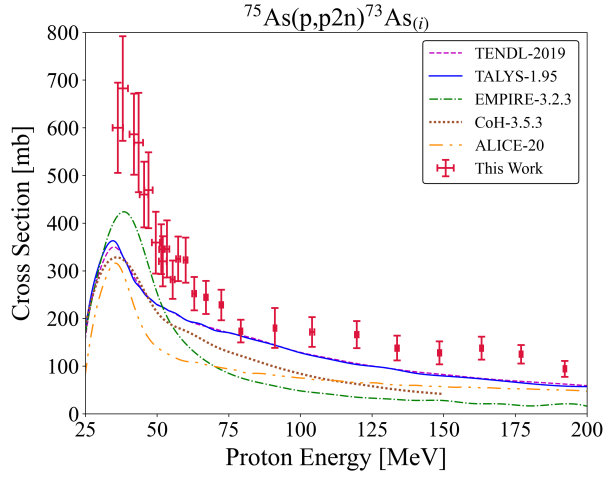
Figure 3.67: Experimental and theoretical cross sections for ^{73}As production.
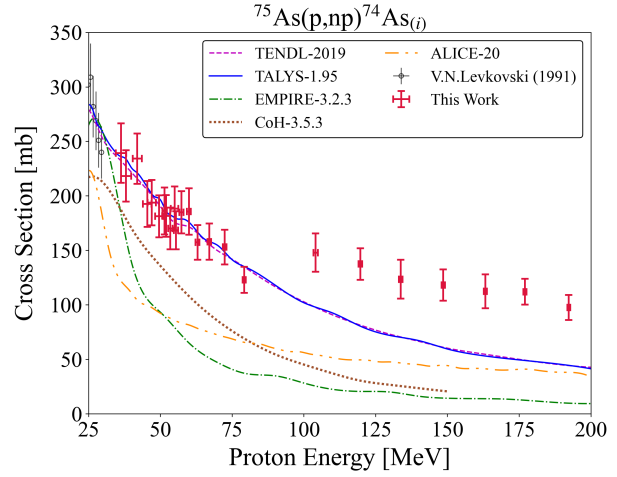
Figure 3.68: Experimental and theoretical cross sections for ^{74}As production.
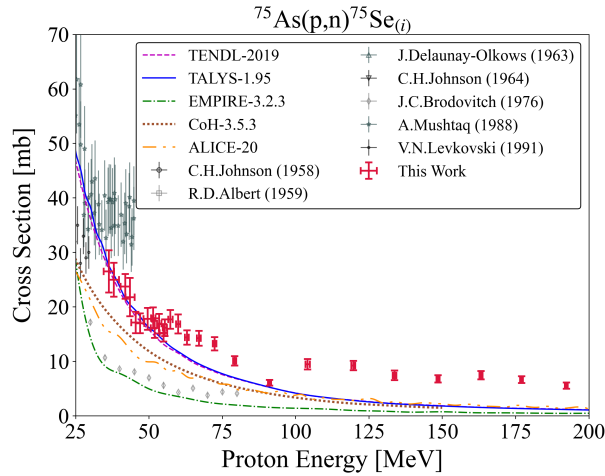
Figure 3.69: Experimental and theoretical cross sections for ^{75}Se production.

3.9 TALYS Parameter Adjustments From Fitting Procedure

The derived parameter adjustments from the fitting procedure applied to the ^{75}As(p,x) data are listed in Table 3.7.

Table 3.7: ^{75}As(p,x) best fit parameter adjustments derived from Fox et al. [34] procedure. The `strength` keyword selects the gamma-ray strength model and has only a small impact in this charged-particle investigation. `strength` 8 performed comparably or slightly better than the other available models in TALYS.

Parameter	Value
ldmodel	6 4 $^{76-72}$Se, ^{68}As 5 ^{69}Ga
strength	8
equidistant	y
M2constant	0.80
M2limit	3.9
M2shift	0.55
Kph	15.16
d1adjust p	1.55
d1adjust n	1.75
w1adjust p	1.21
alphaomp	6
deuteronomp	4
Cstrip	a 0.85 d 2.4 h 0.55 t 0.55
Cknock	a 0.85 d 2.4 h 0.55 t 0.55
ctable	34 73 0.24 33 74 0.3 33 73 0.75 33 71 -0.4 32 69 0.285 31 67 -0.45
ptable	34 73 -0.65 34 72 0.14 33 73 -1.85 32 69 -0.25 31 67 4.5

3.10 A Visual Summary of TREND

A succinct illustration of the nuclear data capability developed from the Tri-lab teaming is shown in Figure 3.70, which demonstrates the great extent of the Chart of Nuclides that was probed in just one year of experiments. In the future, with more specific or differently motivated efforts, the promise for this Tri-lab and other similar experimental campaigns is vast.
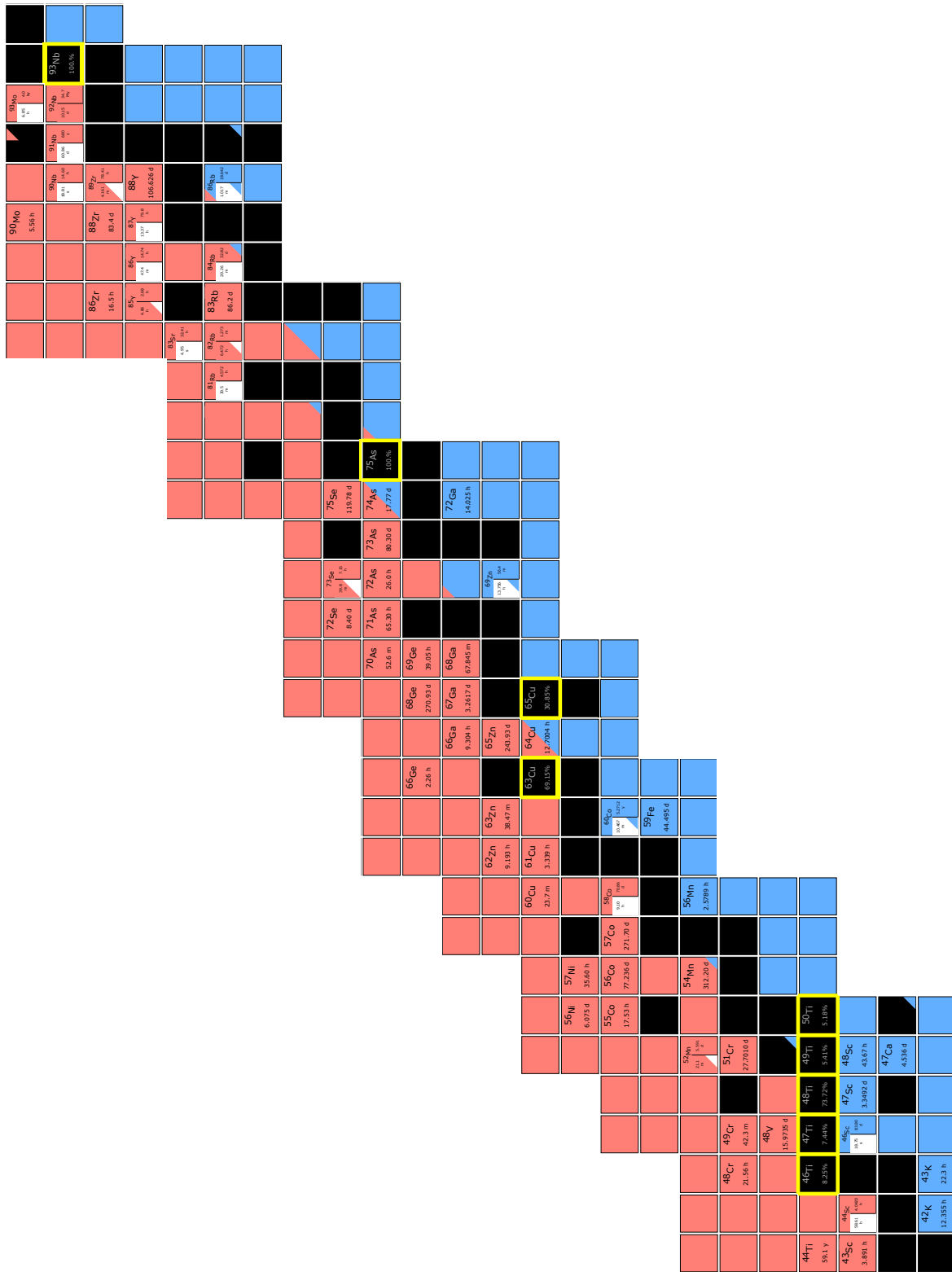
Figure 3.70: Residual products observed in the first year of TREND experiments measuring high-energy proton-induced reactions, overlayed on the Chart of Nuclides. Target nuclei are outlined in the thick yellow boxes.

Chapter 4

Preparation and Characterization of Thin Arsenic Targets for Stacked-Target Experiments

Although target fabrication is a fundamental constraint for many nuclear data experiments, the knowledge base and capabilities for target production and characterization that used to exist throughout the U.S. nuclear physics and chemistry communities have steadily disappeared over the past three decades [212]. The gradual loss of expert personnel, facility closures, and a general failure to maintain passed-down knowledge have contributed to the unfortunate deficiency in this highly-important field.

New specialized measurements require individualized, particular fabrication properties, potentially including unique physical forms and geometry, purity and enrichment minimums, or dissolution capabilities. Nevertheless, the targetry foundation needed to achieve these growing demands have been oft-overlooked. In fact, as experimental data measurement equipment and techniques continue to advance, a lack of information about target fabrication has become a leading source of uncertainty in new measurement campaigns. Targetry work is often not present at each lab and facility, but its critical importance to state-of-the-art experimental investigations and full-scale isotope production demands community-wide action to preserve and improve targetry skills. A sensible path forward involves training new investigators and students in fabrication through dedicated research programs, funding community-collaboration activities for the study of novel production techniques and optimization of existing ones, and developing an inventory of targets and expertise that can serve as a lasting and evolving repository [212].

The TREND measurements of proton-induced reactions on arsenic suffered from these depleted targetry capabilities since minimal established thin-target fabrication routes or

guiding research existed to produce arsenic foils suitable for stacked-target experiments. Furthermore, no dedicated facilities were available to provide external support. As a result, all arsenic target fabrication had to be performed by personnel in the TREND collaboration. This chapter details the trials and laborious process of basic thin-target creation with associated uniformity and quantitative characterization requirements. In this task, we utilized vapor deposition, electrodepositon, scanning electron microscopy, and microanalysis. Most notably, this chapter also introduces a new thin-target characterization methodology, developed using conventional neutron activation tools, that is reliable, convenient, and non-destructive. The work herein is therefore both a contribution to accomplishing the data goals of this thesis and a contribution to the overall targetry needs of the community. It provides techniques valuable to future target creators and adds to a properly archived knowledge base.

4.1   Abstract

Thin uniform arsenic targets suitable for high-fidelity cross section measurements in stacked-target experiments were prepared by electrodeposition of arsenic on titanium backings from aqueous solutions. Electrolytic cells were constructed and capable of arsenic deposits ranging in mass from 1 to 29 mg (0.3–$7.2\,\mathrm{mg/cm^2}$, 0.5–$13\,\mu\mathrm{m}$). Examination of electrodeposit surface morphology by scanning electron microscopy and microanalysis was performed to investigate the uniformity of produced targets. Brief studies of plating growth dynamics and structural properties through cyclic voltammetry were also undertaken. An alternative target fabrication approach by vapor deposition was additionally conducted. We further introduce a non-destructive characterization method for thin targets by neutron activation, which is independent of neutron flux shape, environmental factors, and source geometry, while correcting for any potential scatter or absorption effects.

4.2   Introduction

Thin uniform arsenic (^{75}As) targets were created in support of stacked-target proton-induced isotope production data measurements. The associated measurement campaign of Chapter 3 required arsenic targets of 10-50 μm thickness at a 25 mm diameter to extract high-fidelity production cross sections. Moreover, target material in a stack must balance having enough mass to garner appropriate production during irradiation versus the energy loss and straggle of a beam propagating through thicker targets. Target uniformity is also required since the incident beam through a multi-component stack underfills the target material.

Typically, in experimental cases like Chapter 3, targets of interest meeting these requirements can be sourced from commercial facilities. However, arsenic is resistant to many common thin target fabrication techniques, as has been intensively explored in the semiconductor industry [213, 214]. Arsenic sublimes on heating and cannot be casted, nor can it be subjected to cold/hot rolling due to its brittle nature and propensity for significant cracking [215–217]. Arsenic toxicity further hinders work with bulk quantities as it is very difficult to remediate contamination. As a result, commercial sources only offer unsuitable thick targets (5-20+ mm thickness) or non-uniform bulk "lumps" [218, 219].

Instead, the few prior arsenic-based charged-particle nuclear data investigations have required individualized local target fabrication methods [100, 215, 220–227]. Many of these methods detailed in the literature involve arsenic compounds or metallic powder suspensions in solutions, still generally unsuitable for stacked-target experiments. Specifically, arsenic targets of these forms suffer from amp hour limitations in beam, geometries not conducive for arrangement or beam transport in stacks, or require dissolution for post-irradiation analysis that introduces contaminants, mass loss, and precision errors. Only a select number of the past arsenic reaction data campaigns required pure arsenic thin foils with the same desired qualities of this present work. These choice studies found fabrication success using vacuum evaporation and electroplating [141, 217, 226, 227], though with varying setups and materials.

In turn, we used this foundation and developed fabrication techniques of vapor deposition and electrodeposition to meet our new stacked-target needs. We further performed detailed characterization of the created targets using scanning electron microscopy, particle transmission experiments, and neutron activation analysis. In total, 26 uniform arsenic targets ranging in mass from 1 to 29 mg (0.3–$7.2\,\mathrm{mg/cm^2}$, 0.5–$13\,\mathrm{\mu m}$) were suitably prepared for stacked-target experiments.

4.3 Experimental Arsenic Target Fabrication

4.3.1 Vapor Deposition

The vapor deposition of arsenic was performed at Oak Ridge National Laboratory (ORNL) using arsenic powder source material, purified of As_2O_3 contamination by heating to the compound's evaporation temperature.

For each vapor deposit, approximately $1\,\mathrm{g}$ of arsenic was placed in the bottom of a $24\,\mathrm{mm}$ inside diameter soda lime glass closed bottom vial of $2\,\mathrm{cm}$ length. Source mass of $1\,\mathrm{g}$ represents excess arsenic per desired target but was found to give more uniform deposition coverage with similar experiment times and final deposit mass.

The deposits in this work were prepared on $25\,\mathrm{\mu m}$ thick Kapton film backings, which is a

typical material used for sealing targets in stacked-target activations [34, 36, 40, 41]. Free-standing targets were initially explored but suffered from cracking issues during separations from the substrate. Kapton backings of at least 2.54 cm side length were cut, massed, and fixed to a glass microscope slide (5.08×7.62 cm) by static. The microscope slide was then placed over the top of the vial opening and source mass, as pictured in Figure 4.1, and held in position by gravity. The source and vial apparatus was placed on a resistive wire heating coil made from 7 passes of 24-gauge Kanthal KA1 alloy wire running through a 4 mm thick HBN grade boron nitride insulator, capable of delivering approximately 105 W.

A 12×22 cm Pyrex bell jar cover vacuum chamber was constructed to enclose the equipment and the total deposition system is shown in Figure 4.2. Key components of the vacuum chamber were the Corian baseplate, Welch DryFast Diaphragm Pump 2034 capable of 9 torr ultimate pressure with 25 L/min free air displacement, a Nupro valve, and a 30″ Hg/15 psi Bordon gauge. These were dedicated equipment for the deposition since the relatively low vapor pressure and toxicity of arsenic prohibits use in all instruments that are used for other materials.
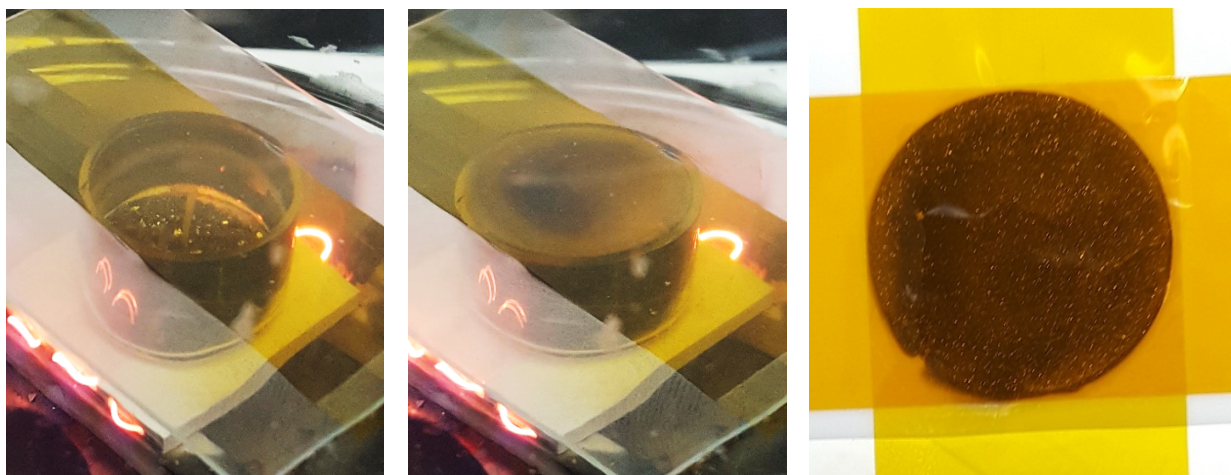
Figure 4.1: Illustration of the vapor deposition process. Coil heating evaporates source arsenic within the glass vial and a thin film deposit results on the Kapton backing stuck to a microscope slide. A fully encapsulated target is the end result after cooling and removal from the vacuum chamber.

In the deposition procedure, the system was first pumped down for at least 10 minutes before the Nupro valve was closed. The heater was then operated at 15.4 V and 7.5 A, where arsenic deposition onto the Kapton backing took approximately 1 minute (Figure 4.1). The deposited arsenic reached a yellow-coloured state ≈45 s into the process and turned black over the subsequent 15 s. It was necessary to terminate heating immediately once the deposition was completely black in colour else the deposited layer reached a point of induced cracking and flaking. A cooling period of 15 minutes was necessary to prevent As_2O_3 formation before the bell jar was vented to atmosphere.

Figure 4.2: Overview of vapor deposition system contained within a bell jar cover. The glass vial and microscope slide over top the coil heater is visible within the jar.

The arsenic layer and Kapton could then be removed from the glass slide, weighed, and further sealed with Kapton tape (44 µm silicone adhesive on 42 µm Kapton film) to prevent any deposition movement or escape.

This repeatable fabrication process produced 18 targets, which could be easily mounted to plastic frames for potential use in stacked-target work. The produced targets had masses ranging from 14.4 to 119.5 mg ($\approx$5-50 µm) and a subset of them can be viewed in Figure 4.3.
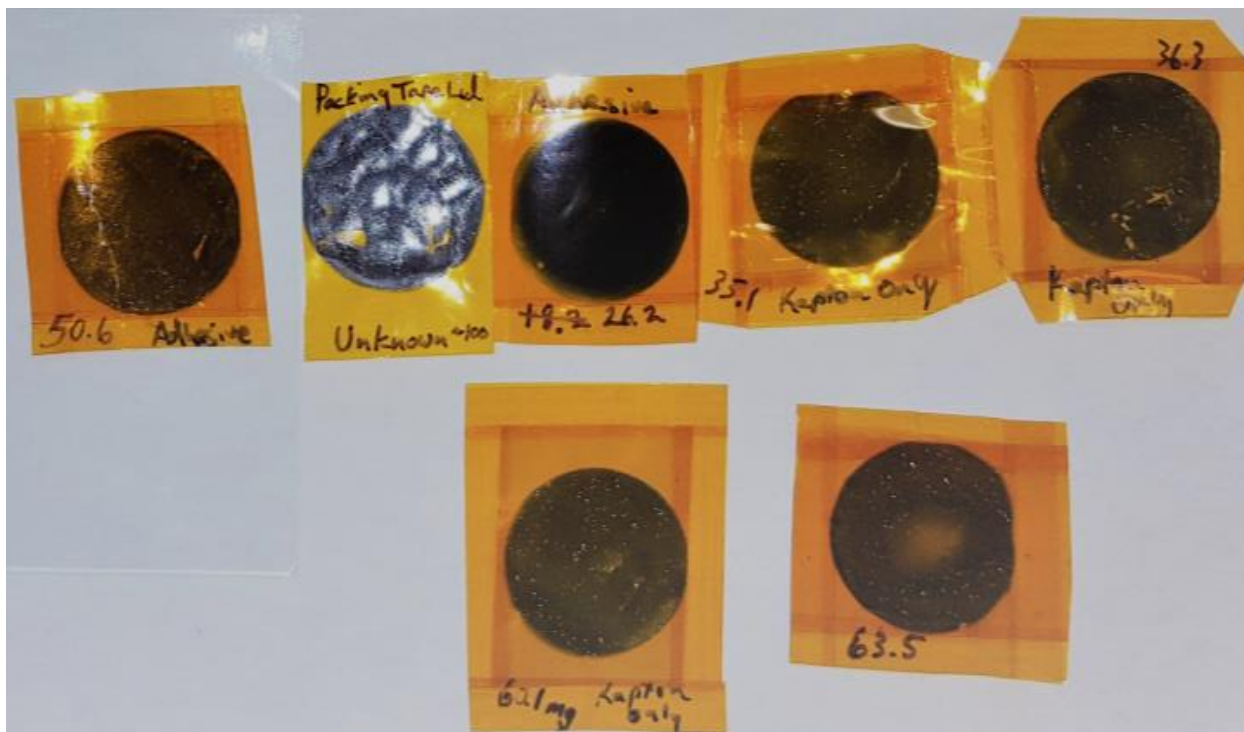
Figure 4.3: Subset of final arsenic targets prepared by vapor deposition.

While vapor deposition proved to be a quick and easy preparation method, deposition uniformity was not adequately achieved. The arsenic targets experienced pinholes, thin spots, stress cracking in the more massive cases, and shape irregularities that would hinder proper nuclear data measurements. Explicitly, uniformity assessments made by transmission measurements of ^{133}Ba and ^{88}Y x-rays using a 2 mm diamater pinhole collimator, at 16 different positions per target, showed variations of up to 90% in the areal density across any given target. Some of this quantified variation is macroscopically visible in Figure 4.3.

Replacing the Kapton backing with thin copper foils may be a pathway to improved uniformity from vapor deposition, however, an alternative fabrication approach for the Chapter 3 measurement campaign was required.

4.3.2   Two Electrode Electrodeposition

Fassbender et al. [228] provides a brief literature review of stable arsenic electroplating methodologies and presents the experimental approach in detail for effective fabrication by electrodeposition from aqueous solutions, building from the early work of Menzies and Owen [229]. Specifically, Fassbender et al. [228] plates arsenic on a titanium metal backing from a solution of As_2O_3 dissolved in aqueous HCl.

The Fassbender et al. [228] methodology was adopted for this work but required modification to move from their 3 mm plating radii, 0.28 cm^2 plating area to targets nearly four times larger for the stacked-target application.

Consequently, we performed electroplating at Lawrence Berkeley National Laboratory (LBNL) initially using the electrolytic cell pictured in Figure 4.4, powered by a Rigol DP832A DC power supply (max 30 V, 3 A, max power output 195 W). The basic cell components included a platinum rode anode, a brass block cathode, and a glass tube (inner diameter 23 mm, length 10 cm) to hold plating solution. All components were contained by a stainless steel base and support meant to hold the assembly in place and create a watertight seal with a nut-and-bolt compression flange.

Figure 4.4: Two electrode plating cell, using a titanium backing placed on a brass cathode and under a Teflon washer and the glass vial. The platinum anode is visible at the top of the vial, touching the surface of the plating solution.

The incorporated plating solution contained As_2O_3 (12.5 g/L) dissolved in aqueous HCl (6M). Total solution volumes of 100 mL were prepared by stirring the materials at $\approx 50°$C until clarified. A 100 mL solution could be split into aliquots to satisfy the requirements for 3–5 electroplating experiments.

Prior to the cell assembly, Ti foils of 10 and 25 µm were cut to act as backings for the arsenic electrodeposits. For each plating experiment, a Ti foil was carefully cleaned with HCl (6M) and acetone, dried and weighed, and placed on the cathode block beneath a Teflon washer and the glass tube. Titanium was an appropriate choice of backing in this application because it is beneficially a proton beam monitor for proton stacked-target work, presents no decay gamma-ray spectroscopy interference from activation with any eventual arsenic residual products, and is insoluble in HCl.

The cell assembly was then filled with plating solution until the platinum anode was immersed less than 1 cm into the solution. The anode was further kept electrically isolated from the plating cell by a Teflon thermocouple adapter (inner diameter 1 cm), which also acted to allow gases produced during electroplating (H_2, AsH_3) to be vented from the cell and avoid any potential pressure buildup.

Optimal plating times varied from 3–7 hours at a constant current supply of 130 mA. The current value was adopted from the optimal macroscopic current density 31.2 mA/cm^2 used in Fassbender et al. [228]. Following shutoff of the power supply, the plated targets were removed from the cell, washed with HCl (6M), dried in air, and weighed.

4.3.3   Three Electrode Electrodeposition

A refined electrolytic cell was additionally created in order to improve plating consistency, quality, and control. This new iteration, pictured in Figure 4.5, was 3D-printed from ABS plastic. In this design, the brass cathode block is placed on top of the Ti backing foil and an O-ring, and plating cell leg stands thread onto the base to form a watertight seal between the plating cell and the backing foil. The previous cell's platinum rod anode is replaced by a platinum plate and mounted opposite the O-ring in this assembly. Luer-lock connectors were also added to control the plating solution addition between the electrodes and to better maintain the cell assembly.
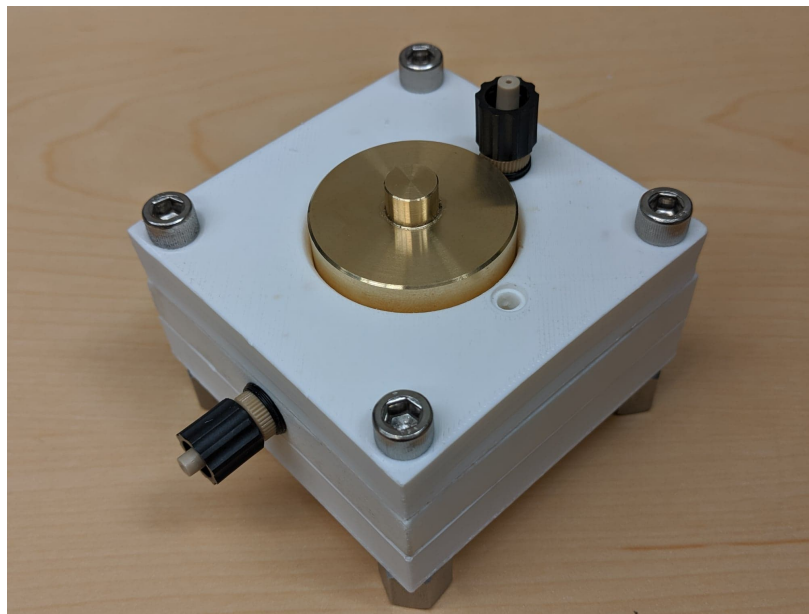
Figure 4.5: Refined plating cell incorporating three electrode capability and more controlled solution handling. The brass cathode is clearly visible but the remainder of the plating components, including the titanium backing and platinum plate anode, are hidden within the cell.

This new cell was further modified to include an Ag/AgCl reference electrode, inserted into the top of the plating cell, held in place by an O-ring. This three electrode system was powered by a Pine Instruments WaveDriver 100 potentiostat (max 24 V, 5 A, max power output 600 W).

An analysis of this cell was conducted by cyclic voltammetry. However, the chemistry-focused explanation of results is currently underway and set to be expounded in a future publication that includes the entirety of this targetry work. In spite of a lacking to-date detailed reflection of the chemistry basis, the voltammetry studies still provided best settings for the fabrication. Electroplating experiments were completed using either galvanostatic mode with a current of < 150 mA, or in potentiostatic mode with a voltage of < 24 V, during 4–12 hours.

Overall, using both electrolytic cells, we developed a consistent plating capability at LBNL and produced over fifty 22.5 mm diameter thin arsenic targets through electrodeposition. The targets ranged in mass from 1 to 40 mg (0.3–10 mg/cm^2), however the heavier cases developed significant stress from formed arsenic dendrites and were prone to flaking during removal and handling. Still, the overall target quality was qualitatively appropriate for stacked-target work and 26 structurally-sound targets (0.3–7.2 mg/cm^2) were chosen for the Chapter 3 experiments. Representative samples from the 26 are shown in Figure 4.6.
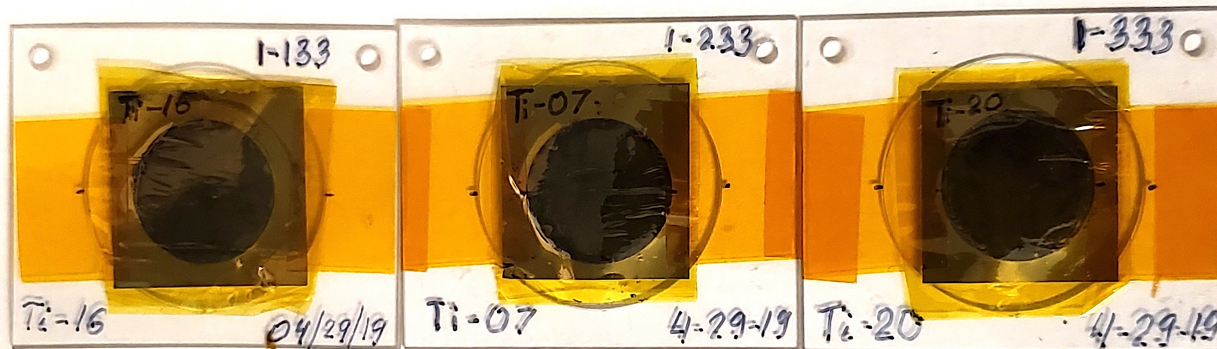
(a) Kapton-encapsulated and frame-mounted arsenic targets ready for stacked-target experiments. The consistency among the targets is a strength of the developed electroplating process.
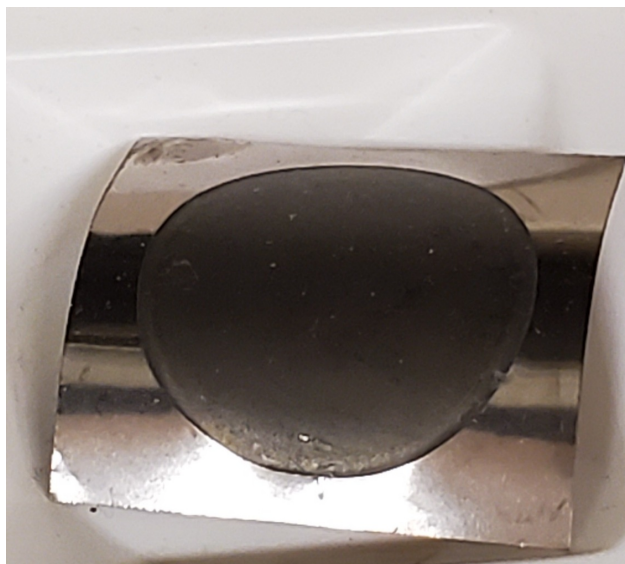
(b) Bare arsenic target prior to any encapsulation in Kapton after removal from the plating cell. Indications of built-up stress from the deposition process are visible through the curved titanium backing.

Figure 4.6: Representative subset of arsenic targets prepared by electrodeposition.

4.4 Target Microscopy and Microanalysis

A necessary more detailed assessment of the plated electrodeposits' uniformity was carried out using a FEI Quanta 3D field emission gun with a focused ion beam (FIB) - scanning electron microscope (SEM) instrument and energy dispersive x-ray spectroscopy (EDS) capabilities [230, 231].

SEM imaging was performed over length scales of 1000–30 µm for sampled targets, captured at 2 mm increments over the surface of the arsenic depositions. Although some cracking and flaking features were present, there were clearly defined arsenic layers with overall uniform

morphology at the length scales probed and no position-dependent properties save for directly at the deposition edges. Specifically, small (<1 mm diameter) irregularities were observed around the outside edge of targets, due to nucleation of hydrolysis gases at the interface between the backing foil and the Teflon washer. However, these minor irregularities existed far outside the expected stacked-target beam spot and were therefore not problematic. Figure 4.7 demonstrates these SEM results.
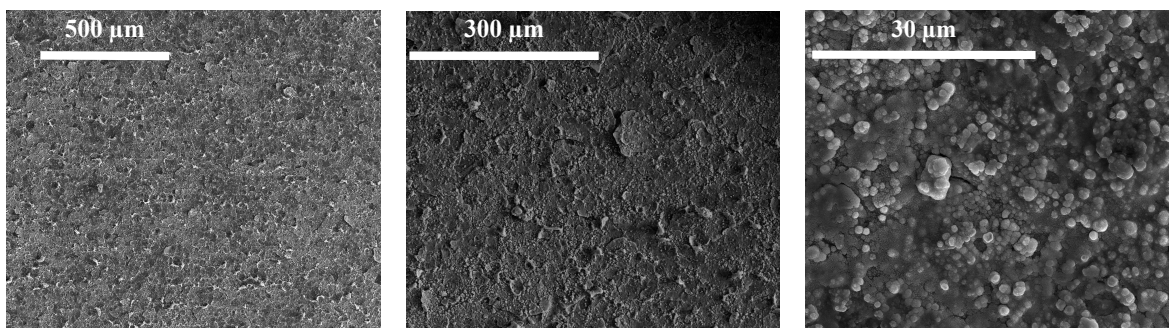
(a) Imaging showing microstructure overview in center region of target.

(b) Increased magnification in central target area.

(c) Maximum used magnification examining central target area.
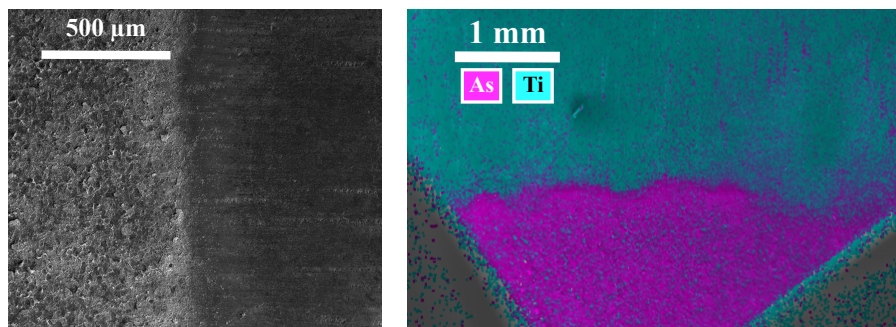
(d) Overview of plating edge, showing clear delineation between the arsenic layer and the titanium backing.

(e) EDS scan along the edge of the arsenic deposition, more quantitatively imaging transition from arsenic layer to titanium backing. Some edge shape irregularity is noted but is smaller than 1 mm. The scan further confirms the consistency and uniformity of the arsenic layer.

Figure 4.7: SEM micrographs of arsenic electroplated from dissolved As_2O_3 (12.5 g/L) in aqueous HCl (6M) using plating times of 4–12 hours.

EDS line and map scans at the deposition edges showed clear delineation between the Ti backing and the arsenic layer. Equivalent scans throughout the central region of the targets showed a consistent, but not perfectly smooth, layer of arsenic. A representative EDS plot can be reviewed in Figure 4.7e.

Analysis of deposit thickness and the arsenic interface with Ti backings was also attempted through trenching using the Ga^+ FIB, however, the beam effects on target prevented any clear insight.

As a result, the microscopy and microanalysis efforts informed that the targets were uniform and consistent but the imaging was insufficient to characterize the necessary target thickness and areal density properties needed for stacked-target activation calculations. Still, the knowledge of uniformity opened the resources appropriate for further characterization work, as whole-target assessments were possible rather than focused analysis on expected beam spot positions of the electrodepositions.

4.5 Target Characterization

Although mass information was recorded prior to and following the electroplating experiments, the scale equipment proved largely insensitive to the arsenic deposition mass versus the much more massive Ti foil backings. This insensitivity resulted in variable or unphysical descriptions of the arsenic layers, which were not useful for the precision demanded from stacked-target applications. Similar issues existed for Waters et al. [224] following their arsenic target fabrication.

Beyond the massing attempts, conventional non-destructive thickness measurements by micrometers were also unavailable here due to the safety and fragility constraints imposed by the target fabrication process.

Instead, the necessary arsenic deposition areal densities had to be characterized through alternative means.

4.5.1 Particle Transmission Experiments

The most accessible substitute approach for target areal density determinations were transmission measurements.

Initially, the x-rays of ^{133}Ba, ^{88}Y, ^{241}Am, and ^{109}Cd were used for the target characterization, similar to the procedure performed for the vapor deposition targets in Section 4.3.1. Point sources of the isotopes were combined with a narrow collimator to investigate the depositions in a grid-like manner and yield both thickness information as well as a continued check of uniformity. An ORTEC GMX series (model GMX-50220-S) High-Purity Germanium (HPGe) detector and a single leaf of an EURISYS MESURES 2 Fold Segmented Clover detector were used for this activity.

Given that the arsenic was deposited onto titanium backings and encapsulated in Kapton tape, the transmission work on the targets had to be performed relative to a pure titanium and

Kapton control case, which provided a baseline transmission intensity for the different x-rays. In practice, the thin layers of arsenic deposited created difficulty in distinguishing between the transmission through the targets versus the control case. Across almost all targets, the transmitted x-ray intensities were found to be greater than or equivalent to the baseline control intensity within uncertainty since the arsenic attenuation was negligible. Further, the transmission work sensitivity could not be increased by using other lower energy x-rays because the relatively large areal density presented by the titanium and Kapton rendered overall photon transmission to zero. Consequently, photon transmission characterization results could not be fully formed.

In turn, charged particle transmission measurements were instead explored because the increase in stopping power versus photons was expected to lead to more pronounced intensity differences through the thin arsenic layers. Therefore, both ^{90}Sr and ^{204}Tl beta-emitting point sources were used with a Geiger-Muller (GM) tube and a Spectech ST360 counter to characterize the produced arsenic foils.

Count data was collected with the GM tube over 10-20 minute periods for each arsenic foil at a supplied bias of $800\,\mathrm{V}$. The beta source was placed $4\,\mathrm{cm}$ from the detector window, with a collimator at a $2\,\mathrm{cm}$ distance, and the targets at a $1\,\mathrm{cm}$ distance. In order to determine an absolute value for the electroplated arsenic areal densities from the count data, additional transmission measurements of control materials and background were collected to generate a beta-transmission calibration curve.

The found target areal densities by electron transmission were all physical results and did not suffer from the insensitivity present in the x-ray work. In spite of this sensitivity improvement, uncertainties for the determined areal densities existed at the 20–30% level and there was unexpected variation in the relative magnitudes between electroplated targets made from the same experimental batch. Likely, an unaccounted for convolution of electron stopping power through multiple materials and the sources' beta-emission spectra was degrading the results. In attempts to remediate this issue, calculations incorporating the continuous slowing down approximation range for electron attenuation, a semi-empirical transmission-based areal density formula derived from the Fermi function of beta-spectra, and Bethe-Bloch focused simulations were applied. Largely, none of these corrective efforts fixed the magnitude variation for targets or provided greater precision than the base experimental work.

Although the theoretical basis for transmission characterization is sound, its application in practice to the prepared thin targets was not trivial. These traditional electromagnetic probes of areal density suffer here because of the significantly greater stopping in the relatively much more massive backings versus the arsenic layers. It is possible that a benefit could be gained from a more precise experimental setup or transitioning to α-transmission work but expected improvements are unknown and may still not qualify the findings for eventual stacked-target calculations [232].

4.5.2 Neutron Activation

Ultimately, with transmission experiments providing inadequate accuracy and precision needed for high fidelity production cross section measurements, another alternative approach to characterizing these foils was conducted using neutron activation of the arsenic relative to known neutron capture reactions. The relative measurement allows for the arsenic target masses and uncertainties to be calculated on the basis of well described capture cross sections. Moreover, given that the target foils were fabricated for proton beam irradiations, the capture products resulting from a neutron irradiation pose no contamination risk to any eventual proton-induced products.

To this end, neutron irradiation experiments were carried out at the UC Davis McClellan Nuclear Research Center. The McClellan site has a 2 MW TRIGA reactor with a unique capability to perform external beam neutron radiography for items such as plane wings and fuel injectors over a large area [233]. Their smallest external imaging bay was consequently an appropriate and easily accessible setting to non-destructively assess the arsenic targets.

4.5.2.1 Experimental Setup and Procedure

The nuclear data properties associated with the arsenic neutron capture reaction were critical to the development of this characterization technique. More specifically, as seen in the ^{75}As(n,γ)^{76}As data shown in Table 4.1, the capture product has an appropriate half-life for gamma spectroscopy, a large enough and well-characterized thermal capture cross section to achieve sufficient activation with a small amount of mass, and an intense decay gamma-ray in a useful energy range for HPGe detection. Furthermore, the reference neutron monitor material chosen in this work had to share similar properties and were too chosen as a function of their half-life, thermal capture cross section magnitude and uncertainty, as well as their capture products' primary decay gamma-ray energy and intensity. Eight total neutron monitor foils were used in this investigation: 5 ^{197}Au, 2 ^{nat}Cu, and 1 ^{nat}Fe. The relevant nuclear data associated with these monitors is also provided in Table 4.1.

Over the course of a year, numerous neutron irradiation experiments were conducted for the electroplated targets of interest to gather the required activation data and account for the particular McClellan beam conditions. In each neutron irradiation, the arsenic targets along with the monitor foils were mounted in a grid-like frame and fastened to the fast shutter of the McClellan bay, as illustrated in Figure 4.8. The fast shutter is typically used as means for ensuring uniform beam exposure in radiography cases but it is additionally centered in the neutron beamline and faces an approximately 6.25×10^6 n/cm^{2}s thermal flux, which made it a useful mounting platform for the targets in this work. The flux impinging on the fast shutter is uniform across an approximately 15-inch diameter, which was preliminarily proven by a radiograph, pictured in Figure 4.9a, and later confirmed by the monitor foils (Figure

4.9b). Irradiation times were $t_{irr} = 7 - 8$ hours and the targets were returned to LBNL for assessment within approximately 5 hours of the end-of-bombardment (EoB).

Table 4.1: Relevant nuclear data properties for neutron capture reactions used in the McClellan-based target characterization process [7, 10, 201, 234–237].

Capture Reaction	Thermal Cross Section, σ_0 [b]	Activation Product $t_{1/2}$	Decay E_γ [keV]	I_γ [%]
^{75}As(n,γ)^{76}As	4.28 (19)	26.261 (17) h	559.10 (5)	45.0 (2)
^{197}Au(n,γ)^{198}Au	98.70 (22)	2.6941 (2) d	411.80205 (17)	95.62 (6)
^{63}Cu(n,γ)^{64}Cu	4.47 (18)	12.701 (2) h	1345.77 (6)	0.475 (11)
^{58}Fe(n,γ)^{59}Fe	1.314 (74)	44.490 (9) d	1099.245 (3)	56.5 (9)
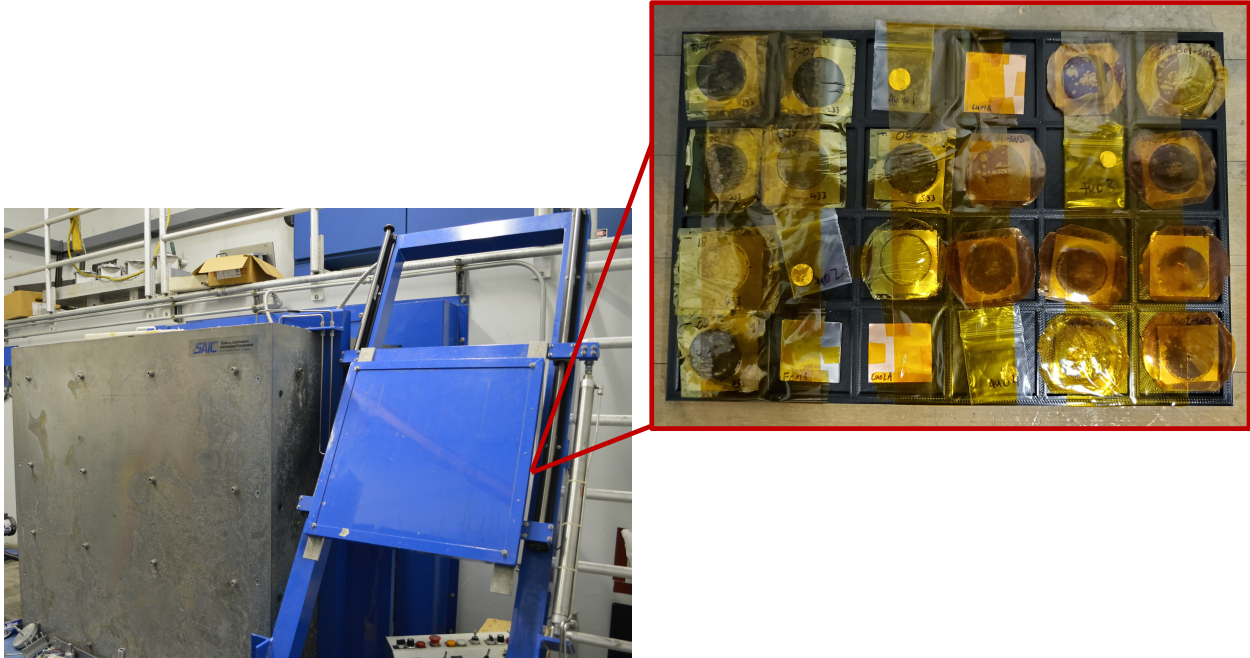
Figure 4.8: Experimental setup in an external imaging bay at the McClellan Nuclear Research Center. The blue fast shutter, situated beside the large beam stop, moves into the neutron beamline as the beam stop moves away. The angled position of the shutter is needed to intersect the incoming angled neutron beam path perpendicularly. The frame holding the arsenic targets and monitor foils is attached to the side of the fast shutter that faces the beam.

At LBNL, the neutron activation was measured through gamma spectroscopy using multiple ORTEC IDM-200-VTM HPGe detectors. The UC Berkeley code package Curie [139], with built-in nuclear structure and reaction databases, was used to analyze the gamma spectra. End-of-bombardment activities A_0 for the activation products of Table 4.1 were determined from the count data with appropriate timing, efficiency, solid angle, and gamma
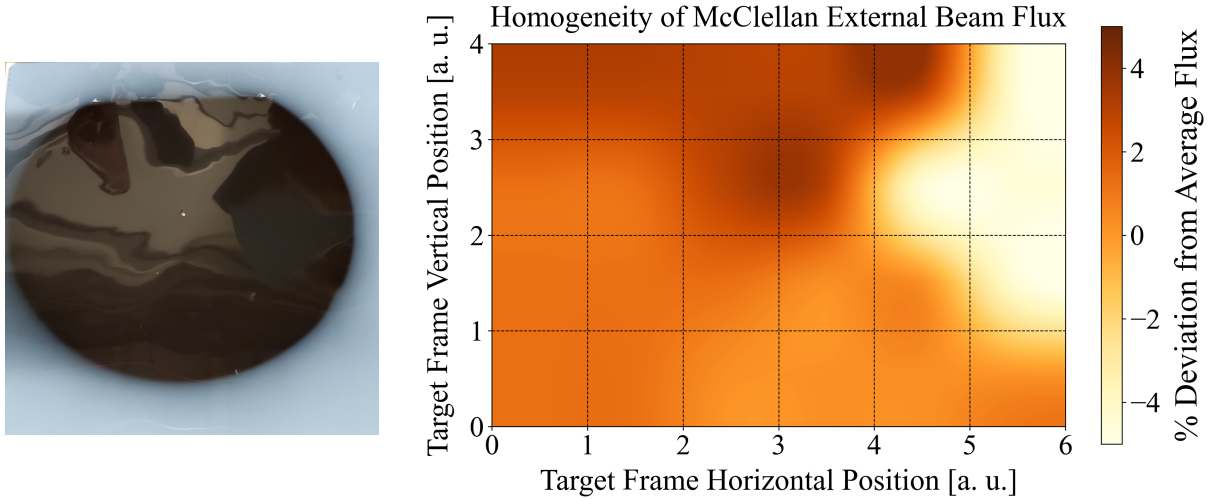
(a) Preliminary radiograph from eventual target frame position on fast shutter.

(b) Flux map across the irradiated target frame showing deviation from the average neutron flux at each position, as calculated from monitor foils.

Figure 4.9: Assessments of McClellan external beam uniformity at target irradiation site.

attenuation corrections [34, 39]. The energy and absolute photopeak efficiency of the IDMs were calibrated using standard ^{57}Co, ^{60}Co, ^{133}Ba, ^{137}Cs, ^{152}Eu, and ^{241}Am sources. The efficiency model used in this work is a Curie-modified form of the semi-empirical formula proposed by Vidmar et al. [238].

4.5.2.2 Activation Analysis

Given the measured count data, the initial calculation methodology for extracting the areal densities of the arsenic targets subsequent to neutron activation from the believed highly thermalized McClellan spectrum begins with [239–241]

$$A_0 = \phi N \sigma_0 G_{th} g (1 - e^{-\lambda t_{irr}}). \tag{4.1}$$

Here, ϕ is the thermal neutron flux in the McClellan imaging bay, N is the number of irradiated nuclei in the target under consideration, σ_0 is the appropriate thermal neutron capture cross section, λ is the activation product decay constant, G_{th} is the thermal neutron self-shielding factor for the irradiated target, and g is the Westcott correction factor that accounts for the deviation of the capture cross section from a pure $1/v$ energy dependence. Typical G_{th} corrective factors for micron-thick targets are in the 0.97–1.0 range and have established calculation methods [241–244]. From Mughabghab [245], the Westcott correction factor for arsenic is 1.0005, for gold is 1.0054, and for copper is 1.0002.

Creating a relative activity measurement between the arsenic targets (subscript As) and a neutron monitor foil (subscript mon) yields,

$$\frac{A_{0,As}}{A_{0,mon}} = \frac{N_{As}\sigma_{0,As}G_{th,As}g_{As}(1 - e^{-\lambda_{As}t_{irr}})}{N_{mon}\sigma_{0,mon}G_{th,mon}g_{mon}(1 - e^{-\lambda_{mon}t_{irr}})} \tag{4.2}$$

where there is no longer a dependence on neutron flux. The unknown arsenic electrodeposit masses, or equivalently the unknown number of arsenic nuclei in an electrodeposit, can be represented as

$$N_{As} = (\rho\Delta r)_{As}A_{plating}N_A/MM_{As}, \tag{4.3}$$

where $(\rho\Delta r)_{As}$ is the arsenic layer areal density, $A_{plating}$ is the electroplated area for the arsenic on the Ti backings, N_A is Avogadro's number, and MM_{As} is the molar mass of ^{75}As. This expression is valid because of the earlier performed SEM work demonstrating the uniformity of the plated arsenic layers. Then, it follows that the desired arsenic target areal densities can be experimentally deduced from

$$(\rho\Delta r)_{As} = \frac{A_{0,As}N_{mon}\sigma_{0,mon}G_{th,mon}g_{mon}(1 - e^{-\lambda_{mon}t_{irr}})}{A_{0,mon}\sigma_{0,As}G_{th,As}g_{As}(1 - e^{-\lambda_{As}t_{irr}})}\frac{MM_{As}}{N_A A_{plating}}. \tag{4.4}$$

However, early results using this methodology suggested that arsenic areal density magnitudes were 5–7× larger than expected based on the constraints set by limitations of the electroplating process and the electron transmission work. As well, the thermal neutron flux that could be extracted independently using the monitor foils, as was done in the flux map of Figure 4.9b, was nearly a factor of five larger than the anticipated 6.25×10^6 n/cm^{2}s. These discrepancies were determined to be artifacts stemming from an as yet unaccounted for epithermal flux component in the McClellan reactor neutron spectrum.

The McClellan site has no descriptive epithermal flux data nor is there sufficient capture and elastic cross section knowledge of the materials under investigation to develop an analytical correction. In turn, it was necessary to perform a cadmium covered irradiation of the targets as one of the numerous experiments. Activation under cadmium sheets would remove the thermal neutron contribution to isolate the epithermal portion needed for activity subtraction as a corrective means for the inflated areal densities. Given the cadmium results, Equation (4.2) is replaced by

$$\frac{R_{As} - F_{As,Cd}R_{As,Cd}}{R_{mon} - F_{mon,Cd}R_{mon,Cd}} = \frac{\sigma_{0,As}G_{th,As}g_{As}}{\sigma_{0,mon}G_{th,mon}g_{mon}}, \tag{4.5}$$

where $R_{As/mon}$ and $R_{As/mon,Cd}$ are the reaction rates per atom for the targets after bare and Cd-covered irradiations and $F_{As/mon,Cd}$ is the cadmium transmission correction factor. The monitor target reaction rates are directly calculated from measured A_0 and N_{mon} values

whereas N_{As} and associated $(\rho \Delta r)_{As}$ remain the unknowns that are then solved for using a similar rearrangement to Equation (4.4).

However, these ensuing Cd-covered results too proved insufficient because it was seen that the approximate thermal-to-epithermal flux ratio was $f \approx 3$, indicating a very strong epithermal portion versus typical thermalized reactor fluxes that exist at $\approx f > 20$ [246–248]. Consequently, the predicted arsenic areal densities derived from the cadmium difference method were only slightly reduced versus the bare irradiations. Therefore, the cadmium work could not fully explain the 5-7× areal density overestimations.

Further analysis of the monitor foil data from the bare and cadmium experiments indicated that the convolution of target thickness and epithermal resonances was a sensitive parameter in the McClellan conditions and in fact played a significant role in the activation. Although the Cd-work should theoretically account for resonance effects and neutron flux perturbations associated with the non-thermal portion of the reactor spectrum, it is likely that the lack of detailed McClellan reactor parameters imparted an unknown influence on the experiments that obscured analysis.

To explore and root out these potential hindering unknown factors would require a thorough reactor investigation that exists outside the aim of our electroplated target work and that can be in fact circumvented empirically in this application instead. Moreover, it is possible to experimentally derive an arsenic-specific calibration curve for the McClellan external beam conditions, which can provide a lump correction factor for combined thermal and epithermal self-shielding (absorption and scatter) effects without additional knowledge of the flux spectrum shape, flux perturbations from resonances in targets, or geometry contributions.

Typically, this type of overall effective self-shielding factor for a mixed neutron spectrum is composed from G_{th} and its epithermal equivalent G_{epi} and can be applied to bare target irradiation measurements [246]. Unfortunately, theoretical calculations for G_{epi} are environment dependent and contain important alterations according to the current unknowns at the McClellan site [241, 248–253]. Therefore, our new empirical calibration approach aims to isolate and still calculate this overall effective self-shielding factor when detailed reactor parameter information is not available.

4.5.2.3 Thick Pellet Calibration

Accordingly, we produced thick pressed pellets of As_2O_3 of varying thickness for this calibration purpose where typical proper mass and dimensioning measurements could be made. Seven thick pressed pellets were created for this work, of approximately 1.3 cm diameter, via hydraulic press and trapezoidal split-sleeve dies with masses ranging from 100 to 900 mg (see Figure 4.10). These pellets were irradiated under identical bare conditions at McClellan to the

electroplated targets of interest and were also equivalently assessed by gamma spectroscopy at LBNL.
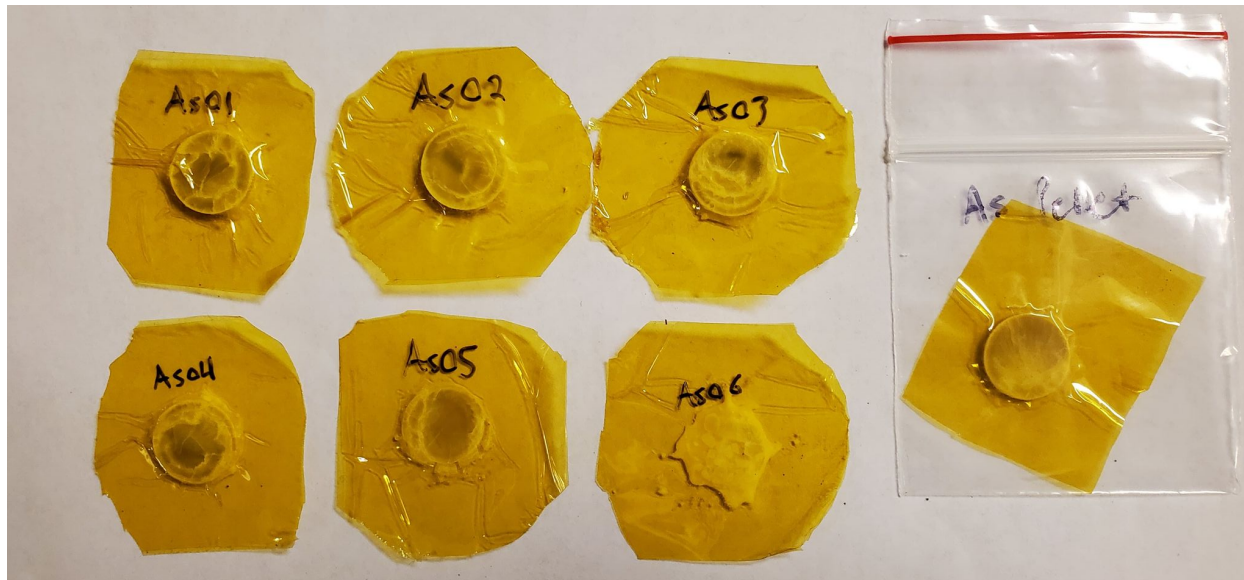
Figure 4.10: Prepared thick pressed pellets of As_2O_3 of varying thickness used for calibration irradiations at McClellan. Note that although the structure of the "As06" pellet could not be equally maintained throughout the pressing process, its mass is known to equivalent uncertainty as all other pellets and its average diameter remains at $13\,\text{mm}$.

In contrast to the electroplated targets, however, the additional knowledge of mass and size for the thick pressed pellets mean that their induced ^{76}As specific activities η could be easily calculated from their determined A_0 values. These η are valuable data points that were used to fit modified versions of theoretical self-shielding models as a function of mass/thickness.

Specifically, the two accepted theoretical epithermal self-shielding corrective models of Karadag et al. [241] and Martinho et al. [254] were utilized for this purpose. They were modified from their original formulations in the sense that regression parameters have been added that account for not only epithermal shielding but also thermal self-shielding and all other non-independently described corrective factors for arsenic targets in the McClellan conditions. In this manner, the activation physics bases of these models are maintained but they are recast to provide general attenuation information.

In turn, this approach made it possible to extract the specific activity of a zero-thickness arsenic target in the McClellan beam, or more precisely, a Bq/atom production standard for ^{76}As to directly apply to the measurements of the electroplated arsenic A_0. This calibration therefore simplifies the neutron activation areal density calculations and even renders the monitor foil data moot.

Explicitly, the fit modified from the Karadag et al. [241] G_{epi} work is a function of the number of arsenic nuclei in a pellet per unit volume N_{pel} and pellet mean chord length $d = 2V/SA$ where V, SA denote volume and total surface area of a pellet, respectively, as given in Equation (4.6).

$$
\eta = \eta_0 \frac{\left[I_v + \frac{\pi}{2} \sum_i \left(\frac{\Gamma_\gamma}{E_r} \right)_i \frac{\sigma(E_{ri})}{\sqrt{1 + 2N_{pel}\sigma(E_{ri})d}} \right]}{\left[I_v + \frac{\pi}{2} \sum_i \left(\frac{\Gamma_\gamma}{E_r} \right)_i \sigma(E_{ri}) \right]},
\tag{4.6}
$$

where η_0 is the zero-thickness specific activity fit parameter, I_v is the fit parameter representing the $1/v$ contribution to the capture cross section resonance integral, E_{ri} and $\Gamma_{\gamma i}$ are the energy and radiative width of the ith neutron resonance, and $\sigma(E_{ri})$ is the maximum total neutron cross section at that ith resonance. The resonance parameters of arsenic used for this work are presented in Table 4.4 (see Section 4.8).

Similarly, from the Martinho et al. [254] G_{epi} approach, the adopted modified fit function is

$$
\eta = a \left[\frac{0.94}{1 + \left(\frac{z}{2.70} \right)^{0.82}} + b \right],
\tag{4.7}
$$

where a and b are fit parameters and z is an effective target thickness defined by Equation (4.8). The desired zero-thickness standard of activation quantity is found here by $\eta_0 = \eta(z = 0)$.

$$
z = 1.5tN_{pel} \sum_i \sigma(E_{ri}) \left(\frac{\Gamma_\gamma}{\Gamma} \right)_i^{0.5},
\tag{4.8}
$$

where t is the measured pellet thickness and Γ_i is the total width of the ith resonance.

Following the irradiation of the pellets at McClellan, and measurements of the accompanying η at LBNL, the Equation (4.6) and (4.7) fits were applied. The fit results of both models are shown in Figure 4.11 and the determined η_0 values are given in Table 4.2. Both models agree within uncertainty on the zero-thickness standard of activation for arsenic at McClellan.

Table 4.2: Zero-thickness standard of activation for arsenic targets in McClellan conditions as derived from the pellet calibration data.

Calibration Fit Form	η_0 [Bq/atom]
Modified Karadag	$(1.502 \pm 0.086) \times 10^{-17}$
Modified Martinho	$(1.446 \pm 0.076) \times 10^{-17}$
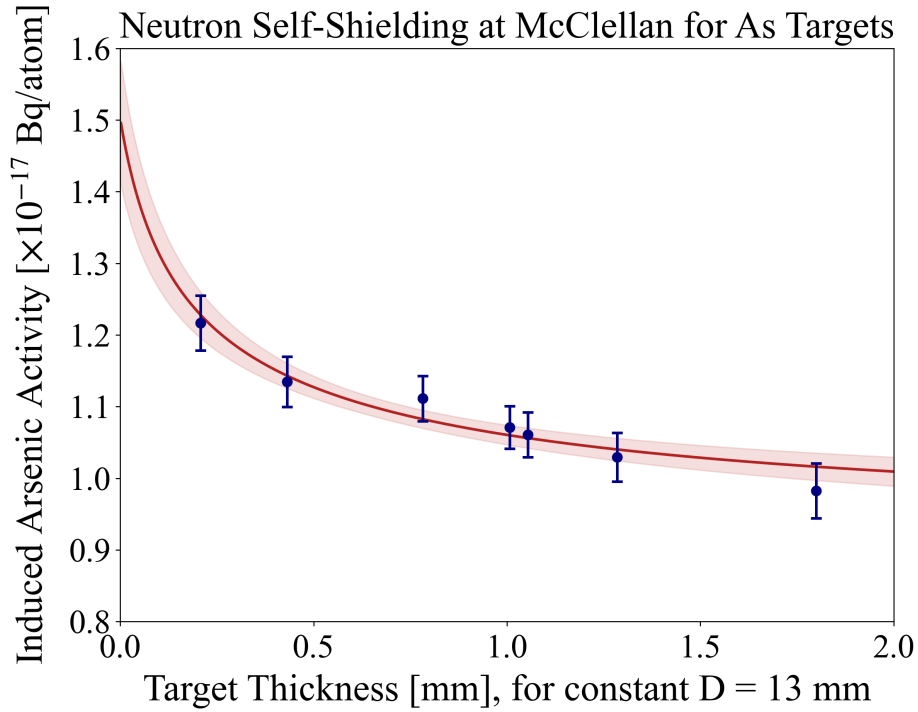
(a) Modified Karadag calibration fit form.
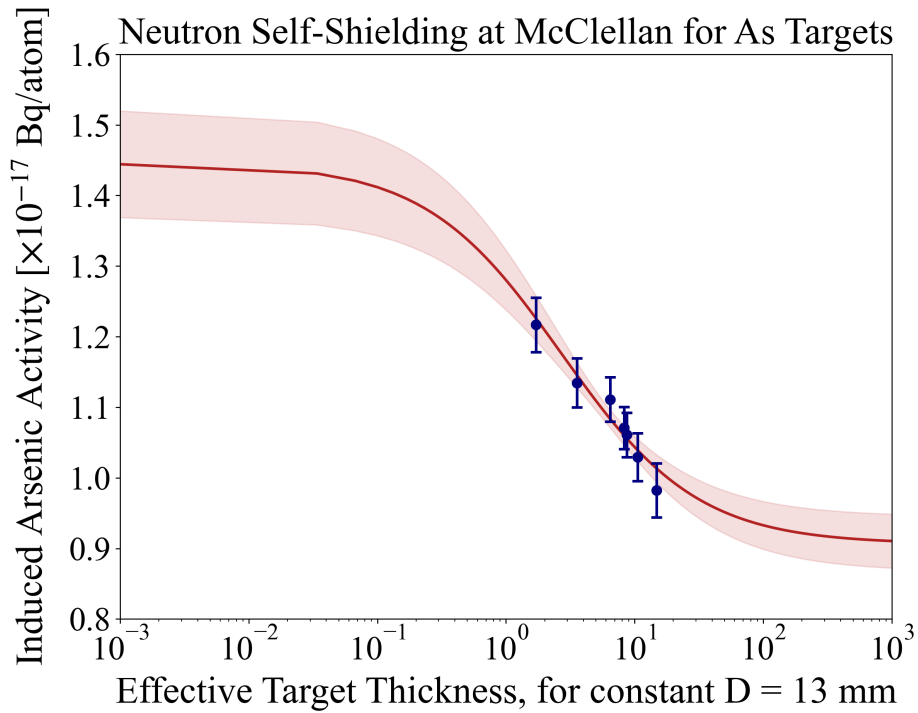
(b) Modified Martinho calibration fit form.

Figure 4.11: Extraction of zero-thickness standard of activation for arsenic targets in McClellan external beam conditions by calibration curves using measured pellet [76]As specific activity data. The bands surrounding the solid calibration curves represent fit errors at one standard deviation.

Given the found η_0, the number of arsenic nuclei on each electroplated arsenic target of interest was very simply calculated using each target's measured EoB activity by

$$N_{As} = \frac{A_{0,As}}{\eta_0}. \tag{4.9}$$

The desired areal density quantity per electroplated target was finally directly calculated as

$$(\rho \Delta r)_{As} = \frac{N_{As} MM_{As}}{N_A A_{plating}}. \tag{4.10}$$

Note that an iterative procedure could have been applied to calculate individual η values specific to each electroplated target. However, the fits do not have relevant precision at such small thickness values and the η_0 uncertainties instead contain any error from using the zero-thickness application to all targets equivalently.

A variation of this effective corrective factor approach was performed by Chilian et al. [246] for a larger variety of target nuclei. Their calculations still utilized measured condition-specific reactor parameters but it is clear that this overall methodology has established roots in literature and is viable. Origins for this technique in nuclear data experiments even reach farther back to Alfassi and Weinreich [223], who performed thin foil mass measurements through neutron activation, though calculation details are not provided.

4.6   Results and Discussion

A summary of the produced electroplated targets for the stacked-target work and their characterization results by neutron activation with the determined η_0 are given in Table 4.3.

The final electroplated target areal density uncertainties lie in the 8–10% range, which can be contrasted with typical 0.1-1.0% characterization uncertainties of commercially produced targets that are conventionally massed and measured. The uncertainties here have contributions from the η_0 calculations, plating edge shape irregularities, and from fitted peak areas, evaluated half-lives and gamma intensities, and detector efficiency calibrations in the gamma spectroscopy measurements.

Uncertainties at the 8–10% level will yield eventual cross section measurements with errors in the 9–15% range. There is evidently room for improvement but this precision is still valid for stacked-target work because the experimental technique maps excitation functions over a range of energies and thus can inherently balance loss in precision with a cumulative result that still amounts to high quality data.

Table 4.3: Properties of the 26 prepared arsenic targets by electrodeposition. The targets are separated into 3 groups according to their use in 3 different stacked-target irradiations and thus creation from different batches/electroplating experiments.

Target Stack #1

Target	Thickness [µm]	Areal Density from Activation [mg/cm^2]	Areal Density Uncertainty [%]
As-SN1	3.24	1.85	9.8
As-SN2	1.69	0.97	9.9
As-SN3	1.81	1.04	9.9
As-SN4	2.22	1.27	10
As-SN5	1.95	1.12	9.9
As-SN6	1.30	0.74	11
As-SN7	2.36	1.35	8.9
As-SN8	0.94	0.54	9.7
As-SN9	0.57	0.32	10

Target Stack #2

Target	Thickness [µm]	Areal Density from Activation [mg/cm^2]	Areal Density Uncertainty [%]
As-SN1	4.27	2.45	8.2
As-SN2	4.30	2.46	8.3
As-SN3	3.62	2.07	9.0
As-SN4	3.54	2.03	9.2
As-SN5	3.90	2.23	8.7
As-SN6	3.11	1.78	10
As-SN7	2.79	1.59	9.2
As-SN8	2.20	1.26	9.0
As-SN9	2.57	1.47	9.9
As-SN10	1.94	1.11	10

Target Stack #3

Target	Thickness [µm]	Areal Density from Activation [mg/cm^2]	Areal Density Uncertainty [%]
As-SN1	1.89	1.08	9.9
As-SN2	2.94	1.68	9.0
As-SN3	3.06	1.75	10
As-SN4	4.85	2.78	9.9
As-SN5	7.26	4.15	12
As-SN6	4.93	2.82	9.0
As-SN7	12.62	7.22	9.3

Furthermore, although these areal density uncertainties are large compared to commercially-sourced foils for other materials, it is important to note that pure arsenic targets, and particularly arsenic thin foils, have not been widely used to measure nuclear reaction data in the past. Most existing arsenic reaction data are from neutron-induced investigations and therefore have markedly different target requirements and measurement techniques. Very few charged-particle, and in turn stacked-target, pure arsenic foil measurements exist, meaning that the contribution from this work is valuable for extending knowledge in this context [141, 142].

In this manner, paths forward from this work may include independent more detailed electroplating studies. These studies exist outside of the applied nuclear data realm but would generate an improved description of underlying arsenic electrochemistry kinetics and consequences, likely deducing optimal cell assemblies and plating parameters, and perhaps leading to an arsenic target fabrication standardization. A fundamental study of this type has been performed by Wang et al. [213], where in-depth voltammetric work was used to explore arsenic electroplating charge-transfer kinetics, chronoamperometry was used to detail aspects of deposition nucleation and growth, and microstructure analysis was performed under different conditions. However, this study held a research focus within the semiconductor industry and was performed for a plating solution meeting associated needs. In turn, there is still demand for similarly conducted investigations for different plating solutions that also further examine substrate effects, deposition stress generation and impact, cell design, and consider precise characterization methods in the context of nuclear data experiments. A similar chemistry and materials science exploration is worthwhile with respect to arsenic vapor deposition as well.

The implementation of neutron activation analysis in this work to extract areal densities rather than neutron reaction data or related structure parameters such as nuclear level densities is less common, but has evidently been shown as a viable target characterization approach. In cases of fragile targets, where appropriate neutron capture properties exist, this is an easily applied and accurate non-destructive technique. In combination with microstructure studies by SEM or similar, this characterization approach would fully describe fabricated targets.

Given the outcomes of this study, if this type of target assessment were to be adopted in future instances, it is clear that numerous improvements can be easily applied. Firstly, acquiring a more precise calibration curve would immediately reduce final uncertainties.

Likely, improved powder pressing technology that could make pellets which cover a broader range of thicknesses is a quickly attainable refinement. In fact, some powder pressing developments, such as the Sugai [232] and Esposito et al. [255] vibrational/electrostatic work, even offer a pathway to the uniformity and thinness of electroplating experiments. However, it is useful to note that powder pressing pellets is also not a requirement for the activation

calibration. Variations such as suspensions in solutions or casting with different compounds of the target of interest, where the secondary material does not offer competing neutron resonances, will all allow for equivalent experiments and derivations of a zero-thickness standard of activation. This foresight in the future means that dedicating more thought and care to this aspect of the experiment will certainly allow for a more precise calibration curve. It seems achievable to reach areal densities at reduced uncertainties near the theoretical minimum, defined by uncertainties of any used capture cross sections, generally in the 1-5% range. Additional changes to experimental conditions such as moving to in-core activation for the targets to increase neutron flux and increasing irradiation time would improve this characterization approach. These changes would result in increased target activities, leading to more favourable gamma spectroscopy conditions that would reduce eventual contributing A_0 uncertainties.

Of course, if it is possible to use a well-characterized and well-thermalized reactor, the need for this calibration approach becomes optional as the cadmium difference method or equivalent techniques will work. However, this calibration approach may still be preferred since it requires only one experiment and relies on an extremely simple relative calculation where even monitor foils are unneeded.

As an aside to target characterization, in our exploitation of neutron activation for this purpose, our fitting analyses have extracted what amounts to an integral strength measurement of resonance absorption and scatter. This easily conducted technique may find application in structure investigations or for integral data measurements relevant for the modeling of new reactor designs.

4.7   Conclusions

Thin uniform ^{75}As targets on titanium backings appropriate for stacked-target experiments with areal densities from 0.32 to 7.22 mg/cm^2 were prepared by electrodeposition using an aqueous plating solution of As_2O_3 dissolved in HCl. Both two and three electrode electrolytic cells were used and best plating parameters were derived through voltammetric investigations. Significant efforts were devoted to target characterization, which included surface morphology studies by SEM and non-destructive thickness assays by neutron activation. The applied neutron activation analysis was formulated to be independent of neutron flux shape, environmental factors, and source geometry, while correcting for any potential scatter or absorption effects.

4.8 Resonance Data for Neutron Self-Shielding Calculations

The properties of neutron resonances in ^{75}As relevant to the epithermal calculations at the McClellan site are listed in Table 4.4.

Table 4.4: Resonance parameters used in self-shielding calculations of arsenic pellets [7, 241, 256, 257].

^{75}**As Neutron Resonance Parameters**			
Resonance Energy E_r [eV]	Radiative Width of the Resonance Γ_γ [eV]	Total Width of the Resonance Γ [eV]	Cross Section at E_r [b]
47.00	0.26	0.29	2544.1
92.40	0.25	0.28	394.4
252.7	0.27	0.32	349.4
318.6	0.30	0.77	1909.7
326.7	0.35	0.89	84.6
455.5	0.34	0.37	1205.6
493.3	0.30	0.35	300.532
533.4	0.28	0.30	2507.0
664.9	0.30	0.62	411.375
733.9	0.35	1.5	802.415
737.4	0.30	2.3	1608.4535

Chapter 5

Conclusions

In this dissertation, we have performed wide-ranging work to address lacking high-energy charged-particle data needs.

The most application-specific outcome of this research is the measurement of 78 excitation functions for high-energy proton-induced reactions of p+^{93}Nb, ^{75}As, ^{nat}Cu, and ^{nat}Ti, as motivated by medical isotope production. The measured data most notably include the first cross section results for ^{75}As(p,x)^{68}Ge and the best characterized excitation function of ^{75}As(p,4n)^{72}Se to-date, which are important for the production of the ^{68}Ge/^{68}Ga and ^{72}Se/^{72}As PET generator systems. We find that ^{75}As(p,4n)^{72}Se is the most favourable route to the ^{72}Se/^{72}As generator and is a truly emblematic case of the TREND project central to this dissertation, aiming to meet the shifting paradigm of isotope production.

While the ^{72}Se and ^{68}Ge production cross sections have the greatest immediate impact on the needs of the isotope production community, the study of reaction theory and modeling predictions for high-energy (p,x) reactions has the more wide-ranging impact. We utilize the TALYS nuclear reaction code to carry out in-depth investigations of pre-equilibrium, nuclear level density, and optical model input parameters. In parallel, we introduce an original standardized procedure as an early evaluation tool for high-energy proton data with inclusion of a validation technique using cumulative production results. The procedure has been applied to and developed from the extracted cross sections, as never before capable prior to the TREND experiments. A meaningful outcome from these studies surrounds the pre-equilibrium two-component exciton model and suggests a required relative decrease for internal transition rates at intermediate proton energies.

This research also sets the path forward in charged-particle evaluation by identifying dataset diversity beyond production cross sections as the key to unambiguously resolving the interplay of different physics models and generating consistent predictive power. Moreover, the preliminary evaluation success in this dissertation validates the calls for new high-

energy prompt-gamma yields and secondary proton/neutron spectra measurements through collaborations that unify different specialists in the nuclear data community and truly revitalize the charged-particle nuclear data effort.

Lastly, this thesis provides a contribution to the target fabrication and characterization infrastructure vital to the outset of any experimental contribution to the nuclear data pipeline. The discussion of experimental failures and successes while creating thin and uniform arsenic targets are relevant for future charged-particle work attempting to generate even more accurate and precise high-energy data, especially as target choices become more differentiated during innovative campaigns. Likely, the most appreciable lasting impact from the targetry studies is the presentation of a new, effective, easily applied, and non-destructive neutron activation target characterization technique.

Three peer-reviewed publications are expected to originate from this doctoral work, thereby necessarily disseminating this information and actively participating in the nuclear data community. The interest in publications further corroborates the applicability of the data work provided here and undeniably reflects the shifted data goals of nuclear medicine toward high-current, high-energy charged-particle accelerators. Through this communication, I also hope that this work serves to promote and preserve the increasingly rare experimental nuclear data evaluator and that it invites the intrigue and talent needed to progress the future of the nuclear data field.

The culmination of this dissertation is a novel merger of experimental work and evaluation techniques for high-energy charged-particle isotope production. The ultimate utility of this research is the promise of a more effective nuclear data pipeline and the optimal development of versatile medical radionuclides with improved diagnostic and therapeutic efficacy that carry a valuable societal impact.

Bibliography

[1]   L.A. Bernstein, D.A. Brown, A.J. Koning, B.T. Rearden, C.E. Romano, A.A. Sonzogni, A.S. Voyles, and W. Younes. Our Future Nuclear Data Needs. *Annual Review of Nuclear and Particle Science*, 69:109–136, 2019. doi:10.1146/annurev-nucl-101918-023708.

[2]   B. Pritychenko, E. Běták, M.A. Kellett, B. Singh, and J. Totans. The Nuclear Science References (NSR) database and Web Retrieval System. *Nuclear Instruments and Methods in Physics Research A*, 640(1):213–218, 2011. doi:10.1016/j.nima.2011.03.018.

[3]   A. Lewis. *Uncertainty Analysis Procedures for Neutron-Induced Cross Section Measurements and Evaluations.* PhD thesis, University of California, Berkeley, 2020. URL `https://search-proquest-com.libproxy.berkeley.edu/dissertations-theses/uncertainty-analysis-procedures-neutron-induced/docview/2453690450/se-2?accountid=14496`.

[4]   V.V. Zerkin and B. Pritychenko. The experimental nuclear reaction data (EXFOR): Extended computer database and Web retrieval system. *Nuclear Instruments and Methods in Physics Research A*, 888:31–43, 2018. doi:10.1016/j.nima.2018.01.045.

[5]   NNDC. XUNDL: Experimental Unevaluated Nuclear Data List. Technical report, Brookhaven National Laboratory, Upton, New York. URL `https://www.nndc.bnl.gov/ensdf/ensdf/xundl.jsp`.

[6]   M. Bhat. Evaluated Nuclear Structure Data File (ENSDF), in: Qaim S.M. (Ed.) Nuclear Data for Science and Technology. Springer, Berlin, Heidelberg, 1992. doi:10.1007/978-3-642-58113-7_227.

[7]   D.A. Brown, M.B. Chadwick, R. Capote, A.C. Kahler, A. Trkov, M.W. Herman, A.A. Sonzogni, Y. Danon, A.D. Carlson, M. Dunn, D.L. Smith, and G.M. Hale. ENDF/B-VIII.0: The 8th Major Release of the Nuclear Reaction Data Library with CIELO-project Cross Sections, New Standard and Thermal Scattering Data. *Nuclear Data Sheets*, 148: 1–142, 2018. doi:10.1016/j.nds.2018.02.001.

[8] K. Shibata, O. Iwamoto, T. Nakagawa, N. Iwamoto, A. Ichihara, S. Kunieda, S. Chiba, K. Futuraka, N. Otuka, T. Ohsawa, T. Murata, H. Matsunobu, A. Zukeran, S. Kamada, and J. Katakura. JENDL-4.0 : A New Library for Nuclear Science and Engineering. *Journal of Nuclear Science and Technology*, 48(1):1–30, 2012. doi:10.1080/18811248.2011.9711675.

[9] A. Koning, R. Forrest, M. Kellett, R. Mills, H. Henriksson, and Y. Rugama. The JEFF-3.1 Nuclear Data Library. Technical Report 6190, Nuclear Energy Agency, 2006.

[10] A. Trkov, P.J. Griffin, S.P. Simakov, L.R. Greenwood, K.I. Zolotarev, R. Capote, D.L. Aldama, V. Chechev, C. Destouches, A.C. Kahler, C. Konno, M. Košťál, M. Majerle, E. Malambu, M. Ohta, V.G. Pronyaev, V. Radulović, S. Sato, M. Schulc, E. Šimečková, I. Vavtar, J. Wagemans, M. White, and H. Yashima. IRDFF-II: A New Neutron Metrology Library. *Nuclear Data Sheets*, 163:1–108, 2020. doi:10.1016/j.nds.2019.12.001.

[11] H. Choi, R. Firestone, R. Lindstrom, G. Molnár, S. Mughabghab, R. Paviotti-Corcuera, Z. Revay, A. Trkov, V. Zerkin, and C. Zhou. *Database of Prompt Gamma Rays from Slow Neutron Capture for Elemental Analysis.* IAEA, Vienna, 2007. URL `http://www-pub.iaea.org/MTCD/publications/PDF/Pub1263_web.pdf`.

[12] F.T. Tárkányi, A.V. Ignatyuk, A. Hermanne, R. Capote, B.V. Carlson, J.W. Engle, M.A. Kellet, T. Kibedi, G.N. Kim, F.G. Kondev, M. Hussain, O. Lebeda, A. Luca, Y. Nagai, H. Naik, A.L. Nichols, F.M. Nortier, S.V. Suryanarayana, S. Takacs, and M. Verpelli. Recommended nuclear data for medical radioisotope production: diagnostic positron emitters. *Journal of Radioanalytical and Nuclear Chemistry*, 319(2):533–666, 2019. doi:10.1007/s10967-018-6380-5.

[13] A.M. Hurst, L.A. Bernstein, and S.A. Chong. Compilation of "Atlas of Gamma-rays from the Inelastic Scattering of Reactor Fast Neutrons" by A.M. Demidov, L.I. Govor, Yu.K. Cherepantsev, M.R. Ahmed, S. Al-Najjar, M.A. Al-Amili, N. Al-Assafi, and N. Rammo. Technical report, Lawrence Berkeley National Laboratory, LBNL-1007259, Berkeley, 2017. URL `https://escholarship.org/uc/item/7pz1t3x7`.

[14] S. Mughabghab. *Atlas of Neutron Resonances.* Elsevier, Amsterdan, sixth edition, 2018. doi:https://doi.org/10.1016/C2015-0-00522-6.

[15] A.J. Koning, D. Rochman, J.C. Sublet, N. Dzysiuk, M. Fleming, and S. van der Marck. TENDL: Complete Nuclear Data Library for Innovative Nuclear Science and Technology. *Nuclear Data Sheets*, 155:1–55, 2019. doi:10.1016/j.nds.2019.01.002.

[16] R. Capote, M. Herman, P. Oblozinsky, P.G. Young, S. Goriely, T. Belgya, A.V. Ignatyuk, A.J. Koning, S. Hilaire, and Others. RIPL – Reference Input Parameter Library for Calculation of Nuclear Reactions and Nuclear Data Evaluations. *Nuclear Data Sheets*, 110:3107–3214, 2009. doi:10.1016/j.nds.2009.10.004.

[17] N. Otuka, E. Dupont, V. Semkova, B. Pritychenko, A.I. Blokhin, M. Aikawa, S. Babykina, M. Bossant, G. Chen, S. Dunaeva, R.A. Forrest, T. Fukahori, N. Furutachi, S. Ganesan, Z. Ge, O.O. Gritzay, M. Herman, S. Hlavač, K. Kato, B. Lalremruata, Y.O. Lee, A. Makinaga, K. Matsumoto, M. Mikhaylyukova, G. Pikulina, V.G. Pronyaev, A. Saxena, O. Schwerer, S.P. Simakov, N. Soppera, R. Suzuki, S. Takács, X. Tao, S. Taova, F. Tárkányi, V.V. Varlamov, J. Wang, S.C. Yang, V. Zerkin, and Y. Zhuang. Towards a More complete and accurate experimental nuclear reaction data library (EXFOR): International collaboration between nuclear reaction data centres (NRDC). *Nuclear Data Sheets*, 120:272–276, 2014. doi:10.1016/j.nds.2014.07.065.

[18] E. Browne and J.K. Tuli. Nuclear Data Sheets for A = 99. *Nuclear Data Sheets*, 145: 25–340, 2017. doi:10.1016/j.nds.2017.09.002.

[19] D. Updegraff and S. Hoedl. Nuclear Medicine without Nuclear Reactors or Uranium Enrichment. In *Center for Science, Technology and Security Policy*, Washington, D.C., 2013. American Association for the Advancement of Science.

[20] S.A. Hoedl and W.D. Updegraff. The production of medical isotopes without nuclear reactors or uranium enrichment. *Science and Global Security*, 23(2):121–153, 2015. doi:10.1080/08929882.2015.1037123.

[21] A.L. Nichols, S.M. Qaim, and R. Capote. Summary Report of the Technical Meeting on Intermediate-term Nuclear Data Needs for Medical Applications: Cross Sections and Decay Data. Technical report, International Atomic Energy Agency, Vienna, 2011. URL https://www-nds.iaea.org/publications/indc/indc-nds-0596/.

[22] R. Capote and F.M. Nortier. Improvements in Charged-Particle Monitor Reactions and Nuclear Data for Medical Isotope Production. Technical report, International Atomic Energy Agency, Vienna, 2011.

[23] L. Bernstein, D. Brown, A. Hurst, J. Kelly, F. Kondev, E. McCutchan, C. Nesaraja, R. Slaybaugh, and A. Sonzogni. Nuclear Data Needs and Capabilities for Applications. 2015. URL http://arxiv.org/abs/1511.07772.

[24] R. Capote, A.L. Nichols, F.M. Nortier, B.V. Carlson, J.W. Engle, A. Hermanne, M. Hussain, A.V. Ignatyuk, M.A. Kellett, T. Kibédi, G. Kim, F.G. Kondev, O. Lebeda,

A. Luca, H. Naik, Y. Nagai, I. Spahn, S.V. Suryanarayana, F.T. Tárkányi, and M. Verpelli. IAEA coordinated research project on nuclear data for charged-particle monitor reactions and medical isotope production. *EPJ Web of Conferences*, 146:08007, 2017. doi:10.1051/epjconf/201714608007.

[25] S.M. Qaim. Nuclear data for production and medical application of radionuclides: Present status and future needs. *Nuclear Medicine and Biology*, 44:31–49, 2017. doi:10.1016/j.nucmedbio.2016.08.016.

[26] H. Schrader. Measurement of the Half-lives of ^{18}F, ^{56}Co, ^{125}I, ^{195}Au, and ^{201}Tl. *Applied Radiation and Isotopes*, 40(5):381–383, 1989. doi:10.1016/0883-2889(89)90201-3.

[27] A.J. Koning and M.C. Duijvestijn. A global pre-equilibrium analysis from 7 to 200 MeV based on the optical model potential. *Nuclear Physics A*, 744:15–76, 2004. doi:10.1016/j.nuclphysa.2004.08.013.

[28] A.S. Voyles. *Nuclear Excitation Functions for the Production of Novel Medical Radionuclides.* PhD thesis, University of California, Berkeley, 2018. URL https://search-proquest-com.libproxy.berkeley.edu/docview/2135771326?accountid=14496.

[29] M. Johnson and LBNL. 88-Inch Cyclotron: BASE - Rad Effects, 2021. URL https://cyclotron.lbl.gov/base-rad-effects.

[30] F.M. Nortier, M.E. Fassbender, M. DeJohn, V. Hamilton, R. Heaton, D. Jamriska, J. Kitten, J. Lenz, C. Lowe, C. Moddrell, L. McCurdy, E. Peterson, L. Pitt, D. Phillips, L. Salazar, P. Smith, and F. Valdez. Targetry at the LANL 100 MeV Isotope Production Facility: Lessons Learned from Facility Commissioning. Technical report, LANL, Los Alamos, NM, 2004. URL https://www.osti.gov/servlets/purl/840202.

[31] Los Alamos National Laboratory, C. Beard, D.L. Clark, G.D. Jarvinen, A. Migliori, W. Runde, M. Coonley, K. Parker, E. Lorusso, and L. Archuleta. Accelerator Radioisotopes Save Lives: Part II. *Actinide Research Quarterly*, pages 1–44, 2010. URL https://www.lanl.gov/discover/publications/actinide-research-quarterly/pdfs/2010-1st-quarter.pdf.

[32] L. Mausner and P. Richards. The Production of Spallation Radionuclides for Medical Applications at BLIP. *IEEE Transactions on Nuclear Science*, 30(2):1793–1796, 1983. doi:10.1109/TNS.1983.4332644.

[33] L.F. Mausner. Isotope Production at Brookhaven National Laboratory. In *AIChE Annual Meeting - Engineering Applications of Radioisotopes*, Philadelphia,

2008. URL `https://www.researchgate.net/publication/267237165_Isotope_Production_at_Brookhaven_National_Laboratory`.

[34] M.B. Fox, A.S. Voyles, J.T. Morrell, L.A. Bernstein, A.M. Lewis, A.J. Koning, J.C. Batchelder, E.R. Birnbaum, C.S. Cutler, D.G. Medvedev, F.M. Nortier, E.M. O'Brien, and C. Vermeulen. Investigating high-energy proton-induced reactions on spherical nuclei: Implications for the preequilibrium exciton model. *Physical Review C*, 103(3): 034601, 2021. doi:10.1103/PhysRevC.103.034601.

[35] National Research Council and Institue of Medicine of the National Academies. *Advancing Nuclear Medicine Through Innovation*. The National Academies Press, Washington, D.C., 2007.

[36] A.S. Voyles, L.A. Bernstein, E.R. Birnbaum, J.W. Engle, S.A. Graves, T. Kawano, A.M. Lewis, and F.M. Nortier. Excitation functions for (p,x) reactions of niobium in the energy range of $E_p = 40 - 90$ MeV. *Nuclear Instruments and Methods in Physics Research B*, 429:53–74, 2018. doi:10.1016/j.nimb.2018.05.028.

[37] K.V. Becker, E. Vermeulen, C.J. Kutyreff, E.M. O'Brien, J.T. Morrell, E.R. Birnbaum, L.A. Bernstein, F.M. Nortier, and J.W. Engle. Cross section measurements for proton induced reactions on natural La. *Nuclear Instruments and Methods in Physics Research B*, 468:81–88, 2020. doi:10.1016/j.nimb.2020.02.024.

[38] M.U. Khandaker, K. Kim, M.W. Lee, K.S. Kim, G.N. Kim, Y.S. Cho, and Y.O. Lee. Investigations of the ^{nat}Ti(p,x) ^{43,44m,44g,46,47,48}Sc, ^{48}V nuclear processes up to 40 MeV. *Applied Radiation and Isotopes*, 67(7-8):1348–1354, 2009. doi:10.1016/j.apradiso.2009.02.030.

[39] J.T. Morrell, A.S. Voyles, M.S. Basunia, J.C. Batchelder, E.F. Matthews, and L.A. Bernstein. Measurement of ^{139}La(p,x) cross sections from 35-60 MeV by stacked-target activation. *The European Physical Journal A*, 56:13, 2020. doi:10.1140/epja/s10050-019-00010-0.

[40] S.A. Graves, P.A. Ellison, T.E. Barnhart, H.F. Valdovinos, R. Eva, F.M. Nortier, R.J. Nickles, and J.W. Engle. Nuclear excitation functions of proton-induced reactions ($E_p = 35 - 90$ MeV) from Fe, Cu, Al. *Nuclear Instruments and Methods in Physics Research B*, 386:44–53, 2016. doi:10.1016/j.nimb.2016.09.018.Nuclear.

[41] L.A. Marus, J.W. Engle, K.D. John, E.R. Birnbaum, and F.M. Nortier. Experimental and computational techniques for the analysis of proton beam propagation through a target stack. *Nuclear Instruments and Methods in Physics Research B*, 345:48–52, 2015. doi:10.1016/j.nimb.2014.12.048.

[42] B.P. Singh, M.K. Sharma, M.M. Musthafa, H.D. Bhardwaj, and R. Prasad. A study of pre-equilibrium emission in some proton- and alpha-induced reactions. *Nuclear Instruments and Methods in Physics Research A*, 562:717–720, 2006. doi:10.1016/j.nima.2006.02.030.

[43] M. Blann. Preequilibrium Decay. *Annual Review of Nuclear Science*, 25:123–166, 1975. doi:10.1146/annurev.ns.25.120175.001011.

[44] K.S. Babu, Y.O. Lee, and S. Mukherjee. Analysis of charged particle induced reactions for beam monitor applications. *Nuclear Instruments and Methods in Physics Research B*, 283:46–54, 2012. doi:10.1016/j.nimb.2012.04.009.

[45] S.J. Mills, G.F. Steyn, and F.M. Nortier. Experimental and Theoretical Excitation Functions of Radionuclides Produced in Proton Bombardment of Copper up to 200 MeV. *International Journal of Radiation Applications and Instrumentation Part A*, 43 (8):1019–1030, 1992. doi:10.1016/0883-2889(92)90221-Y.

[46] E. Alhassan, D. Rochman, A. Vasiliev, R.M. Bergmann, M. Wohlmuther, A.J. Koning, and H. Ferroukhi. In search of the best nuclear data file for proton induced reactions: varying both models and their parameters. *2019 International Conference on Nuclear data for Science and Technology*, 5, 2019. doi:10.1051/epjconf/202023913005.

[47] A.J. Koning, S. Hilaire, and S. Goriely. TALYS-1.95 - A Nuclear Reaction Program, 2019. URL http://www.talys.eu.

[48] T. Kawano. Unified Coupled-Channels and Hauser-Feshbach Model Calculation for Nuclear Data Evaluation. Technical report, 2019.

[49] M. Herman, R. Capote, B.V. Carlson, P. Oblozinsky, M. Sin, A. Trkov, H. Wienke, and V. Zerkin. EMPIRE: Nuclear Reaction Model Code System for Data Evaluation. *Nuclear Data Sheets*, 108:2655–2715, 2007. doi:10.1016/j.nds.2007.11.003.

[50] M. Blann and J. Bisplinghoff. ALICE/LIVERMORE Precompound Compound Decay. Technical report, Lawrence Livermore National Laboratory, 1982.

[51] A.J. Koning and D. Rochman. Modern Nuclear Data Evaluation with the TALYS Code System. *Nuclear Data Sheets*, 113(12):2841–2934, 2012. doi:10.1016/j.nds.2012.11.002.

[52] S.M. Grimes. Hauser-Feshbach calculations in deformed nuclei. *Physical Review C*, 88 (2):24613, 2013. doi:10.1103/PhysRevC.88.024613.

[53] E.M. O'Brien. Novel design and diagnostics improvements for increased production capacity and improved reliability at the Los Alamos Isotope Production Facility. *Nuclear Instruments and Methods in Physics Research A*, 956:163316, 2020. doi:10.1016/j.nima.2019.163316.

[54] C.S. Cutler, D.G. Medvedev, A.J. Degraffenreid, V. Sanders, S.S. Jurisson, and K.J. Mausner. Production of Medical Radioisotopes for Medical Applications. In *First Biennial African Conference on Fundamental Physics and Applications*, Namibia University of Science and Technology, 2018. Brookhaven National Laboratory.

[55] A.J. DeGraffenreid, D.G. Medvedev, T.E. Phelps, M.D. Gott, S.V. Smith, S.S. Jurisson, and C.S. Cutler. Cross-section measurements and production of Se with medium to high energy protons using arsenic containing targets. *Radiochimica Acta*, 107(4):279–287, 2019. doi:10.1515/ract-2018-2931.

[56] W.J. Gallagher and S.J. Cipolla. A Model-Based Efficiency Calibration of a Si(Li) Detector in the Energy Region From 3 to 140 keV. *Nuclear Instruments and Methods*, 122:405–414, 1974. doi:10.1016/0029-554X(74)90508-4.

[57] J.T. Morrell. NPAT: Nuclear physics analysis tools, 2019. URL `https://jtmorrell.github.io/npat/build/html/index.html`.

[58] M.J. Berger, J.H. Hubbell, S.M. Seltzer, J. Chang, J.S. Coursey, R. Sukumar, D.S. Zucker, and K. Olsen. XCOM: Photon Cross Section Database (version 1.5), 2010.

[59] A. Hermanne, A.V. Ignatyuk, R. Capote, B.V. Carlson, J.W. Engle, M.A. Kellett, and T. Kib. Reference Cross Sections for Charged-particle Monitor Reactions. *Nuclear Data Sheets*, 148:338–382, 2018. doi:10.1016/j.nds.2018.02.009.

[60] J.F. Ziegler, M.D. Ziegler, and J.P. Biersack. SRIM – The stopping and range of ions in matter. *Nuclear Instruments and Methods in Physics Research B*, 268:1818–1823, 2010. doi:10.1016/j.nimb.2010.02.091.

[61] A.J. Koning and J.P. Delaroche. Local and global nucleon optical models from 1 keV to 200 MeV. *Nuclear Physics A*, 713:231–310, 2003. doi:10.1016/S0375-9474(02)01321-0.

[62] V. Avrigeanu, M. Avrigeanu, and C. Manailescu. Further explorations of the α-particle optical model potential at low energies for the mass range $A \approx 45 - 209$. *Physical Review C*, 90(4):44612, 2014. doi:10.1103/PhysRevC.90.044612.

[63] V. Avrigeanu and P.E. Hodgson. Global optical potentials for emitted alpha particles. *Physical Review C*, 49(4):2136–2141, 1994. doi:10.1103/PhysRevC.49.2136.

[64] M. Avrigeanu, A.C. Obreja, F.L. Roman, and V. Avrigeanu. Complementary optical-potential analysis of α-particle elastic scattering and induced reactions at low energies. *Atomic Data and Nuclear Data Tables*, 95(4):501–532, 2009. doi:10.1016/j.adt.2009.02.001.

[65] F.D. Becchetti and G.W. Greenlees. Nucleon-Nucleus Optical-Model Parameters, A>40, E<50 MeV. *Physical Review*, 182(4):1190–1209, 1969. doi:10.1103/PhysRev.182.1190.

[66] G. Igo. Optical-Model Analysis of Excitation Function Data and Theoretical Reaction Cross Sections for Alpha Particles. *Physical Review*, 115(6):1665–1674, 1959. doi:10.1103/PhysRev.115.1665.

[67] R. Michel, R. Bodemann, H. Busemann, R. Daunke, M. Gloris, H.J. Lange, B. Klug, A. Krins, I. Leya, M. Lüpke, S. Neumann, H. Reinhardt, M. Schnatz-Büttgen, U. Herpers, T. Schiekel, F. Sudbrock, B. Holmqvist, H. Condé, P. Malmborg, M. Suter, B. Dittrich-Hannen, P.W. Kubik, H.A. Synal, and D. Filges. Cross sections for the production of residual nuclides by low- and medium-energy protons from the target elements C, N, O, Mg, Al, Si, Ca, Ti, V, Mn, Fe, Co, Ni, Cu, Sr, Y, Zr, Nb, Ba and Au. *Nuclear Instruments and Methods in Physics Research B*, 129(2):153–193, 1997. doi:10.1016/S0168-583X(97)00213-9.

[68] Y. Titarenko, V.F. Batyaev, A. Titarenko, M.A. Butko, K.V. Pavlov, S.N. Florya, R.S. Tikhonov, V.M. Zhivun, A.V. Ignatyuk, S.G. Mashnik, S. Leray, A. Boudard, J. Cugnon, D. Mancusi, Y. Yariv, K. Nishihara, N. Matsuda, H. Kumawat, G. Mank, and W. Gudowski. Measurement and Simulation of the Cross Sections for Nuclide Production in ^{93}Nb and ^{nat}Ni Targets Irradiated with 0.04- to 2.6-GeV Protons. *Physics of Atomic Nuclei*, 74(4):537–550, 2011. doi:10.1134/S106377881104017X.

[69] F. Ditrói, S. Takács, F. Tárkányi, M. Baba, E. Corniani, and Y. Shubin. Study of proton induced reactions on niobium targets up to 70 MeV. *Nuclear Instruments and Methods in Physics Research B*, 266(24):5087–5100, 2008. doi:10.1016/j.nimb.2008.09.023.

[70] G.F. Steyn, C. Vermeulen, F. Szelecsenyi, Z. Kovacs, K. Suzuki, T. Fukumara, and K. Nagatsu. Excitation Functions of Proton Induced Reactions on ^{89}Y and ^{93}Nb with Emphasis on the Production of Selected Radio-Zirconiums. *Journal of Korean Physical Society*, 59:1991–1994, 2011. doi:10.3938/jkps.59.1991.

[71] F. Ditrói, A. Hermanne, E. Corniani, S. Takács, F. Tárkányi, J. Csikai, and Y. Shubin. Investigation of proton induced reactions on niobium at low and medium energies. *Nuclear Instruments and Methods in Physics Research B*, 267(19):3364–3374, 2009. doi:10.1016/j.nimb.2009.07.010.

[72] G. Albouy, J.P. Cohen, M. Gusakow, N. Poffé, H. Sergolle, and L. Valentin. Réactions (p,3p3n) Entre 30 et 150 MeV. *Le Journal De Physique et Le Radium*, 24:67–68, 1963. doi:10.1051/jphysrad:0196300240106700.

[73] R.G. Korteling and E.K. Hyde. Interaction of High-Energy Protons and Helium Ions with Niobium. *Physical Review*, 136(2B):B425–437, 1964. doi:10.1103/PhysRev.136.B425.

[74] M.A. Avila-Rodriguez, J.S. Wilson, M.J. Schueller, and S.A. Mcquarrie. Measurement of the activation cross section for the (p,xn) reactions in niobium with potential applications as monitor reactions. *Nuclear Instruments and Methods in Physics Research B*, 266: 3353–3358, 2008. doi:10.1016/j.nimb.2008.05.015.

[75] V.N. Levkovskii, V.F. Reutov, and K.V. Botvin. Formation of Hydrogen in Zirconium, Niobium, and Molybdenum During Irradiation with Alpha Particles in the Energy Interval From 10 to 46 MeV. *Atomnaya Énergiya*, 69(2):99–101, 1990.

[76] B.G. Kiselev and N.R. Faizrakhmanova. Reaction Cross Sections of (p,n), (p,pn), and (p,$\alpha + n$) on 93-Nb. In *Program and Abstracts of Reports at the Twenty-Fourth Conference on Nuclear Spectroscopy and Nuclear Structure*, page 356, Leningrad, 1974.

[77] I.A. Rizvi, K. Kumar, T. Ahmad, A. Agarwal, and A.K. Chaubey. Energy dependence of pre-equilibrium emission for the (p,xn) reactions in niobium. *Indian Journal of Physics*, 86(10):913–918, 2012. doi:10.1007/s12648-012-0134-y.

[78] B. Lawriniang, R. Ghosh, S. Badwar, V. Vansola, and Y.S. Sheela. Measurement of cross-sections for the ^{93}Nb(p,n)^{93m}Mo and ^{93}Nb(p,pn)^{92m}Nb reactions up to ∼20 MeV energy. *Nuclear Physics A*, 973:79–88, 2018. doi:10.1016/j.nuclphysa.2018.02.008.

[79] S. Parashari, S. Mukherjee, B.K. Nayak, and R. Makwana. Excitation functions of the p + ^{93}Nb reaction in the energy range 10-22 MeV. *Nuclear Physics A*, 978:160–172, 2018. doi:10.1016/j.nuclphysa.2018.08.002.

[80] R.A. James. Excitation Functions of Proton-Induced Reactions of Nb^{93}. *Physical Review*, 93(2):288–290, 1954. doi:10.1103/PhysRev.93.288.

[81] C.W. Forsthoff, R.H. Goeckermann, and R.A. Naumann. Formation and Decay of Mo^{93m}. *Physical Review*, 90(5):1004–1005, 1953. doi:10.1103/PhysRev.90.1004.

[82] J.P. Blaser, F. Boehm, P. Marmier, and P. Scherrer. Anregungsfunktionen und Wirkungs-querschnitte der (p,n)-Reaktion (II). *Helvetica Physica Acta*, 24:441, 1951.

[83] E. Browne. Nuclear Data Sheets for A = 90. *Nuclear Data Sheets*, 82(3):379–546, 1997. doi:10.1006/ndsh.1997.0021.

[84] B. Singh. Nuclear Data Sheets for A = 89. *Nuclear Data Sheets*, 114(1):1–208, 2013. doi:10.1016/j.nds.2013.01.001.

[85] G.W. Severin, J.W. Engle, R.J. Nickles, and T.E. Barnhart. ^{89}Zr Radiochemistry for PET. *Journal of Medicinal Chemistry*, 7(5):389–394, 2011. doi:10.2174/157340611796799186.

[86] M. Sadeghi, M. Enferadi, and M. Bakhtiari. Accelerator production of the positron emitter zirconium-89. *Annals of Nuclear Energy*, 41:97–103, 2012. doi:10.1016/j.anucene.2011.11.014.

[87] E.A. Mccutchan and A.A. Sonzogni. Nuclear Data Sheets for A = 88. *Nuclear Data Sheets*, 115:135–304, 2014. doi:10.1016/j.nds.2013.12.002.

[88] A. Negret and B. Singh. Nuclear Data Sheets for A = 86. *Nuclear Data Sheets*, 124: 1–156, 2015. doi:10.1016/j.nds.2014.12.045.

[89] T.K. Nayak and M.W. Brechbiel. ^{86}Y based PET radiopharmaceuticals: radiochemistry and biological applications. *Journal of Medicinal Chemistry*, 7(5):380–388, 2011. doi:10.2174/157340611796799249.

[90] International Atomic Energy Agency. Cyclotron Produced Radionuclides: Physical Characteristics and Production Methods. Technical Report 468, 2009.

[91] J.J. Griffin. Statistical Model of Intermediate Structure. *Physical Review Letters*, 17 (9):478–481, 1966. doi:10.1103/PhysRevLett.17.478.

[92] C. Kalbach. Two-component exciton model: Basic formalism away from shell closures. *Physical Review C*, 33:818–833, 1986. doi:10.1103/PhysRevC.33.818.

[93] C.K. Cline and M. Blann. The Pre-equilibrium Statistical Model: Description of the Nuclear Equilibration Process and Parameterization of the Model. *Nuclear Physics A*, 172:225–229, 1971. doi:10.1016/0375-9474(71)90713-5.

[94] J. Dobeš and E. Běták. Two-Component Exciton Model. *Zeitschrift fur Physik A*, 310: 329–338, 1983. doi:10.1007/BF01419519.

[95] A.A. Selman. *Neutron Induced Preequilibrium Nuclear Reactions Using the Exciton Model*. PhD thesis, University of Baghdad, 2009.

[96] H. Fuladvand, M. Bakhtiari, M. Sadeghi, and M. Amiri. Pre-equilibrium effects on proton, deuteron, and alpha induced reactions for the production of ^{72}As as a PET

imaging radioisotope. *Journal of Radioanalytical and Nuclear Chemistry*, 298:501–512, 2013. doi:10.1007/s10967-013-2447-5.

[97] T. Kakavand, M. Taghilo, and M. Sadeghi. Determination of ^{89}Zr Production Parameters via Different Reactions Using ALICE and TALYS Codes. In *Proceedings of the 18th International Conference on Nuclear Engineering - Volume 3*, pages 279–283, Xi'an, China (ASME, 2010), 2010.

[98] A.J. Koning. Status of the TALYS Evaluated Nuclear Data Library - TENDL. In *25th WPEC Meeting*, Issy-les-Moulineaux, France, 2013.

[99] A.J. Koning. Status of TENDL : TENDL-2014 and beyond. In *27th WPEC Meeting*, Issy-les-Moulineaux, France, 2015.

[100] J.C. Brodovitch, J.J. Hogan, and K. Burns. The Pre-equilibrium Statistical Model: Comparison of Calculations With Two (p,xn) Reactions. *Journal of Inorganic and Nuclear Chemistry*, 38:1581–1586, 1976. doi:10.1016/0022-1902(76)80639-2.

[101] B.V. Carlson. The Optical Model. Technical report, Joint ICTP-IAEA Workshop on Nuclear Reaction Data for Advanced Reactor Technologies, The Abdus Salam International Centre for Theoretical Physics, 2010.

[102] E. Alhassan, D. Rochman, A. Vasiliev, M. Wohlmuther, M. Hursin, A.J. Koning, and H. Ferroukhi. Iterative Bayesian Monte Carlo for nuclear data evaluation.

[103] A.J. Koning. Bayesian Monte Carlo Method for Nuclear Data Evaluation. *Nuclear Data Sheets*, 123:207–213, 2015. doi:10.1016/j.nds.2014.12.036.

[104] E. Alhassan, D. Rochman, A. Vasiliev, A.J. Koning, and H. Ferroukhi. Bayesian updating for data adjustments and multi-level uncertainty propagation within Total Monte Carlo. *Annals of Nuclear Energy*, 139:1–21, 2020.

[105] F.T. Tárkányi, A. Hermanne, F. Ditrói, and S. Takács. Activation cross section data of proton induced nuclear reactions on lanthanum in the 34-65 MeV energy range and application for production of medical radionuclides. *Journal of Radioanalytical and Nuclear Chemistry*, 312:691–704, 2017. doi:10.1007/s10967-017-5253-7.

[106] G. Albouy, M. Gusakow, N. Poffé, H. Sergolle, and L. Valentin. Réactions (p,n) A Moyenne Énergie. *Le Journal De Physique et Le Radium*, 23:1000–1002, 1962. doi:10.1051/jphysrad:0196200230120100001.

[107] H.E. Hassan, F.S. Al-Saleh, K.F. Hassan, A. Sayed, and Z.A. Saleh. Proton induced reactions on ^{159}Tb and ^{139}La for producing ^{159}Dy and ^{139}Ce. In *Arab Journal of Nuclear Sciences and Applications*, volume 43, pages 233–242, Luxor, Egypt, 2010.

[108] J. Wing and J.R. Huizenga. (p,n) Cross Sections of V^{51}, Cr^{52}, Cu^{63}, Cu^{65}, Ag^{107}, Ag^{109}, Cd^{111}, Cd^{114}, and La^{139} from 5 to 10.5 MeV. *Physical Review*, 128:280–290, 1962. doi:10.1103/PhysRev.128.280.

[109] P. Kirby and W.T. Link. Farady-Cup Measurement of Proton Total Reaction Cross Sections at 100 MeV. *Canadian Journal of Physics*, 44:1847–1862, 1966. doi:10.1139/p66-155.

[110] M. Trzaska, D. Pelte, M. Lemaire, D. Bachelier, N. Bastid, J. Boyard, C. Cavata, P. Charmensat, J. Cugnon, P. Dupieux, P. Gorodetzky, J. Gosset, and T. Hennino. Excitation of the $\Delta(1232)$-resonance in proton nucleus collisions. *Zeitschrift fur Physik A - Hadrons and Nuclei*, 340:325–331, 1991. doi:10.1007/BF01294681.

[111] B.D. Wilkins and G. Igo. 10-MeV Proton Reaction Cross Sections for Several Elements. *Physical Review*, 129(5):2198–2206, 1963. doi:10.1103/PhysRev.129.2198.

[112] S.M. Grimes. Energy dependence of the nuclear level density at energies above 100 MeV. *Physical Review C*, 42(6):2744–2747, 1990. doi:10.1103/PhysRevC.42.2744.

[113] S.M. Grimes, J.D. Anderson, A.K. Kerman, and C. Wong. Role of Isospin in Statistical Processes. *Physical Review C*, 5(1):85–95, 1972. doi:10.1103/PhysRevC.5.85.

[114] D. Robson, A. Richter, and H.L. Harney. Consequences of Isospin and Other Conserved Quantum Numbers for Compound-Nucleus Reactions. *Physical Review C*, 8(1):153–160, 1973. doi:10.1103/PhysRevC.8.153.

[115] C.C. Lu, J.R. Huizenga, C.J. Stephan, and A.J. Gorski. Effects of Isospin on Statistical Nuclear Decay. *Nuclear Physics A*, 164(2):225–245, 1971. doi:10.1016/0375-9474(71)90210-7.

[116] C. Kalbach-Cline, J.R. Huizenga, and H.K. Vonach. Isospin Conservation and Pre-Equilibrium Decay in (p,p$'$) Reactions on Neutron Rich Tin Isotopes. *Nuclear Physics A*, 222(2):405–428, 1974. doi:10.1016/0375-9474(74)90400-X.

[117] L.A. Bernstein, C. Romano, D.A. Brown, R. Casperson, M. Descalle, M. Devlin, and C. Pickett. Final Report for the Workshop for Applied Nuclear Data Activities. Technical report, George Washington University, Washington, D.C., 2019.

[118] M.B. Fox. TREND As, Nb, Cu, Ti Gamma Spectroscopy [Data set], 2021. URL http://doi.org/10.5281/zenodo.4648950.

[119] D. Abriola and A.A. Sonzogni. Nuclear Data Sheets for A = 72. *Nuclear Data Sheets*, 111(1):1–140, 2010. doi:10.1016/j.nds.2009.12.001.

[120] M. Jennewein, S.M. Qaim, P.V. Kulkarni, R.P. Mason, A. Hermanne, and F. Rösch. A no-carrier-added ^{72}Se/^{72}As radionuclide generator based on solid phase extraction. *Radiochimica Acta*, 93:579–583, 2005. doi:https://doi.org/10.1524/ract.92.4.245.35611.

[121] J. Katakura and Z.D. Wu. Nuclear Data Sheets for A = 124. *Nuclear Data Sheets*, 109 (7):1655–1877, 2008. doi:10.1016/j.nds.2008.06.001.

[122] G.L. Cascini, A.N. Asabella, A. Notaristefano, A. Restuccia, C. Ferrari, D. Rubini, C. Altini, and G. Rubini. ^{124}Iodine: A Longer-Life Positron Emitter Isotope - New Opportunities in Molecular Imaging. *BioMed Research International*, 2014(672094): 1–7, 2014. doi:https://doi.org/10.1155/2014/672094.

[123] B. Singh and N. Nica. Nuclear Data Sheets for A = 77. *Nuclear Data Sheets*, 113(5): 1115–1314, 2012. doi:10.1016/j.nds.2012.05.001.

[124] M. Jennewein, M.A. Lewis, D. Zhao, E. Tsyganov, N. Slavine, J. He, L. Watkins, V.D. Kodibagkar, S.O. Kelly, P. Kulkarni, P.P. Antich, A. Hermanne, F. Ro, R.P. Mason, and P.E. Thorpe. Vascular Imaging of Solid Tumors in Rats with a Radioactive Arsenic-Labeled Antibody that Binds Exposed Phosphatidylserine. *Clinical Cancer Research*, 14(5):1377–1386, 2008. doi:10.1158/1078-0432.CCR-07-1516.

[125] V.A. Sanders and C.S. Cutler. Radioarsenic: A promising theragnostic candidate for nuclear medicine. *Nuclear Medicine and Biology*, 92:184–201, 2021. doi:10.1016/j.nucmedbio.2020.03.004.

[126] P.A. Ellison, T.E. Barnhart, F. Chen, H. Hong, Y. Zhang, C.P. Theuer, W. Cai, R.J. Nickles, and O.T. DeJesus. High Yield Production and Radiochemical Isolation of Isotopically Pure Arsenic-72 and Novel Radioarsenic Labeling Strategies for the Development of Theranostic Radiopharmaceuticals. *Bioconjugate Chemistry*, 27(1): 179–188, 2017. doi:10.1021/acs.bioconjchem.5b00592.High.

[127] B. Ballard, F.M. Nortier, E.R. Birnbaum, K.D. John, D.R. Phillips, and M. Fassbender. Radioarsenic from a Portable ^{72}Se/^{72}As Generator: A Current Perspective. *Current Radiopharmaceuticals*, 5:264–270, 2012. doi:10.2174/1874471011205030264.

[128] B. Ballard, D. Wycoff, E.R. Birnbaum, K.D. John, J.W. Lenz, S.S. Jurisson, C.S. Cutler, F.M. Nortier, W.A. Taylor, and M.E. Fassbender. Selenium-72 formation via ^{nat}Br(p,x) induced by 100MeV Protons: Steps towards a novel ^{72}Se/ ^{72}As generator system. *Applied Radiation and Isotopes*, 70(4):595–601, 2012. doi:10.1016/j.apradiso.2012.01.018.

[129] M. Fassbender, D. De Villiers, M. Nortier, and N. Van der Walt. The ^{nat}Br(p,x)^{73,75}Se nuclear processes: a convenient route for the production of radioselenium tracers relevant to amino acid labelling. *Applied Radiation and Isotopes*, 54(6):905–913, 2001. doi:10.1016/S0969-8043(00)00359-6.

[130] S. Takács, M.P. Takács, F. Ditrói, M. Aikawa, H. Haba, and Y. Komori. Activation cross sections of longer-lived radionuclides produced in germanium by alpha particle irradiation. *Nuclear Instruments and Methods in Physics Research B*, 383:213–226, 2016. doi:10.1016/j.nimb.2016.07.015.

[131] E.A. McCutchan. Nuclear Data Sheets for A = 68. *Nuclear Data Sheets*, 113(6-7): 1735–1870, 2012. doi:10.1016/j.nds.2012.06.002.

[132] L. Martiniova, L.D. Palatis, E. Etchebehere, and G. Ravizzini. Gallium-68 in Medical Imaging. *Current Radiopharmaceuticals*, 9:187–207, 2016. doi:10.2174/1874471009666161028150.

[133] F. Roesch and D.V. Filosofov. Production of Long Lived Parent Radionuclides for Generators : ^{68}Ge, ^{82}Sr, ^{90}Sr and ^{188}W. *IAEA Radioisotopes and Radiopharmaceuticals Series*, 2, 2010.

[134] B.P. Burke and S.J. Archibald. *Labeling with Gallium-68*. Second edition, 2020. doi:10.1002/9781119500575.ch9.

[135] C. Kratochwil, F. Bruchertseifer, H. Rathke, M. Hohenfellner, F.L. Giesel, U. Haberkorn, and A. Morgenstern. Targeted α-Therapy of Metastatic Castration-Resistant Prostate Cancer with ^{225}Ac-PSMA-617: Swimmer-Plot Analysis Suggests Efficacy Regarding Duration of Tumor Control. *Journal of Nuclear Medicine*, 59(5):795–803, 2018. doi:10.2967/jnumed.117.203539.

[136] S. Hogle, E. O'Brien, A.S. Voyles, K. Kolos, and V. Sobes. Predictive Codes for Isotope Production. In *Workshop for Applied Nuclear Data Activities (WANDA 2021)*, Washington, D.C., 2021. URL `https://conferences.lbl.gov/event/504/`.

[137] J.W. Engle, S.G. Mashnik, J.W. Weidner, L.E. Wolfsberg, M. Fassbender, K. Jackman, A. Couture, L.J. Bitteker, J.L. Ullmann, M.S. Gulley, C. Pillai, K.D. John, E.R.

Birnbaum, and F.M. Nortier. Cross sections from proton irradiation of thorium at 800 MeV. *Physical Review C*, 88(1):014604, 2013. doi:10.1103/PhysRevC.88.014604.

[138] J.W. Engle, S.G. Mashnik, L.A. Parker, K.R. Jackman, L.J. Bitteker, J.L. Ullmann, M.S. Gulley, C. Pillai, K.D. John, E.R. Birnbaum, and F.M. Nortier. Nuclear excitation functions from 40 to 200 MeV proton irradiation of terbium. *Nuclear Instruments and Methods in Physics Research B*, 366:206–216, 2016. doi:10.1016/j.nimb.2015.10.049.

[139] J.T. Morrell. Curie: Python Toolkit for Experimental Nuclear Data, 2020. URL https://pypi.org/project/curie/.

[140] A.S. Voyles, A.M. Lewis, J.T. Morrell, M. Shamsuzzoha Basunia, L.A. Bernstein, J.W. Engle, S.A. Graves, and E.F. Matthews. Proton-induced reactions on Fe, Cu, & Ti from threshold to 55 MeV. *European Physics Journal A*, 57(94):1–23, 2021. doi:10.1140/epja/s10050-021-00401-2.

[141] A. Mushtaq, S.M. Qaim, and G. Stöcklin. Production of ^{73}Se via (p, 3n) and (d, 4n) Reactions on Arsenic. *International Journal of Radiation Applications and Instrumentation Part A*, 39(10):1085–1091, 1988. doi:10.1016/0883-2889(88)90146-3.

[142] S.M. Qaim, A. Mushtaq, and M. Uhl. Isomeric cross-section ratio for the formation of ^{73m,g}Se in various nuclear processes. *Physical Review C*, 38(2):645–650, 1988.

[143] V.N. Levkovski. *Middle Mass Nuclides (A=40-100) Activation Cross Sections by Medium Energy (E=10- 50 MeV) Protons and α-particles (Experiments and Systematics)*. Inter-Vesi, Moscow, 1991.

[144] B.L. Cohen and E.G. Newman. (p,pn) and (p,2n) Cross Sections in Medium Weight Elements. *Physical Review*, 99(3):718–723, 1953. doi:10.1103/PhysRev.99.718.

[145] S. Neumann. *Activation experiments with medium-energy neutrons and the production of extraterrestrial matter*. PhD thesis, University of Hanover, Germany, 1999.

[146] E. Garrido, C. Duchemin, A. Guertin, F. Haddad, N. Michel, and V. Métivier. New excitation functions for proton induced reactions on natural titanium, nickel and copper up to 70 MeV. *Nuclear Instruments and Methods in Physics Research B*, 383:191–212, 2016. doi:10.1016/j.nimb.2016.07.011.

[147] R.L. Brodzinski, L.A. Rancitelli, J.A. Cooper, and N.A. Wogman. High-Energy Proton Spallation of Titanium. *Physical Review C*, 4(4):1250–1257, 1971. doi:10.1103/PhysRevC.4.1250.

[148] R. Michel, F. Peiffer, and R. Stuck. Measurement and hybrid model analysis of integral excitation functions for proton-induced reactions on vanadium, manganese and cobalt up to 200 MeV. *Nuclear Physics A*, 441(4):617–639, 1985. doi:10.1016/0375-9474(85)90441-5.

[149] D. Fink, J. Sisterson, S. Vogt, G. Herzog, A. Magliss, J. Klein, R. Middleton, A. Koehler, and A. Magliss. Production of ^{41}Ca and K, Sc and V short-lived isotopes by the irradiation of Ti with 35 to 150 MeV protons: applications to solar cosmic ray studies. *Nuclear Instruments and Methods in Physics Research B*, 52:601–607, 1990. doi:10.1016/0168-583X(90)90483-B.

[150] R. Michel, G. Brinkmann, H. Weigel, and W. Herr. Proton-induced Reactions on Titanium with Energies Between 13 and 45 MeV. *Journal of Inorganic and Nuclear Chemistry*, 40(11):1845–1851, 1978. doi:10.1016/0022-1902(78)80241-3.

[151] K. Zarie, N. Al-Hammad, and A. Azzam. Experimental study of excitation functions of some proton induced reactions on ^{nat}Ti for beam monitoring purposes. *Radiochimica Acta*, 94(12):795–799, 2006. doi:10.1524/ract.2006.94.12.795.

[152] J. Cervenak and O. Lebeda. New cross-section data for proton-induced reactions on ^{nat}Ti and ^{nat}Cu with special regard to the beam monitoring. *Nuclear Instruments and Methods in Physics Research B*, 480:78–97, 2020. doi:10.1016/j.nimb.2020.08.006.

[153] P. Kopecky, F. Szelecsenyi, T. Molnar, P. Mikecz, and F.T. Tárkányi. Excitation Functions of (p,xn) Reactions on ^{nat}Ti: Monitoring of Bombarding Proton Beams. *Applied Radiation and Isotopes*, 44(4):687–692, 1993. doi:10.1016/0969-8043(93)90133-U.

[154] F. Bringas, M.T. Yamashita, I.D. Goldman, P.R. Pascholati, and V. Sciani. Measurement of Proton-Induced Reaction Cross Sections in Ti, Ni and Zr near the Threshold. *AIP Conference Proceedings*, 769(1):13–17, 2005.

[155] A. Hermanne, F.T. Tárkányi, S. Takács, F. Ditrói, and N. Amjed. Excitation functions for production of ^{46}Sc by deuteron and proton beams in ^{nat}Ti: A basis for additional monitor reactions. *Nuclear Instruments and Methods in Physics Research B*, 338:31–41, 2014. doi:10.1016/j.nimb.2014.07.026.

[156] B. Dittrich, U. Herpers, and T. Schiffmann. Thin-Target excitation functions for proton-produced long-lived radionuclides. Technical report, Fed. Rep. Germ. Report to the I.N.D.C. No.32/LN+SPECIAL, 1988.

[157] F.T. Tárkányi, F. Szelecsenyi, and P. Kopecky. Cross Section Data for Proton, ^{3}He and α-particle Induced Reactions onf ^{nat}Ni, ^{nat}Cu and ^{nat}Ti for Monitoring Beam Performance, in: Qaim S.M. (Ed.) Nuclear Data for Science and Technology. Springer, Berlin, Heidelberg, 1992. doi:10.1007/978-3-642-58113-7_151.

[158] J.R. Walton, D. Heymann, A. Yaniv, D. Edgerley, and M.W. Rowe. Cross Sections for He and Ne Isotopes in Natural Mg, Al, and Si, He Isotopes in CaF$_2$, Ar Isotopes in Natural Ca, and Radionuclides in Natural Al, Si, Ti, Cr, and Stainless Steel Induced by 12- to 45-MeV Protons. *Journal of Geophysical Research*, 81(32):5689–5699, 1976.

[159] S. Takács, F.T. Tárkányi, M. Sonck, and A. Hermanne. New cross-sections and intercomparison of proton monitor reactions on Ti, Ni and Cu. *Nuclear Instruments and Methods in Physics Research B*, 188:106–111, 2002. doi:10.1016/S0168-583X(01)01032-1.

[160] A. Grütter. Excitation Functions for Radioactive Isotopes Produced by Proton Bombardment of Cu and Al in the Energy Range of 16 to 70 MeV. *Nuclear Physics A*, 383 (1):98–108, 1982. doi:10.1016/0375-9474(82)90078-1.

[161] H.R. Heydegger, C.K. Garrett, and A. Van Ginneken. Thin-Target Cross Sections for Some Cr, Mn, Fe, Co, Ni, and Zn Nuclides Produced in Copper by 82- to 416- MeV Protons. *Physical Review C*, 6(4):1235–1240, 1972. doi:10.1103/PhysRevC.6.1235.

[162] C.J. Orth, B.J. Dropesky, R.A. Williams, G.C. Giesler, and J. Hudis. Pion-induced spallation of copper across the (3,3) resonance. *Physical Review C*, 18(3):1426–1435, 1978. doi:10.1103/PhysRevC.18.1426.

[163] H. Yashima, Y. Uwamino, H. Iwase, H. Sugita, T. Nakamura, S. Ito, and A. Fukumura. Measurement and calculation of radioactivities of spallation products by high-energy heavy ions. *Radiochimica Acta*, 91(12):689–696, 2003. doi:10.1524/ract.91.12.689.23423.

[164] L.R. Greenwood and R.K. Smither. Measurement of Cu spallation cross sections at IPNS. Technical report, U.S. Dept. of Energy, Fusion Energy Series, No.0046-18, 1984.

[165] I.R. Williams and C.B. Fulmer. Excitation Functions for Radioactive Isotopes Produced by Protons Below 60 MeV on Al, Fe, and Cu. *Physical Review*, 162(4):1055–1061, 1967.

[166] M. Shahid, K. Kim, H. Naik, M. Zaman, S.C. Yang, and G. Kim. Measurement of excitation functions in proton induced reactions on natural copper from their threshold to 43 MeV. *Nuclear Instruments and Methods in Physics Research B*, 342:305–313, 2015. doi:10.1016/j.nimb.2014.10.019.

[167] M.S. Uddin, M. Hagiwara, F.T. Tárkányi, F. Ditrói, and M. Baba. Experimental studies on the proton-induced activation reactions of molybdenum in the energy range 22-67 MeV. *Applied Radiation and Isotopes*, 60(6):911–920, 2004. doi:10.1016/j.apradiso.2004.02.004.

[168] A. Hermanne, F. Szelecsenyi, M. Sonck, S. Takács, F.T. Tárkányi, and P. Van den Winkel. New cross section data on ^{68}Zn(p,2n)^{67}Ga and ^{nat}Zn(p,xn)^{67}Ga nuclear reactions for the development of a reference data base. *Journal of Radioanalytical and Nuclear Chemistry*, 240(2):623–630, 1999. doi:10.1007/BF02349423.

[169] P. Kopecky. Proton Beam Monitoring via the Cu(p,x)^{58}Co, ^{63}Cu(p,2n)^{62}Zn and ^{65}Cu(p,n)^{65}Zn Reactions in Copper. *International Journal of Applied Radiation and Isotopes*, 36(8):657–661, 1985. doi:10.1016/0020-708X(85)90008-0.

[170] E.Z. Buthelezi, F.M. Nortier, and I.W. Schroeder. Excitation functions for the production of ^{82}Sr by proton bombardment of ^{nat}Rb at energies up to 100 MeV. *Applied Radiation and Isotopes*, 64(8):915–924, 2006. doi:10.1016/j.apradiso.2006.03.009.

[171] M.U. Khandaker, M.S. Uddin, K.S. Kim, Y.S. Lee, and G.N. Kim. Measurement of cross-sections for the (p,xn) reactions in natural molybdenum. *Nuclear Instruments and Methods in Physics Research B*, 262(2):171–181, 2007. doi:10.1016/j.nimb.2007.05.028.

[172] Y. Yoshizawa, H. Noma, T. Horiguchi, T. Katoh, S. Amemiya, M. Itoh, K. Hisatake, M. Sekikawa, and K. Chida. Isotope Separator On-Line at INS FM Cyclotron. *Nuclear Instruments and Methods*, 134(1):93–100, 1976. doi:10.1016/0029-554X(76)90128-2.

[173] F.S. Al-Saleh, A.A. Al-Harbi, and A. Azzam. Excitation functions of proton induced nuclear reactions on natural copper using a medium-sized cyclotron. *Radiochimica Acta*, 94(8):391–396, 2006. doi:10.1524/ract.2006.94.8.391.

[174] Y. Titarenko, V.F. Batyaev, V.M. Zhivun, A.B. Koldobsky, Y. Trebukhovsky, E.I. Karpikhin, R.D. Mulambetov, S.V. Mulambetova, Y. Nekrasov, A. Titarenko, K.A. Lipatov, B. Sharkov, A.A. Golubev, A.D. Fertman, V.I. Turtikov, A.V. Kantsyrev, I.V. Roudskoy, G.N. Smirnov, V.S. Barashenkov, K.K. Gudima, M.I. Baznat, S.G. Mashnik, and R.E. Prael. Nuclide Production Cross Sections for ^{59}Co and ^{nat}Cu Irradiated with 0.2 GeV and 2.6 GeV Protons and 0.2 GeV/Nucleon Carbon Ions. In *AccApp'03 Meeting*, page 8, San Diego, California, 2003.

[175] V.N. Aleksandrov, M.P. Semenova, and V.G. Semenov. Production Cross Section of Radionuclies in (p,x) Reaction at Copper and Nickel Nuclei. *Soviet Atomic Energy*, 62 (6):411–413, 1987. doi:10.1007/BF01124118.

[176] J. Kuhnhenn, U. Herpers, W. Glasser, R. Michel, P.W. Kubik, and M. Suter. Thin target cross sections for proton-induced formation of radionuclides from lead for $E_p \leq 71$ MeV. *Radiochimica Acta*, 89(11-12):697–702, 2001. doi:10.1524/ract.2001.89.11-12.697.

[177] C.U. Jost, J.R. Griswold, S.H. Bruffey, S. Mirzadeh, D.W. Stracener, and C.L. Williams. Measurement of cross sections for the ^{232}Th(p,4n)^{229}Pa reaction at low proton energies. *AIP Conference Proceedings*, 1525(1), 2013. doi:10.1063/1.4802383.

[178] H. Junde, H. Xiaolong, and J.K. Tuli. Nuclear Data Sheets for A = 67. *Nuclear Data Sheets*, 106(2):159–250, 2005. doi:10.1016/j.nds.2005.10.006.

[179] B. Singh and J. Chen. Nuclear data sheets for A = 73. *Nuclear Data Sheets*, 158:1–257, 2019. doi:10.1016/j.nds.2019.02.006.

[180] S.M. Qaim and I. Spahn. Development of novel radionuclides for medical applications. *Journal of Labelled Compounds and Radiopharmaceuticals*, 61(3):126–140, 2018. doi:10.1002/jlcr.3578.

[181] J. Chen, B. Singh, and J.A. Cameron. Nuclear Data Sheets for A = 44. *Nuclear Data Sheets*, 112(9):2357–2495, 2011. doi:10.1016/j.nds.2011.08.005.

[182] I.F. Chaple and S.E. Lapi. Production and use of first row transition metal PET radionuclides, ^{43,44}Sc, ^{52}Mn, and ^{45}Ti. *Journal of Nuclear Medicine*, 59(11):1655–1658, 2018. doi:10.2967/jnumed.118.213264.

[183] S. Ferguson, H. Jans, M. Wuest, T. Riauka, and F. Wuest. Comparison of scandium-44g with other PET radionuclides in pre-clinical PET phantom imaging. *European Journal of Nuclear Medicine and Molecular Imaging Physics*, 6(23):1–14, 2019. doi:10.1186/s40658-019-0260-0.

[184] Y. Nagame, H. Nakahara, and M. Furukawa. Excitation Functions for α and ^{3}He Particles Induced Reactions on Zinc. *Radiochimica Acta*, 46(1):5–12, 1989. doi:10.1524/ract.1989.46.1.5.

[185] F.H. Ruddy and B.D. Pate. Formation and decay of the compound nucleus ^{68}Ge. *Nuclear Physics A*, 127(2):305–322, 1969. doi:10.1016/0375-9474(69)90573-9.

[186] N.T. Porile, S. Tanaka, H. Amano, M. Furukawa, S. Iwata, and M. Yagi. Nuclear Reactions of Ga^{69} and Ga^{71} with 13-56 MeV Protons. *Nuclear Physics*, 43:500–522, 1963. doi:10.1016/0029-5582(63)90370-5.

[187] S. Amiel. Reactions of Alpha Particles with Germanium-70 and Zinc-70. *Physical Review*, 116(2):415, 1959. doi:10.1103/PhysRev.116.415.

[188] D.D. Villiers, M. Nortier, and W. Richter. Experimental and theoretical excitation functions for ^{nat}Br(p,x) reactions. *Applied Radiation and Isotopes*, 57(6):907–913, 2002. doi:10.1016/S0969-8043(02)00234-8.

[189] R. Adam-Rebeles, A. Hermanne, P. Van Den Winkel, L. De Vis, R. Waegeneer, F. Tárkányi, S. Takács, and M.P. Takács. ^{68}Ge/^{68}Ga production revisited: Excitation curves, target preparation and chemical separation - purification. *Radiochimica Acta*, 101(8):481–489, 2013. doi:10.1524/ract.2013.2057.

[190] A. Hermanne, R. Adam-Rebeles, F. Tárkányi, S. Takács, and F. Ditrói. Proton and deuteron induced reactions on ^{nat}Ga: Experimental and calculated excitation functions. *Nuclear Instruments and Methods in Physics Research B*, 359:145–154, 2015. doi:10.1016/j.nimb.2015.07.008.

[191] A. Mushtaq and S.M. Qaim. Excitation Functions of α- and ^{3}He-Particle Induced Nuclear Reactions on Natural Germanium: Evaluation of Production Routes for ^{73}Se. *Radiochimica Acta*, 50(1-2):27–32, 1990. doi:10.1524/ract.1990.50.12.27.

[192] B. Effenberger, W. Kunold, W. Oesterle, M. Schneider, L.M. Simons, R. Abela, and J. Wüest. Determination of the spectroscopic quadrupole moments of ^{75}As$_{33}$ and ^{63}Cu$_{29}$. *Zeitschrift fur Physik A - Atoms and Nuclei*, 309(1):77–81, 1982. doi:10.1007/BF01420154.

[193] P. Verma, C. Sharma, S. Singh, A. Bharti, and S.K. Khosa. Theoretical Overview of Back-bending in Arsenic Isotopes. *AIP Conference Proceedings*, 1524(1):101–104, 2013. doi:10.1063/1.4801687.

[194] S. Goriely, M. Samyn, and J.M. Pearson. Further explorations of Skyrme-Hartree-Fock-Bogoliubov mass formulas. VII. Simultaneous fits to masses and fission barriers. *Physical Review C*, 75(6):064312, 2007. doi:10.1103/PhysRevC.75.064312.

[195] C.G. Li, Q.B. Chen, S.Q. Zhang, C. Xu, H. Hua, X.Q. Li, X.G. Wu, S.P. Hu, J. Meng, F.R. Xu, W.Y. Liang, Z.H. Li, Y.L. Ye, D.X. Jiang, J.J. Sun, R. Han, C.Y. Niu, X.C. Chen, P.J. Li, C.G. Wang, H.Y. Wu, G.S. Li, C.Y. He, Y. Zheng, C.B. Li, Q.M. Chen, J. Zhong, and W.K. Zhou. Observation of a novel stapler band in ^{75}As. *Physics Letters B*, 766:107–111, 2017. doi:10.1016/j.physletb.2016.12.059.

[196] A. Obertelli, T. Baugher, D. Bazin, S. Boissinot, J.P. Delaroche, A. Dijon, F. Flavigny, A. Gade, M. Girod, T. Glasmacher, G.F. Grinyer, W. Korten, J. Ljungvall, S. McDaniel, A. Ratkiewicz, B. Sulignano, P. Van Isacker, and D. Weisshaar. First spectroscopy of ^{66}Se and ^{65}As: Investigating shape coexistence beyond the N=Z line. *Physics Letters B*, 701(4):417–421, 2011. doi:10.1016/j.physletb.2011.06.032.

[197] A.M. Bruce, J. Simpson, D.D. Warner, C. Baktash, C.J. Barton, M.A. Bentley, M.J. Brinkman, R.A. Cunningham, E. Dragulescu, L. Frankland, T.N. Ginter, C.J. Gross, R.C. Lemmon, B. MacDonald, C.D. O'Leary, S.M. Vincent, R. Wyss, C.H. Yu, and N.V. Zamfir. Two-neutron alignment and shape changes in ^{69}As. *Physical Review C*, 62(2):027303, 2000. doi:10.1103/PhysRevC.62.027303.

[198] T. Kawano. New Arsenic Cross Section Calculations. Technical report, LA-UR-15-21585, Los Alamos National Laboratory, Nuclear Data Team, Los Alamos, NM, 2015.

[199] K. Shibata, G. Chiba, A. Ichihara, and S. Kunieda. Evaluation of Neutron Nuclear Data on Arsenic-75 for JENDL-4. *Journal of Nuclear Science and Technology*, 47(1): 40–46, 2012. doi:10.1080/18811248.2010.9711925.

[200] B. Singh and A.R. Farhan. Nuclear Data Sheets for A = 74. *Nuclear Data Sheets*, 107 (7):1923–2102, 2006. doi:10.1016/j.nds.2006.05.006.

[201] B. Singh. Nuclear Data Sheets Update for A = 76. *Nuclear Data Sheets*, 74:63–164, 1995. doi:10.1006/ndsh.1994.1047.

[202] A.D. Ayangeakaa, R.V. Janssens, S. Zhu, D. Little, J. Henderson, C.Y. Wu, D.J. Hartley, M. Albers, K. Auranen, B. Bucher, M.P. Carpenter, P. Chowdhury, D. Cline, H.L. Crawford, P. Fallon, A.M. Forney, A. Gade, A.B. Hayes, F.G. Kondev, Krishichayan, T. Lauritsen, J. Li, A.O. MacChiavelli, D. Rhodes, D. Seweryniak, S.M. Stolze, W.B. Walters, and J. Wu. Evidence for Rigid Triaxial Deformation in ^{76}Ge from a Model-Independent Analysis. *Physical Review Letters*, 123(10):102501, 2019. doi:10.1103/PhysRevLett.123.102501.

[203] S. Goriely, F. Tondeur, and J.M. Pearson. A Hartree-Fock Nuclear Mass Table. *Atomic Data and Nuclear Data Tables*, 77(2):311–381, 2001. doi:10.1006/adnd.2000.0857.

[204] S. Hilaire, M. Girod, S. Goriely, and A.J. Koning. Temperature-dependent combinatorial level densities with the D1M Gogny force. *Physical Review C*, 86(6):064317, 2012. doi:10.1103/PhysRevC.86.064317.

[205] Y. Han, Y. Shi, and Q. Shen. Deuteron global optical model potential for energies up to 200 MeV. *Physical Review C*, 74(4):044615, 2006. doi:10.1103/PhysRevC.74.044615.

[206] S. Watanabe. High energy scattering of deuterons by complex nuclei. *Nuclear Physics*, 8(C):484–492, 1958. doi:10.1016/0029-5582(58)90180-9.

[207] G.P. Nobre, D.A. Brown, M.W. Herman, and A. Golas. Constraining level densities through quantitative correlations with cross-section data. *Physical Review C*, 101(3): 1–14, 2020. doi:10.1103/PhysRevC.101.034608.

[208] T. Kawano, S. Chiba, and H. Koura. Phenomenological Nuclear Level Densities using the KTUY05 Nuclear Mass Formula for Applications Off-Stability. *Journal of Nuclear Science and Technology*, 43(1):1–8, 2006. doi:10.1080/18811248.2006.9711062.

[209] S.M. Grimes, T.N. Massey, B.M. Oginni, S. Shukla, and A. Voinov. Nuclear Level Densities Off of the Stability Line. *AIP Conference Proceedings*, 1005:57–60, 2008. doi:10.1063/1.2920746.

[210] P. Roy, K. Banerjee, T.K. Rana, S. Kundu, S. Manna, A. Sen, D. Mondal, J. Sadhukhan, M.T. Senthil Kannan, T.K. Ghosh, S. Mukhopadhyay, D. Pandit, G. Mukherjee, S. Pal, D. Paul, K. Atreya, and C. Bhattacharya. Evidence for the reduction of nuclear level density away from the β-stability line. *Physical Review C*, 102:061601(R), 2020. doi:10.1103/physrevc.102.061601.

[211] E. Vagena, M. Axiotis, and P. Dimitriou. Systematics of semi-microscopic proton-nucleus optical potential at low energies relevant to nuclear astrophysics. *arXiv*, 2021. URL http://arxiv.org/abs/2103.07129.

[212] C. Romano, L.A. Bernstein, T. Bailey, F. Bostelmann, D. Brown, Y. Danon, R. Casperson, J. Conlin, M. Devlin, B. Goldblum, M. Grosskopf, A. Lewis, D. Neudecker, E.M. O'Brien, B. Pierson, B. Quiter, A. Ratkiewicz, G.W. Severin, M. Smith, V. Sobes, A. Sonzogni, P. Talou, F. Tovesson, E. Vermeulen, K. Wendt, and M. Zerkle. Proceedings of the Workshop for Applied Nuclear Data: WANDA2020. Technical report, ORNL/TM-2020/1617, Oak Ridge National Laboratory, Washington, D.C., 2020.

[213] P. Wang, Y. Hsieh, and I. Sun. On the Electrodeposition of Arsenic in a Choline Chloride/Ethylene Glycol Deep Eutectic Solvent. *Journal of The Electrochemical Society*, 164(4):D204–D209, 2017. doi:10.1149/2.1061704jes.

[214] S. Chandra, N. Khare, and H.M. Upadhyaya. Photoelectrochemical solar cells using electrodeposited GaAs and AlSb semiconductor films. *Bulletin of Materials Science*, 10 (4):323–332, 1988. doi:10.1007/BF02744303.

[215] H.F. Rohm and H. Munzel. Excitation Functions for Deuteron Reactions with ^{75}As. *Journal of Inorganic and Nuclear Chemistry*, 34(6):1773–1784, 1972. doi:10.1016/0022-1902(72)80523-2.

[216] A.S. Voyles. Targetry Fabrication for Nuclear Data Measurements. In *Workshop for Applied Nuclear Data Activities*, Washington, D.C., 2020. URL https://conferences.lbl.gov/event/292/.

[217] S.M. Qaim, G. Blessing, and H. Ollig. Excitation Functions of ^{75}As(α,n)^{78}Br and ^{75}As(α,2n)^{77m,g}Br Reactions from Threshold to 28 MeV. *Radiochimica Acta*, 39:57–60, 1986. doi:10.1524/ract.1986.39.2.57.

[218] Alfa Aesar. Arsenic Foil Products, 2021. URL `https://www.alfa.com/en/search/?q=arsenic+foil`.

[219] Goodfellow. Arsenic Product Search, 2021. URL `http://www.goodfellow.com/catalogue/GFCat4.php?ewd_token=UiV5M4AHpBAqPJii1ozeO1Tzq0koaE&n=VL5x23JEGfW6jv6polbD1iNwYNHr9c`.

[220] K. Breunig, I. Spahn, A. Hermanne, S. Spellerberg, B. Scholten, and H.H. Coenen. Cross section measurements of ^{75}As(α,xn)^{76,77,78}Br and ^{75}As(α,x)^{74}As nuclear reactions using the monitor radionuclides ^{67}Ga and ^{66}Ga for beam evaluation. *Radiochimica Acta*, 105(6):431–439, 2017. doi:10.1515/ract-2016-2593.

[221] T. Nozaki, M. Iwamoto, and Y. Itoh. Production of ^{77}Br by various nuclear reactions. *The International Journal Of Applied Radiation And Isotopes*, 30(2):79–83, 1979. doi:10.1016/0020-708X(79)90137-6.

[222] A.M. Paans, J. Welleweerd, W. Vaalburg, S. Reiffers, and M.G. Woldring. Excitation functions for the production of bromine-75: A potential nuclide for the labelling of radiopharmaceuticals. *The International Journal Of Applied Radiation And Isotopes*, 31(5):267–273, 1980. doi:10.1016/0020-708X(80)90032-0.

[223] Z. Alfassi and R. Weinreich. The Production of Positron Emitters ^{75}Br and ^{76}Br: Excitation Functions and Yields for ^{3}He and α-Particle Induced Nuclear Reactions on Arsenic. *Radiochimica Acta*, 30(2):67–71, 1982. doi:10.1524/ract.1982.30.2.67.

[224] S.L. Waters, A.D. Nunn, and M.L. Thakur. Cross-Section Measurements for the ^{75}As(α,2n)^{77}Br Reaction. *Journal of Inorganic Nuclear Chemistry*, 35(10):3413–3416, 1973. doi:10.1016/0022-1902(73)80346-X.

[225] D. Morrison and A. Caretto Jr. Excitation Functions of (p,xp) Reactions. *Physical Review*, 127(5):1731, 1962. doi:10.1103/PhysRev.127.1731.

[226] C.H. Johnson, A. Galonsky, and J.P. Ulrich. Proton strength functions from (p,n) cross sections. *Physical Review*, 109(4):1243–1254, 1958. doi:10.1103/PhysRev.109.1243.

[227] L. Bowen and J. Irvine Jr. Nuclear Excitation Functions and Thick-Target Yields F^{19}, Na^{23}, As^{75}(d,t), and Na^{23}, As^{75}(d,p). *Physical Review*, 127(5):1698, 1962. doi:10.1103/PhysRev.127.1698.

[228] M. Fassbender, H. Bach, E. Bond, F.M. Nortier, and D. Vieira. Preparation of thin arsenic and radioarsenic targets for neutron capture studies. *Journal of Radioanalytical and Nuclear Chemistry*, 282:365–368, 2009. doi:10.1007/s10967-009-0145-0.

[229] I.A. Menzies and L.W. Owen. The electrodeposition of arsenic from aqueous and non-aqueous solutions. *Electrochimica Acta*, 11(2):251–265, 1966. doi:10.1016/0013-4686(66)80012-9.

[230] A. Lupinacci, J. Kacher, A. Eilenberg, A.A. Shapiro, P. Hosemann, and A.M. Minor. Cryogenic in situ microcompression testing of Sn. *Acta Materialia*, 78:56–64, 2014. doi:10.1016/j.actamat.2014.06.026.

[231] D. Frazer, M.D. Abad, D. Krumwiede, C.A. Back, H.E. Khalifa, C.P. Deck, and P. Hosemann. Localized mechanical property assessment of SiC/SiC composite materials. *Composites: Part A*, 70:93–101, 2015. doi:10.1016/j.compositesa.2014.11.008.

[232] I. Sugai. An application of a new type deposition method to nuclear target preparation. *Nuclear Instruments and Methods in Physics Research A*, 397(1):81–90, 1997. doi:10.1016/S0168-9002(97)00733-X.

[233] Research Reactor Safety Analysis Services. McClellan Nuclear Radiation Center Reactor Safety Analysis Report. Technical report, University of California, Davis, Sacramento, California, 2000.

[234] X. Huang and M. Kang. Nuclear Data Sheets for A = 198. *Nuclear Data Sheets*, 133:221–416, 2016. doi:10.1016/j.nds.2016.02.002.

[235] B. Singh. Nuclear Data Sheets for A = 64. *Nuclear Data Sheets*, 108(2):197–364, 2007. doi:10.1016/j.nds.2007.01.003.

[236] M. Shamsuzzoha Basunia. Nuclear Data Sheets for A = 59. *Nuclear Data Sheets*, 151:1–333, 2018. doi:10.1016/j.nds.2018.08.001.

[237] B.J. Nyarko, R.B. Sogbadji, E.H. Akaho, and S. Agbemava. Cross Section Determination of Short-to-Medium Lived Nuclides in a Low Power Research and an Am-Be Neutron Source. In *Proceedings of the IAEA Technical Meeting in collaboration with NEA on Specific Applications of Research Reactors: Provision of Nuclear Data*, pages 72–84, Vienna, Austria, 2010. International Atomic Energy Agency. URL `http://www-nds.iaea.org/reports-new/indc-reports/indc-nds/indc-nds-0574.pdf`.

[238] T. Vidmar, M. Korun, A. Likar, and R. Martinčič. A semi-empirical model of the efficiency curve for extended sources in gamma-ray spectrometry. *Nuclear Instruments and*

Methods in Physics Research A, 470(3):533–547, 2001. doi:10.1016/S0168-9002(01)00799-9.

[239] M. Blaauw, D. Ridikas, S. Baytelesov, P.S. Salas, Y. Chakrova, C. Eun-Ha, R. Dahalan, A.H. Fortunato, R. Jacimovic, A. Kling, L. Muñoz, N.M. Mohamed, D. Párkányi, T. Singh, and V.D. Duong. Estimation of ^{99}Mo production rates from natural molybdenum in research reactors. *Journal of Radioanalytical and Nuclear Chemistry*, 311(1):409–418, 2017. doi:10.1007/s10967-016-5036-6.

[240] G. Steinhauser, S. Merz, F. Stadlbauer, P. Kregsamer, C. Streli, and M. Villa. Performance and comparison of gold-based neutron flux monitors. *Gold Bulletin*, 45(1): 17–22, 2012. doi:10.1007/s13404-011-0039-0.

[241] M. Karadag, H. Yücel, M. Tan, and A. Özmen. Measurement of thermal neutron cross-sections and resonance integrals for ^{71}Ga(n,γ)^{72}Ga and ^{75}As(n,γ)^{76}As by using ^{241}241Am-Be isotopic neutron source. *Nuclear Instruments and Methods in Physics Research A*, 501(2-3):524–535, 2003. doi:10.1016/S0168-9002(03)00408-X.

[242] M. Blaauw. The confusing issue of the neutron capture cross-section to use in thermal neutron self-shielding computations. *Nuclear Instruments and Methods in Physics Research A*, 356(2-3):403–407, 1995. doi:10.1016/0168-9002(94)01316-0.

[243] N.V. Do, P.D. Khue, K.T. Thanh, L.T. Son, G. Kim, Y.S. Lee, Y. Oh, H. Lee, M. Cho, I.S. Ko, and W. Namkung. Thermal neutron cross-section and resonance integral of the ^{186}W(n,γ)^{187}W reaction. *Nuclear Instruments and Methods in Physics Research B*, 266:863–871, 2008. doi:10.1016/j.nimb.2008.02.021.

[244] N.V. Do, P.D. Khue, K.T. Thanh, N.T. Hien, G. Kim, K. Kim, S.G. Shin, M.H. Cho, and M. Lee. Thermal neutron capture and resonance integral cross sections of ^{45}Sc. *Nuclear Instruments and Methods in Physics Research B*, 362:9–13, 2015. doi:10.1016/j.nimb.2015.08.075.

[245] S.F. Mughabghab. Thermal Neutron Capture Cross Sections, Resonance Integrals, and G-Factors. Technical report, International Nuclear Data Committee, IAEA, Vienna, 2003.

[246] C. Chilian, J. St-Pierre, and G. Kennedy. Complete thermal and epithermal neutron self-shielding corrections for NAA using a spreadsheet. *Journal of Radioanalytical and Nuclear Chemistry*, 278(3):745–749, 2008. doi:10.1007/s10967-008-1604-8.

[247] G.V. Kumar, S. Sen, E. Radha, J.S. Rao, R. Acharya, R. Kumar, C.R. Venkatasubramani, A.V. Reddy, and M. Joseph. Studies on neutron spectrum characterization for

the Pneumatic Fast Transfer System (PFTS) of KAMINI reactor. *Applied Radiation and Isotopes*, 124:49–55, 2017. doi:10.1016/j.apradiso.2017.03.009.

[248] H.M. Dung and F. Sasajima. Determination of α and f for k_0-NAA in irradiation sites with high thermalized neutrons. *Journal of Radioanalytical and Nuclear Chemistry*, 257 (3):509–512, 2003. doi:10.1023/A:1025472011260.

[249] F. De Corte, A. Simonits, and A.D. Wispelaere. Comparative Study of Measured and Critically Evaluated Resonance Integral To Thermal Cross Section Ratios, III. *Journal of Radioanalytical and Chemistry*, 133(1):131–151, 1989. doi:10.1007/BF02039971.

[250] H. Yücel and M. Karadag. Experimental determination of the α-shape factor in the $1/E^{1+\alpha}$ epithermal-isotopic neutron source-spectrum by dual monitor method. *Annals of Nuclear Energy*, 31(6):681–695, 2004. doi:10.1016/j.anucene.2003.10.002.

[251] F. De Corte, L. Moens, A. Simonits, A. De Wispelaere, and J. Hoste. Instantaneous α-determination without Cd-cover in the $1/E^{1+\alpha}$ epithermal neutron spectrum. *Journal of Radioanalytical Chemistry*, 52(2):295–304, 1979. doi:10.1007/BF02521280.

[252] T.A. Eastwood and R.D. Werner. Resonance and Thermal Neutron Self-Shielding in Cobalt Foils and Wires. *Nuclear Science and Engineering*, 13(4):385–390, 1962. doi:10.13182/nse62-a26181.

[253] S. Jovanovic, F.D. Corte, A. Simonits, L. Moens, P. Vukotic, R. Zejnilovic, and J. Hoste. Epithermal Neutron Flux Distribution and Its Impact on (n,γ) Activation Analysis Result. In *First Balkan conference on activation analysis*, page 196, Bulgaria, 1985.

[254] E. Martinho, I.F. Gonçalves, and J. Salgado. Universal curve of epithermal neutron resonance self-shielding factors in foils, wires and spheres. *Applied Radiation and Isotopes*, 58(3):371–375, 2003. doi:10.1016/S0969-8043(02)00313-5.

[255] J. Esposito, D. Bettoni, A. Boschi, M. Calderolla, S. Cisternino, G. Fiorentini, G. Keppel, P. Martini, M. Maggiore, L. Mou, M. Pasquali, L. Pranovi, G. Pupillo, C.R. Alvarez, L. Sarchiapone, G. Sciacca, H. Skliarova, P. Favaron, A. Lombardi, P. Antonini, and A. Duatti. LARAMED: A Laboratory for Radioisotopes of Medical Interest. *Molecules*, 24(1):20, 2019. doi:10.3390/molecules24010020.

[256] S.I. Sukhoruchkin and Z.N. Soroko. *Neutron Resonance Parameters for As-75 (Arsenic)*. Springer Materials, 2015. doi:10.1007/978-3-662-45603-3.

[257] S. Mughabghab and D. Garber. Neutron Cross Sections. Volume 1, Resonance Parameters. Technical report, National Neutron Cross Section Center, Brookhaven National Laboratory, Upton, New York, 1973.